Universitá degli studi di Padova

Dipartimento di fisica e astronomia “Galileo Galilei”

Corso di laurea magistrale in Astronomia

Redefining radio-loudness for low redshift quasars

Relatori

Prof. **Mauro D’Onofrio**

Prof.ssa **Paola Marziani**

Laureando: **Valerio Ganci**

Matricola: **1149652**

Anno accademico 2017/2018

Abstract

Nowadays it is thought that all Active Galactic Nuclei (AGNs) are different manifestations of the same physical process that is, accretion onto a super massive black hole (SMBH). Through the years, AGN have been observed showing different characteristics one from the other in almost all wavelength ranges. Different classes were defined on the base of radio morphology and optical spectroscopic features. Different attempts were made to unify all these classes, but the issue is still open. Unification schemes explain the differences among AGNs through the effect of the viewing angle. An AGN seen edgeways will show only narrow lines due to the presence of a thick torus obscuring the broad line region and not the narrow line region (type-2 AGN). Anyway, other aspects are not explained by Unification scheme. A first one is the diversity of properties in type-1 AGNs. A second one is the dichotomy between radio-loud (RL) and radio-quiet (RQ, but not radio-silent!) AGNs. To obtain more clues on this problem, we start by identifying all radio-detected type-1 AGN. The sample was selected by the cross-match between the Faint Images of the Radio Sky at Twenty-Centimeters (FIRST) Survey and the 12th data release of the Sloan Digital Sky Survey Quasar Catalogue by Paris et al. (2017). Sources were selected up to redshift 1 and according to a flux limit at magnitude i = 19.5. The sample was then split into three subsamples on the basis of their radio power estimated by the Kellerman parameter (R_K). We defined radio-detected (RD, $R_K < 10$), radio-intermediate (RI, $10 < R_K < 100$) and RL ($R_K > 100$) samples. The three samples are analyzed in the Hβ spectral range, isolating spectral types along the quasar main sequence defined by Sulentic et al. (2000) and Shen & Ho (2014) which organized the diversity of type-1 AGN properties. We also explored the effectiveness of the RL/RQ selection criterion recently set forth by Bonzini et al. (2015) who identified RLs by their deviation from the correlation between far-infrared (FIR) and radio luminosity. We could locate only seven of our objects in the FIR- vs. radio-power diagram of Bonzini et al., and we obtained results consistent with the ones based on the RK parameter. For each spectral type and for different radio-power classes and morphologies, a composite median spectrum is computed in order to find possible correlations between spectroscopic characteristics and radio properties. The results obtained can be listed as follows.

• *E1 parameter space characteristics.* The concept of two populations A and B (FWHM$H\beta < 4000 km/s$ for the former and FWHM$H\beta > 4000 km/s$ for the latter) manifests itself in the E1 parameter space with population A characterized by an Hβ broad component best fitted by a Lorentzian profile and the population B by two Gaussians. The anti-correlation between the [OIII] doublet line intensity and the FWHM(Hβ) with the FeII emission blend is also observed but not in RI/RL classes. These results, with the measures of the Eddington ratios and BH masses, reinforces the idea that the two populations correspond to different systems in term of accretion and dynamical characteristics.

• *Radio power emission classes distinction.* RD sources are found in the core-dominated (CD) class but not in the Fanaroff-Riley II (FRII) ones. Population A sources are present in a significant way only in CD AGN. RI and RL objects do not show differences in their optical spectra. Differences show up between population A RI/RL and RD objects. Endeed the [OIII]-FeII anticorrelation is only followed by the RD class. Instead in the RI-RL classes the [OIII] emission lines are still strong even in xA bins. Finally, we notice a different behaviour of the Hβ and [OIII] centroid shifts $c(x)$ in the different radio-power classes. The broadening of optical and UV emission lines is thought to be associated with the Doppler effect reflecting emitting gas motions relative to the observer. High ionization line blueshifts suggest the presence of an outflow. The [OIII] lines in the RD and RI classes can be considered asymmetric, i.e. the line is blueshifted only close to the base, but not in A2 and xA objects where the whole [OIII] lines show a blue-shift. Instead in the RL class the sources show almost symmetric [OIII] and only in the xA bins the lines are systematically blue-shifted. As regard to the broad Hβ components we see that, going bins with higher FWHM(Hβ) the line gets more redshifted. Moreover, the amplitude of the centroid line $c(x)$ displacement is higher for RL sources.

Contents

CHAPTER 1

Introduction

1.1 Active galactic nuclei

Active galactic nuclei (AGN) are the most energetic persistent objects in the Universe and are observed in the center of some galaxies. The first evidence of the hosting of these strongly emitting components was found by Carl Seyfert in the 1940s. Analysing six galaxies spectra, he noted high-excitation nuclear emission lines superposed on a normal star-like spectrum; moreover some galaxies showed broad emission lines, others only narrow ones.

There are several observational aspects that made AGNs peculiar objects, really different from sources already known in the 1940-50s. The first observed characteristics were the presence of emission lines with widths larger than 1000 kms^{-1} and the fact that the centers of these broad emission lines did not correspond to the laboratory wavelengths of any known atomic species. This is explained by the super massive black hole (SMBH) model through the deep gravitational potential of the BH itself, responsible for the dynamical broadening of the observed lines. The problem with the line identification was solved with the realization of the distances involved; for example in the case of 3C273, Martin Schmidt, solving the unidentified lines problem by matching lines of the Balmer series mesured a redshift of $z = 0.158$ that, by the Hubble law, it translates into a distance near to 500 Mpc and a luminosity 100 times greater than normal galaxies.
The second characteristic is the presence of narrow, non-variable forbidden emission lines similar to those of galactic nebulae, however the AGN narrow lines require a broad-band ionizing continuum extending far bluewards of the stellar radiation fields responsible for photoionizing the galactic nebulae and a peculiar structure called big blue bump (BBB) [141] interpreted as the first observational evidence of an accretion disk surrounding the BH [101]. Finally, with the improvement of radio interferometry techniques, it was possible to notice that some AGN show highly collimated, bipolar outflows or jets from their core. The generation and propagation of these AGN jets, the amount of energy produced and the enormous size remains unexplained in many regards and make a hot topic in modern astrophysics.

Various kind of AGN were discovered and grouped in different classes through years of observations. First we will talk about the most important ones with their defining characteristics and then we will consider the possible scenarios for their unification.

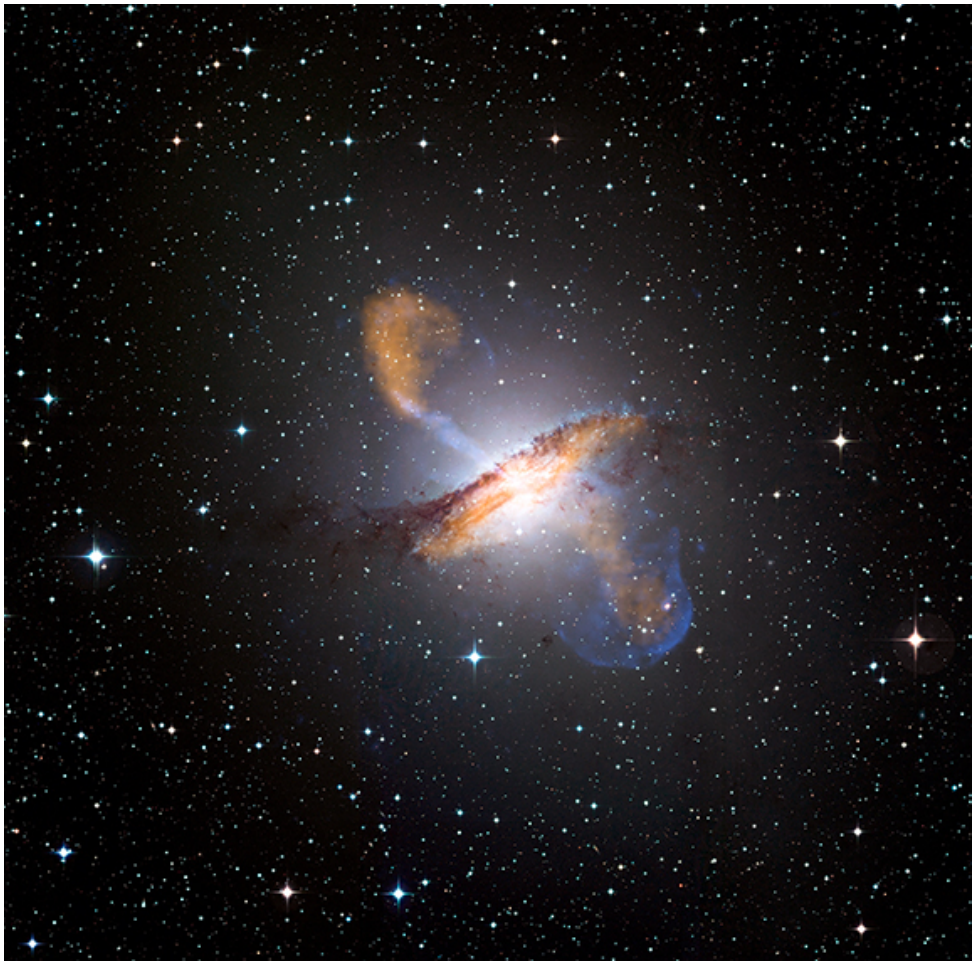

Figure 1.1: Colour composite image of Centaurus A obtained with three instruments. The 870-micron submillimetre data, from LABOCA on APEX, are shown in orange. X-ray data from the Chandra X-ray Observatory in blue. Visible light data from the Wide Field Imager (WFI) on the MPG/ESO 2.2 m telescope in close to "true colour". Image taken from The European Southern Observatory (ESO) website.

- **Radio-quiet and Radio-loud AGN**.

  Historically all the AGNs were classified in two dinstinct classes called radio-loud (RL) and radio-quiet (RQ). This classification goes all the way back to Sandage (1965), who discovered, soon after the discovery of the first quasar 3C 273 (a very strong radio source), that there were many similar sources in the sky which were however undetected by the radio telescopes of the time. These RQ objects make up the large majority ($> 90\%$) of the AGN class (e.g., [133]).
  It was later realized that these quasars emit in the radio range but the emission is really weak, as for the same optical power their radio power were $\approx 3 - 4$ orders of magnitude smaller than their RL counterparts.

The two classes represent intrinsically different objects, with most RL AGN emitting a large fraction of their energy non-thermally over the whole electromagnetic spectrum while the multi-wavelength emission of RQ AGN is dominated by thermal emission related to the accretion disk which forms around the SMBH.

RQ and RL AGNs differ clearly in the presence or absence of a strong relativistic jet hence nowdays these classes are called also jetted and non-jetted AGN [134]. In the hard X-ray to γ-ray band many RL sources emit all the way up to GeV energies, while nearby RQ bright Seyfert galaxies have a sharp cut-off at energies $\lesssim 1MeV$ (e.g., [100]). This cut-off has to apply to the whole RQ AGN population in order not to violate the X-ray background above this energies [34]. Furthermore no RQ AGN has ever been detected in γ-rays [2].

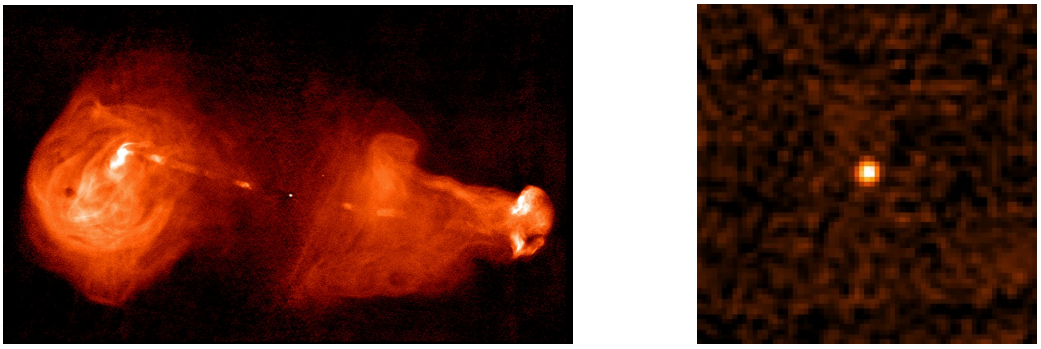

Figure 1.2: Left: radio map at 1.4 GHz of Radio-Loud galaxy 3C353; image courtesy of National Radio Astronomy Observatory (NRAO). Right: radio map at 1.4 GHz of radio-quiet galaxy taken from the FIRST catalouge.

- **Seyfert galaxies, type I-II AGN**.

Seyfert galaxies are usually spiral galaxies which host a bright ($10^{11} - 5 \times 10^{12} L_{\odot}$), star-like active nucleus. The original definition of the class was proposed by Seyfert according the morphology, i.e. galaxies with high surface brightness nuclei. Subsequent spectroscopy studies revealed unusual emission-line characteristics and the definition has evolved so that Seyfert galaxies are now identified spectroscopically by the presence of strong, optical, UV and IR emission lines.

There are two subclasses of Seyfert galaxies found by Khachikian and Weedman in the 1970s which are distinguished by the presence or absence of broad bases on the permitted emission lines. Type 1 Seyfert galaxies have two sets of emission lines, superposed on one another. One set includes lines from permitted and forbidden transitions and is characteristic of a low-density (electron density $n_e \approx 10^3 - 10^6$ cm^{-3}) ionized gas. These are referred to as the narrow lines with widths of several hundred km/s. The second set is due to broad lines arising from dense matter ($n_e \approx 10^9 cm^{-3}$) with widths ranging from 1000 km/s to 20000 km/s at the line base. The two sets of lines are emitted in different regions, called the broad line region and the narrow line region respectively. The presence of broad lines is a defining feature of type-I AGN, a more general class which includes also quasars since they show emission line properties very similar to that of Seyfert 1 nuclei.

Type 2 Seyfert galaxies show permitted and forbidden strong emission narrow lines ($300 - 1000 km/s$) and no broad permitted lines showing indications of photoionization by a non-stellar source. The absence of broad lines, that defines the type-II AGN class, has been explained with the presence of a thick torus of molecular gas that completely obscure the central source in some directions. The model is yet a subject of debate; more information will be given in the next section.

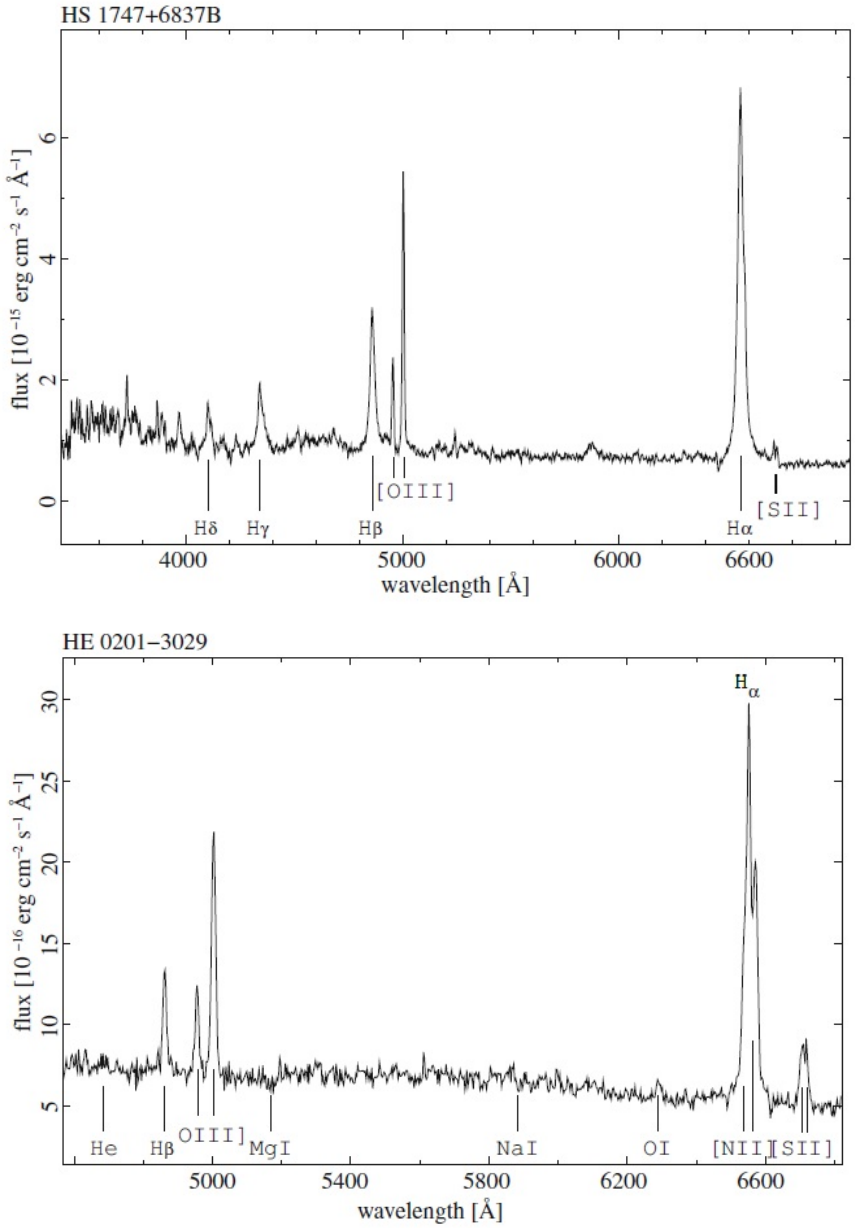

Figure 1.3: Top: Optical spectrum of the narrow-line Seyfert 1 galaxy HS 1747 +6837B. Bottom: Optical spectrum of the Seyfert 2 galaxy HE 0201-3029. Images taken from [10]

- **Radio galaxies**.

  Radio galaxies (RGs) are usually giant elliptical. They are characterised by relativistic jets extending beyond the galaxy itself and by GHz radio power emission higher than $10^{22}\ WHz^{-1}$(e.g. [93]). Their GHz spectra show an index $\alpha \approx 0.7$; this suggests an extended source emitting synchrotron radiation at relatively high frequencies where they are optically thin, which implies the existence of fast electrons moving in a magnetic field. However there are compact radio sources that show also a steep-spectrum; usually their spectra are flatter due to synchrotron self-absorption. Together with GHz peaked-spectrum, they are generally considered to be young radio sources.

  During the Seventies Fanaroff and Riley found out that RGs separate into two distinct luminosity classes, each with its own characteristic radio morphology. The first one, called Faranoff-Riley (FR) I, is characterised by lower luminosity and by a diffuse radio emission with smooth two-sided and poorly collimated jets. The second one, called FR II, has higher luminosity and shows edge brightened lobes, often with prominent hot spots at the inner end of the lobes, connected to the nucleus by thin jets that in some source are difficult to see. The distinction between the two classes manifests clearly at 178 MHz, with FR Is and FR IIs lying below and above, respectively, the fiducial luminosity $P_{178MHz} \approx 10^{26}/(H_0/70)^2\ WHz^{-1}$.

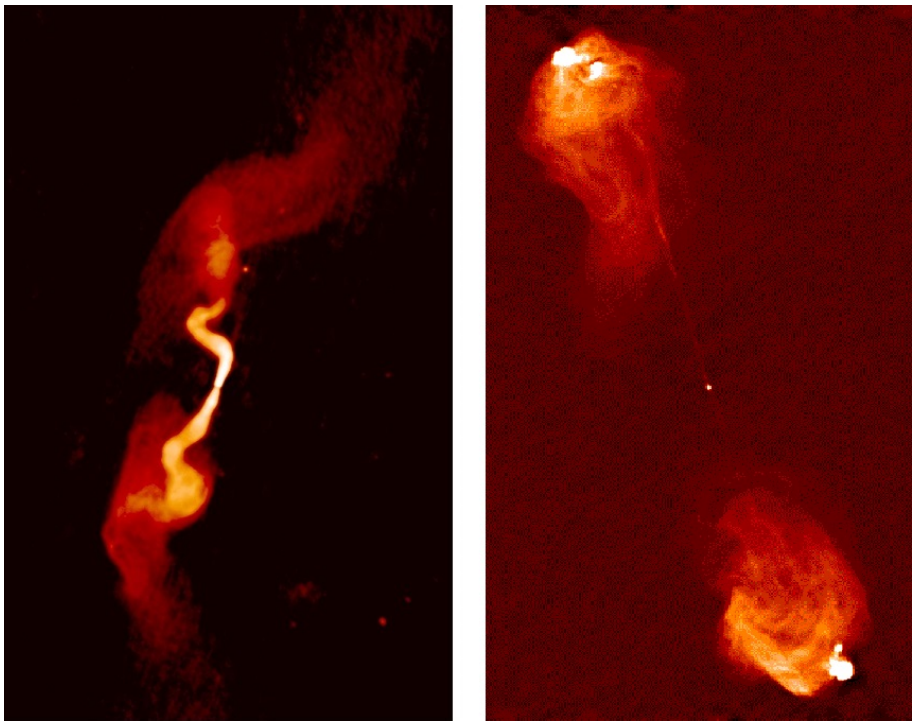

Figure 1.4: Left: radio map at 1.4 GHz of FR-I galaxy 3C31. Right: radio map at 1.4 GHz of FR-II galaxy Cygnus A. Images from NRAO.

The optical spectra of RGs display the absorption features associated with an old stellar population, with some also revealing powerful high ionization emission lines, and others instead weak low ionization emission lines. Indeed the FR classes differ also in their emission line properties [70], with FR IIs producing, for the same radio power, 5 - 30 times as much emission line luminosity [182] than FRI.
Researchers point out that this could be due to different central engines (e.g., [60]): low accretion rate sources produce weak jets and display FR I-type structure meanwhile higher accretion rates sources generate stronger and FR II-type jets.

The different accretion rates have also been related with the excitation mode of the narrow line region gas in the host galaxy [89]: in low-excitation RGs the accretion on to the black hole is thought to be radiatively inefficient [30], while high-excitation RGs, are instead linked to radiatively efficient accretion discs of the type discussed by Shakura and Sunyaev (1973). Heckman and Best (2014) used the terms *jet-mode* and *radiative-mode* for these two classes, respectively.
The radiative-mode AGN are associated with black holes that produce radiant energy powered by accretion, in an high density cold gas environment associated with on-going star-formation, at rates in excess of $\sim 1\%$ the Eddington Limit.
The jet-mode AGN is associated with the more massive black holes in the more massive bulges and elliptical galaxies. Neither the accretion onto these black holes nor star-formation in their host bulge is significant today. The two classes show different Eddington ratio with radiative-mode and jet-mode sources typically above and below $L/L_{Edd} \approx 0.01$ respectively (e.g., [68]). The two FR classes have both jet and radiative-mode sources but the majority of FR I are jet-mode meanwhile the majority of FR II are radiative-mode [58].

- **Radio Quasars and Blazars**.

Quasars were originally defined to be star-like (quasistellar) objects with large redshifts. Nowdays there is plenty of evidence indicating that RL quasars are simply FR II/radiative-mode RGs with their jets at an angle $\lesssim 45^\circ$ with respect to the line of sight [173]. Anyway RL quasars display strong and Doppler broadened lines in their spectra unlike RGs; this is explained by the presence of dust in a torus configuration, roughly perpendicular to the jet. The broad lines, emitted by clouds moving fast close to the black hole, can be seen only looking inside the torus while for RGs the central nucleus and the nearby surrounding like the broad line regin are obscured by the torus. Quasar spectra are similar to those of Seyfert galaxies but stellar absorption features are very weak and the narrow lines are generally weaker relative to the broad lines than is the case in Seyfert galaxies. Moreover Seyfert galaxies have a lower luminosity AGN and the host galaxy is visible.

As regards FR I-II/jet-mode RGs, obscuration towards their nuclei appears to be much smaller than that of FR II radiative-mode RGs (e.g., [50]), which indicates, also with their weak IR emission, that a torus might be not present. For this reason jet-mode RGs, irrespective of their radio morphology, are unified with BL Lacertae objects (BL Lacs), a class of AGN with very weak emission lines. BL Lacs, together with flat-spectrum radio quasars ($\alpha \leq 0.5$), make up the class of blazars.
A blazar is a very compact quasar with jets oriented at a very small angle ($15 - 20°$) with respect to the line of sight. It shows extreme properties, including relativistic beaming, superluminal motion, large and rapid variability, and strong, non-thermal emission over the entire electromagnetic spectrum [173].

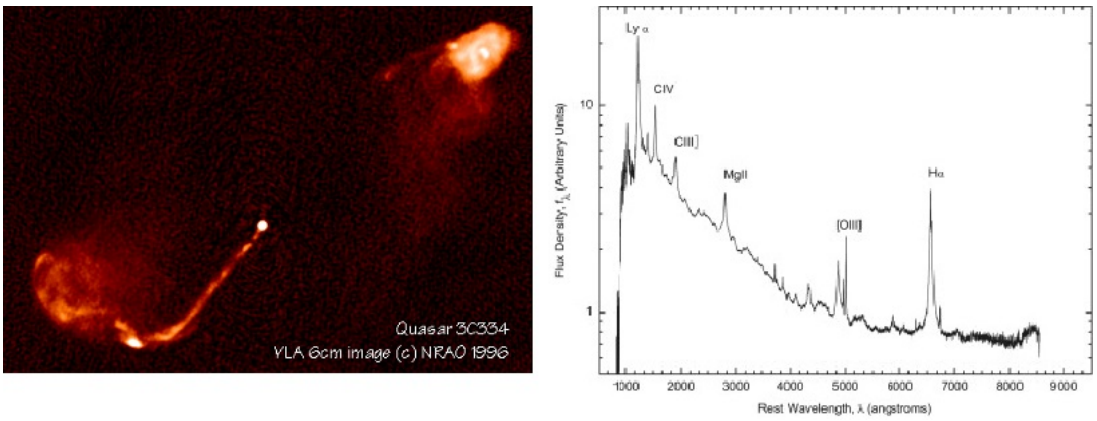

Figure 1.5: Left: radio map at 1.4 GHz of quasar 3C334; image from NRAO. Right: composite quasar spectrum from Vanden Berk et al. (2001)

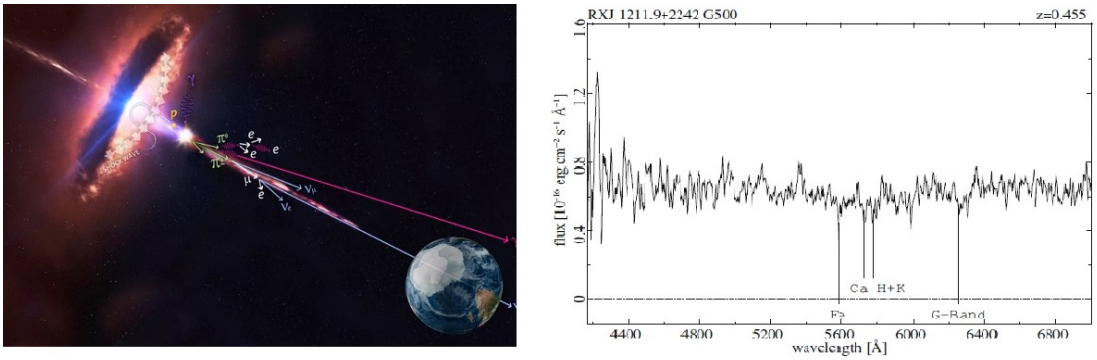

Figure 1.6: Left: blazar artistic representation from the IceCube/NASA website. Right: blazar RX J1211.9C2242 spectrum from [10]

- **LINERs**.

  LINERs are a very low nuclear-luminosity class of low-ionization nuclear emission-line region galaxies identified by Heckman (1980). They are the most common type of active nuclei. Their optical and UV spectra have notable differences from classical Seyfert 1 and Seyfert 2 galaxies, namely lower nuclear luminosity, and stronger forbidden lines from low-ionization species, such as neutral oxygen and singly and doubly ionized nitrogen.
  The ionization mechanism of the line-emitting gas is unclear. An explanation sees LINERs as the lowest luminosity active galactic nuclei, photoionized by a non-stellar continuum weaker than that of more powerful active nuclei. In alternative, gas may be heated mechanically by shocks, or may be photoionized in dense clouds embedding hot stars of the first spectral types. LINERs are frequently observed in the nuclei of both spiral and elliptical galaxies, and might be detectable in nearly half of all spiral galaxies.

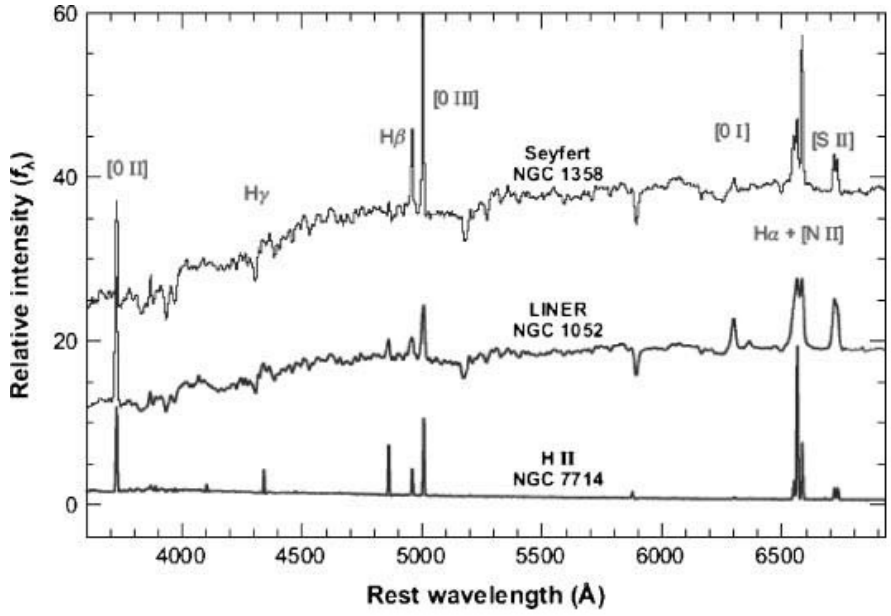

Figure 1.7: Three optical example spectra showing the differences between a typical Seyfert 2 galaxy, a LINER and an HII galaxy.

1.2 Unification models

The most general AGN is tought to include the majority of the following components as described in [4, 129] and visualized in the next image:

- a massive ($> 10^5 M_{\odot}$) accreting black hole with Eddington ratio exceeding the limit of $L_{AGN}/L_{Edd} = 10^{-5}$, where L_{AGN} is the bolometric luminosity and $L_{Edd} = 1.5 \times 10^{38}(M_{BH}/M_{\odot}) ergs^{-1}$ is the Eddington luminosity for a solar composition gas.
- a rotating accretion disk that can be optically thick or thin with a size of $\sim 0.001 - 0.01pc$.
- The broad line region, a region with high density, dust-free gas clouds moving at roughly Keplerian velocities at a luminosity dependent distance of $0.01 - 1pc$ from the BH.
- an axisymmetric dust structure with a toroidal geometry surrounding the central accretion disk and with luminosity dependent dimensions of $0.1 - 10pc$.
- the narrow line region, a region with lower density, lower velocity ionized gas extending from just outside the torus to $\sim 100 - 1000pc$ along the direction containing the torus' holes. Dust is present except in a very inner region referred to as *the coronal line region*.
- A central radio jet, an ejection of matter at velocity close to the speed of light, occasionally associated with γ-ray emission. Their linear size range from 1 pc to tens of kpc for the most powerful radio galaxies.

Since the current perspective is to hypothesize a common type of central engine at the core of all these different AGN, an effort is being made to try to unify disparate subclasses and to explain the large diversity of observed AGN properties by a small number of physical parameters.

The unification scheme proposed by Antonucci in the early 1990s, tries to combine the AGN sub-groups into a general picture through two parameters: the torus inclination with respect to the line of sight (LOS) and the source luminosity. First let's analyze the distinction between the various types of sources made by the model based only on the viewing angle without considering for the moment the differences between radio-loud versus radio-quiet (or jetted vs non-jetted) AGN.
In this case the differences between the AGN populations is assumed to be caused by the different level of absorption in the LOS especially due to the torus. The model predicts that the BLR should be at smaller radii than the absorbing material, whereas the narrow-line region resides further out. The model is based on the spectral differences between the two types of Seyfert galaxies, mainly the precence or absence of broad emission lines. The discovery of broad Balmer lines in polarized light in the prototype Seyfert 2 galaxy NGC 1068 and in other nearby Seyfert 2 nuclei by Antonucci and Miller (1985), was a strong argument in favor of the unification model; free electrons slightly above the torus should scatter the broad line photons into the line of sight, letting them be detected only in polarized light. Moreover the narrow forbidden lines showed little or no polarization at all, confirming that the NLR is observed directly. However some type-II Seyfert galaxies were found with no hint for polarized broad lines.

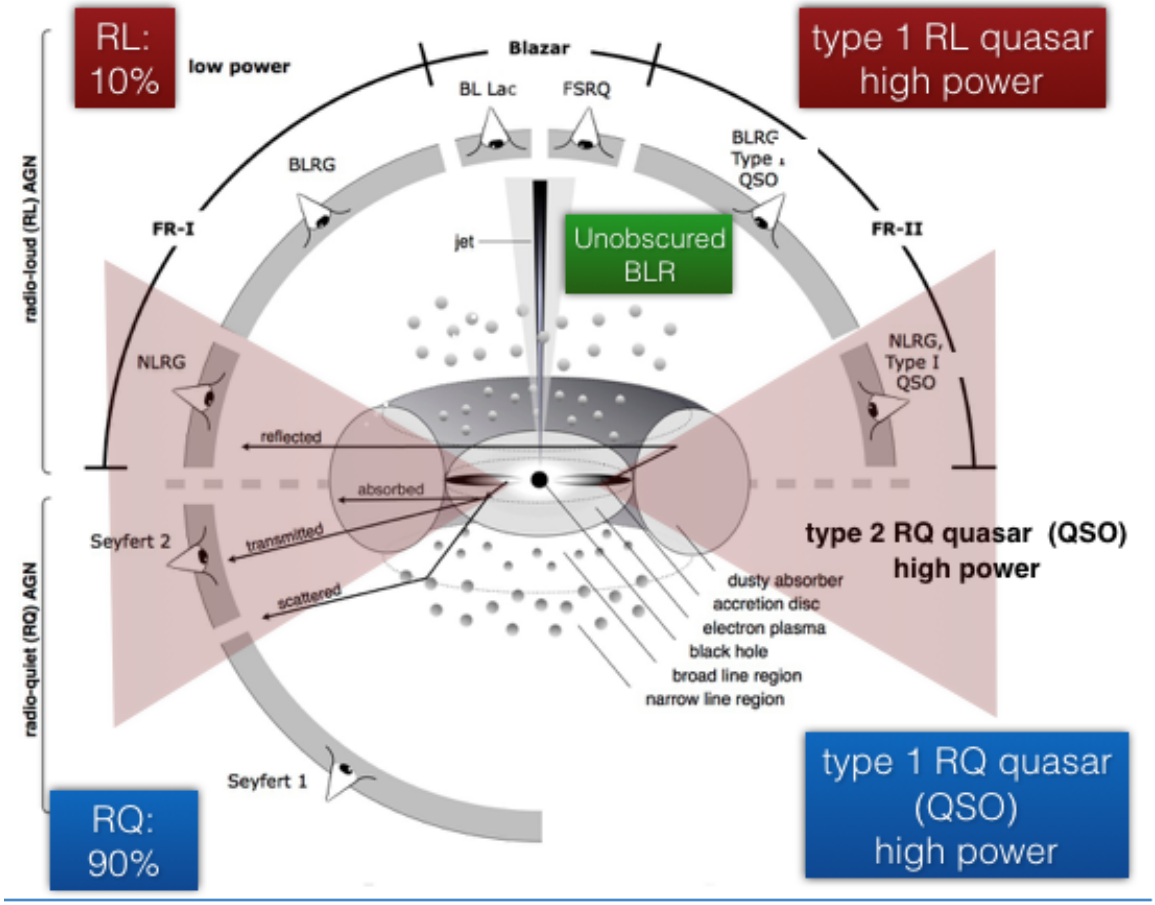

Figure 1.8: An artistic depiction showing the AGNs unification model. Image from [10], graphic by Marie-Luise Menzel, annoted by Paola Marziani.

Later works ([63], [169]) found that those which show polarized broad lines are mainly the AGN which have a very powerful central engine and thus a high accretion rate. Broad emission lines would only be created in objects with a relatively high Eddington ratio $L_{AGN}/L_{Edd} > 0.001$. Anyway the nondetectability of the broad-line region does not necessarily unvalidate the unification, but adds the strength of the AGN activity as another dependency.

Other problems arised from later studies. Since the central engines of different AGN types are supposed to be the same, then the average unabsorbed luminosity should be the same as well. It is convenient to use the $[OIII]$ line at $\lambda = 5007\mathring{A}$ that is a strong indicator of AGN power. Moreover since it is a narrow forbidden line, it should be produced outside of the absorbing material and his strength not be affected by a possible jet. So, for example, flat spectrum radio quasars and radio galaxies of similar power should have similar $[OIII]$ line strengths. This result was found by Dicken (2009) but the opposite one was found by Jackson and Browne (1990). More of these opposing cases showed up also in the Seyfert types [87] and made the narrow line tests inconclusives.

Later investigations have tried to explain the differences between the Seyfert types, which cannot be covered in the unified model. Considering only the viewing angle as a parameter is not enough to explain all the differences between the AGN classes especially the dichotomy between RL (broad-line radio galaxies, radio-loud quasars, FR-I, FR-II) and RQ AGN (Seyfert galaxies, LINER). A second parameter could be the BH mass. Indeed a correlation of the radio luminosity with BH mass had been found in several investigations (eg., [53], [127]) in the form of $L_r \propto M_{BH}^{2.5}$, for both RL and RQ AGN. So a strong radio emission, and therefore a strong relativistic jet, is connected to the higher mass central engine.
A similar correlation was found between the BH mass and the radio-loudness of the AGN; for example Laor (2000) discovered that almost all of the quasars he studied with $M_{BH} > 10^9 M_\odot$ are radio-loud while almost the ones with $M_{BH} < 3 \times 10^8 M_\odot$ are radio-quiet. From this we can think that L_{bol}/L_{Edd} could be a good parameter as well.
However a different result was also found by Ho (2002) as the $L_r - M_{BH}$ relation appears to be $L_r < M_{BH}^{2.5}$. Moreover it showed an anticorrelation between the radio-loudness and the Eddington ratio. From this we infer that objects accreting at a low rate do not have a prominent accretion disk and therefore show a weak thermal disk emission and a weak blue bump. Later and more extended studies ([153, 24]) showed that scatter of the Eddington ratio versus radio-loudness gets wider and then it was explained with the BH spin: if the rotational energy of the BH can be extracted through the interaction with an external magnetic field, for instance from the accretion disk, then powerful jets can be produced.

We see that the separation of AGN into sources with and without a jet is more complicated than it was tought in the past. Future high-quality data of AGN and future studies will reduce the differences between the two classes and will tell if the BH spin can solve the problem.

1.3 SED

AGNs are observed to emit in a wide range of wavelenght namely from radio to X-rays or in some cases even to γ-rays. This opens different channels on the AGN physics; in fact as we can see in the graph below, it is clear that the entire AGN emission cannot be due to a single component. Moreover we note that jetted and non-jetted sources show a very different spectral energy distribution (SED).

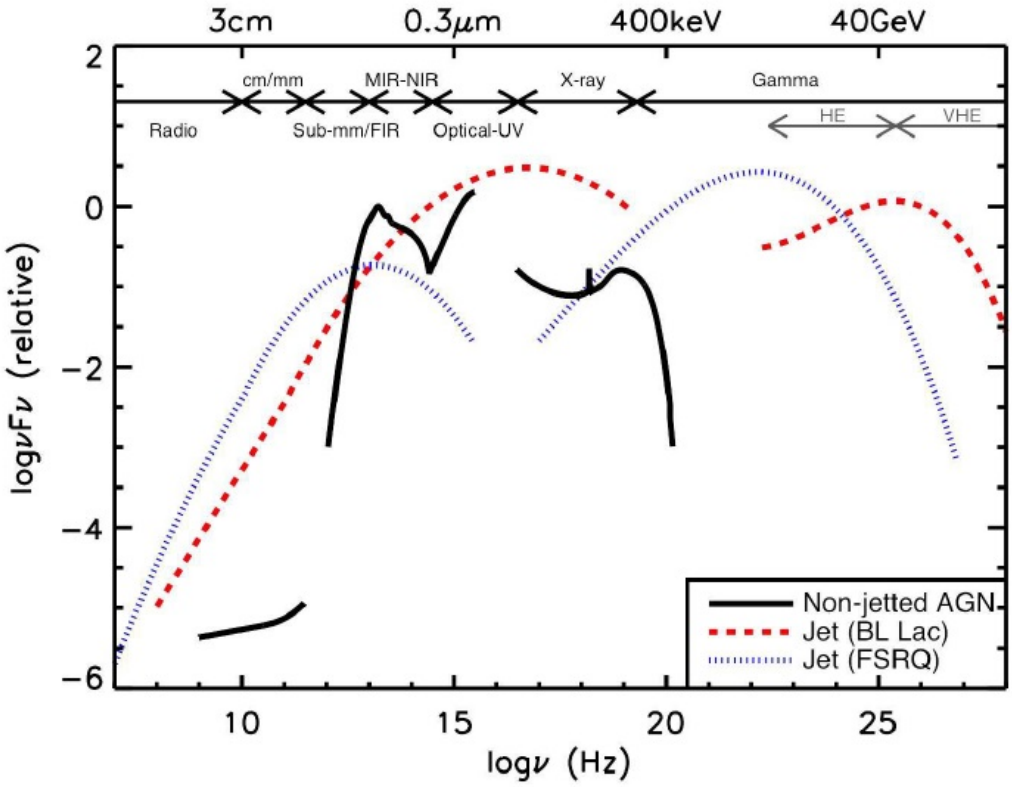

Figure 1.9: Schematic representation of AGN spectral energy distribution. Image from [135]. Image credit: C. M. Harrison.

Non-jetted sources have more complicated SED than jetted ones since the former ones lack jets that would outshine all the other emitting components. So in the radio band the nonthermal emission is missing or barely visible. For this reason these AGNs show a steep spectra with $\alpha = 0.7$ for $S_\nu \propto \nu^{-\alpha}$, where S_ν is the flux density at frequency ν, and α is the spectral index, and exhibit a brightness temperature of $T_B \geqslant 10^5 K$ [88]. Furthermore their SED turns over sharply in the far-IR and the radio emission is 100-1000 times weaker than jetted AGNs ones. The emission in this band is tought to derive from SMBH accretion-related processes in the innermost region not farther than 1 kpc from the central engine for the majority of non-jetted AGNs but opposing evidence were found that gives more importance to star formation in the host galaxy [39] and/or to AGN activity [134].

The SED infrared range can be caotic since different components contribute and the dominant one changes from AGN to AGN. One of the most important is the dust torus emission. The dust, present from a region farther than the limit set by the dust grains sublimation temperature [9], surrounds the accretion disk and absorbing its high energy emission re-emits into the IR from $\sim 1\mu m$ to a few tens of micron. Another process that can occur and give a contribution to the FIR emission is star formation that can be dominating in the IR [67]. The starlight is absorbed by the HII regions gas and then re-emitted by a thermal free-free process. It should be noted that there is also another emission near these wavelenght that should not be attributed to the star formation process. This stems from gigantic clouds of infinitesimally small interstellar dust particles, referred as galactic cirrus, at a lower temperature ($T \sim 20K$) than that of HII regions ($T \sim 60K$). The plots below show the SEDs for two sources strongly affected by the host galaxy (top) and for two sources (bottom) with a SED dominated by AGN emission. In the bottom panels we see a minimum in the SED at $\sim 1\mu m$ due to the different spectral index of the accretion disk and dust emissions. Instead in the top panels the free-free emission overcome these two processes leading to a different SED shape.

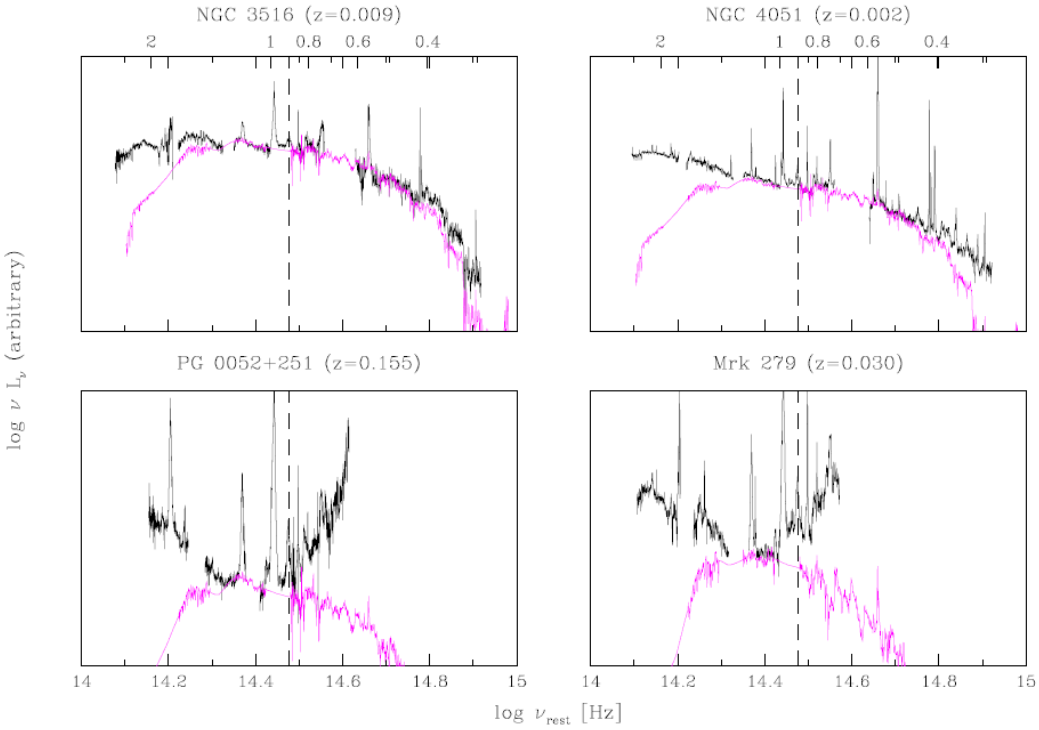

Figure 1.10: Rest-frame SEDs for NGC 3516 and NGC 4051 that are strongly affected by the host galaxy (top) and for PG 0052+251 and Mrk 279 having a SED dominated by AGN emission. Figures from [91]

In the UV/optical band both non-jetted AGNs, and also some jetted ones, are characterized by a broad emission peak at around $\lambda = 1100$Å called big blue bump (BBB) [150]. From its shape it is thought to be due to thermal emission from gas in the optically thick accretion disk [152] that become hotter getting closer to the central engine. Another source that is thought to be the origin of the BBB is a population of cold ($T \sim 10^4 K$) and thick clouds [92]. These absorb and re-emit the extreme UV emission of the central engine and since the clouds are orbiting the BH the line emission would appear like the BBB. However the first case has something that goes in his favour.

Scott et al. (2004) showed that the low luminosity objects observed by the Far Ultraviolet Spectroscopic Explorer (FUSE) had bluer spectra than AGN with large UV luminosity taken by the Hubble Space Telescope (HST). If the emission is generated by the accretion disk then low luminosity objects would have higher temperature disks with respect to the high luminosity objects ones and this is consisten with the Baldwin effect: an anticorrelation found by Baldwin between AGN luminosity and the emission line equivalent width. This means that the larger is the ionizing power the bluer the UV spectrum becomes [7], as indicated by decreasing luminosities.

Talking about the X-emission range, the non-jetted AGN emission stem from processes occuring in the accretion disk and the major one is thought to be inverse Compton scattering of the accretion disk photon [149] via a corona surrounding the disk itself. This model made by Liang (1979) is based on the fact that the X-ray and UV emission have almost the same power so we predict that the two former band emission regions are at nearly the same distance from the central engine. The model was improved by Haardt and Maraschi (1991, 1993) in a way that explains and couples the three main components: the disk photons, the inverse Compton photons and the Compton reflection component. The accretion disk provides multicolor black body spectrum photons in the optical/UV range meanwhile the relativistic electrons necessary for the inverse Compton scattering are located in a hot electron plasma in the form of a corona surrounding the accretion disk. As the disk photons cool the corona electrons, the majority of the Comptonized photons will be absorbed heating the accretion disk and a minority will be reflected.
Above energies of the order of 100keV, the non-jetted AGN spectrum shows a cutoff and indeed in the γ-ray range a non-jetted AGN has never been detected [2].
Summarizing, in non-jetted AGN the SED has a multipeak structure with local maxima in the infrared, optical/UV band, and in the X-rays.

In regard to jetted AGNs, as we already mentioned, these are characterized by non-thermal spectra and polarization. Thanks to the unification models we can reassume the SED of all jetted AGNs with the one of blazars. Their emission stem from synchrotron emission or/and inverse Compton that overshine the other processes. The former process translates to a power-law shaped photon spectrum and so to the hump in the SED radio-optical range. The latter leads to the SED second hump peaking in the X-ray to γ-ray domain. Two major models try to interpret the second hump. Leptonic models (e.g.[104]) explain the emission through inverse Compton scattering between the electron in the jet and their own synchrotron emission (synchrotron self-Compton) or an external photon fiels (external inverse Compton). Hadronic models (e.g. [23]) instead through high-energy protons either loosing energy via synchrotron emission [3] or via photo-meson interactions [103]. In this case neutrinos would also be emitted by the blazars whom SED would extend outside the electromagnetic spectrum [134].

More informations about thermal and non-thermal processes will be given in upcoming sections. Finally, we remind that overimposed to the AGN continuum there are several emission lines called broad and narrow lines, on the base of their FWHM, that stem from regions close to the AGN with different physical and geometrical conditions, called broad-line and narrow-line regions already mentioned.

1.4 AGN and Quasars physical interpretation as accreting BHs

1.4.1 Bondi accretion and Eddington luminosity

The idea of a supermassive black hole (SMBH) in the center of AGN was firstly proposed by Salpeter, ZelDovich and Novikov during the Sixties soon after the discovery of 3C273. Indeed, since its light days size set from its variability time scale and its inferred luminosity of $\sim 10^{47} erg$, a dense conglomeration of stars is not enough to explain these properties. Instead the SMBH model explained the large energy output based on the release of gravitational energy through accretion phenomena, the compact size of the emitting regions and the short variability time scales.
In this section we review the general properties of black holes and the accretion processes following the general relativy (GR) approach of Blandford (1990) and Netzer (2013).

The only properties a stationary (Schwarzschild) black hole it's tought to possess are mass, charge, and angular momentum. To describe them it's common to define the gravitational radius r_g as $r_g = GM/c^2$ where M is the BH mass. If one wants to deal with rotating (Kerr) BHs, Thorne [167] defined two other useful quantities: the angular momentum of the BH, $s \sim I\Omega \simeq Mr_g v$, with Ω the angular velocity at the horizon, and the specific angular momentum of the BH, s/M. The second one is usually re-written as $s/M = ar_g c$, where a is a parameter defined such that $\alpha = ar_g$ and α defined such that $s/M = \alpha c$. So a can be between -1 and 0.998$\sim$ 1 where opposite sign means opposite rotation direction. Once these parameter are defined one can solve the GR line element near a rotating BH to get the location of the BH event horizon, a region where the gravitational escape velocity equals the speed of light so it's a boundary in through which matter and light can fall inward towards the black hole, but can never re-emerge. The equation was first derived by Kerr in 1963, reported in Boyer-Lindquist coordinates:

$$ds^2 = (1-\frac{2r_g r}{\Sigma})c^2dt^2 + \frac{4\alpha r_g r sin^2\theta}{\Sigma}dtd\phi - \frac{\Sigma}{\Delta}dr^2 - \Sigma d\theta^2 - (r^2+\alpha^2+\frac{2r_g r\alpha^2 sin^2\theta}{\Sigma})sin^2\theta d\phi^2,$$

where $\Sigma = r^2 + \alpha^2 cos^2\theta$, and $\Delta = r^2 - 2rr_g + \alpha^2$.
In the case of stationary holes, where $a = 0$ and $\alpha = 0$ the solution is the Schwarzschild radius $r_s = 2r_g$. For Kerr BHs, setting $\Delta = 0$, there are instead two event horizons $r_\pm = r_g[1 \pm (1-a^2)^{1/2}]$. In addition at the event horizons the Kerr metric also features a surface of interest called the static limit, given by $r_0 = r_g[1 + (1 - a^2 cos^2\theta)^{1/2}]$, and the region between r_0 and r_+ is called ergosphere. With GR we can also calculate the orbits of particles in the vicinity of BHs in order to find the location of the innermost stable circular orbit (ISCO) or the marginal stability radius, r_{ms}. Its value sets the fraction of the gravitational potential energy that is converted to electromagnetic radiation during the accretion process since a particle going beyond the r_{ms} falls directly into the event horizon. The fraction is higher for smaller r_{ms}. The value of r_{ms} depends on the nature of the BH, namely stationary or rotating ($6r_g$ for stationary BHs, $1 \leq r_{ms} \leq 6r_g$ varying with a for Kerr BHs), the direction of rotation ($a < 0$ and r_{ms} is higher) and also the nature of the accretion disk which we will talk about in the next section.

In general, the efficiency of converting rest mass to electromagnetic radiation, due to the infall of mass m from infinity to r is $\eta = [E(\infty) - E(r)]/mc^2$ and the BH mass increase due to the fall of this mass in the BH itself is $(1-\eta)m$. From GR calculations one can demonstrate that, for an ISCO at a normalized radius $x = r/r_g$, the efficiency is $\eta = 1 - [1 - 2/(3x)]^{1/2}$. Examples are shown in the table below with different a values.

Table 1.1: Mass-radiation convertion efficiency factor η for different values of a and r_{ms}/r_g.

a	r_{ms}/r_g	η
-1.0	9.0	0.038
0	6.0	0.057
0.1	5.67	0.061
0.5	4.23	0.082
0.9	2.32	0.156
0.998	1.24	0.321
1.0	1.0	0.423

Focusing now on the accretion processes, these are geometry dependent and can happen in various different ways but theoretical arguments support disk accretion scenarios [82]. Considering first the simplest case, that is a spherically symmetric accretion reffered as Bondi accretion [19], this starts in a distant region from the BH where the gas is at rest. We can make a simple estimate of the spherical accretion rate of a hot gas, with constant temperature and no radiation pressure force, writing a mass conservation equation $\dot{M}_{Bondi} = 4\pi\lambda v_s \rho r_a^2$, where $v_s = \sqrt{\gamma kT/\mu m_p}$, is the sound speed in the gas with μ being the mean atomic weight per particle and γ the adiabatic index of the gas, λ is a correction factor of order 0.1 that depends on γ and $r_a = 2GM/v_s^2$ is an accretion radius within which the gravitational potential of the BH overcome the thermal energy of the surrounding gas, with M being the BH mass.
Anyway the accretion is quenched by the effects of the radiation pressure by which the in-falling gas is affected. The maximum mass-accretion rate depends on the mass of the BH and on the mean opacity of the in-falling material, basically ionized hydrogen and helium. The spherical accretion can proceed as long as the gravitational force per particle

$$f_g = \frac{GM\mu m_p N_e}{r^2},$$

with r the distance from the source and $\mu = 1.2$ to account for the ioned helium contribution, is larger than the radiation pressure force acting on a gas particle

$$f_{rad} = \frac{N_e \sigma_T}{4\pi r^2 c} \int_0^\infty L_\nu d\nu = \frac{N_e L \sigma_T}{4\pi r^2 c} L,$$

where N_e is the electron density and σ_T is the Thomson cross section.

The equality of the two quantities leads to the definition of the observable quantity that corresponds to the critical mass-accretion rate for a source at a known distance, i.e. its luminosity, called in this case the Eddington luminosity:

$$L_{Edd} = \frac{4\pi cGM\mu m_p}{\sigma_T} \simeq 1.5 \times 10^{38}(M/M_\odot) ergs^{-1},$$

where the numerical value is for solar metallicity gas. Then L_{Edd} is the maximum luminosity allowed for objects powered by a steady-state accretion. From this quantity usually one defines the Eddington ratio or Eddington rate $\lambda = L_{Bol}/L_{Edd}$, where L_{Bol} is the bolometric luminosity; the Eddington limit is for $\lambda = 1$.
In the Bondi accretion the radiation is emitted by two-body collisional processes in the ionized gas that has no angular momentum. In low-density gas, these are relatively inefficient compared with the gravitational energy release, and the gas is accreted onto the BH before it radiate its thermal energy. Then most of the gravitational energy is advected into the central object, and the mass-to-radiation efficiency factor η is much smaller than the value derived earlier. The situation is different for accretion disk processes that we will address in the next section.

1.4.2 Accretion disks: α-disk model

As we said in the precedent section, the Bondi accretion has a low mass-to-radiation efficiency factor and moreover the assumption that the gas has not angular momentum simplifies too much the real case. It's known from dynamical arguments that matter orbiting a central massive object will spread into a flattened disk structure that we will call accretion disk if the matter spirals inwards onto the massive object. It is the viscosity that is tought to provide the necessary mechanism to transfer outward the angular momentum of the gas and therefore the latter spirals towards the center losing some of its gravitational energy. Part of the energy lost is converted into radiation with high efficiency, $\sim 4 - 42\%$, part is converted to kinetic energy of gas, that can be blown away from the disk, or otherwise can heat the gas to high temperatures.

Accretion disks can be geometrically thin, slim or thick and each one of these can be optically thin or thick, on the base of their column density and ionization gas level. If the accretion rate is lower than the Eddington accretion rate $\dot{M}_{Edd} = L_{Edd}/\eta c^2$, that is the accretion rate required to produce a luminosity of L_{Edd}, and if the opacity is very high then the disk is called standard thin accretion disk or α-disk model. This geometrically thin, optically thick model, proposed by Shakura and Sunyaev [149], gives an approximate solution for the angular momentum transport problem that is not well understood yet. It is assumed that the energy from accreted material is dissipated within a small region at its radius r and since the gas is optically thick, the disk shows a black body like spectrum with a temperature $T(r)$. This with the fact that the disk gas moves approximately on the Keplerian orbits and radial pressure gradients are negligible, make simple the α model. Therefore the solution is fully determined by mass and angular momentum conservation laws.

To start off, we can derive the radial dependence of the disk temperature in a simplified way but that gives the same result one obtains following a more rigorous treatment. Assuming that a disk region releases gravitational energy at a rate $GM\dot{M}/2r$, we can relate it to the local temperature applying the virial theorem: half of this goes into the kinetic energy of the gas and the other half is radiated away to hold the local equilibrium, then:

$$L = GM\dot{M}/2r = 2\pi r^2 \sigma T^4 \Rightarrow T \propto (M\dot{M})^{1/4} r^{-3/4}.$$

The α-model deals with the angular momentum tranfer problem in the means of turbulence in the gas as the source of increased viscosity. In the case of subsonic turbulence and disk height as an upper limit for the linear scale of the turbulent structures, the viscosity ν is approximated as $\nu = \alpha c_s h$, where $0 \leq \alpha \leq 1$ is a dimensionless quantity that corresponds to the accretion rate (1 maximum rate), c_s is the speed sound in the gas and h the disk scale height. Accounting the viscous dissipation of energy and resolving the equation of hydrostatic equilibrium with the conservation of angular momentum one obtains:

$$T(r) = \left[\frac{3GM\dot{M}}{8\pi\sigma r^3}\left(1 - \sqrt{\frac{R_{in}}{r}}\right)\right]^{1/4} \longrightarrow \left(\frac{3GM\dot{M}}{8\pi\sigma r_s^3}\right)\left(\frac{r}{r_s}\right)^{-3/4},$$

where the limit holds for $r \gg R_{in}$, with R_{in} being the radius of the inner edge of the disk. We note that the relation has the same parameter dependencies as the expression derived earlier.

To calculate the emitted spectrum let's consider the black body emission of each annular segment of the disk with a monochromatic luminosity $dL_\nu = 2\pi r(\pi B_\nu)dr$. The total monochromatic luminosity is then

$$L_\nu = \int_{r_{int}}^{r_{out}} dL_\nu = \frac{2 \times 2\pi^2 2h\nu^3}{c^2} \int_{r_{int}}^{r_{out}} \frac{rdr}{exp(h\nu/kT) - 1},$$

where the factor 2 is to account both surfaces of the disk. If $r_{out} \gg r_{in}$ then for a certain frequency interval the spectral shape can be approximated as $L_\nu \propto \dot{M}^{2/3} M^{2/3} \nu^{1/3}$. This part of the SED allows to estimate the accretion rate $\dot{M}$ from direct measurements of the luminosity:

$$\dot{M} \simeq 2.6\left[\frac{L_{5100,45}}{cosi}\right]^{3/2}\left(\frac{10^8 M_\odot}{M}\right)\left[\frac{M_\odot}{yr}\right],$$

where $L_{5100,45} = L_{5100}/10^{45} ergs^{-1}$ is the luminosity at 5100 Åand i the inclination with respect to the line of sight.

Returning to the SED, the outer disk boundary r_{out} sets a minimal disk temperature and below the frequency associated the spectrum is black body like with $L_\nu \propto \nu^2$. Instead beyond the frequency associated with the temperature at the inner disk boundary r_{in}, L_ν drops exponentially with a functional dependence that depends on the maximum disk tempearture. The resulting spectral energy distribution is shown in the figure below.

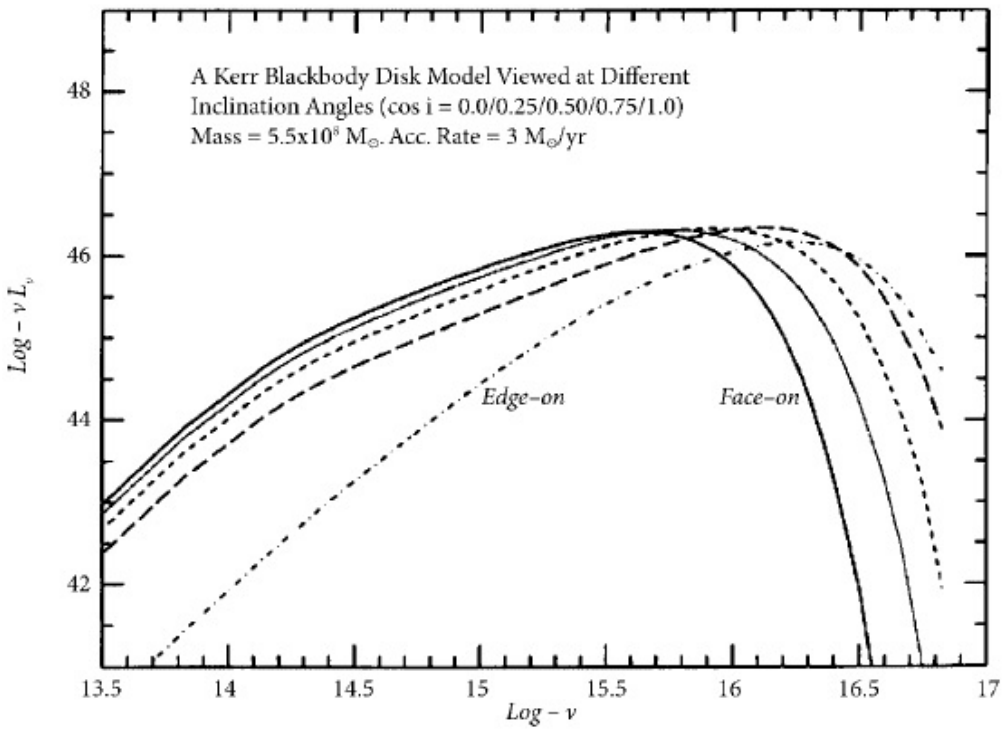

Figure 1.11: The graph illustrates calculations from Sun and Malkan (1989). It shows possible optical-UV spectral energy distributions assuming that the BBB component is due to an α-accretion disk. Different curves have different viewing angle.

The current most accrediteted model, capable to give the necessary turbulent stresses to make accretion work, uses the magneto-rotational instability re-discovered by Balbus and Hawley [5]. This model, that corresponds to a value of the viscosity parameter α between $0.03 - 0.3$ [137], provides an angular momentum transfer mechanism by the means of small-scale magnetic field. The instability can be understood through a simple mechanical model explained in the Marek et al. (2013) paper that we report here.
Consider two gas particles initially located at the same cylindrical distance from the BH but with some vertical separation and connected by a magnetic field line. Let's suppose that we give to the upper particle an extra little amount of angular momentum and substract it to the lower one. Then the upper one moves outward with a lower angular velocity and the lower one moves to a smaller radius with higher angular velocity. Due to the differing orbital speeds, the field line will get stretched and this additional tension provides a torque, which transfers angular momentum from the lower particle to the upper one so the initial perturbation grows enhancing the angular momentum transfer.

The simple α-disk model is a useful approximation since it can predict the overall spectrum and can explain the formation of the BLR [42]. Anyway it does not produce relativistic jets since for this model it is assumed that the radial pressure, needed to accelerate them, is negligible.

1.4.3 Non-keplerian disks

One of the α-disk model assumptions is the lower value of the accretion rate, from which the disk temperature is set and hence the local radiation pressure, with respect to the Eddington accretion rate. When $\dot{M} \gtrsim \dot{M}_{Edd}$, the temperature increases and the radiation pressure dominates over large parts of the disk. Moreover the optical depth increases and the radiation emission becomes inefficient since the accretion time scale becomes shorter than the diffusion time of the radiation towards the surface of the disk. Then photons emitted in the radiation pressure dominated regions are trapped in the accretion flow and advected to the BH. In this case the disk is geometrically slim or thick [1]. They are part of the more general class of disks in which the flow into the BH is adiabatic.
Another case with adiabatic flow occurs when the accretion rate is very low, called advection dominated accretion flows (ADAFs) or radiatively inefficient accretion flow (RIAF) [74, 124]. The low accretion rate translates in really low densities and hence cooling times that become equal or longer than the inflow time of the gas. Since the cooling is much less efficient, the gas retains the dissipated gravitational energy for a longer time. Then the disk temperature rises to the virial temperature and the gas is advected into the BH without releasing their energy.

As we saw from the figure 1.9, the AGN accretion cannot be described with a single model. For example considering RQ AGNs, the optical part of their spectrum can be described with an α-disk [29] but this cannot fit the additional emission present in the soft and hard X-ray band. So the debate in saying which final model is the correct one and which is suitable for jet production is still going on. We will address these questions in the next section.

Before talking about jet production, it should be noted that, in principle, it's possible to determine the correct disk model directly from observations. This can be done through the Fundamental Plane, a tight relation, discovered by Merloni et al. (2003), between the radio luminosity of radio loud AGN, the X-ray luminosity and the BH mass in the logarithmic plane:

$$\log L_{radio} = 0.6 \log L_{X-ray} + 0.78 \log M_{BH} + 7.33.$$

From theoretical predictions of the coefficients based on a disk model and jet formation, one can compare them to the observed ones and so determine the disk properties from the slope of the Fundamental Plane. However the scatter is still large, enforced by the disk and jet variability [96], so this approach it's not really reliable [116, 117].

1.5 Radio emission mechanism

1.5.1 Jets formation

Relativistic jets, ionised matter beams accelerated close to the speed of light, have been observed being emitted by different objects. These are: microquasars [122], the lower mass versions of quasars (central engine mass between 1.4 $M_\odot$ and 10 $M_\odot$, neutron star for the first case and BH for the second one), scattered about the Milky Way Galaxy characterized by an accretion process that consist in stripping atmospheric layers from a single companion star; supernovae that explode in an aspherical manner, the latter explained as due to ejection of twin jets by the supernova core collapse [81]; gamma-ray bursts and finally the objects we are considering, radio galaxies and quasars. These produce the largest and most energetic jets in the universe with speed between $0.1c$ and $0.99c$. The jets are detectable thanks to the radio synchrotron emission by high energy electrons in the plasma trapped in a magnetic field.

The production of relativistic jets requires a geometrically thick accretion flow, like a RIAF, or a coronal flow in a cold thin Keplerian disk, or a super Eddington slim disk. However this is not sufficient by itself and a large scale magnetic field is also necessary. This field is tought to be created in two different ways. The first one is through magnetic field line dragging, proposed by Bisnovatyi-Kogan and Ruzmaikin (1974). Further elaborations [154] pointed out that an efficient dragging is reached only by a hot geometrically thick flow. Through this mechanism the magnetic field is accumulated close to the BH horizon and leads to the formation of a magnetically arrested disk (MAD) [125]. Anyway, based on the initial configuration of the magnetic field, the resulting jets can be relativistic [113] or non-relativistic [179], with a non-collimated shape or a jet-like one [131, 165]. The second scenario is through a cosmic battery, proposed by Contopoulos and Kazanas (1998). In this case the relative motion of electrons and protons, due to the different action of the radiation pressure on them, creates an electric field and then a magnetic one. Anyway it is still not sure if relativistic jets can be produced in this way.

Regarding the source of energy needed for jets formation and acceleration two cases are possible: the energy can be obtained from the accretion process or from the BH rotational energy. If the large scale magnetic field stems from the line dragging mechanism and a MAD develops, the extraction of the BH rotational energy is necessary [43]. To extract it, two ways were proposed. One is the Penrose mechanism theorised by Roger Penrose in 1969 [138]. The energy derives from the entrance of particles in the ergosphere of the BH and their subsequent decay from which one of the decay products fall into the BH and one escape to infinity. Even though momentum is conserved, the net effect is more energy extracted than the one originally provided where the extra energy comes from the BH itself. The maximum gain possible for a single particle is 20.7 % [32].
The second one is called the Blandford-Znajek process proposed by Blandford and Znajek in 1977 [15]. The extraction is done through the action of the elecromagnetic fields. This mechanism requires an accretion disk with a strong poloidal magnetic field around the BH rotating with a high spin, above ~ 0.5 [56].

Having said that, the most accreditated model that explains jets production, acceleration and collimation is the magnetohydrodynamic (MHD) one. As pointed out by Meier et al. in their 2001 article, one can easily see the model properties through two simplifying assumptions: fluid-like plasma particle and high conductivity that turn down electric fields generated by free charges and so the magnetic field lines are tied to the plasma. Three important features characterize the lines. The first one is that the plasma can only flow parallel to them. In case the field is strong, that means a lower hydrodynamic pressure of the plasma ρv^2 with respect to the the magnetic pressure $B^2/8\pi$, and it is settled in a rotating disk then plasma trapped in the field will be launched centrifugally outward following the field lines. Instead with a weak field the lines will be bent backward. The second feature is that parallel lines repels each other producing pressure on the plasma perpendicular to the lines themselves. The third is the fact that the lines stay in a straight shape unless there are forces acting on them by plasma or other field lines. If forced in a spiral, the field will try to return in its initial configuration eliminating all but the straight axial component of the field. This create stress that leads to the pinch effect of plasma physics and jets collimation.

The figure 1.12 depicts the MHD acceleration and collimation model. A massive body collects material from a thick disk that is threaded by a poloidal magnetic field. The disk is initially in rotational equilibrium about the central object, producing differential rotation in the radial direction. The differential rotation swings about the rotation axis the field lines that, trying to uncoil, remove angular momentum from the disk pushing outward and pinching the plasma trapped in the field along the lines themselves. The resulting outflow varies from broad uncollimated wind and highly collimated jet depending on the relative importance of rotation, magnetic field and plasma density. Losing angular momentum, the disk material falls toward the central object. This accretion releases the material gravitational energy, half of which becomes additional kinetic energy of rotation that feeds the whole process. Dynamical general relativistic MHD simulations [84, 85] have shown that the process occurs in one or two rotation times. Moreover if the rate of the disk material infall into the BH plus the one of material ejection by jets is comparable to the disk material and magnetic field supplying rate, then the system reaches a steady state continuously producing a jet.

The MHD predicted power emitted by the jet depends only on the poloidal magnetic field B_p coming out from jet-production region at R_0, that is the characteristic size of the jet production region itself, and on the angular velocity of that field Ω_0 [15]: $P_{MHD} = B_{p,0}^4 \Omega_0^2 / 32c$. The power corresponding to the energy the plasma need to reach escape speed divided by the dynamical time, that in a magnetized plasma is $t_d = R_0/c_{ms}$, where c_{ms} is the magnetosonic sound speed accounting both plasma and magnetic field pressure, is defined as critical power $L_{crit} = 4\pi\rho_0 R_0^2 (GM_{BH}/R_0)^{3/2}$, where ρ_0 is the plasma density. In this extreme case, if the MHD power conversion efficiency to kinetic power is high ($\gtrsim 50\%$) near the BH, then the jet material reaches its terminal speed in a time shorter than t_d and within R_0. Moreover its final kinetic power $P_k = \Gamma \dot{M}_{jet} c^2$, where $\dot{M}_{jet}$ is the rate of mass outflow in the jet and Γ the Lorentz factor, will be equal to half of P_{MHD}, and the other half will be carried by the waves generated by the rotating twisted magnetic field.

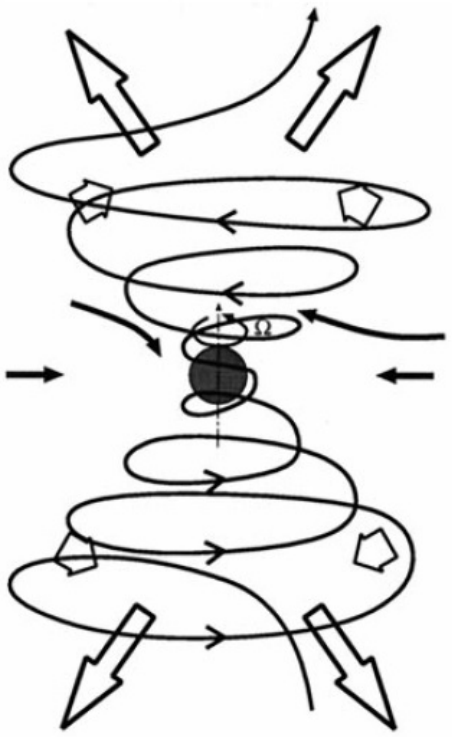

Figure 1.12: MHD acceleration and collimation model representation. Image from [114].

Since standard accretion disk models explain the material spiraling infall onto the BH with a considerable toroidal magnetic field strength B_Φ in the disk, we can write the MHD predicted power as $P_{MHD} = B^2_{\Phi,0} H_0^2 R_0^2 \Omega_0^2 / 32c$, since $B_p \sim B_\Phi (H/R)^n$ with H the half-thickness of the disk and $n \sim 1$ [97]. We see that for standard accretion disk, which are geometrically thin ($H_0 \ll R_0$), the power will be small. For example a $10^9 M_\odot$ BH with an accretion rate corresponding to 10% of the maximum rate allowed by the Eddington limit, will generate a jet with a maximum power $\sim 10^{43} ergs^{-1}$, much lower than the power observed from the most powerful objects, $3 \times 10^{45} ergs^{-1}$, thought to have a BH with that mass [93]. To reach higher power one can think to use geometrically thick disks model in order to have a stronger poloidal magnetic field. However, using RIAF model for example, the equation still gives a low power and that's because thick disks are partially pressure supported and therefore don't rotate at the Keplerian rate. The solution can be the BH spin. A high spin, and so the frame dragging near the BH ergosphere, produces a differential rotation nearly fast as a Keplerian rotation correspondent to higher values of H_0 and Ω_0. The spin paradigm is a possible key for the different AGN classes since it explains why not all the RL and RQ AGNs can have jets though an AGN with a rapidly spinning BH and one with a slowly spinning BH look similar in the optical range [176].

1.5.2 Free-free and synchrotron emission

When considering the emission in the radio range from a galaxy, one must not forget that its source may not be the AGN relativistic jet. Important contribution may arise from HII region free-free emission and from the synchrotron one by electrons accelerated through supernova explosions.
The plot below shows the radio/FIR spectrum of M82.
We see that the two emission mechanism introduced above dominate this wavelenght range, the first one, weaker, showing an almost flat spectrum ($S_\nu \propto \nu^{-0.1}$) and the second one a steeper spectrum ($S_\nu \propto \nu^{-0.8}$). For frequencies $\nu \gtrsim 200GHz$ we note that the two emissions are overcomed by dust thermal reradiation of starlight meanwhile at low radio frequencies these are dampened by free-free absorption.

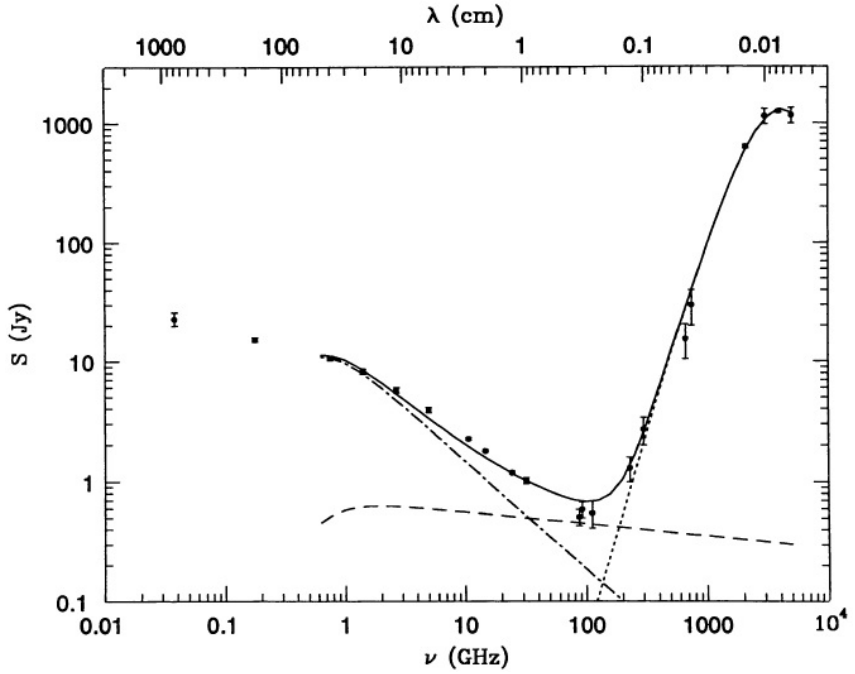

Figure 1.13: M82 radio/FIR spectrum, sum (solid line) of synchrotron (dot-dashed line), free-free (dashed line) and dust (dotted line) components. Figure from [83].

The difference in the emission mechanisms spectral index should make easy to distinguish the two spectra one from the other through the total flux density or a two frequiencies map. However most of the normal galaxies aren't bright enough to be detected at $\nu \gtrsim 10GHz$ then the observed thermal fraction S_T/S, where S_T and S are respectively the thermal and total flux density, is small with a factor 2 uncertainty on S_T. Moreover even in brighter sources the situation is not simplier since the non-thermal emission may not have a straight spectrum. To estimate the average thermal fraction for noraml galaxies, the FIR/radio correlation can be used [36] that leads, for small ($\ll 1$) free-free opacity, to:

$$\frac{S_T}{S} \sim 1 + 10\left(\frac{\nu}{GHz}\right)^{0.1-\alpha},$$

with $\alpha \sim 0.8$ for a typical non-thermal spectrum.

A normal galaxy that have coextensive thermal and non-thermal sources will have a total radio emissivity proportional everywhere to the free-free absorption coefficient $k \propto n_e^2 T_e^{-1.35} \nu^{-2.1}$ where n_e is the electron density of the HII regions and T_e its electron temperature. Therefore the galaxy radio-brightness tempearture spectrum is approximated by:

$$T_b \sim T_e[1 - exp(-\tau)]\left[1 + 10\left(\frac{\nu}{GHz}\right)^{0.1-\alpha}\right],$$

where τ is the average free-free optical depth along the line of sight. The plot below shows different radio-brightness spectrum for different values of frequency at which $\tau = 1$. Brighter radio sources will have higher turnover frequencies.

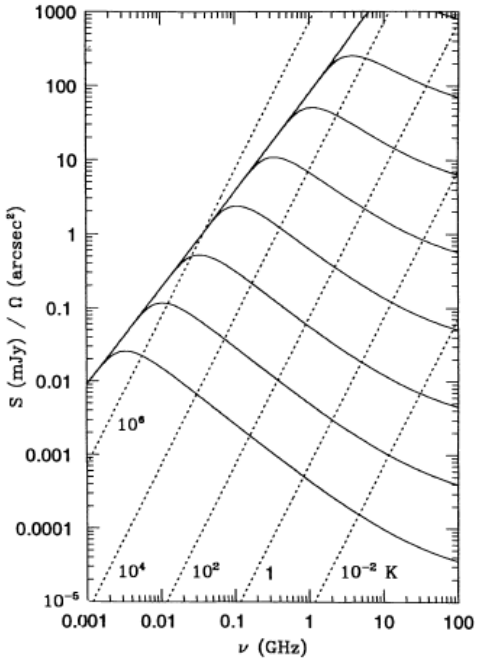

Figure 1.14: Radio-brightness spectra for different values of frequency at which $\tau = 1$. Figure from [38].

The compact starbust nuclei of ultraluminous IRAS objects are the brightest radio sources known in normal galaxies. They show a spectral flattening above 1.49 GHz [37]. For example flattening of the compact source spectrum in IC694 implied $T_b > 10^{10}$ and for this reason it was tought to be too bright to be a starbust and instead tought to be synchrotron self-absorbed [59]. However later studies showed that this source is extended with a peak brightness temperature of $T_b \sim 10^4$, so a flat spectrum even at high frequencies is not sufficient to prove the AGN origin of the radio emission.

The current radio luminosity is proportional to the recent star-formation rate (SFR). This is true because the massive stars responsible for most of the radio emission in normal galaxies have a lifetimes shorter than the Hubble time. Galaxy models started to include thermal and non-thermal mesaurement since 1976, when Biermann compared (B-V) colours with blue/radio flux ratios. He assumed a time-indipendent powerlaw initial mass function (IMF) $\psi(M) \propto M^{-\gamma}$, with slope $\gamma = 2.35$ and upper mass limit M_U, and that all stars with $M \geq M_{SN} \sim 6.7 M_\odot$ produce radio-emitting supernova remnents.

In this way the radio supernova rate is:

$$\nu_{SN} = \int_{M_{SN}}^{M_U} \psi(M) dM.$$

The integral for each supernova remnant corresponds to the observed [33] surface brightness-diameter ($\Sigma - D$) relation for galactic supernova remnents. As pointed out by Condon (1992), Biermann derived that the lower mass limit M_{SN} for radio supernovae is more critical than $M_U \gg M_{SN}$ due to the steep IMF slope. Assuming a higher non-thermal radio energy per supernova, the model results are made in agreement with the observed blue/radio flux ratios. The observed Galactic relation between supernova rate and non-thermal radio luminosity implied by the $\Sigma - D$ relation was derived by Condon & Yin (1990):

$$\left(\frac{L_N}{10^{22} W Hz^{-1}}\right) \sim 13 \left(\frac{\nu}{GHz}\right)^{-\alpha} \left(\frac{\nu_{SN}}{yr^{-1}}\right),$$

where L_N is the non-thermal luminosity and α the spectral index. Ulvestad (1982) used a similar relation on Seyfert galaxies deriving a ν_{SN} value that exceeded by at least a factor of 10 the observed ones. This result suggested that it is the AGN that powers the radio source in most Seyfert galaxies. Gehrz et al. (1983) found a similar result in the sense of a difficult agreement between the high ν_{NS} needed to explain the radio non-thermal radio emission with the observed FIR luminosity, giving more credit to the AGN dominance idea for this kind of sources.

A simple model for normal galaxies approximates the global radio non-thermal and thermal luminosities and the FIR/radio ratio through a single free parameter that is the average SFR of stars with $M > 5M_\odot$:

$$\left(\frac{SFR}{M_\odot/yr}\right) \equiv \int_{5M_\odot}^{M_U} M\psi(M) dM.$$

Stars with $M_{SN} = 8M_\odot$ become radio emitters, therefore the radio supernova rate and the SFR are directly linked:

$$\left(\frac{\nu_{SN}}{yr^{-1}}\right) \sim 0.041 \left[\frac{SFR(M \geq 5M_\odot)}{M_\odot yr^{-1}}\right].$$

Finally one can determine the non-thermal luminosity through the $L_N - \nu_{SN}$ relation reported above with $\alpha \sim 0.8$:

$$\left(\frac{L_N}{10^{22} W Hz^{-1}}\right) \sim 5.3 \times 10^{21} \left(\frac{\nu}{ghZ}\right)^{-\alpha} \left[\frac{SFR(M \geq 5M_\odot)}{M_\odot yr^{-1}}\right],$$

and the radio thermal fraction from stellar models assuming an electron temperature $T_e \sim 10^4$K if dust absorption of Lyman continuum photons is negligible [80]:

$$\left(\frac{L_T}{10^{22} W Hz^{-1}}\right) \sim 5.5 \times 10^{20} \left(\frac{\nu}{ghZ}\right)^{-0.1} \left[\frac{SFR(M \geq 5M_\odot)}{M_\odot yr^{-1}}\right]$$

.

Massive stars are formed in dusty regions that absorb the starlight and re-emit it in the IR. Only a small fraction of the UV/optical photons can escape the absorption process and nearly all the luminosity produced by stars in HII regions emerges in the FIR. Then the FIR luminosity is a better quantitative measure of recent SF. It can be shown [38] that each logarithmic stellar mass range contributes equally to L_{FIR} and that:

$$\left(\frac{L_{FIR}}{L_\odot}\right) \sim 1.1 \times 10^{10} \left(\frac{\nu}{ghZ}\right)^{-0.1} \left[\frac{SFR(M \geq 5M_\odot)}{M_\odot yr^{-1}}\right].$$

We notice that in this model L_T, L_N and L_{FIR} are proportional to the star formation rate implying a linear FIR/radio correlation.

1.5.3 Relativistic jet, host galaxy and its star formation

At high redshift where cold gas is abundant and galaxy merging events are frequent, SF activity and nuclear accretion are tought to occur simultaneously at high rates. When the AGN has evolved enough, it starts to expel the gas reducing the rate of the two processes untill what remains is an elliptical galaxy hosting a quiescent SMBH. SF and accretion processes can reignite again with high rates at low redshift if the remaining gas is destabilized in some means like for example galaxy interactions.
Observationally, the star-forming processes becomes increasingly important with respect to the jet one going towards flux densities fainter than 1 mJy [132]. For this reason, the radio emission of RD AGNs has been debated for a long time. One idea sees them as scaled versions of RL AGNs, in which the relativistic jets dominate the radio, charachterized by mini radio jets [120] but it has also been proposed that the emission comes from the host galaxy star formation process [159]. Recent works [112] have suggested that these objects can be represented by the Narrow-Line Seyfert 1 galaxies (NLS1) class since these sources are frequently associated to high star forming host galaxies [145]. Moreover the small RL fraction (7 % of all the NLS1 [86]) do not show extended radio structures, with few exceptions [47], and so are tought to be young radio galaxies where the jets formation is in its initial phase [26].

The presence of SF activity in RL NLS1 sources has been questioned in recents works [26, 27] studying their SED through the mid-IR data at 12 and 22μm from the Wide field Infrared Survey Explorer (WISE) catalogue [177]. One of the results is shown in figure 1.15. The figure shows the positions of 42 NLS1 AGNs with different shapes of IR spectrum on the W1-W2 vs W2-W3 (left) and W1-W2 vs W3-W4 (right) plots where the Ws are the WISE magnitudes measured with different filters.
If the non-thermal jet of an AGN dominates the WISE emission then we expect it to have a power-law spectral shape, described in the plots by the black line (PL line), or a broken power-law one, represented by the darker blue area above the PL line. From the left plot we see that a large number of sources are found above the line but the majority have a higher W1-W2 colour value expected from a broken power-law. Since the sources studied are type I the extinction cannot be considered as the cause of this effect [111]. Instead the answer can be the radio-quiet component of the source [31], like the dusty torus, capable of producing the observed IR emission partially or globally. The case in which both jet and torus emission coexist is represented in the plots by the lighter blue area.
The sources below the PL line, higher in number in the right plot where the longest wavelength magnitude W_4 is considered, are not explained by these models and require a different component. This is tought to be the host galaxy and its predicted dilution effect on a power-law emission is shown in figure 1.16.

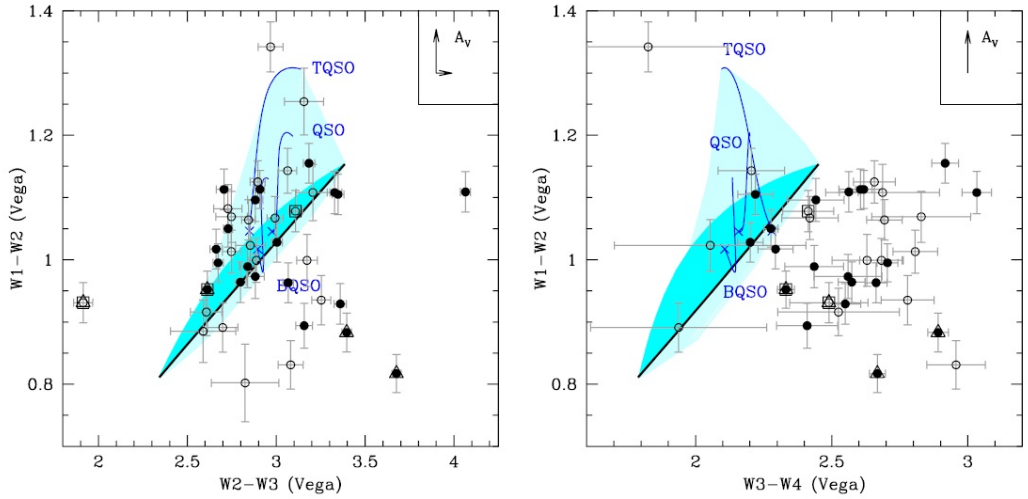

Figure 1.15: W1-W2 vs W2-W3 (left) and W1-W2 vs W3-W4 (right) plot of AGNs with different IR spectrum shapes: a power-law (black tick line), a smooth broken power law (dark blue shaded area), a combination of RQ AGN emission plus a power-law spectrum (light blue shaded area). The arrows in the upper-right corners show the expected effect of an extinction of $A_V = 2$ mag. Figure from [27]

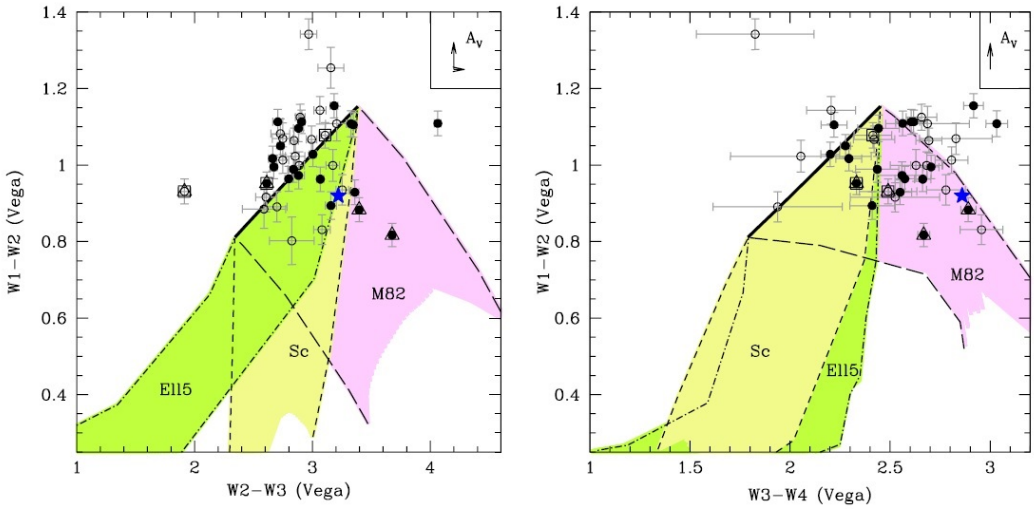

Figure 1.16: Host galaxy emission effects on a power-law spectrum, in the WISE colours plots. More info in the text. Figure from [27].

The three colored regions correspond to the expected paths of a combination of power-law plus a galaxy template varying the relative intensity of the two components, the power-law slopes and the redshift of the source: for the green one it was used an early-type galaxy template, for the yellow one an Sc galaxy one and for the pink one a starburst galaxy one. From the left plot we can see that the mid-IR emission of the sources below the PL line in the right plot of figure 1.15 can have a significant contribution from the host galaxy. Moreover from the right plot we can better see the host galaxy type of a given source. In particular, AGNs with $W3 - W4 > 2.5$ can be explained only by the effects of a starburst galaxy host that make the W1-W2 values bluer than the PL line and the W2-W3, W3-W4 values redder.

Disentangling the jet and SF emission we can aquire information about the host galaxy properties, study the AGN effects on the host galaxy SF activity and try to find some clues on the RD-RL dichotomy. There are different ways to see which component dominates at these wavelenghts. For example one can see the shape of the radio spectrum or measure a radio-loudness parameter, like the Kellerman one [79]. A flat radio spectrum and high values of radio-loudness paramter are considered strong indicators of the dominance in the radio emission by relativistic jets pointing towards the observer. Anyway for faint radio sources the situation is more difficult since the RD AGN class include also star-forming and radio galaxies so a multiwavelength study is needed [133].

A recent work [20] has obtained interesting results using only two bands, the radio and the IR one. Endeed is well known that SFGs are characterized by a tight correlation between the radio and FIR luminosity [45] even tough the physical reason for its tightness and linearity over several decades in luminosity is still unclear.
The FIR luminosity can be used as a tracer of recent SF activity since the dust absorbs UV radiation from young stars and re-emits it in the FIR, emission that will be no longer affected by dust extinction. Like already mentioned the radio continuum emission can be used too as a tracer if the AGN contamination is not dominant. Their results are shown in the figure below that plots the SFR estimate from the FIR luminosity against the SFR derived from the radio one. This confermed that the SFGs follow the radio-FIR luminosity correlation over four decades in SFR with a 0.2 dex disperion. Moreover the two SFRs estimate are in good agreement also for RD AGNs with a 0.23 dex disperion. This means that the radio power is a good SFR tracer also for RD AGNs but more importantly it suggests that the main contribution to the radio emission in this class stems from the SF process in the host galaxy and not from the jets. Finally, the fact that RL AGNs are found below the correlation line suggests that their radio power is affected by the jet contribution, then RD and RL AGNs are powered by two different radio emission mechanism.

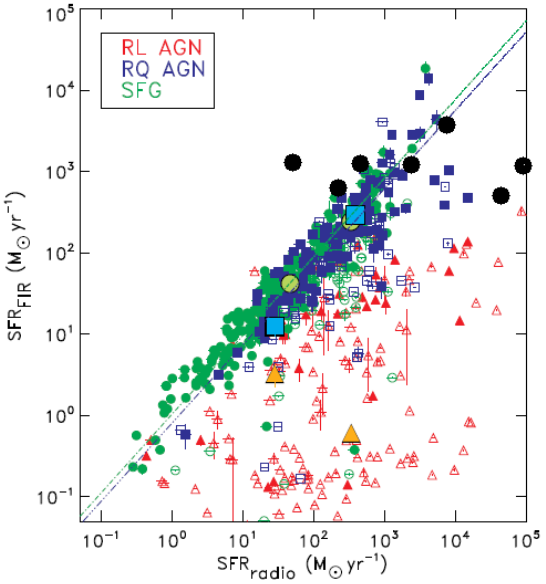

Figure 1.17: Infrared to radio star-formation rate estimate. Green circles represent SFGs, blue squares RQ AGNs and red triangles RL AGNs. The big black dots represent the 7 sources of our sample for which we could calculate the SFR_{IR} estimate. Figure from [20]

Unfortunately only 7 objects of our sample have IR measures taken by the Herschel Space Observatory at 70, 100, and 160 μm that are reported in the NASA/IPAC Ifrared Science Archive (IRAS). Nonetheless for these objects we calculated their luminosity at 60 μm in order to give an estimate of their star formation rate and finally classify these sources as RD or RL through the method followed by Bonzini et al. (2015). The sources considered are listed in the table 1.2 below where some physical parameters are reported. How some of these were calculated will be explained in the upcoming section 2.

Table 1.2: Sample objects with IR measurements.

SDSS ID	**z**	**mag**$_g$ mag	**f**$_{IR}$ mJy	**P**$_{1.4GHz}$ W/Hz	**SFR**$_{IR}$ $M_\odot/yr$	**SFR**$_{1.4GHz}$ $M_\odot/yr$	**log**R_K
J100943.55+052953.8	0.94236	17.122	19.09	1.92E26	5.08E2	7.9E4	1.71
J111908.67+211917.9	0.17569	14.32	85.466	4.65E23	8.07E2	1.9E2	-0.15
J143157.94+341650.2	0.71543	17.146	69.287	4.09E24	2.76E3	1.67E3	0.38
J162052.59+540058.6	0.14561	18.305	164.687	7.12E22	1.71E3	2.9E1	0.81
J122449.90+062917.1	0.84574	20.535	140.571	1.90E25	5.51E3	7.82E3	2.20
J021640.73-044404.8	0.87437	16.331	18.654	5.60E26	7.26E2	2.29E5	1.95
J123547.98+090801.0	0.31722	21.75	55.484	8.43E23	1.47E3	3.45E2	2.46

To obtain an estimate of the SFR from the IR luminosity we used the local calibration derived by Li et al. (2010):

$$SFR_{70\mu m} = 9.4 \times 10^{-44} L_{70\mu m},$$

with $SFR_{70\mu m}$ in $M_\odot/yr$ and $L_{70\mu m}$ in erg/s. The formal uncertainty on the calibration constant is $\sim 2\%$, but the scatter in the datapoints is about 35% [28]. From the Herschel flux density we derived the luminosity as: $L_{70\mu m} = 4\pi D_l^2 \lambda f_{70\mu m}$ where D_l is the luminosity distance. A necessary step is the K-correction of the density flux. The K correction factor can be written as:

$$f_{\nu,0} = \frac{L_{\nu,0}}{4\pi D_l^2} \left[\frac{f_\nu(\nu_e = \nu_0(1+z))}{f_{\nu,0}} (1+z) \right]$$

. Following the work of Smith et al. (2014), we assume a single-component modified blackbody model of the standard form:

$$f_\nu \propto \frac{\nu^{3+\beta}}{exp(h\nu/kT) - 1},$$

where h is the Planck constant, k the Boltzmann constant and T the dust temperature. We assume the latter near $60K$ since, as we already mentioned, this is the temperature of the HII regions gas that correlates to the SFR in contrast with the galactic cirrus whose gas is at $T \sim 20K$ not connected to the SFR. The β term, referred as emissivity index, modifies the classic Planck function with the assumption that the dust emissivity varies as a power law of frequency. We assume a constant $\beta = 1.82$ following Smith et al. (2013).

A more consistent approach would be the fitting of the IR SED with the various components acting at those wavelenght. Anyway our goal is not an accurate measure of the SFR but a first estimate that allows us a comparision with the one derivated from the radio power therefore we can gain information about the dominating process in the radio AGN activity, SF or relativistic jet. Our estimates should be anyway fairly reliable because we expect that the main contributor to the flux at 70μm, the dusty torus, has a steeply declining emission from a maximum at around 10-20μm. The only model that predicts emission from the torus at a level close to the maximum (Symeonidis et al. (2016)) is probably not correct as pointed out by Duraset al. (2017).

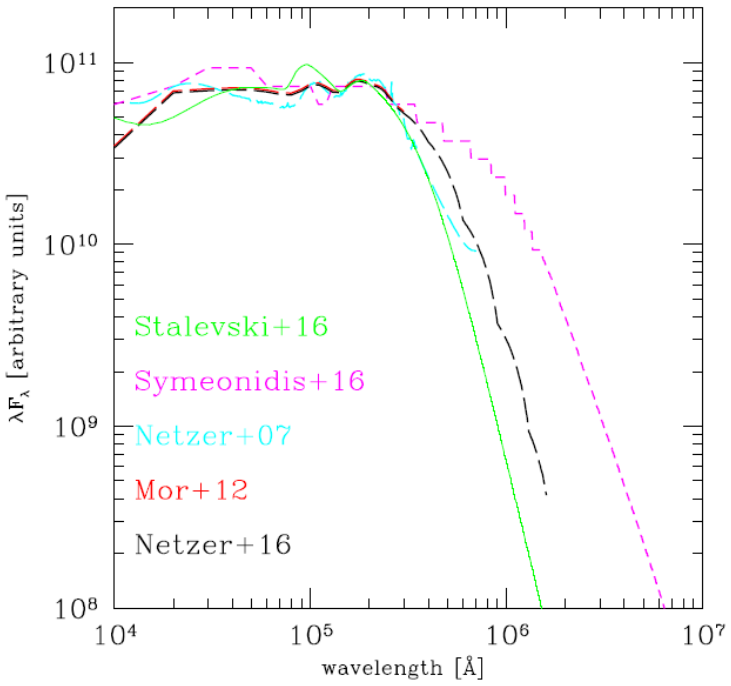

Figure 1.18: Infrared torus model by Stalevski et al. (2016) compared with the empirical SEDs by Netzer et al. (2007), Mor & Netzer (2012), Netzer et al. (2016), and Symeonidis et al. (2016). Figure from [49]

As we can see from Fig. 1.17, the results we obtain following the method by Bonzini et al. (2015) are in agreement with that we obtain using the Kellerman parameter. Indeed our 7 objects are in regions of the $SFR_{IR} - SFR_r$ that reflect the radio-power class assigned by the Kellerman paramater. There are however three particuar cases. Two objects of our sample have a Kellerman parameter value near the limit between RI and RL classes and for this reason they do not fall clearly in a $SFR_{IR} - SFR_r$ plane loud region. Finally one object show such a strong SFR_{IR} with respect to the SFR_r that put the source itself in a abnormal region of the $SFR_{IR} - SFR_r$ plane. If this is the case the source would not follow the FIR-radio luminosity. A deeper study with a SED fit is required.

1.6 The Eigenvector 1 parameter space

1.6.1 The quasar main-sequence

As we mentioned, AGN spectra show emission lines with a wide variety of strengths and velocity widths. Anyway, Boroson and Green (1992) showed significant correlations between the measured parameters through Principal Component Analysis (PCA). The PCA operates a linear combinations of the parameters, each considered as a dimension of a parameter space, in order to find a lower dimension parameter space. The study was done on a 87 low-redshift broadline quasars sample that led to the discovery of an anti-correlation between the strength of the narrow $[OIII]\lambda5007$ and broad Fe II emission. Accounting other properties that also correlate with Fe II strength [160, 174], the main variance (Eigenvector 1, or E1) in their optical properties gave the possibility to define a quasar main sequence, in close analogy to the stellar main sequence on the Hertzsprung-Russel (HR) diagram [162].

In the left image below we see 20000 broadline quasars from the SDSS plotted by the Fe II strength in abscissa, given by the parameter R_{FeII} defined as the ratio between the integrated flux of FeIIλ4570 blend of multiplets, and that of the $H\beta$ broad component, $R_{FeII} = I(FeII\lambda4570)/I(H\beta)$, and the FWHM of $H\beta$ in ordinate. E1 is defined as the average $[OIII]$ strength and FWHM($H\beta$) decreasing horizontal trend with R_{FeII}.

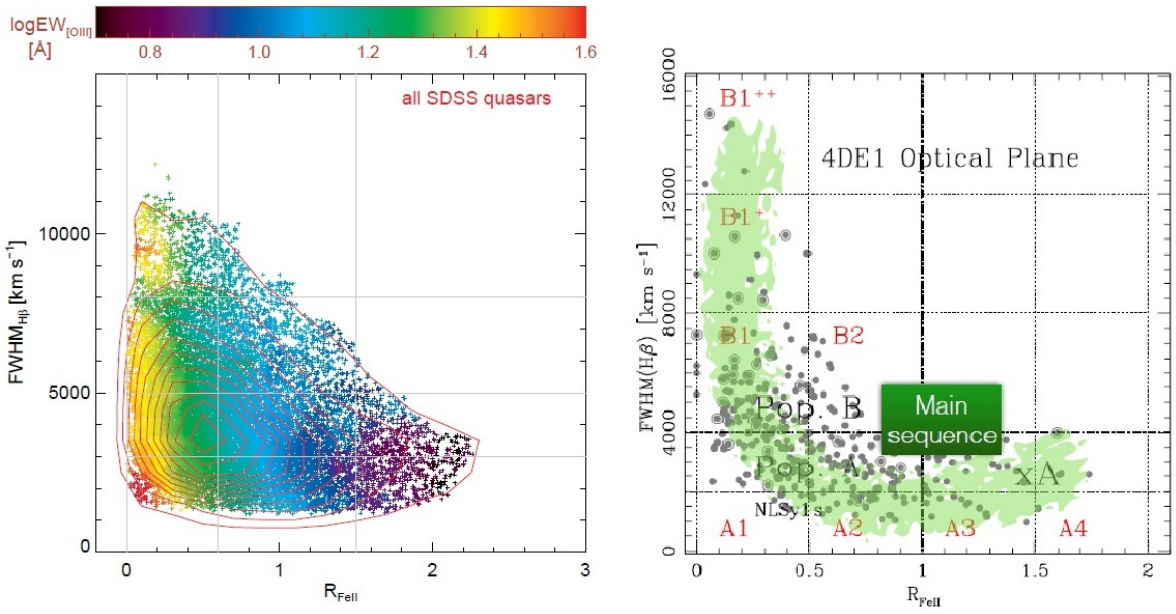

Figure 1.19: Left: The E1 sequence for $\sim$ 20, 000 broadline quasars drawn from the SDSS6. The color-code is the [OIII]λ5007 strength, averaged over all nearby objects in a smoothing box of $\Delta R_{FeII}II = 0.2$ and Δ FWHMH($H\beta$) = 1000 kms^{-1}. Graph from [151] Right: In this E1 graph are shown the spectral class separations as the thin dotted line. The thick horizontal dot-dashed line separates populations A and B and the vertical one marks the limit for extreme Population A (xA) sources with $R_{FeII} \gtrsim 1$. The green shaded area indicatively traces the distribution of a quasar sample from Zamfir et al. (2010), defining the quasar MS. Graph from [110].

The shape distribution allows us to divide the sample into bins of R_{FeII} and FWHM($H\beta$) and to define a sequence of spectral types. Population A bins are defined in terms of increasing R_{FeII} with bin size $\Delta R_{FeII} = 0.5$ while Population B bins in terms of increasing $\mathrm{FWHM}_{H\beta}$ with Δ FWHM($H\beta$) = 4000kms^{-1}. The population division A and B, set by the value of FWHM($H\beta$) = 4000 km with Population B having FWHM($H\beta$) $> 4000km$ [161], has been confirmed as a division of two distinct quasar classes. The figure 1.20 shows composite median spectra of the E1 parameter bins highlighting the differences between these classes.

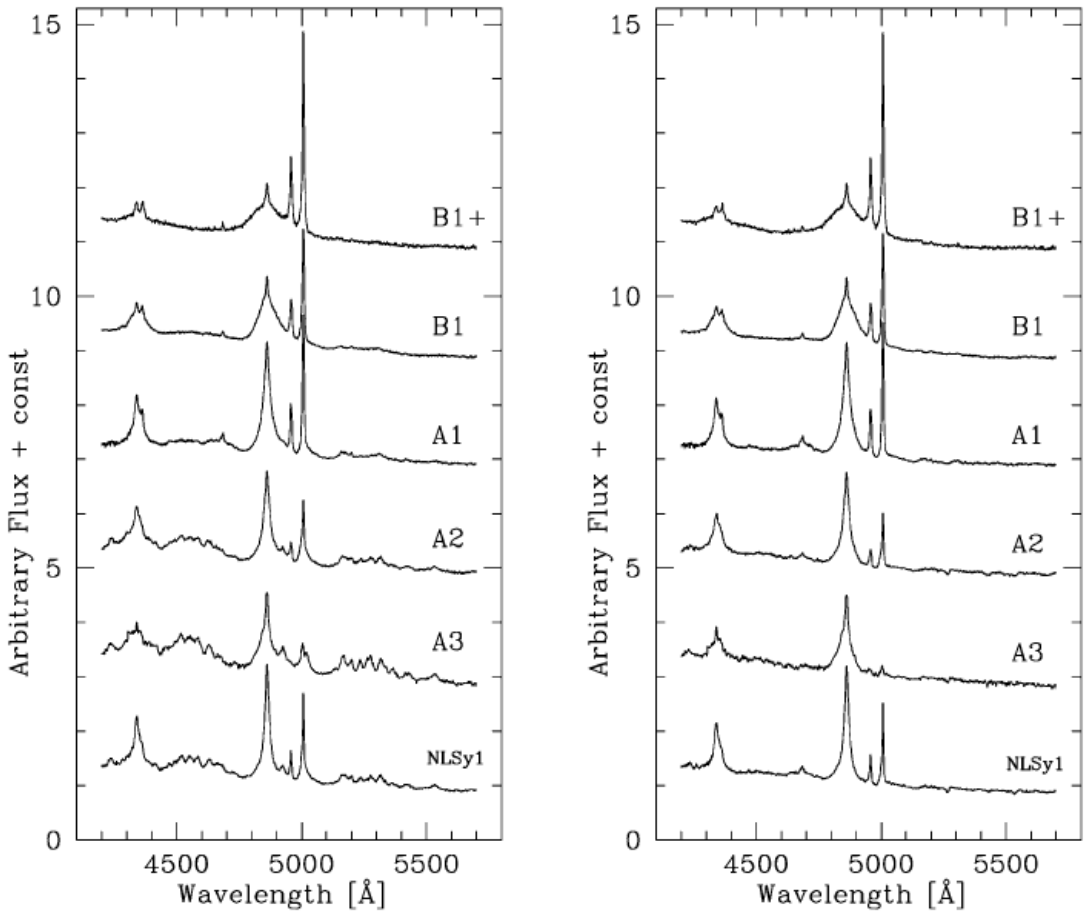

Figure 1.20: Composite median spectra of the E1 parameter bins with (left) and without (right) the FeII blend emission. Figure from [163].

The differences are not given only by the value of the parameters already mentioned. Other parameters are listed in Table 1.3. As regard the spectral characteristics, a clear distinction is in terms of the Balmer line profile shapes [163] with Population A showing symmetric and unshifted Lorentzian Balmer line profiles, while Population B objects show a double Gaussian often redward asymmetric. Pop. A shows an CIV emission line having a blue-shifted centroid at 1/2 of the line height [164]. Instead Pop. B shows an CIV emission line having a centroid at 1/2 of the line height that can be in some cases blue-shifted and in other cases red-shifted [164]. Pop. A sources are charactherized by a stronger FeII optical emission than Pop. B sources [21]. Pop. A objects show often large steepness of the soft X-ray continuum Γ_{soft} [160] while B objects have it rarely large.

Pop. A sources frequently show an extreme X-ray variability [171] and a possible optical varibility [62]. Instead Pop. B objects are less common variable in the X-ray but they are more frequently variable in the optical. Finally we see that Pop. A sources have smaller BH masses than the ones of Pop. B but the latter objects have a smaller Eddington ratio with respect to Pop. A sources [22].

Table 1.3: Population A and B physical parameters, from [54].

Parameter	**Pop. A**	**Pop. B**
FWHM($H\beta$)	800-4000 kms^{-1}	4000-10000 kms^{-1}
$c(1/2)$CIV	-800 kms^{-1}	-250/+70 kms^{-1}
R_{FeII}	0.7	0.3
Γ_{soft}	> 2	≈ 2
$c(1/2)$Hβ	~ 0	500 kms^{-1}
Hβ profile shape	Lorentzian	double Gaussian
X-ray variability	extreme common	less common
optical variability	possible	more frequent
log$M_{BH}[M_\odot]$	6.5-8.5	8.0-9.5
L/L_{Edd}	$\approx$ 0.2-1.0	$\approx$ 0.01-0.2

The most significant parameters were used by Sulentic to introduce a 4DE1 parameter space: these are FWHM$_{H\beta}$, R_{FeII}, Γ_{soft} and the centroid shift of CIVλ1549 at half maximum, $c(1/2)$CIV. The interpretation of these parameters is summarized in Table 1.4. The FWHM($H\beta$) is related to the velocity dispersion in the low-ionization line (LIL) emitting part of the BLR; $c_{CIV}(1/2)$ gives an estimate of the high-ionization outflow detected in the high-ionization line (HIL) profile [105]; R_{FeII} gives an estimate of the metallicity but it mainly depends probably on the ionization conditions, density and column density [110]; a $\Gamma_{soft} > 2$ is usually related to Compton thick soft X-ray emission from a hot corona above the disk or, if the inner disk is very hot, it may be the high-energy tail of its spectral energy distribution [48].

Table 1.4: E1 parameter and their physical interpretation, from [161].

Parameter	**Interpretation**	**Relation to accretion parameters**
FWHM($H\beta$)	LIL-BLR velocity field	$L/L_{Edd}, \theta, M_{BH}$
$c(1/2)CIV$	HIL-BLR velocity field (outflow)	$L/L_{Edd}, \theta$
R_{FeII}	LIL ionization and density, $Z/Z_\odot$	$L/L_{Edd}, \theta$
Γ_{soft}	Compton-thick X-ray emission	L/L_{Edd}

The parameters of the E1 sequence are then affected by different physical parameters like the black hole mass, the Eddington ratio, the black hole spin, and the inclination angle. Shen and Ho (2014) proposed the M_{BH} as the main parameter for the sequence in R_{FeII} and the inclination with respect to the line of sight for the dispersion in FWHM($H\beta$) at fixed R_{FeII}. They first demonstrate that the average M_{BH} decreases with R_{FeII} by measuring the clustering of SDSS quasars with low and high R_{FeII} values. Indeed in the hierarchical clustering Universe model, more massive BH forms in more massive galaxies

that are born in rarer density peaks and are more strongly clustered [8]; this translates in a lower R_{FeII} value. The result is shown in the right graph of 1.21.

We see a significant clustering difference at 3.48σ: quasars with larger R_{FeII} are less strongly clustered, confirming that they have on average lower BH masses.
With respect to the FWHM($H\beta$) dispersion, they estimated the orientation of the accretion disk, and so the one of the BLR, for a small subset of quasars that are radio-loud since for this class, the parameter can be obtained through the inclination of the jet using resolved radio morphology. Results from these studies [175] gave that high inclination, more edge-one, broad-line radio quasars have on average larger FWHM($H\beta$) confirming the orientation hypothesis.

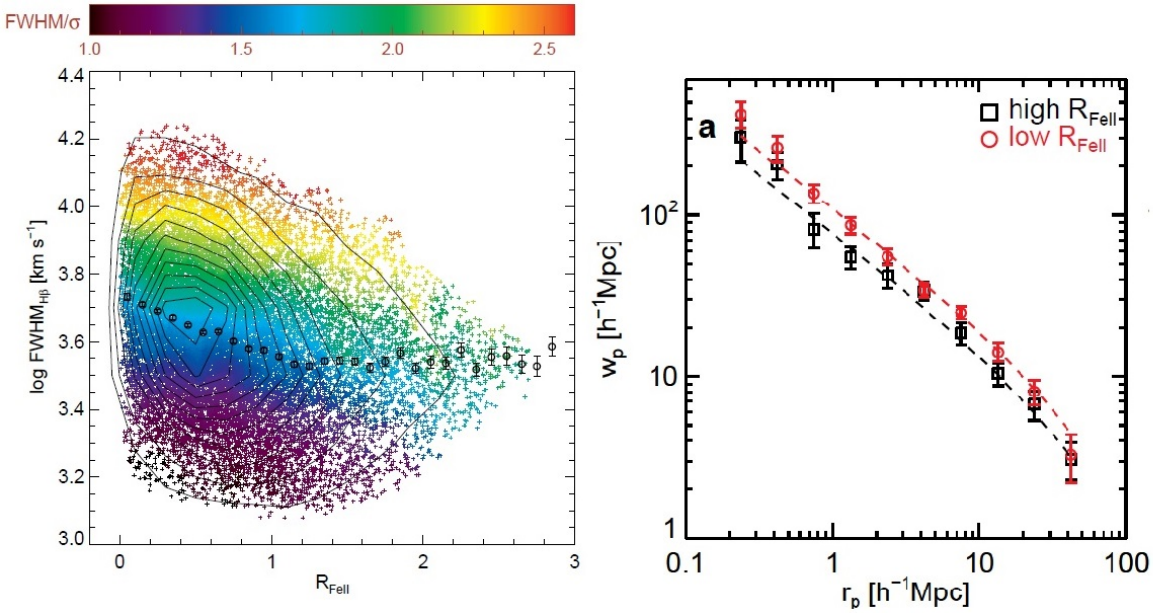

Figure 1.21: Left: E1 plane color-coded by the $FWHM/\sigma$ ratio. The transition in $FWHM/\sigma$ reflects the change in orientation of the broad-line region disk relative to the line of sight. Right: Cross-correlation functions between different quasar subsamples and a galaxy sample; the graph shows the difference in the clustering strength when the quasar sample is divided by the median R_{FeII}. Graphs from [151]

1.6.2 xA objects as cosmological standard candles

Objects belonging to the xA bin are tought to be sources with an extreme Eddington ratio. These Super-Eddington accreting BHs can reach saturated Eddington ratios due to photon trapping and advection in slim accretion disk and thanks to this they can be used to estimate cosmological distances even in the high redshift Universe [77]. The luminosity saturation stem from the fact that Super-Eddington accretion is possible in slim disk characterized by thermally stable radiation pressure-dominated regions [1]. Photons emitted in these disks are trapped inside the accretion flow and are advected into the BH leading to the Eddington ratio saturation.

The luminosity results to be proportional linearly to M_{BH} and logarithmically to the accretion rate [121]: $L_{BH} = l_0(1 + aln(\dot{m}/15))M_{BH}$, where $\dot{m} = \dot{M_{BH}}/\dot{M_{Edd}}$, $l_0 = 5.29 \times 10^{38} ergs^{-1} M_{\odot}^{-1}$ and $a \approx 0.476$.

One requires then the estimates of M_{BH} and $\dot{m}$. For the first one there are different measure techniques. One of the most famous regarding the AGN is the reverberation mapping (RM) that supposes a virialized gas disk. The RM takes advantage of the rapid variability of AGN. A variation of the continuum luminosity in the accretion disk leads with a time delay to a flux variation of the BLR emission lines. This time lag can be estimated from the cross-correlation function obtained from the continuum and the line emission light curves from which we obtain an estimate of the BLR size R_{BLR}.
An useful correlation between R_{BLR} and the underlying continuum luminosity is given by [77]: $R_{BLR} = R_0(L_{5100}/10^{44} ergs^{-1})^{\alpha}$, where $R_0 \simeq 9 \times 10^{16} cm$, $\alpha = 0.6 \pm 0.1$ and L_{5100} is the AGN continuum luminosity at 5100 Å. Finally the reverberation mapping-based virial mass estimate is:

$$M_{BH} \approx f_{BLR} G^{-1} FWHM^2 R_{BLR}$$

or

$$log\left(\frac{M_{BH}}{M_{\odot}}\right) = a + b \log\left(\frac{L}{10^{44} ergs^{-1}}\right) + c \log\left(\frac{FWHM}{kms^{-1}}\right)$$

where the FWHM is the width for the specific line used to derive the time lag, G is the gravitational constant, L is the continuum or line luminosity, the a,b,c coefficients are to be determined by linear regression analysis, and $f_{BLR} \simeq 1.2 \pm 0.2$ is a factor accounting the geometry of the sistem, calibrated from direct M_{BH} measurements based on the $M_{BH} - \sigma_*$ relation, whith σ_* being the stellar velocity dispersion in the bulge of the host galaxy.

Regarding the accretion rate, this can be estimated from X-ray spectroscopy.
We remind that the X-ray radiation is tought to stem from a hot corona above the accretion disk and the emission efficiency depends on the Eddington ratio and so the accretion rate. One of the effect of increasing the accretion rate is the steepening of the X-ray photon index Γ. Past works [116] have shown that in the radiation pressure-dominated regions of the disk $f_X \propto M_{BH}^{-1/18} \dot{m}^{-4/9}$, where $f_X = L_X/L_{BH}$ is the X-ray fraction of the emitted luminosity, and so one expect that the coronae emits a luminosity of $f_X L_{BH}$. Due to the fact that the main cooling process is Comptonization, from the heating and cooling balance, we have that $n_e \propto f_X$ and then $n_e \propto \dot{m}^{-4/9}$. Under these assumptions Γ can be approximated as $\Gamma \approx 2.25 y^{-2/9}$, where y is Comptonization parameter expected to be $y \propto n_e^{\gamma} \propto \dot{m}^{-4\gamma/9}$, with γ equal to 1 for unsaturated Comptonization and equal to 2 for saturated Comptonization [13]. Finally, considering the cutoff at 50-100 keV of the hard X-ray spectra [136], we obtain $\gamma \propto \dot{m}^{8\gamma/81}$, in agreement with the observed $\gamma - L_{Bol}/L_{Edd}$ correlation of AGN hosting α model accretion disks [98].

As we mentioned, high L/L_{Edd} quasars can be used as redshift-independent luminosity estimators where the constant parameter is Eddington ratio. A method to do so, that we summarize here, was proposed by Mariziani & Sulentic (2014) who also proposed a way to identify high Eddington ratio sources through the E1 space for low-z objects and the 1900 emission line blend of Al IIIλ1860, Si III]λ1892 and C III]λ1909 for high-z sources. Low-z sources were defined xA if they have $R_{FeII} > 1.0$ while high-z sources were defined xA if (Al IIIλ1860)/(Si III]λ1892) ≥ 0.5 and if (Si III]λ1892)/(C III]λ1909) ≥ 1.0.

The bolometric luminosity-black hole mass ratio of a source radiating at Eddington ratio λ_{Edd} can be written as:

$$\frac{L_{Bol}}{M_{BH}} \approx 10^{4.53}\lambda_{Edd}\left(\frac{L_{Bol}}{M_{BH}}\right)_{\odot} \approx 10^{4.81}\lambda_{Edd}\ \mathrm{erg\ s^{-1}\ g^{-1}}.$$

Assuming virial motion, the bolometric luminosity is:

$$L_{Bol} \approx \xi\lambda_{Edd}M_{BH} \approx \xi\lambda_{Edd}f_{BLR}\frac{R_{BLR}\delta v}{G},$$

where $\xi \approx 10^{4.81}\mathrm{erg\ s^{-1}\ g^{-1}}$ and δv is a virial velocity dispersion estimator. If one has a good estimate of the product of the ionization parameter U and the the hydrogen number density n_H, the broad line region size can be estimated as:

$$R_{BLR} = \left[\frac{\int_{\nu_0}^{+\infty}\frac{L_\nu}{h\nu}d\nu}{4\pi U n_H c}\right]^{1/2} = \left(\frac{\kappa L}{4\pi U n_H c h\bar{\nu_i}}\right)^{1/2},$$

where $\bar{\nu_i}$ is the average frequency of the ionizing photons and κL the ionizing luminosity with $\kappa = 0.5$. Past work have shown that estimating in this way R_{BLR} one obtains results not significantly different from reverberation values [126]. Therefore the bolometric luminosity can be expressed as:

$$L \approx 7.8\times10^{44}\frac{\lambda_{Edd}\kappa_{0.5}f_{BLR}^2}{h\nu_{i,\bar{100}eV}}\frac{1}{n_H U}_{10^{9.6}}(\delta v)^4_{1000}\mathrm{erg\ s^{-1}},$$

where the energy value has been normalized to 100 eV, the product $(n_H U)$ to the 'typical' value $10^{9.6}$ cm^3 and δv to 1000 km s^{-1}. The equation is formally valid for all λ_{Edd}.

CHAPTER 2

Sample selection and data analysis

2.1 Sample definition

2.1.1 SDSS-FIRST cross-match

The AGNs studied in this work are selected from the twelfth release of the Sloan Digital Sky Survey (SDSS) Quasar Catalog by Isabelle Paris et al. published in 2017. It contains 297 301 quasars detected over 9376 deg^2 that were spectroscopically targeted as quasars during the making of the Baryon Oscillation Spectroscopic Survey (BOSS) of the Sloan Digital Sky Survey III. The catalog presents for each object five-band (u, g, r, i, z) [55] CCD-based photometry with accuracy of 0.03 mag done with a dedicated 2.5 m wide-field telescope [64] during dark photometric nights of good seeing [72]. The objects properties were measured by the photometric pipeline [99] and calibrated photometrically [156] and astrometrically [139]. Moreover each object has been observed with the BOSS spectrographs with a resolution of $\sim$ 1300 at 3600 Åand of $\sim$ 2500 at 10 000 Å [155]. The observations consist in a series of at least three 15-min exposures until the squared signal-to-noise ratio per pixel $(S/N)^2$ reaches the survey-quality threshold for each CCD that are $(S/N)^2 \geq 22$ at i-band magnitude 21 for the red camera and $(S/N)^2 \geq 10$ at g-band magnitude 22 for the blue camera. To know more about the spectroscopic reduction pipeline we address to the 2012 Bolton et al. paper.

From the SDSS Quasar Catalog we selected all the objects with a i-band magnitude m_i value below 19.5 and with a BOSS pipeline redshift value z below 1.0 obtaining a first catalouge of 6505 sources. Sources with a higher magnitude with respect to that limit, have low S/N individual spectra that make difficult to estimate the FWHM(Hβ), the FeII flux and then the EV1 class. This sample was then cross-matched with the Very Large Array (VLA) Faint Images of the Radio Sky at Twenty-Centimeters (FIRST) survey.

The FIRST survey gives a high-resolution (5") map of the radio sky containing 946,432 sources distribuited over 10,575 deg^2 largely coincident with the SDSS area. The next figure shows the coverage map. The data were acquired using the VLA in its B-configuration with 3 minute exposures covering a hexagonal grid using 2×7 3-MHz frequency channels centered at 1365 and 1435 MHz. The source detection threshold is 1 mJy. Through the cross-match we selected only the SDSS objects that have one or more radio sources that are not more distant than 150" with respect to the SDSS object position, given by their right ascension (J2000) and declination (J2000). All the objects with only one radio source within an annulus of $2.5'' < r \leq 150''$ were rejected. Moreover, objects with missing or clearly wrong data (such as redshift or b-band magnitude) were rejected.

2.1.2 Radio morphology selection and classification

SDSS objects with one radio source within 120" were classified as core dominated (CD) AGN if the source is within 2.5" from the optical coordinates of the quasar. Objects with two radio sources within 120" were classified as CD AGN if one of the sources is within 2.5"; in this case the other radio source is not considered part of the system. Through an eye study of the FIRST images of these CD AGNs, they were divided in jetted and non-jetted CD AGNs. A CD AGN was classified as jetted if it shows a clear presence of a component that break the spherical symmetry like shown in figure 2.1.

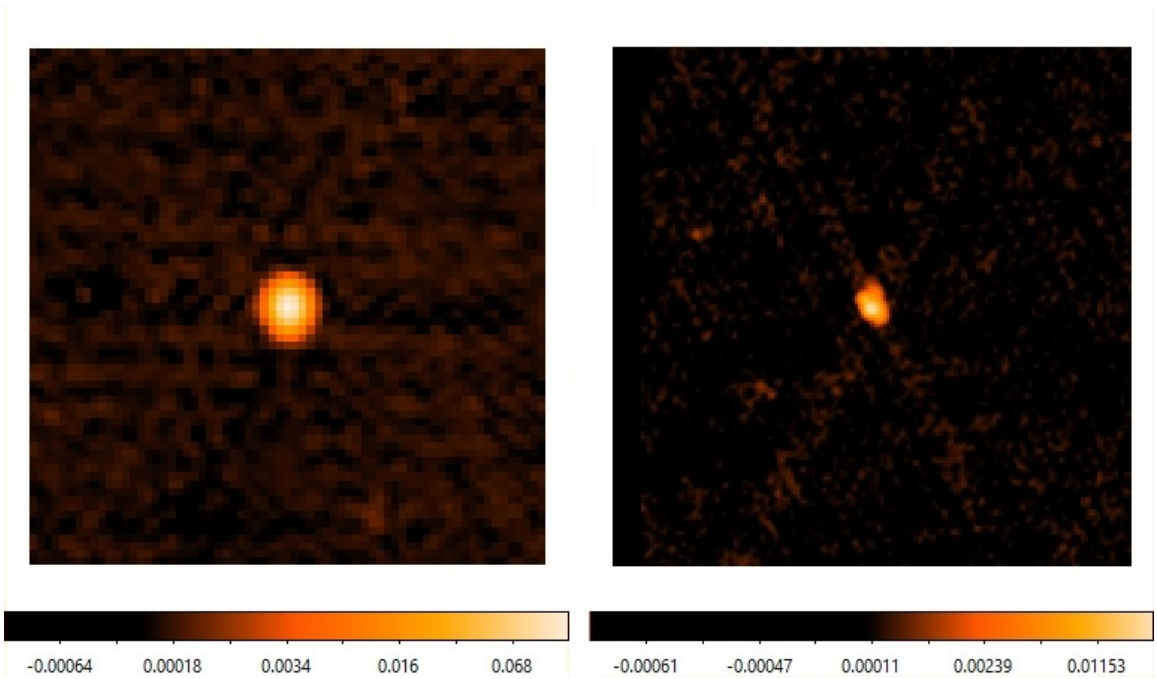

Figure 2.1: Left: non-jetted core dominated AGN. Right: jetted core dominated AGN. Images from FIRST catalouge.

The remaning objects are SDSS sources with 2 radio components in $2.5'' < r \leq 120''$ or with more than 2 whithin 120". These are FRII AGNs candidates. In order to select the real FRII AGN systems we adopted the objective procedure suggested by W. H. De Vries and R. H. Becker (2006). This consist in considering as pairwise the radio sources around a SDSS quasar and each pair a possible set of radio lobes. Pairs were ranked by the value of the following parameter:

$$w_{i,j} = \frac{\Psi/50^\circ}{(r_i + r_j)^2},$$

where Ψ is the opening angles (in degrees) as seen from the quasar position and $r_{i,j}$ are the distance rank numbers of the components under consideration, equal to zero for the closest component to the quasar, equal to 1 for the next closest and so on. In this way the closest radio components to the quasar have more weight. The opening angle is divided by 50° to weight against pairs of sources unrelated to the quasar that tend to have small opening angles. Then a higher value of $w_{i,j}$, means radio components closer to the quasar with an opening angle closer to 180°, and so a higher probability of the configuration to be a FRII AGN. The configuration with the highest $w_{i,j}$ value for each SDSS objects is kept and considered as a real FRII AGN if $130^\circ \leq \Psi \leq 180^\circ$ in the case the two radio components are within 60" or if $150^\circ \leq \Psi \leq 180^\circ$ in the case one or both are within 120" but not both within 60". This choice was made considering the result found by De Vries et al. (2006) shown in figure 2.2. In this are displayed the number of FRII AGN candidates as a function of Ψ around both the true quasar position (gray line) and the offset positions (black line) for different FRII AGN sizes. We see for the smallest size that, even though the distribution has a peak at opening angles of 180°, the distribution is quite broad and from this stem the choice of $130^\circ \leq \Psi \leq 180^\circ$. Looking at the larger sizes, we note that the relative importance of chance FRII occurrences (black line), becomes progressively more prevalent. From this derives the choice to consider only the FIRST objects within 120" from the SDSS sources positions.

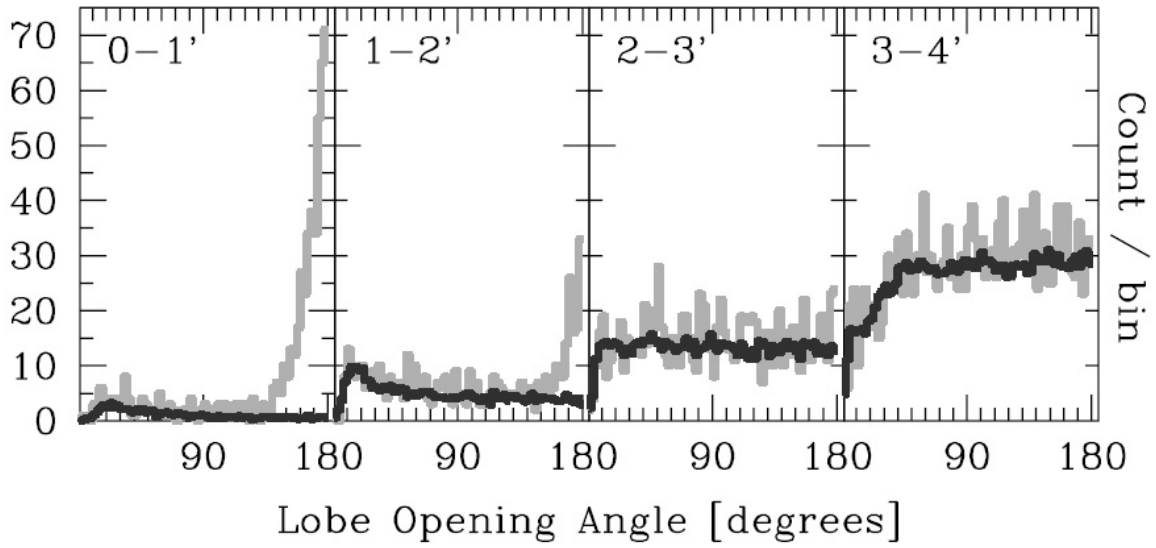

Figure 2.2: Number of FRII AGN candidates as a function of Ψ. Different FR size bin, given by their diameter in arcminutes, are shown in different pannels. The gray histogram represents the candidate count, and the black one the corresponding random-match baseline.

In this way we define two groups of FRII AGN, one that shows a radio source in correspondence of the SDSS quasar position (within 2.5") beside the two radio lobes and a group that shows only the two radio lobes and no radio source in correspondence of the SDSS quasar. We call the first one *cored Faranoff-Riley* (FRII) and the second one *non-cored Faranoff-Riley* (FRII_{nc}). Finally we check if each radio source corresponding to a radio lobe has an optical counterpart (within 2.5") through the NASA/IPAC Extragalactic Database (NED) and the configuration is rejected if one or both lobes have an optical counterpart. An example of FRII_{nc} and FRII AGN are shown in image 2.3. The final sample has 575 SDSS objects, 376 unresolved CD, 31 partially resolved CD, 90 FRII_{nc} and 76 FRII. Some properties are listed in tables A.1.

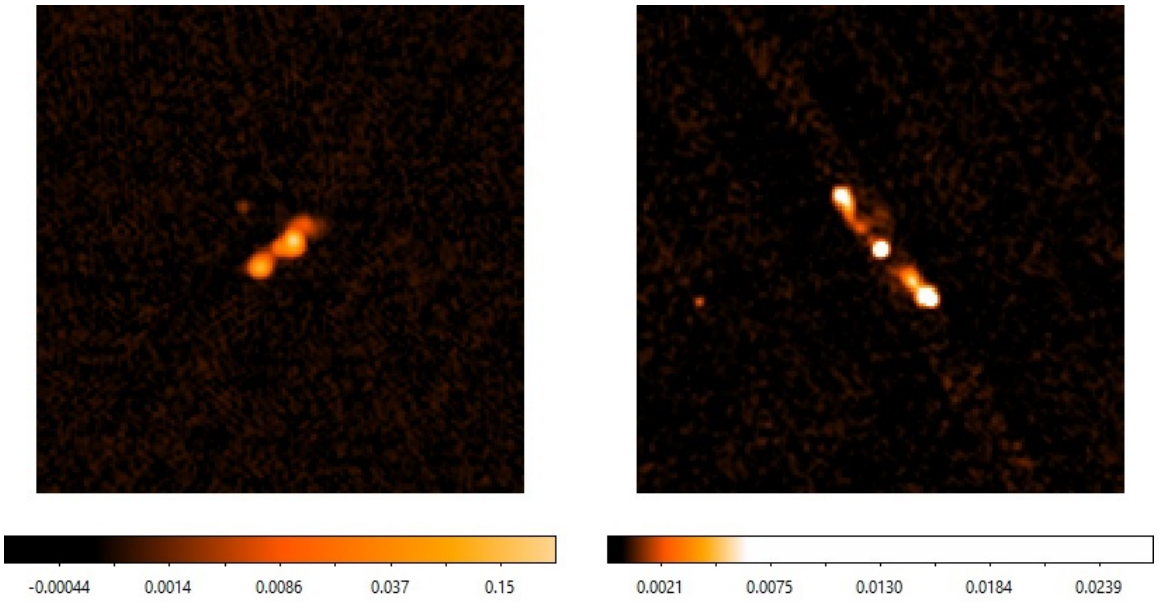

Figure 2.3: Left: FRII_{nc} AGN. Right: FRII AGN. Images from FIRST catalouge.

2.2 Radio-power emission based classification

Once we defined the sample, we studied the sources radio power emission and classified them in radio-detected, radio-intermediate and radio-loud. In order to do so we used the Kellerman's parameter $R_K = F_{radio}/F_{optical}$, where the numerator is the radio flux density and the denominator is the optical flux density [79]. To get the optical flux density $F_{optical}$ we started from the g-band magnitudes m_g aquired from the SDSS quasar catalogue. First we corrected them for the galactic extinction using the absortion parameter A_b values for each object aquired from the Nasa Extra Galactic Database (NED) and calculated by Schlafly et al. [146]. Endeed the light absortion and scattering due to the presence of dust and gas, mainly neutral hydrogen, in our galaxy between the emitting source and the observer, was already studied in 1930 [170]. In the optical and infrared (IR) range, the absortion can be approximated by the Whitford law: $A_\lambda = \lambda^{-\alpha(\lambda)}$, where $\alpha(\lambda)$ is equal to 0.9 in the visual and to 0.4 in te IR range. From this we note that the absortion is stronger at shorter wavelenghts than at longer ones. In the image below we see a full-sky $100\mu m$ dust map that show the presence of neutral hydrogen in our galaxy [147] since its distribution can be considered as the one of the dust.

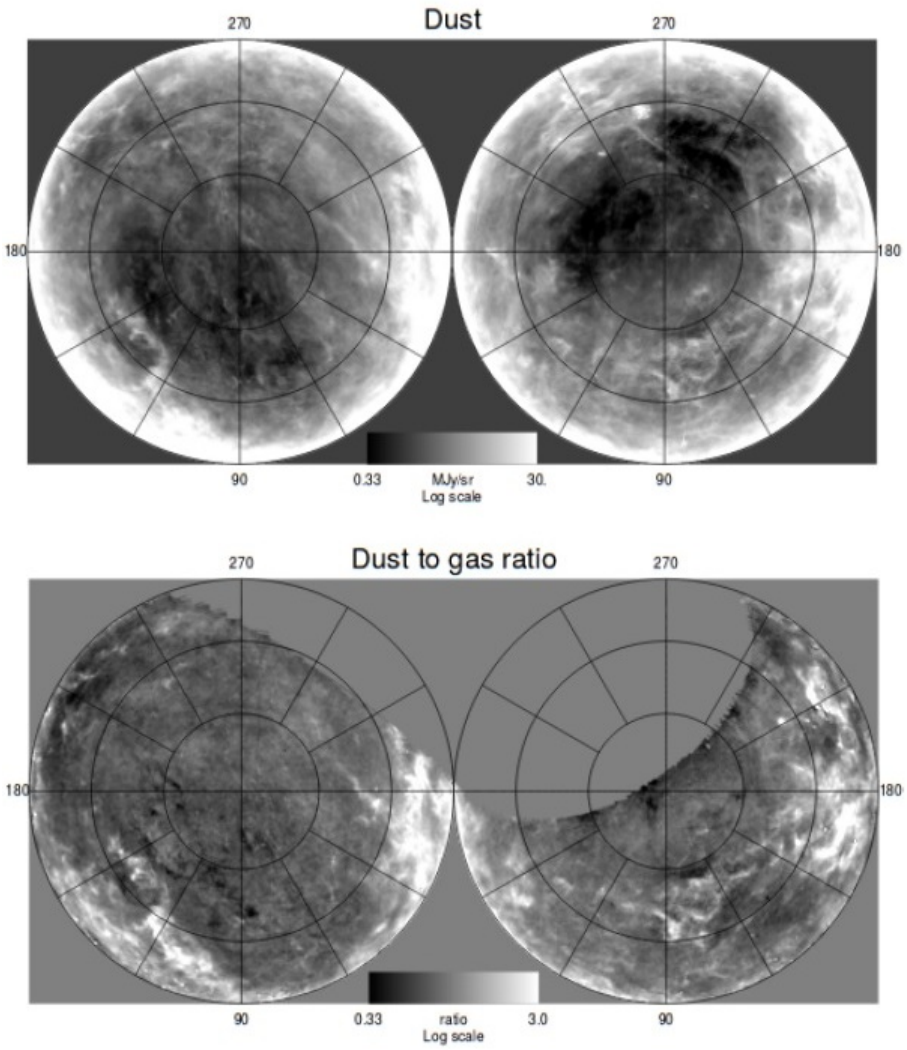

Figure 2.4: Top: full-sky $100\mu m$ dust map for the NGP (right) and SGP (left). Bottom: Dust-to-HI gas ratio for the NGP (right) and SGP (left). Images from [147]

After the extinction correction we calculated the flux density in Jy from the magnitude through the Pogson law obtaining: $F_b = 3631 \times 10^{-m_b/2.5}$. Before the calculation of R_K we must correct the fluxes with the K correction. This step is needed beacuse of the redshift effects. Indeed, due to the cosmic expansion, photons that we observe at frequency ν_{obs} are instead emitted at $\nu_e = \nu_{obs}(1+z)$, then $\nu_e > \nu_{obs}$. So if we do measurements through a single filter or a single bandpass, like our telescopes do, we see only a fraction of the total spectrum redshifted into the frame of the observer. To simplify the K correction we use the fact that in a wide wavelenght range the AGNs spectra can be rappresented by a power law: $L(\nu) \propto \nu^{-\alpha}$, where α is the spectral index at that frequency. From:

$$F_{obs,\nu} d\nu_{obs} = \frac{L_{\nu_e} d\nu_e}{4\pi d_L^2},$$

we can write the K corrected flux density as:

$$F_\nu = \frac{L_{\nu_{obs}}(1+z)^{-\alpha}(1+z)}{4\pi d_L^2} = F_{obs,\nu}(1+z)^{1-\alpha}.$$

For the SDSS sources and the FIRST objects corresponding to an SDSS source we used

$\alpha = 0.3$, instead for the radio lobes $\alpha = 1$. Having all the quantities required, we calculated R_K using for F_{radio} the flux density at 1.4 GHz aquired from the FIRST catalogue and the g-band flux density for $F_{optical}$. It should be noted that in the case of FRII AGNs, the radio flux density is the flux densities sum of all the radio components, core (if present) and lobes. Sources with $logR_K < 1.0$ are classified as radio-detected, with $1.0 < logR_K < 1.8$ as radio-intermediate and with $logR_K > 1.8$ as radio-loud. In tables A.7 the corrected fluxes and the R_K values are shown.
From the flux density at 1.4 GHz we calculated an estimate of the star formation rate as in the paper of Yun et al. (2001):

$$SFR_r = 4.1 \times 10^{-22} P_{1.4GHz},$$

where

$$\log(P_{1.4GHz}) = 20.08 + 2\log D + \log F_{1.4GHz},$$

with D the luminosity distance in Mpc and $F_{1.4GHz}$ the flux density in [W/Hz].

2.3 Optical spectroscopic study

2.3.1 E1 spectral classification

Once we grouped the sources in radio-power emission classes, the objects were classified in base of their optical spectroscopic characteristics in terms of the E1. We took the spectrum of each object from the SDSS Data release 14 (DR14) that includes the complete dataset of optical spectroscopy collected by the BOSS. First of all we rejected objects that show a type II AGN spectrum, spectra in which the host galaxy contamination is so strong to make impossible a reliable measure of the FWHM(Hβ), or spectra spoiled by noise such as bad spectra reduction due to strong atmosphere contamination. It should be noted that two objects from the original sample were rejected since they have a stellar spectrum and for this reason are not listed in tables. After these rejections, the final sample size is shown in table 2.1.

Table 2.1: Final sample size. The number of rejected sources on the base of their spectrum is also shown.

	CD	**CD$_j$**	**FRII$_{nc}$**	**FRII**
n. objects	376	31	90	76
Type II objects	52	4	5	5
Galaxy contaminated obj.	34	1	1	2
Damaged spectrum obj.	33	4	11	9
Spectral studied obj.	257	22	73	60

The spectral study was done with the Image Reduction and Analysis Facility (IRAF). The first step was the redshift correction of the spectra using the z values aquired from the SDSS quasars catalogue listed in tables. We used the **dopcor** task from the National Optical Astronomy Observatories (NOAO) **onedspec** package.

This process accounted also a k-correction. It should be noted that, from an inspection of the spectra, some sources show a different redshift with respect to that listed by the SDSS catalogue. In this case the correct redshift is calculated from the position of the [OII] emission line doublet which provides a redshift identification that can minimize confusion with other single emission lines [35] or, if this is not present, from the Hβ position. An accurate rest frame definition is important to identificate and have a correct physical interpretation of internal broad and narrow line shifts.
After the z-correction, we normalized each spectrum to their continuum value at 5100 Å through the **sarith** task from the **onedspec** package. This was measured through the **splot** task from the same package by measuring the mean over a region between 5050 and 5110 Å. From this value we calculated the luminosity at 5100 Å of each sources as: $L_{5100} = 4\pi(d_c)^2(\lambda f_\lambda)$, where d_c is the radial comoving distance, $\lambda = 5100$Å and f_λ is the continuum flux density at the quasar rest-frame.

The next step was the measure of the FWHM(Hβ), Hβ and FeII blend flux. This was done manually using the **splot** task from the NOAO **onedspec** package through a gaussian fit for the Hβ quantities. Meanwhile, by marking two continuum points at 4440 and 4680 Å and summing the pixels with partial pixels at the ends, we obtain the FeII flux. In case the FWHM(Hβ) is difficult to measure, like for example for high noise, we estimated it from the value of the FWHM(MgII) following the method described in the 2013 article by Marziani et al. [108]. From their value we calculated the parameter $R_{FeII} = I(FeII\lambda4570)/I(H\beta)$, and so we were able to classify them in the E1 spectral classes. Since the Hβ and FeII measures reflect physical conditions in the BLR, the classification groups sources with similar values of density, ionization parameter, and L/L_{Edd} [107]. Moreover it helps regard to the line profiles complexity, separating major flux contributions that are due to gas that is not virialized, like the redshifted very broad component (VBC) of Hβ in spectral type B sources.
From the measure of L_{5100} and FWHM(Hβ) we were able to calculate the BH mass for each object through the equation of Vestergaard and Peterson (2006):

$$\log(M_{BH}/M_\odot) = a + b\log(L_{5100}/10^{44}ergs^{-1}) + c\log(FWHM/kms^{-1})),$$

where $a = 0.895$, $b = 0.520$ and $c = 2.0$. Table 3.1 shows the resulting binning meanwhile table 3.4 shows for each class their L_{5100} and M_{BH} values.
The plots in the next pages show the redshift and luminosity distribution of our sample.

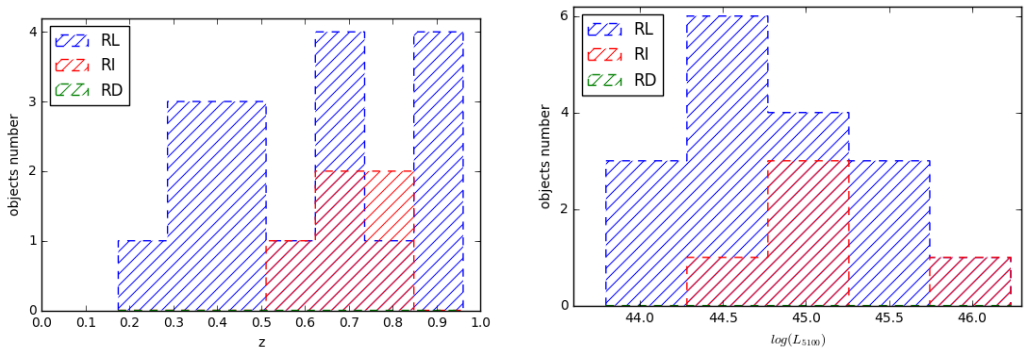

Figure 2.5: z (left) and L_{5100} (right) distributions of CD$_j$ sources

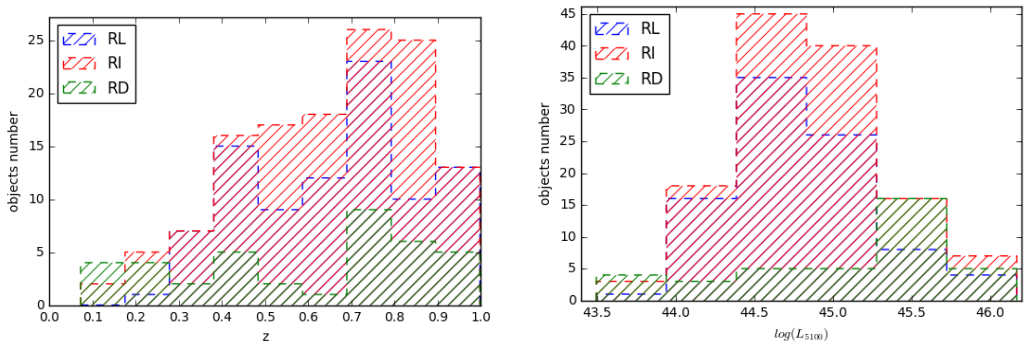

Figure 2.6: z (left) and L_{5100} (right) distributions of CD sources

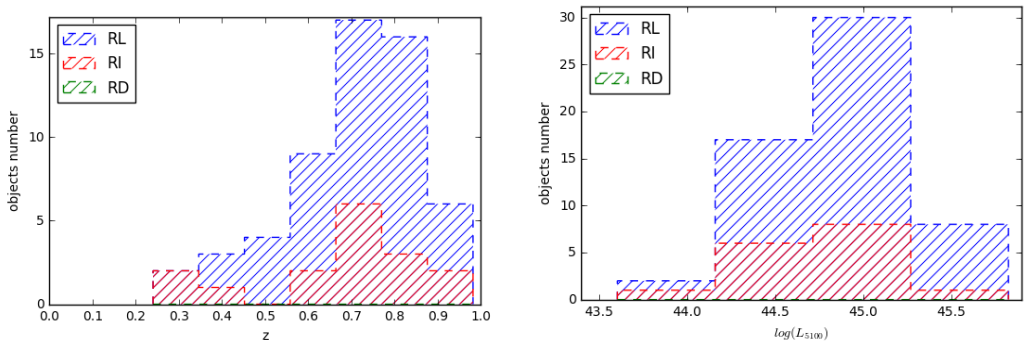

Figure 2.7: z (left) and L_{5100} (right) distributions of FRII$_{nc}$ sources

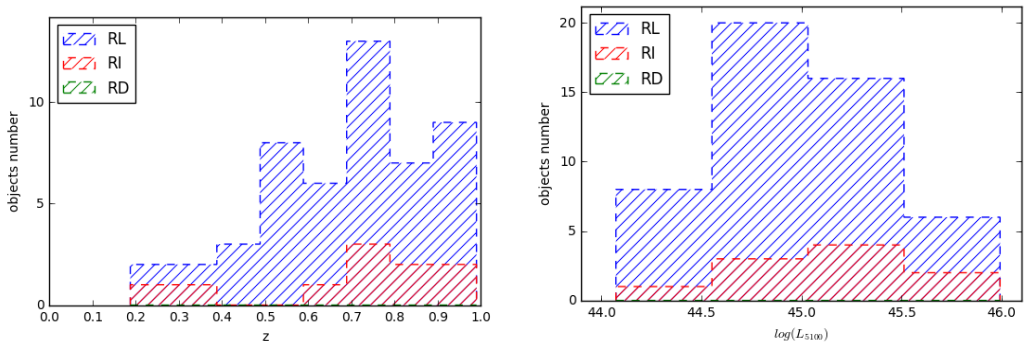

Figure 2.8: z (left) and L_{5100} (right) distributions of FRII sources

2.3.2 Composite spectra and model fitting

Thanks to the E1 spectral classification we are able to generate higher S/N composite spectra, with respect to a single spectrum, for each class and for each radio-power emission range (RD, RI, RL). The composite spectra were done with the **scombine** task from the NOAO **onedspec** package doing a median of the spectra belonging to a certain class. A first attempt was done averaging the spectra instead of making a median, but since the objects are not numerous, especially for classes with a high R_{FeII} value, the resulting composite spectra had high rms.

The next step was the creation of a model fitting the composite spectrum of each class with a non-linear chi-square minimization. This was done with the **specfit** task from the Space Telescope Science Data Analysis Software Package (**stsdas**). The spectral range fitted goes from 4430 to 5550 Å for both populations. The models for Population A and B accounts a similar number of components with some differences. For Population B these are:

- the continuum, fitted with a power-law (cyan);
- the Hβ narrow (yellow), broad (black) and very-broad (red) components, fitted with three gaussian line profiles;
- the FeII emission (green), modeled with the $FeII_{UV}$ emission template provided by the last model in Table 1 in Bruhweiler e Verner (2008);
- the [OIII] doublet, each line fitted with two gaussian line profiles (yellow) in order to account the blue-shifted emission;
- the broad and narrow components of HeII, fitted with two gaussians (blue).

For Population A the components fitted are:

- the continuum, fitted with a power-law (cyan);
- the Hβ narrow and broad components, the first one fitted with a gaussian (yellow) and the second one with a lorentzian line profile (black);
- the FeII emission, fitted as the Pop. B (green);
- the [OIII] doublet, each line fitted with three gaussian (yellow);
- NI and HeI emission lines, the former fitted with a gaussian (red) and the latter with a lorentzian (magenta);
- $[FeVI]$ and HeII (narrow and broad) emission if needed, each line fitted with a gaussian (blue).

The plots in table 3.2 and the images in Appendix B show the resulting fitting models.

CHAPTER 3

Results

3.1 Sample distribution in the EV1 and radio-power classes

The number of sources in each EV1 spectral bin for each AGN type (CD, CD_j, $FRII_{nc}$, FRII) and for each radio-power emission range (RD, RI, RL) is reported in table 3.1. There are a total of 38 radio detected objects, 162 radio intermediate and 214 radio loud.

• Radio-detected sources. We note that radio-detected sources are present only with a CD radio morphology. Population A and B are similar in number (20 A and 18 B) but population B sources with an FeII blend and Hβ flux ratio (R_{FeII}) higher than 0.5 are very rare (only 3 objects) in contrast with population A objects.

• Radio-intermidiate sources. In contrast with the RD class, RI sources are more numerous in population B than in A (87 CD in B and 42 CD in A). xA bins are populated in a significant way by CD objects (64% of all the xA CD sources are RI). In this radio-power range we see the first FRII objects but they are small in number (16 $FRII_{nc}$ and 10 FRII) with respect to the RL FRII galaxies. Also these radio morphology classes appear more frequently in population B. Moreover we note that in the RI class there aren't population A FRII while 6 $FRII_{nc}$ objects are observed in this bin.

• Radio-loud sources. In the same way of the RI class, RL objects are more numerous in population B for both CD and FRII classes (60 CD in B and 30 CD in A, 48 $FRII_{nc}$ in B and 9 $FRII_{nc}$ in A, 42 FRII in B and 8 FRII in A). We see then that the FRII classes are dominated by RL sources in contrast with the CD one where all the three radio-power classes are significantly populated, RD in a smaller way than RI and RL.

On a global view, we see that the most populated bins are the Pop. B ones, especially B1 and $B1^+$ bins. The number of objects in each bin goes down going towards bins with higher FWHM(Hβ) values (e.g. $B1^{++}$) and towards bins with lower ones (e.g. A1). The same happens in a stronger way going towards bins with higher R_{FeII} values. This reflects the behaviour of the quasar main sequence in the EV1 plane.

Table 3.1: Number of sources in each spectral type and radio-power emission range. Bold numbers refer to classes for which a fitting model was created.

	CD			**CD$_j$**		
	RD	**RI**	**RL**	**RD**	**RI**	**RL**
A1	**4**	**10**	**14**	-	1	1
A2	**11**	**14**	**11**	-	-	-
A3	**4**	**10**	**4**	-	-	-
A4	-	**6**	1	-	-	-
A5	1	2	-	-	-	-
B1	**7**	**33**	**26**	-	1	**13**
B1+	**8**	**29**	**20**	-	2	1
B1++	-	**9**	-	-	-	-
B1+++	-	2	3	-	-	1
B2	2	**10**	**6**	-	1	1
B2+	-	-	3	-	-	-
B2++	-	1	1	-	-	-
B3	1	3	1	-	-	-
Total	38	129	90	0	5	17

	FRII$_{nc}$			**FRII**		
	RD	**RI**	**RL**	**RD**	**RI**	**RL**
A1	-	3	3	-	-	**7**
A2	-	3	3	-	-	1
A3	-	-	3	-	-	-
B1	-	**5**	**27**	-	**5**	**25**
B1+	-	3	**12**	-	**4**	**11**
B1++	-	-	**7**	-	-	**5**
B1+++	-	-	-	-	-	1
B2	-	2	1	-	1	-
B2+	-	-	1	-	-	-
Total	0	16	57	0	10	50

3.2 xA sources

Thirty percent of Pop. A CD are xA, a fraction that is higher than the one measured in optically selected samples with no constraints on radio emission [181]. About 20% of the xA CD have RL power while in the A1 and A2 bins the RL objects are 63%.
As we mentioned before, xA objects have attracted a substantial attention of the astronomy community in the last decades. A key question is which mechanism is responsible for their strong radio power emission. Both relativistic jets and star formation process may contribute. A recent work [144] found, through a mid-infrared spectroscopy study of a radio-detected NLS1 sample, that all the objects show a strong AGN continuum and 70% of them show also a clear polycyclic aromatic hydrocarbon (PAH) emission whose

luminosity goes from 10^{39} to $10^{42} erg/s$ suggesting a strong star formation in the circumnuclear regions of these sources. Regarding the RL objects, as we already mentioned in section 1.5.3, a recent work [27] using also a mid-infrared study approach presented some radio-loud NLS1 galaxies likely powered by a starbust.
Other approaches have also been used. For example Komossa et al. (2006) used the correlation between IR luminosity and radio luminosity of starburst galaxies to gain some clues about the problem. Their results show that the radio emission of radio-loud NLS1s is several orders of magnitude more luminous than expected from starbursts suggesting that the radio emission is dominated by the relativistic jets contribution.

Other evidences that gives more favour to the jet emission domination in the radio range come from both theory [41] and observation. An example is 3C 57, an atypical RL quasar studied by Sulentic et a. (2015). This AGN shows extreme optical and radio properties with respect to the local RL sources ($l_{1415mhZ} \approx 34.4$ and $\log R_K \approx 3$). However its optical FeII emission ($R_{Fe} \sim 1$), C_{IV} $\lambda 1549$ blueshift ($-1500 km/s$) and Eddington ratio ($\log \lambda_E \approx -0.26$) show values unusual for the RL classes and more similar to the ones of population A2, associated with higher accretion rates and enhanced star formation, then apparently violating the EV1 empiricism. Thanks to the VLA maps this source was resolved showing two main emission components with projected separation of ≈17 kpc consistent with a compact steep spectrum (CSS) SED source. The characteristics of both high C_{IV} $\lambda 1549$ blueshift and an aligned lobe-dominated structure suggests that relativistic and a high-ionization wind, associated with the accretion disk, can coexist. Moreover it disproves previous ideas that high Eddington ratio and powerfull radio emission cannot occur at the same time [140].
Another more general example comes from Wu et al. (2009) who focused their attention in Gigahertz-peaked spectrum (GPS) and CSS radio sources. The most accreditated model to explain these two type of objects is the youth scenario: their compactness stems from their young age in which the jet will expand into the large scale lobe we usually see during the lifetime of powerful radio-loud sources [51]. This scenario is supported by kinematic age estimates from proper motions of hot spots [61] and radiative age estimates from synchrotron theory based on lobe radio spectra [123]. In their previous work [178], Wu et al. obtained, for most of their young radio galaxies sample, high accretion rates with average Eddington ratio ($< \lambda_E >= -0.56$) suggesting that the accretion disks in these sources may have suffered events of radiation pressure instability. This would provide an explanation of their short-lived activities. To test this theory, estimating the bolometric luminosity for a sample of young radio galaxies with known ages, they looked for a correlation between these two quantities, L_{bol} and age. A positive correlation was found roughly consistent with the prediction based on the radiation pressure instability of accretion disks of Czerny et al. (2009). Moreover, comparing the sources ages with half of the outbursts durations, which are assumed to stem from radiation pressure instabilities [41], they found out that they are consistent with the theoretical prediction. Then radiation pressure instability may also be the key to GPS and CSS sources. CSS may be the more powerful counterparts of RL NLSy1 [12], also experiencing a high accretion rate that leads to a relatively high Eddington ratio, and makes them possible intrinsically RL xA sources. Summing up, we expect that both non thermal emission associated with the jet and thermal emission due to SF, might be relevant in xA sources. As pointed out by Komossa (2018), RL NLSy1s which are strong FeII emitters do exist, but they are also extremely rare. This leaves open the possibility that xA sources may be predomantly thermal in their radio emission.

3.3 Orientation as possible explanation of FRII A1 objects

The existence of the A1 FRII sources may be explained in term of the angle between the radio axis and the line of sight and if this is the case they should be simply end-on extended doubles sources with a Doppler-boosted core [16]. Previous studies in the radio range have reinforced this idea [25]. To understand better this effect, Wills et al. (1986) investigate how the FWHM(β) changes as a function of parameter R, ratio between the radio flux density of the core to that of the extended lobes that reflects the angle between the radio axis and the line of sight in the relativistic beaming model for radio sources. Their result is shown in figure 3.1. It shows a continuous distribution in both R and FWHM that goes against the idea of the two distint classes characterized by a flat and a steep spectrum. Instead the trend may translate into an intrinsic difference between sources with high low R values or, if relativistic beaming models are correct, it may translate in a different viewing angle of the emission line regions. The motions of the emission-line gas would be on a disk perpendicular to the radio axis. In figure 3.1, our A1 FRII sources are represented by the red dots and the B1 sources by the blue ones. As we can see they follow the trend. On average the A1 sources have a higher R, with the exception of two, meanwhile B1 sources have lower values suggesting that the orientation might be the answer of the A1 FRII existence.

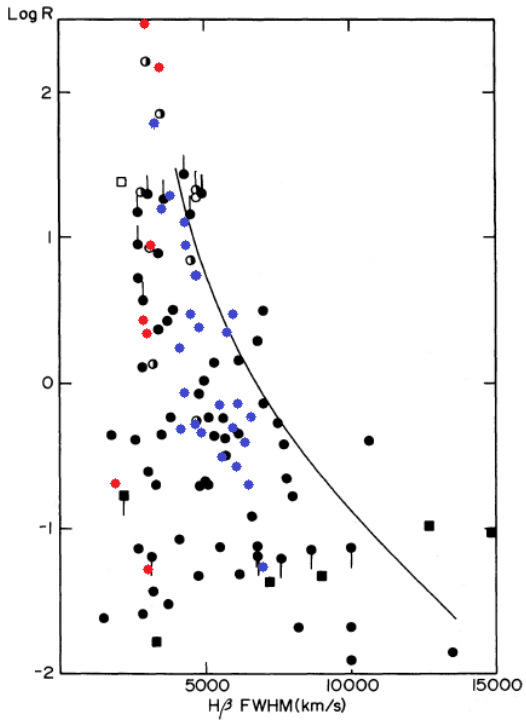

Figure 3.1: Ratio of 5 GHz core to lobe component flux density R against FWHM(Hβ) for quasars (black circles) and BLRGs (squares), observed superluminal expansion sources (open circle) and optically violent variables sources (half open). The curve represents the change of R with FWHM, as predicted by beaming model discussed in [175]. Red and blue circles represent A1 and B1 CFRII objects of our sample. Plot from [175].

3.4 Population A and B optical spectroscopic differences in the different radio-power classes

Tables 3.2 and 3.3 report the identification and show the original composite spectrum, the fitting model and the components decomposition for each EV1 and radio-power class. Table 3.6 reports the measures of the equivalent width (EW), FWHM, and centroid shifts $c(x)$ of Hβ and [OIII] emission line. The centroid shifts were defined as proposed by Marziani (1996):

$$c(x) = \frac{v_{r,R}(x) + v_{r,B}(x)}{2},$$

where x is a specific height of the profile (we considered 1/4, 1/2 and 9/10), $v_{r,R}$ and $v_{r,B}$ refer respectively to the velocity shift on the red and blue wing calculated relative to the rest-frame of the quasar.

Looking at tables 3.2 and 3.3 with respect to the EV1 classes (from left to right), we see the first differences between population A and B sources.
Regarding the Hβ line profile, we note that population A sources have a broad Hβ component best fitted with a Lorentzian profile while the population B ones are best fitted with two gaussians one of the which is tought to represent a distinct emitting region referred as very-broad component [106]. This was expected and confirms results of previous studies [106]. In addition going towards higher values of FWHM(Hβ) we note that the peak of the broad and very broad components of Hβ get more and more separated inducing to think that hat the broad line region might be made produced by a binary black system, with each black hole giving rise to a single broad component. This suggests that the system may be aa binary black-hole (BBH) one. In the next paragraph, we will discuss a little this idea.

BBH are tought to be produced during the merging of two galaxies [119]. Their detection and number estimates can give us constraints on formation and evolution galaxy models [73]. More importantly to our topic, BBHs are tought to be a possible cause of the different classes of RL AGN and of the misalignments between the direction of radio jet and the accretion disk [118]. The presence of a BBH in the nucleus of a RL AGN was hypothesized was suggested by Begelman Blandford, & Rees (1980). BBHs are suggested to increase the AGN activity [57] and trigger starburst processes [166]. Moreover ideas have been proposed that see the formation of radio jets associated with the merger of a BBHs [176]. In addition to these effects the presence of two BHs may affects the dynamics of the broad-line region gas marking the profiles of the emission lines [11], creating in some cases highly shifted double-peaked emission lines. Figure 3.2 displays these effects for two cases: both BHs have the BLR (left) and only one BH has it (right). Then from the broad optical lines stems a way to detect BBHs system with sub-parsec separation. Bon et al. (2012) analyzed the Hα line shape and flux variability in NGC 4151, one of the best studied Seyfert galaxies with a complex sub-parsec structure, through 20 years observations. The analysis indicated a periodic variations of the total flux with the period being of 5700 days. Moreover the radial velocity curves of Hα give evidence for orbital motion that are consistent with the presence of a sub-parsec scale BBH system with an orbital period of about 5780 days. This interpretation is in agreement with past theoretical results (e.g. [17]) and gives credit to the idea that BHs grow through merging processes and not by accretion ones.

Looking at the spectra shown in Table 3.2, we see that the Hβ profile includes a broader component close to the rest frame, but slightly displaced toward the blue, and a narrower and fainter component with a larger displacement to the red for the case of RI CD B1^{++}, and RL CD B1^{+}. The model fits are not biased as the BC and VBC were left free to vary in the χ^2 minimization process.
This configuration is consistent with the expectation of two BLRs, one associated with a more massive BH (the less-shifted component) and one associated with a less massive black hole orbiting around a common center of mass. We stress that the consistency is for a median spectrum, which means that one has to consider individual spectra before even making any tentative assessment. However, looking at the individual spectra, we can say that our analysis may have identified spectral types with a higher prevalence of super massive BBH (SMBBH). For instance, one may think of the Pop. A spectra which are always almost unshifted and symmetric and therefore to be excluded in a systematic search for SMBBH candidates.

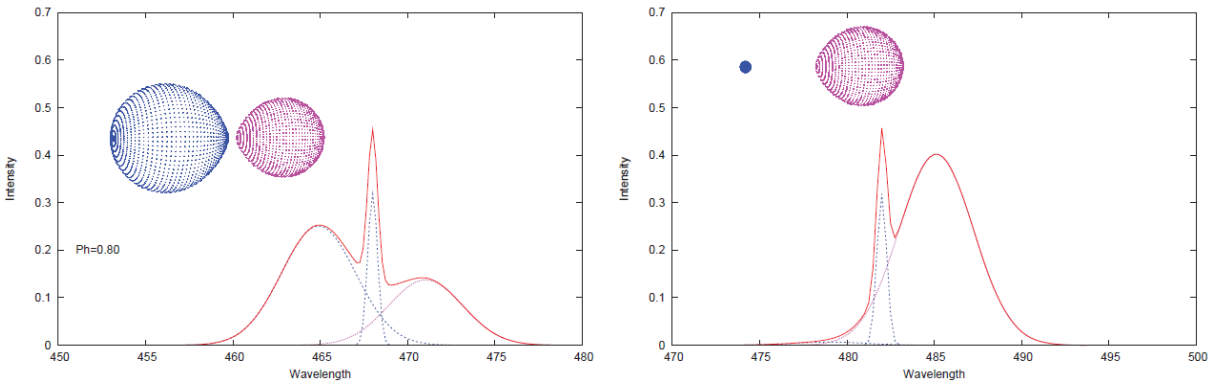

Figure 3.2: Hβ line profile emitted from BBH system where both of BHs have the BLR (left) and only one BH has it (right). Figure from [75].

Focusing on the other emission lines, we observe that in population A sources the [OIII] doublet becomes weaker and weaker going towards bins with a higher R_{FeII} value and a lower FWHM(Hβ) untill the [OIII] almost disappears in A3 and A4 bins. This anticorrelation was also expected since it is one of the well known and strongest trends of the quasar main sequence [160]. Another interesting fact about the [OIII] lines is the behaviour of the centroid shifts. As we can notice from Figure 3.3, in the CD classes the value of $c(1/4)$, $c(1/2)$ and $c(9/10)$ gets lower and lower below zero reflecting a an increasing blue-shift toward the line base. The blue-shifting of the [OIII] wing component, represented by $c(1/4)$, is very common in AGN but not every AGN shows a whole blue-shifted line, a negative $c(x)$ for all x. Sources that shows a blue-shift higher than $250km/s$ have been termed as *blue outliers* [180]. Blue outliers are common in the xA class but no [OIII] profile in our sample qualifies the source as a blue outlier. NCFRII and CFRII do not show an evident trend instead and the [OIII] line can be considered symmetric.

Looking now with respect to the radio-power emission classes (from top to bottom) we can notice interesting results as shown in Figure 3.3 and 3.4. As regard to the Hβ line, we note that going from the RD to the RL class the centroids are more redshifted as we can see from the top plot of Fig. 3.4. Focusing on the [OIII] lines we notice that in the

RD class the [OIII] intensity follows the anti-correllation with the FeII emission blend, instead in the RI and RL the [OIII] line is still visible even in xA bins. Other informations about the [OIII] line can be extracted from its centroid shifts. In the RD and RI class the [OIII] line can be considered asymmetric, in the sense that only the $c(1/4)$ shows a significant blueshift, from the B1^{++} to the A1 bins while in the A2 and xA bins the whole line is blue-shifted. Instead the [OIII] lines in RL sources can be considered symmetric up to the A2 bin, as we can se from the bottom plot of Fig. 3.4, and only from the A3 bin the line shows a sistematic blue-shift.
Taken as a whole, these result suggest that [OIII] is strengthened in RL sources. At the same time, the profile becomes more symmetric and less shifted.

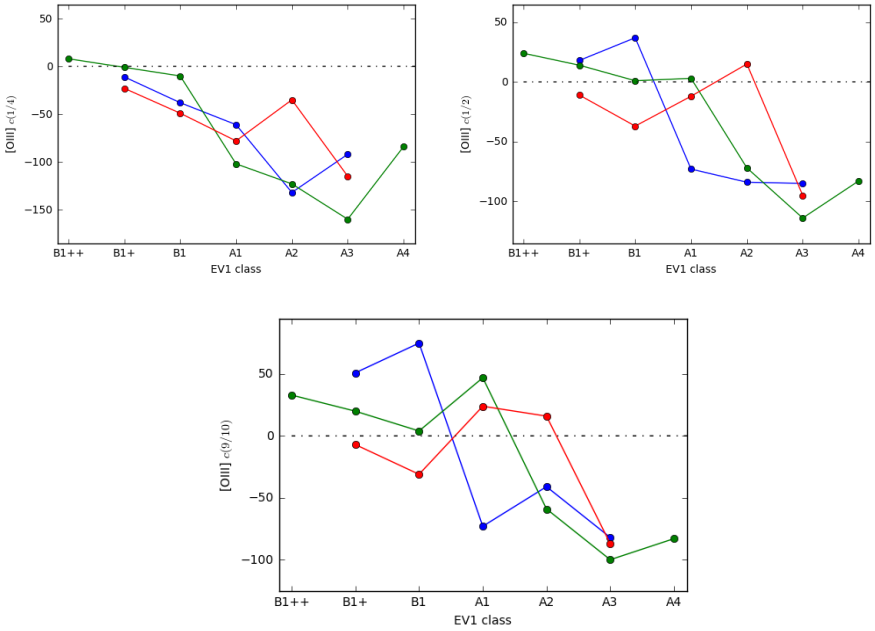

Figure 3.3: CD OIII centroid shifts $c(x)$ at different line height x (topleft $x = 1/4$, topright $x = 1/2$, bottom $x = 9/10$). Blue lines represents RD classes, green the RI and red the RL ones.

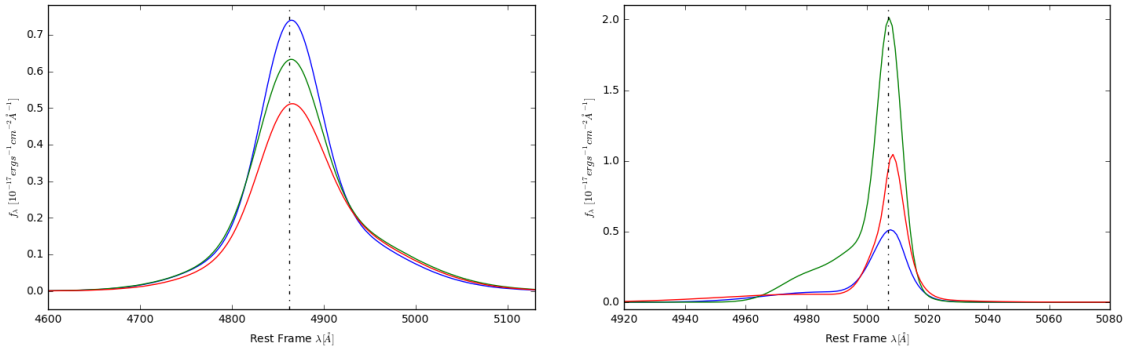

Figure 3.4: Top: B1 CD Hβ broad component for the different radio-power classes. Bottom: A2 CD [OIII] emission line for the different radio-power classes. The blue line represents RD class, the green one the RI and red one the RL class. We note the growing redshift of Hβ going from RD to RL and the different shifts between RD/RI and RL classes, the latter being more redshifted.

Table 3.2: Specfit fitting models.

		B1++	B1+	B1
$\mathbf{CD}_j$	**RD**	-	-	-
	RI	-	2	1
	RL	-	1	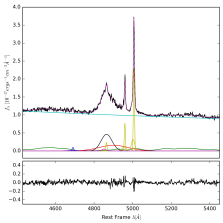
CD	**RD**	-	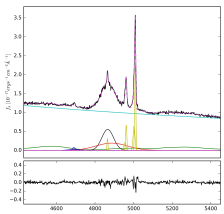	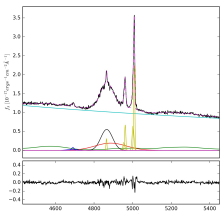
	RI	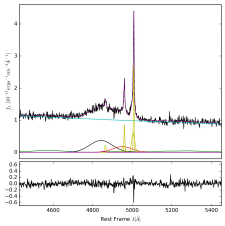	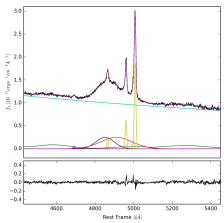	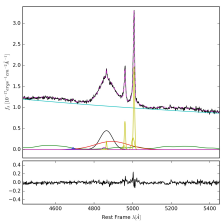
	RL	-	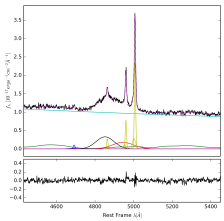	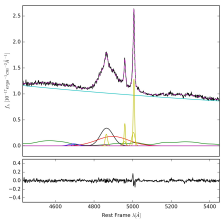
$\mathbf{FRII}_{nc}$	**RD**	-	-	-
	RI	-	3	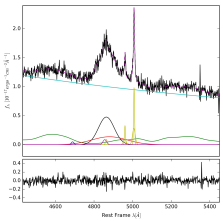
	RL	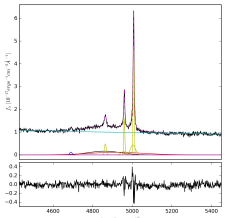	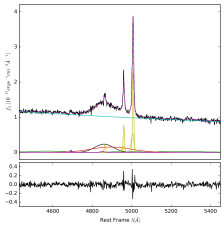	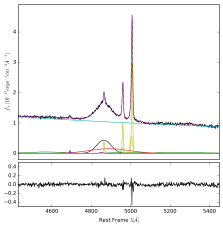
FRII	**RD**	-	-	-
	RI	-	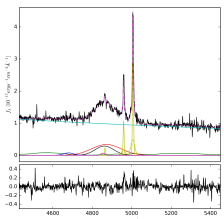	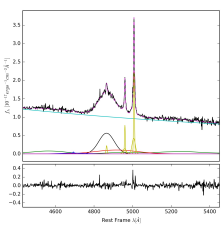
	RL	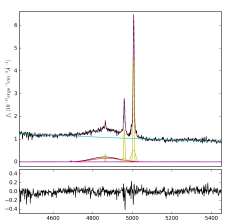	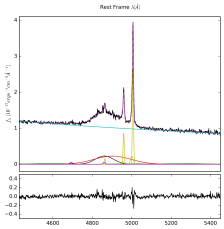	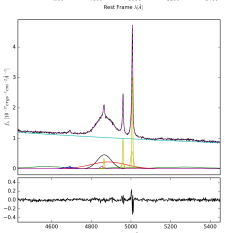

Table 3.3: Specfit fitting models (2)

A1	A2	A3	A4
-	-	-	-
1	-	-	-
1	-	-	-
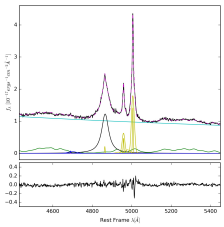	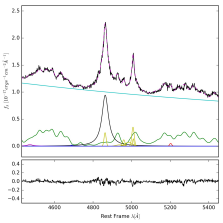	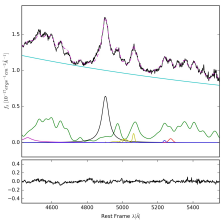	1
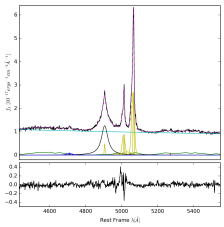	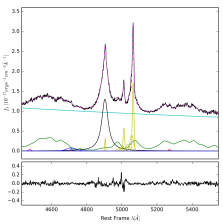	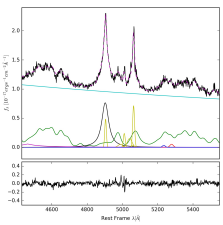	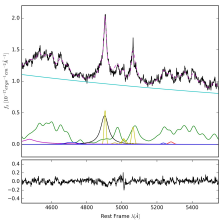
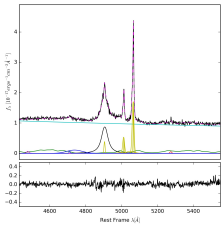	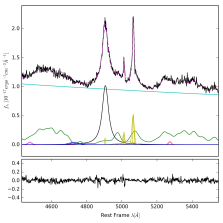	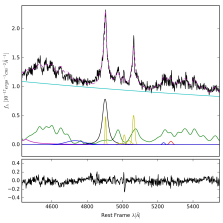	-
-	-	-	-
3	3	-	-
3	3	3	-
-	-	-	-
-	1	-	-
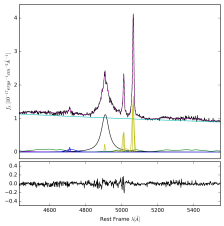	-	-	-

3.5 Population A and B physical parameter differences in the different radio-power classes

Table 3.4 reports some physical parameters for each E1, radio-power and radio-morphology class. These are the luminosity at 5100 Å L_{5100}, the black hole mass M_{BH}, the Eddington ratio λ_E, the radio power at 1.4 GHz P_ν, the Kellerman logarithm parameter $\log R_K$ and the star-formation rate estimate calculated from the radio-power. These were calculated following the methods described in section 2.2 and 2.3.
Focusing on the trend along the E1 main sequence we note that L_{5100} and P_ν show similar values among all classes. However going from the B1^{++} to the A4 class we see an increase of the Eddington ratio and a decrease of the black hole mass. This fact is in agreement with past works (e.g. Marconi et al. (2009)) suggesting that around the critical value $\lambda_E \sim 0.2 \pm 0.1$ the active nucleus may change fundamentally in its properties and structures therefore confirming the existence of two distinct populations A and B. Population A sources being fast accreting objects with small black hole masses and population B ones being slow accreting and with high black hole mass. Our values obey the limit with population B classes having $\lambda_E < 0.2$. The converse is true for population A. Focusing on the different radio-power emission classes we notice that in general the black hole masses and the Eddington ratios are higher in the RD classes than in the RI-RL ones in Pop. A. The opposite happens for the star formation rate, higher in the RI class and lower in the RD ones. As regard the star formation rate we see that, in general, population B sources show a lower value with respect to population A. Moreover going from the RD to the RL the rate increases since the radio power increases and the SFR estimate is based on the latter. This suggests that in population B sources and especially in the RL class the estimate is overestimated due to the strong contribution to the radio power from the relativistic jets meanwhile in population A and RD classes the estimate of the SFR can be considered more reliable and the star formation process as a possible mechanism dominating the AGN activity.

• *The meaning of radio SFR.* The diagram of Bonzini et al. (2015) reported in section 1.5.3 is helpful to set an upper limit to the radio power that is associated with star formation: RD quasars have a maximum SFR around 1000 $M_\odot/yr$. Higher SFR are unphysical, as the feedback effect due to stellar winds and supernova explosions may bring star formation to a halt on a very short timescale. We cannot also exclude that, in any class we identified, there is contribution from the non-thermal activity of the nucleus. This is already known to be dominant in RL, and the typical SFR values would be $> 10^4 M_\odot/yr$ so that no SFR is reported for all RL spectral types save CD A3 that still has a value consistent with SF. A major result is that RD and RI CD are consistent with SFR induced by SF, on average. Especially striking is the result for xA sources which are known by the FIR data to be highly star forming system. Our analysis has identified a small sample of sources which are the best candidates (RL CD A3) to test the SF contribution to the total radio power. This may have profound consequences in our understanding of galaxy evolution, as xA sources are the ones expected to provide the maximum feedback effect on the host galaxy. In other words, they are the AGN most likely to affect the dynamical and structural properties of the host, ultimately leading to the well-known correlation between BH mass and bulge mass [102, 52]. Whether the feedback effect is produced by the AGN itself or by induced star formation is still an open issue.

Table 3.4: Physical parameters of each E1, radio-power and radio morphology class.

			B1++	B1+	B1	A1	A2	A3	A4
$\mathbf{CD}_j$	**RD**	L_{5100}	-	-	-	-	-	-	-
		λ_E	-	-	-	-	-	-	-
		M_{BH}	-	-	-	-	-	-	-
		P_ν	-	-	-	-	-	-	-
		$\log R_K$	-	-	-	-	-	-	-
		SFR_r	-	-	-	-	-	-	-
	RI	L_{5100}	-	-	-	-	-	-	-
		λ_E	-	-	-	-	-	-	-
		M_{BH}	-	-	-	-	-	-	-
		P_ν	-	-	-	-	-	-	-
		$\log R_K$	-	-	-	-	-	-	-
		SFR_r	-	-	-	-	-	-	-
	RL	L_{5100}	-	-	1.43×10^{45}	-	-	-	-
		λ_E	-	-	0.173	-	-	-	-
		M_{BH}	-	-	5.54×10^{8}	-	-	-	-
		P_ν	-	-	6.24×10^{25}	-	-	-	-
		$\log R_K$	-	-	2.54	-	-	-	-
		SFR_r	-	-	-	-	-	-	-
CD	**RD**	L_{5100}	-	3.38×10^{45}	1.40×10^{45}	2.68×10^{45}	2.51×10^{45}	4.65×10^{45}	-
		λ_E	-	0.093	0.149	0.573	0.632	0.718	-
		M_{BH}	-	2.40×10^{9}	6.28×10^{8}	3.12×10^{8}	2.64×10^{8}	4.31×10^{8}	-
		P_ν	-	6.0×10^{24}	1.51×10^{24}	2.45×10^{24}	2.8×10^{24}	8.75×10^{24}	-
		$\log R_K$	-	0.83	0.61	0.65	0.62	0.66	-
		SFR_r	-	2.46×10^{3}	6.21×10^{2}	1.0×10^{3}	1.14×10^{3}	3.58×10^{3}	-
	RI	L_{5100}	1.15×10^{45}	1.88×10^{45}	1.30×10^{45}	9.01×10^{44}	7.96×10^{44}	1.07×10^{45}	5.26×10^{44}
		λ_E	0.0380	0.070	0.121	0.411	0.384	0.330	0.158
		M_{BH}	2.02×10^{9}	1.77×10^{9}	7.16×10^{8}	1.46×10^{8}	1.38×10^{8}	1.38×10^{8}	2.20×10^{8}
		P_ν	1.2×10^{25}	9.13×10^{24}	7.64×10^{24}	2.83×10^{24}	2.48×10^{24}	5.41×10^{24}	3.26×10^{24}
		$\log R_K$	1.46	1.45	1.44	1.51	1.32	1.42	1.41
		SFR_r	4.92×10^{3}	3.74×10^{3}	3.13×10^{3}	1.16×10^{3}	1.01×10^{3}	2.22×10^{3}	1.33×10^{3}
	RL	L_{5100}	-	9.78×10^{44}	1.89×10^{45}	8.73×10^{44}	7.11×10^{44}	3.18×10^{44}	-
		λ_E	-	0.053	0.151	0.219	0.298	0.164	-
		M_{BH}	-	1.22×10^{9}	8.35×10^{8}	2.65×10^{8}	1.58×10^{8}	1.29×10^{8}	-
		P_ν	-	1.94×10^{25}	1.44×10^{26}	1.12×10^{26}	1.45×10^{25}	8.06×10^{24}	-
		$\log R_K$	-	2.34	2.57	2.79	2.4	2.0	-
		SFR_r	-	-	-	-	5.94×10^{3}	3.3×10^{3}	-
$\mathbf{FRII}_{nc}$	**RD**	L_{5100}	-	-	-	-	-	-	-
		λ_E	-	-	-	-	-	-	-
		M_{BH}	-	-	-	-	-	-	-
		P_ν	-	-	-	-	-	-	-
		$\log R_K$	-	-	-	-	-	-	-
		SFR_r	-	-	-	-	-	-	-
	RI	L_{5100}	-	-	4.99×10^{44}	-	-	-	-
		λ_E	-	-	0.050	-	-	-	-
		M_{BH}	-	-	6.64×10^{8}	-	-	-	-
		P_ν	-	-	6.86×10^{24}	-	-	-	-
		$\log R_K$	-	-	1.46	-	-	-	-
		SFR_r	-	-	-	-	-	-	-
	RL	L_{5100}	1.01×10^{45}	8.74×10^{44}	1.40×10^{45}	-	-	-	-
		λ_E	0.0179	0.049	0.101	-	-	-	-
		M_{BH}	3.77×10^{9}	1.18×10^{9}	9.19×10^{8}	-	-	-	-
		P_ν	9.33×10^{25}	8.55×10^{25}	7.88×10^{25}	-	-	-	-
		$\log R_K$	2.80	2.62	2.52	-	-	-	-
		SFR_r	-	-	-	-	-	-	-
FRII	**RD**	L_{5100}	-	-	-	-	-	-	-
		λ_E	-	-	-	-	-	-	-
		M_{BH}	-	-	-	-	-	-	-
		P_ν	-	-	-	-	-	-	-
		$\log R_K$	-	-	-	-	-	-	-
		SFR_r	-	-	-	-	-	-	-
	RI	L_{5100}	-	6.42×10^{44}	2.67×10^{45}	-	-	-	-
		λ_E	-	0.0423	0.118	-	-	-	-
		M_{BH}	-	1.01×10^{9}	1.50×10^{9}	-	-	-	-
		P_ν	-	1.54×10^{25}	4.56×10^{25}	-	-	-	-
		$\log R_K$	-	1.57	1.70	-	-	-	-
		SFR_r	-	-	-	-	-	-	-
	RL	L_{5100}	9.98×10^{44}	1.06×10^{45}	2.37×10^{45}	1.27×10^{45}	-	-	-
		λ_E	0.025	0.056	0.143	0.355	-	-	-
		M_{BH}	2.59×10^{9}	1.25×10^{9}	1.10×10^{9}	2.38×10^{8}	-	-	-
		P_ν	6.70×10^{25}	5.16×10^{25}	1.25×10^{26}	1.46×10^{26}	-	-	-
		$\log R_K$	2.57	2.44	2.43	2.71	-	-	-
		SFR_r	-	-	-	-	-	-	-

Note: luminosity at 5100 Å L_{5100} in $[ergs^{-1}]$, M_{BH} in solar masses $M_\odot$, λ_E Eddington ratio, radio power P_ν at 1.4 GHz in W/Hz, star formation rate in $M_\odot/yr$.

Table 3.5: Hβ and [OIII] properties of each E1, radio-power and radio morphology class.

Hβ			**B1++**	**B1+**	**B1**	**A1**	**A2**	**A3**	**A4**				**B1++**	**B1+**	**B1**	**A1**	**A2**	**A3**	**A4**
		EW	-	-	-	-	-	-	-			EW	-	-	-	-	-	-	-
		FWHM	-	-	-	-	-	-	-			FWHM	-	-	-	-	-	-	-
	RD	c(1/4)	-	-	-	-	-	-	-		**RD**	c(1/4)	-	-	-	-	-	-	-
		c(1/2)	-	-	-	-	-	-	-			c(1/2)	-	-	-	-	-	-	-
		c(9/10)	-	-	-	-	-	-	-			c(9/10)	-	-	-	-	-	-	-
		EW	-	-	-	-	-	-	-			EW	-	-	81.4	-	-	-	-
		FWHM	-	-	-	-	-	-	-			FWHM	-	-	6919	-	-	-	-
CD$_j$	**RI**	c(1/4)	-	-	-	-	-	-	-	**FRII$_{nc}$**	**RI**	c(1/4)	-	-	190	-	-	-	-
		c(1/2)	-	-	-	-	-	-	-			c(1/2)	-	-	63	-	-	-	-
		c(9/10)	-	-	-	-	-	-	-			c(9/10)	-	-	15	-	-	-	-
		EW	-	-	63.2	-	-	-	-			EW	74.1	67.2	77.8	-	-	-	-
		FWHM	-	-	5005	-	-	-	-			FWHM	14974	9160	6544	-	-	-	-
	RL	c(1/4)	-	-	690	-	-	-	-		**RL**	c(1/4)	1745	1054	459	-	-	-	-
		c(1/2)	-	-	235	-	-	-	-			c(1/2)	952	295	121	-	-	-	-
		c(9/10)	-	-	125	-	-	-	-			c(9/10)	490	8	37	-	-	-	-
		EW	-	93.6	81.7	82.3	60.1	42.6	-			EW	-	-	-	-	-	-	-
		FWHM	-	11329	5385	2681	2511	2731	-			FWHM	-	-	-	-	-	-	-
	RD	c(1/4)	-	2073	441	-	-	-	-		**RD**	c(1/4)	-	-	-	-	-	-	-
		c(1/2)	-	1663	199	-	-	-	-			c(1/2)	-	-	-	-	-	-	-
		c(9/10)	-	-253	134	-	-	-	-			c(9/10)	-	-	-	-	-	-	-
		EW	74.7	82.6	76.7	77.1	83.3	51.9	33.4			EW	-	100.7	86.4	-	-	-	-
		FWHM	12154	10161	5920	2434	2444	2831	3444			FWHM	-	8822	6521	-	-	-	-
CD	**RI**	c(1/4)	810	1745	664	-	-	-	-	**FRII**	**RI**	c(1/4)	-	238	361	-	-	-	-
		c(1/2)	581	911	175	-	-	-	-			c(1/2)	-	125	162	-	-	-	-
		c(9/10)	-690	157	99	-	-	-	-			c(9/10)	-	42	95	-	-	-	-
		EW	-	65.1	66.2	50.4	62.3	36.3	-			EW	62.8	79.7	88.9	79.0	-	-	-
		FWHM	-	10112	6363	3308	2700	3000	-			FWHM	10381	9839	6558	2844.39	-	-	-
	RL	c(1/4)	-	1784	1136	-	-	-	-		**RL**	c(1/4)	121	1754	680	-	-	-	-
		c(1/2)	-	1109	440	-	-	-	-			c(1/2)	103	897	287	-	-	-	-
		c(9/10)	-	5	214	-	-	-	-			c(9/10)	88	375	180	-	-	-	-

[OIII]			**B1++**	**B1+**	**B1**	**A1**	**A2**	**A3**	**A4**				**B1++**	**B1+**	**B1**	**A1**	**A2**	**A3**	**A4**
		EW	-	-	-	-	-	-	-			EW	-	-	-	-	-	-	-
		FWHM	-	-	-	-	-	-	-			FWHM	-	-	-	-	-	-	-
	RD	c(1/4)	-	-	-	-	-	-	-		**RD**	c(1/4)	-	-	-	-	-	-	-
		c(1/2)	-	-	-	-	-	-	-			c(1/2)	-	-	-	-	-	-	-
		c(9/10)	-	-	-	-	-	-	-			c(9/10)	-	-	-	-	-	-	-
		EW	-	-	-	-	-	-	-			EW	-	-	12.3	-	-	-	-
		FWHM	-	-	-	-	-	-	-			FWHM	-	-	444	-	-	-	-
CD$_j$	**RI**	c(1/4)	-	-	-	-	-	-	-	**FRII$_{nc}$**	**RI**	c(1/4)	-	-	12	-	-	-	-
		c(1/2)	-	-	-	-	-	-	-			c(1/2)	-	-	20	-	-	-	-
		c(9/10)	-	-	-	-	-	-	-			c(9/10)	-	-	22	-	-	-	-
		EW	-	-	24.7	-	-	-	-			EW	48.3	27.9	31.8	-	-	-	-
		FWHM	-	-	453	-	-	-	-			FWHM	418	505	471	-	-	-	-
	RL	c(1/4)	-	-	-32	-	-	-	-		**RL**	c(1/4)	-3	-14	-14	-	-	-	-
		c(1/2)	-	-	-22	-	-	-	-			c(1/2)	-1	-1	0	-	-	-	-
		c(9/10)	-	-	-18	-	-	-	-			c(9/10)	-1	5	6	-	-	-	-
		EW	-	45.2	25.4	45.1	10.4	3.8	-			EW	-	-	-	-	-	-	-
		FWHM	-	669	500	538	820	779	-			FWHM	-	-	-	-	-	-	-
	RD	c(1/4)	-	-11	-38	-61	-132	-92	-		**RD**	c(1/4)	-	-	-	-	-	-	-
		c(1/2)	-	18	37	-73	-84	-85	-			c(1/2)	-	-	-	-	-	-	-
		c(9/10)	-	51	75	-73	-41	-82	-			c(9/10)	-	-	-	-	-	-	-
		EW	26.2	23.4	21.4	71.3	31.8	15.1	7.7			EW	-	33.9	23.4	-	-	-	-
		FWHM	332	623	497	538	617	748	970			FWHM	-	428	384	-	-	-	-
CD	**RI**	c(1/4)	8	-1	-10	-102	-123	-160	-84	**FRII**	**RI**	c(1/4)	-	53	79	-	-	-	-
		c(1/2)	24	14	1	3	-72	-114	-83			c(1/2)	-	-25	9	-	-	-	-
		c(9/10)	33	20	4	47	-59	-100	-83			c(9/10)	-	-38	3	-	-	-	-
		EW	-	27.1	17.4	11.2	16.0	10.2	-			EW	46.7	23.8	29.0	33.0	-	-	-
		FWHM	-	514	557	359	555	857	-			FWHM	437	431	383	470	-	-	-
	RL	c(1/4)	-	-23	-49	-78	-35	-115	-		**RL**	c(1/4)	-21	-45	0	-53	-	-	-
		c(1/2)	-	-11	-37	-12	15	-95	-			c(1/2)	-10	-37	6	-13	-	-	-
		c(9/10)	-	-7	-31	24	16	-87	-			c(9/10)	6	-32	12	-4	-	-	-

Note: equivalent width (EW) in [Å], FWHM in [km/s], centroid shifts $c(x)$ at fraction intensity of 1/4, 1/2 and 9/10 in [km/s].

CHAPTER 4

Conclusion

The goal of this thesis was to define the meaning of the radio emission in large samples of quasars. We have focused our attention on RD and RI quasars which may not be "jetted" quasars in the sense of Padovani (2017), that is sources with radio emission due to a relativistic jet. We studied a sample of AGN defined by the cross-match between the FIRST and the 12th release of the SDSS quasar catalogue by Paris et al. (2017), considering only objects with $z < 1$ and i magnitude below 19.5. We divided our sample in RD, RI, RL, on the base of the Kellerman parameter, and for each radio-power class we distinguished between CDs and FRIIs, where the latter ones were selected following the method by De Vries (2006). Each class based on radio power and morphology was then subdivided into spectral types defined along the E1 MS of quasars. We present composite spectra for all radio-classes and spectral types, along with spectrophotometric measurements and measurements on the line profiles of Hβ and [OIII], obtained through a multi-component, non-linear fitting procedure. The main results are listed below.

- *Sample distribution in radio-classes and spectral types.*
  To start with, we obtained that our sample sources follows the E1 main sequence, although the distribution of sources in the various spectral type is different from the one of RD sources, and depends on both radio power and morphology (see Table 3.1). The majority of objects belongs in the B1 and B1^{+} bins while the number goes down in bins with higher FWHM(Hβ), like B1^{++}, and higher R_{FeII}, like xA bins. FRII classes do not have RD objects in contrast with the CD class. Moreover FRII classes show a small amount of population A sources. The existence of population A FRII objects may be explained in term of the angle between the line of sight and the radio axis. As regard to the CD class, this exhibits a significant number of xA sources, 30% of all population A CD objects. Interestingly, only 20% of xA CD AGNs have a radio-power emission in the loud range.

- *Optical spectroscopic trends.*
  As regard to the optical spectra features, the most evident trend is the anti-correlation between the [OIII] doublet emission lines and the FWHM(Hβ) with the R_{FeII}. Only the radio-detected class ($logR_K < 1.0$) follows the anti-correlation, with the [OIII]

lines becoming indistinguishable from the FeII blend in the xA bins. Instead radio-intermediate and radio-loud objects show [OIII] lines still strong even in the A4 bin. Moreover RD and RI classes show asymmetric [OIII] lines in the sense of a blue-shifted $c(1/4)$, from $B1^{++}$ to A1 bin while in A2 and xA bins the whole line is blue-shifted. Instead RL objects show almost symmetric and unshifted [OIII] from $B1^{++}$ to A2 and only in A3 they show a blue-shifted [OIII].
Talking about the broad component of Hβ, firstly we noticed that going from B1 to $B1^{++}$ the line gets more red-shifted, moreover the amplitude of the centroid line c(x) displacement is higher for RL sources. Thanks to the Hβ line profile study, we were able to highlight the RI CD $B1^{++}$ and RL CD $B1^{+}$ classes as possible representatives of SMBBH systems. Indeed these two classes show an Hβ profile consistent with the expectation of two BLRs, one less-shifted component associated with a more massive BH and one associated with a less massive black hole orbiting around a common center of mass.

- *Eddington ratio and radio SFR estimates.*
  The optical spectral and radio measures tell us additional informations. Populations A and B show difference in terms of the black mass and Eddington ratios, with population B showing more massive BH having a lower λ_E with respect to the population A. This suggests that the numerous observed differences are driven by different central engine structure and kinematics. Finally we found that, as a population, RI and RD have average $\mathrm{SFR}_r \lesssim 10^3$, which are consistent with emission from thermal sources. This is may be especially true for extreme Pop. A sources which are already known to belong to star forming systems.

We conclude reminding that this thesis is a preliminary but important work for future studies. The inspection of our sample made possible the selection of objects with interesting characteristics that attracted particular attentions. As we said, these sources are the ones belonging to the xA CD, the RI CD $B1^{++}$ and RL CD $B1^{+}$ classes.
The xA CD class is important since its objects show extreme Eddington ratio and hence the maximum radiative feedback effect per unit mass. This characteristics suggest an impactful feedback of the AGN on the host galaxy and therefore xA sources are useful to study the coevolution of the BH with the host galaxy and galaxy evolution in a more general way. RI CD $B1^{++}$ and RL CD $B1^{+}$ classes are interesting since they show objects with an Hβ profile consistent with two BLRs associated to two BHs orbiting around a common center of mass, therefore a BBH system. The merging process of massive binary black holes produce strong gravitational wave signals [168] that can be used in order to obtain several informations like, for example, merger rates and the merger history of BHs/galaxies [115].

APPENDIX A

Tables

Table A.1: Partially resolved CD sample. *Note.* SDSS ID: SDSS-DR12 designation HHMMSS.ss+DDMMSS.s (J2000) corrected by CDS. R, DEC: right ascension and declination (J2000) in equatorial coordinates (deg) of the SDSS source. **z**: redshift from BOSS pipeline. m_g: PSF magnitude in g band (mag). Δm_g error in PSF magnitude in g band (mag). A_g: total absorption at g (mag). RA_r, DEC_r: right ascension and declination (J2000) in equatorial coordinates (deg) of the SDSS counterpart FIRST radio source. $Sep._r$: distance between the SDSS source and its radio counterpart. F_r: peak flux density of the core radio source (mJy). Rms_r: local noise estimate at the core radio source position (mJy). $RA_{rl,n}$, $DEC_{rl,n}$, $Sep._{rl,n}$, $F_{rl,n}$, $Rms_{rl,n}$: as above but for the two ($n = 1, 2$) radio lobes. w: De Vries parameter. Ψ: opening angles (deg) as seen from the quasar position

Partially resolved core dominated AGN sample

SDSS ID	**RA** (deg)	**DEC** (deg)	**z**	m_g (mag)	Δm_g (mag)	A_g (mag)	RA_r (deg)	DEC_r (deg)	$Sep._r$ (arcsec)	F_r (mJy)	Rms_r (mJy)
J005327.77-065651.2	13.36572	-6.94756	0.88786	19.777	0.024	0.193	13.36566	-6.94766	0.39870	5.72	0.204
J014540.95+073217.2	26.42066	7.53811	0.69292	20.051	0.024	0.126	26.42060	7.53812	0.22127	1.06	0.132
J014756.74+124912.5	26.98643	12.82015	0.75197	19.447	0.026	0.195	26.98638	12.81978	1.34136	10.64	0.26
J020514.77-045639.7	31.31157	-4.94437	0.36213	20.37	0.036	0.085	31.31153	-4.94459	0.82323	4.79	0.158
J082753.69+521758.6	126.97371	52.29961	0.33782	19.906	0.021	0.181	126.97399	52.29953	0.68502	136.99	0.144
J083928.53+260614.3	129.86889	26.10399	0.96032	19.387	0.016	0.135	129.86894	26.10395	0.21447	9.85	0.136
J095427.81+301912.9	148.61591	30.32026	0.53343	17.488	0.022	0.071	148.61597	30.32033	0.29451	23.11	0.136
J095637.65+155125.0	149.15687	15.85695	0.68563	19.319	0.022	0.1	149.15685	15.85686	0.32786	20.9	0.143
J095753.84+121606.7	149.47434	12.26854	0.61646	19.16	0.014	0.12	149.47438	12.26854	0.15494	41.94	0.151
J101326.05-000136.4	153.35855	-0.02679	0.25522	19.71	0.019	0.116	153.35847	-0.02693	0.60197	1.21	0.151
J102329.79+441414.2	155.87416	44.2373	0.75146	17.44	0.013	0.05	155.87416	44.23725	0.18029	8.1	0.141
J111006.79+405000.7	167.52831	40.83353	0.6599	19.446	0.017	0.065	167.52835	40.83371	0.63047	1.04	0.145
J111018.12+104619.5	167.57552	10.77208	0.17429	19.151	0.031	0.085	167.57556	10.77145	2.26399	73.64	0.265
J115324.46+493108.7	178.35194	49.51910	0.33383	17.442	0.02	0.075	178.35189	49.51903	0.26927	548.12	0.153
J124557.17+215616.1	191.48823	21.93781	0.70173	19.184	0.022	0.129	191.4878	21.93795	1.54189	6.43	0.149
J133152.22+111649.6	202.96761	11.28045	0.09045	18.882	0.019	0.106	202.96787	11.28038	0.94022	2.55	0.147
J135222.05+420313.4	208.09190	42.05372	0.88090	19.432	0.018	0.019	208.09182	42.05388	0.59615	7.41	0.129
J141159.73+423950.3	212.99889	42.66398	0.88645	17.059	0.013	0.027	212.99889	42.66400	0.08740	71.17	0.142
J141238.66+484447.1	213.16110	48.74642	0.90596	18.711	0.02	0.057	213.16108	48.74638	0.16157	52.83	0.141
J141324.26+530527.2	213.35110	53.09089	0.45586	20.66	0.03	0.028	213.35101	53.09046	1.53161	53.04	0.331
J141927.40+283537.9	214.86418	28.59386	0.97178	19.546	0.018	0.044	214.86415	28.59395	0.31990	16.6	0.133
J145922.15+152654.7	224.84231	15.44855	0.36972	19.438	0.02	0.103	224.84226	15.44851	0.22215	94.67	0.149
J150725.62+112635.6	226.85675	11.44324	0.67477	19.467	0.02	0.134	226.85686	11.44296	1.08459	20.6	0.14
J152039.69+421111.1	230.16538	42.18644	0.48476	19.497	0.028	0.07	230.1657	42.18657	0.96558	53.63	0.135
J152548.29+582851.3	231.45124	58.48092	0.31031	20.417	0.027	0.04	231.45092	58.48076	0.83634	63.62	0.133
J153145.14+431933.8	232.93809	43.32605	0.50820	19.791	0.021	0.085	232.93818	43.32603	0.24874	8.91	0.15
J153934.80+473531.2	234.89502	47.59202	0.77150	16.082	0.028	0.059	234.8951	47.59190	0.46694	40.36	0.14
J161706.32+410647.0	244.27633	41.11307	0.26672	18.761	0.021	0.024	244.2765	41.11304	0.44712	55.61	0.139
J162637.91+523804.5	246.65799	52.63460	0.48348	18.809	0.025	0.102	246.65789	52.63449	0.45891	27.76	0.144
J163116.54+492739.5	247.81891	49.46097	0.51794	19.746	0.018	0.053	247.81866	49.46099	0.60573	154.29	0.13
J170717.75+453610.5	256.82397	45.60292	0.64467	17.16	0.019	0.122	256.82396	45.60293	0.05138	681.26	0.155

Table A.2: Unresolved CD sample. Same notation of table A.1

Unresolved core dominated AGN sample											
SDSS ID	**RA**	**DEC**	**z**	m_g	Δm_g	A_g	RA_r	DEC_r	$Sep._r$	F_r	Rms_r
J000652.00+061509.2	1.71667	6.25256	0.87276	18.547	0.03	0.252	1.71664	6.25264	0.31127	2.96	0.129
J000727.89+055701.3	1.86623	5.95038	0.79167	18.941	0.022	0.194	1.86624	5.95029	0.33276	8.32	0.113
J000804.16-012917.0	2.01737	-1.48806	0.31380	20.367	0.029	0.115	2.01717	-1.48793	0.83704	1.9	0.144
J001932.63-070302.6	4.88597	-7.05072	0.77379	19.355	0.021	0.139	4.88570	-7.05057	1.09161	1.02	0.14
J002312.69+072455.4	5.80288	7.41540	0.66057	18.01	0.027	0.075	5.80293	7.41538	0.19509	2.83	0.126
J002554.26+083711.3	6.47609	8.61982	0.81416	18.181	0.017	0.155	6.47605	8.61981	0.17884	137.4	0.115
J003706.29-050111.3	9.27624	-5.01981	0.71832	19.373	0.029	0.162	9.27616	-5.01979	0.28363	4.49	0.171
J003848.49+075059.6	9.70205	7.84989	0.55326	19.572	0.021	0.131	9.70211	7.85007	0.69619	1.84	0.117
J004428.66+090959.4	11.11942	9.16651	0.71791	19.47	0.023	0.185	11.11961	9.16620	1.31115	5.04	0.126
J010123.42+005013.3	15.34760	0.83703	0.69825	20.675	0.031	0.098	15.34756	0.83699	0.21637	2.0	0.128
J010352.47+003739.7	15.96863	0.62772	0.70376	17.659	0.027	0.116	15.96857	0.62775	0.25293	2.12	0.107
J010717.05+074446.4	16.82105	7.74624	0.88342	19.601	0.023	0.132	16.82107	7.74619	0.20964	1.14	0.123
J010927.10-031714.4	17.36293	-3.28734	0.75153	18.766	0.025	0.116	17.3629	-3.28731	0.15858	7.27	0.136
J011239.13-032842.8	18.16305	-3.47855	0.77169	18.774	0.02	0.219	18.16309	-3.47856	0.14562	123.72	0.133
J011533.41+101456.5	18.88923	10.24903	0.47192	18.815	0.021	0.254	18.88913	10.24903	0.35787	2.03	0.152
J012209.02+102020.0	20.53759	10.33891	0.39540	18.545	0.021	0.218	20.53768	10.33913	0.84174	1.2	0.16
J013034.90+111803.9	22.64544	11.30109	0.73636	19.164	0.017	0.336	22.64536	11.30113	0.34932	10.58	0.145
J013224.25+080103.1	23.10106	8.01753	0.62578	19.704	0.025	0.191	23.10106	8.01757	0.13198	5.46	0.135
J013427.29-013350.3	23.61372	-1.56397	0.78539	18.294	0.015	0.122	23.61372	-1.56393	0.16622	9.57	0.133
J013908.45+044911.7	24.78523	4.81992	0.77145	19.237	0.017	0.092	24.78518	4.81982	0.41035	2.25	0.118
J014738.38-082718.0	26.90995	-8.45502	0.69336	19.545	0.026	0.09	26.90999	-8.45504	0.15959	86.66	0.158
J014817.84-054404.1	27.07434	-5.73448	0.72651	19.819	0.051	0.094	27.07436	-5.73448	0.07888	2.05	0.099
J015646.33+115644.3	29.19304	11.94566	0.82552	18.303	0.021	0.249	29.19316	11.94572	0.48569	13.36	0.18
J020350.85-020651.1	30.96191	-2.11419	0.96829	19.317	0.036	0.098	30.96199	-2.11413	0.38220	2.28	0.15
J020809.63-053839.1	32.04013	-5.64421	0.64207	18.959	0.037	0.077	32.04003	-5.64412	0.48491	5.22	0.172
J021640.73-044404.8	34.16973	-4.73469	0.87437	16.396	0.031	0.065	34.16977	-4.73472	0.17313	95.8	0.157
J021705.52-042253.5	34.27303	-4.38155	0.78847	19.426	0.027	0.07	34.27296	-4.38167	0.48928	68.5	0.159
J021859.74-040237.1	34.74895	-4.04365	0.20331	19.616	0.042	0.071	34.74884	-4.04378	0.61748	1.79	0.148
J022508.07+001707.2	36.28365	0.28534	0.52482	18.686	0.025	0.139	36.28369	0.28533	0.14560	273.92	0.101
J022712.98-044636.4	36.80409	-4.77678	0.98141	18.062	0.016	0.091	36.80413	-4.77686	0.34488	4.86	0.11
J022845.62-050232.0	37.19012	-5.04222	0.25926	20.497	0.033	0.114	37.19018	-5.04227	0.28581	3.41	0.116
J023313.12-033924.0	38.30469	-3.65669	0.60096	19.013	0.028	0.081	38.3046	-3.65667	0.35321	9.23	0.153
J023859.18-000158.1	39.74662	-0.03282	0.81288	18.731	0.021	0.101	39.74681	-0.03271	0.79273	1.09	0.096
J024706.65+002318.1	41.77773	0.38837	0.36323	19.238	0.02	0.118	41.7778	0.38856	0.72309	1.74	0.107
J024817.69+024128.4	42.07372	2.69123	0.80392	19.367	0.021	0.201	42.073717	2.69133	0.37938	1.3	0.126
J071933.35+403253.0	109.88896	40.54807	0.51517	18.825	0.016	0.203	109.88895	40.54795	0.41457	1.49	0.134
J072729.35+413632.9	111.87230	41.60914	0.19611	19.939	0.022	0.265	111.87233	41.60901	0.49050	2.19	0.14
J073638.86+435316.6	114.16193	43.88795	0.11383	18.523	0.018	0.169	114.16187	43.88784	0.40647	4.59	0.135
J073945.16+215636.1	114.93819	21.94338	0.86109	20.165	0.02	0.152	114.93801	21.94343	0.65616	23.65	0.144
J074026.41+365534.4	115.11006	36.92622	0.92449	19.026	0.022	0.182	115.11003	36.92625	0.10711	2.64	0.127
J074140.45+365544.6	115.41855	36.92907	0.47834	19.13	0.016	0.2	115.41850	36.92896	0.40682	3.57	0.142
J074559.61+450434.3	116.49838	45.07621	0.12004	19.2	0.022	0.15	116.49838	45.07621	0.01686	5.5	0.143
J074630.61+440433.5	116.62756	44.07598	0.19362	18.7	0.024	0.132	116.62755	44.07604	0.21606	1.2	0.133
J075001.55+442845.1	117.50648	44.47920	0.23223	20.759	0.033	0.139	117.50645	44.47913	0.26783	2.14	0.139
J075052.04+480345.6	117.71687	48.06267	0.92384	19.56	0.021	0.161	117.71692	48.06281	0.52804	1.05	0.141
J075244.63+434105.3	118.18596	43.68481	0.17983	19.966	0.025	0.161	118.18601	43.68474	0.26168	10.7	0.125
J075659.58+452830.5	119.24827	45.47516	0.20536	21.098	0.04	0.176	119.24820	45.47514	0.17876	5.16	0.129
J075813.13+524451.2	119.55471	52.74758	0.81606	19.314	0.016	0.131	119.55475	52.74749	0.31125	29.6	0.131
J080037.62+461257.9	120.15677	46.21609	0.23880	18.775	0.017	0.253	120.1567	46.21605	0.24384	1.96	0.133
J080424.20+065456.9	121.10085	6.91582	0.56877	20.528	0.032	0.086	121.10101	6.91578	0.59334	2.03	0.153
J081209.24+560038.1	123.03852	56.01060	0.61720	19.463	0.019	0.151	123.03861	56.01058	0.19491	2.05	0.14
J081305.92+371958.0	123.27466	37.33278	0.53099	20.477	0.026	0.159	123.27458	37.33273	0.29361	5.31	0.133
J081347.53+534754.0	123.44807	53.79835	0.94540	18.326	0.02	0.114	123.44804	53.79832	0.12124	70.51	0.177
J081425.89+294115.6	123.6079	29.68769	0.37400	18.327	0.016	0.119	123.60788	29.68770	0.07179	4.83	0.145
J081516.86+460430.8	123.82029	46.07524	0.04096	16.664	0.02	0.174	123.82034	46.07527	0.17252	5.47	0.151
J081929.48+522345.2	124.87283	52.39591	0.62369	19.483	0.021	0.131	124.87279	52.39588	0.14069	2.62	0.209
J082149.22+245159.5	125.45509	24.86654	0.69926	19.405	0.021	0.102	125.45507	24.86656	0.11639	3.81	0.14
J082311.26+435318.5	125.79693	43.88848	0.18237	18.705	0.058	0.186	125.79714	43.88833	0.74085	2.04	0.144
J082456.93+215539.4	126.23721	21.92762	0.33948	17.311	0.013	0.147	126.23712	21.92769	0.38248	1.71	0.149
J082808.65+394816.2	127.03605	39.80451	0.98858	19.392	0.02	0.115	127.03619	39.80441	0.51840	37.22	0.138
J082826.20+394436.8	127.10916	39.74358	0.88593	19.664	0.034	0.112	127.10943	39.74365	0.78582	1.21	0.145
J082911.95+341055.8	127.29982	34.18217	0.61252	20.01	0.032	0.151	127.29967	34.18209	0.53544	1.29	0.142
J083307.86+501000.3	128.28276	50.16677	0.05328	18.032	0.019	0.133	128.28278	50.16678	0.07664	4.37	0.144
J083354.46+565816.1	128.47693	56.97116	0.93820	18.162	0.023	0.248	128.47708	56.97110	0.36984	9.74	0.144
J083413.91+511214.6	128.55796	51.20406	0.36764	22.308	0.11	0.115	128.55784	51.20406	0.27892	2.23	0.14
J083431.37+582425.7	128.63074	58.40715	0.51358	19.58	0.276	0.321	128.63055	58.40714	0.37404	1.75	0.144
J083522.77+424258.3	128.84489	42.71620	0.80641	17.919	0.017	0.091	128.84472	42.71633	0.64172	1.28	0.138
J083525.97+435211.2	128.85825	43.86979	0.56750	17.617	0.013	0.106	128.85824	43.86971	0.27797	1.71	0.133
J083537.33+284712.9	128.90557	28.78694	0.43607	20.157	0.029	0.149	128.9056	28.78694	0.09574	1.35	0.14
J083558.43+261444.4	128.99346	26.24569	0.78871	20.423	0.035	0.137	128.99353	26.24564	0.29226	3.92	0.146
J084348.64+620626.6	130.95267	62.10740	0.88545	19.493	0.019	0.474	130.95284	62.10755	0.59532	1.29	0.157
J084515.98+391412.1	131.31658	39.23671	0.67200	18.983	0.021	0.121	131.31649	39.23658	0.53954	2.1	0.136
J084744.55+442610.6	131.93563	44.43629	0.46570	19.475	0.035	0.088	131.93563	44.43628	0.04327	6.29	0.125
J085031.81+163913.0	132.63254	16.65361	0.65871	20.56	0.03	0.058	132.6323	16.65353	0.90354	1.52	0.139
J085106.74+582656.5	132.77809	58.44904	0.74077	19.265	0.025	0.123	132.77816	58.44905	0.13696	1.67	0.112
J085206.15+465050.5	133.02562	46.84737	0.35990	18.698	0.024	0.096	133.02574	46.84732	0.34808	1.51	0.141
J085726.27+484518.8	134.35946	48.75525	0.40595	20.242	0.027	0.075	134.35945	48.75526	0.06653	13.47	0.142
J085943.79+155232.8	134.93248	15.87578	0.61644	18.193	0.014	0.14	134.9329	15.87576	1.42536	74.97	0.146
J090245.60+111619.9	135.69001	11.27219	0.91710	19.212	0.017	0.089	135.69005	11.27230	0.41247	2.98	0.133
J090508.17+523527.5	136.28406	52.59099	0.56112	20.191	0.025	0.05	136.28382	52.59088	0.64662	1.03	0.139
J090512.95+233139.6	136.30397	23.52767	0.47324	20.217	0.026	0.108	136.30407	23.52773	0.38585	5.27	0.141
J090712.21+091056.4	136.80089	9.18234	0.89350	19.686	0.019	0.259	136.80085	9.18237	0.20584	7.86	0.144
J090745.28+532421.4	136.93870	53.40596	0.71296	17.426	0.025	0.053	136.93866	53.40598	0.09809	8.42	0.141
J090858.81+472617.2	137.24507	47.43811	0.74436	18.898	0.021	0.058	137.24520	47.43803	0.43942	1.55	0.133
J091542.24+251939.0	138.92601	25.32751	0.71191	17.894	0.023	0.11	138.92597	25.3275	0.12057	112.32	0.143
J092058.62+232317.0	140.24426	23.38806	0.62712	20.914	0.03	0.124	140.24432	23.38803	0.25124	1.84	0.133
J092206.67+630334.9	140.52779	63.05970	0.87794	20.41	0.025	0.14	140.52797	63.05955	0.64479	3.91	0.212
J092518.10+044529.8	141.32542	4.75829	0.75021	18.985	0.02	0.181	141.32547	4.75828	0.18581	2.19	0.152
J092551.85+361235.6	141.46605	36.20990	0.99818	19.153	0.019	0.044	141.46597	36.20988	0.22944	205.81	0.15
J092708.11+143413.5	141.78383	14.57043	0.56676	20.016	0.024	0.108	141.78384	14.57042	0.06275	4.73	0.145
J092725.19+043851.5	141.85497	4.64765	0.64675	18.663	0.015	0.161	141.85505	4.647744	0.41528	1.1	0.148
J093230.89+405720.2	143.12871	40.95562	0.49605	22.591	0.109	0.048	143.12866	40.95563	0.13070	5.13	0.177

J093509.47+481910.6	143.78948	48.31961	0.22363	18.025	0.024	0.072	143.78963	48.31951	0.51356	1.85	0.139
J093601.69+193850.2	144.00705	19.64728	0.84519	17.86	0.013	0.166	144.00695	19.64722	0.36945	1.25	0.131
J093712.32+500852.1	144.30134	50.14781	0.27546	19.619	0.017	0.043	144.30143	50.14778	0.24280	164.63	0.158
J094033.75+462315.0	145.14065	46.38752	0.69743	17.582	0.032	0.037	145.14071	46.38740	0.44173	1.45	0.127
J094100.81+143614.4	145.25339	14.60401	0.38396	20.366	0.027	0.137	145.25337	14.60407	0.23497	7.39	0.141
J094248.08+112934.3	145.70035	11.49288	0.56599	19.551	0.029	0.066	145.70035	11.49296	0.29882	2.98	0.149
J094406.99+321444.6	146.02915	32.24574	0.16732	19.784	0.036	0.061	146.02923	32.24564	0.43730	2.05	0.144
J094804.86+270042.0	147.02026	27.01169	0.52250	20.352	0.031	0.081	147.02035	27.01168	0.27264	2.82	0.136
J095150.49-025545.5	147.96038	-2.92930	0.90290	18.564	0.016	0.123	147.96037	-2.92928	0.10182	8.38	0.151
J095633.93+562216.0	149.14138	56.37111	0.89296	17.826	0.016	0.026	149.14123	56.37111	0.28908	2.35	0.161
J095738.18+552257.7	149.40909	55.38270	0.90342	17.916	0.031	0.029	149.40897	55.38274	0.29209	2804.15	0.554
J095746.55+474549.4	149.44398	47.76372	0.43041	20.256	0.024	0.039	149.44397	47.76363	0.29942	13.51	0.144
J100256.22+475027.7	150.73428	47.84105	0.39055	19.368	0.027	0.037	150.7342	47.84107	0.22059	1.87	0.126
J100432.83+124831.4	151.13681	12.80873	0.78845	20.231	0.017	0.115	151.13674	12.80874	0.24197	1.74	0.132
J100458.31+202449.2	151.24298	20.41368	0.91479	18.283	0.016	0.089	151.24309	20.41371	0.36932	6.93	0.137
J100507.89+341424.1	151.28290	34.24005	0.16193	17.704	0.026	0.041	151.28293	34.24003	0.13112	3.4	0.143
J100603.11+195917.4	151.51298	19.98818	0.65179	18.828	0.022	0.088	151.51285	19.98816	0.43399	1.25	0.151
J100651.13+565654.6	151.71306	56.94851	0.75250	19.492	0.019	0.021	151.71313	56.94836	0.52292	3.74	0.145
J100933.22+255901.1	152.38843	25.98366	0.37401	22.669	0.101	0.099	152.38845	25.98365	0.09747	1.21	0.148
J101425.63+031434.5	153.60681	3.24293	0.31186	18.452	0.024	0.099	153.60684	3.24266	0.96805	1.3	0.156
J101643.72+455051.1	154.18217	45.84755	0.33258	19.878	0.033	0.023	154.18215	45.84755	0.06780	14.2	0.13
J101857.98+103625.6	154.74158	10.60712	0.65957	19.933	0.025	0.116	154.74158	10.60709	0.11165	72.75	0.145
J101931.79+262643.2	154.88247	26.44534	0.24974	18.545	0.021	0.1	154.88277	26.44538	0.97293	1.12	0.14
J101952.59+073050.8	154.96913	7.51413	0.52320	19.626	0.026	0.08	154.96920	7.51390	0.86567	1.45	0.142
J102009.69-012758.7	155.04038	-1.46631	0.94333	19.678	0.02	0.184	155.04054	-1.46642	0.71003	2.36	0.135
J102011.66+281635.8	155.04859	28.27661	0.67254	19.423	0.024	0.107	155.04866	28.27659	0.24407	5.95	0.139
J102041.14+395811.2	155.17145	39.96978	0.82662	18.7	0.019	0.05	155.17154	39.96968	0.42218	2.71	0.168
J102144.05+233738.6	155.43356	23.62740	0.19694	19.31	0.027	0.07	155.43382	23.62731	0.90187	1.28	0.143
J102152.49+131146.4	155.46871	13.19624	0.55080	19.385	0.033	0.169	155.46875	13.19617	0.27385	2.56	0.148
J102222.61+495216.4	155.59424	49.87123	0.67332	19.438	0.022	0.026	155.59427	49.87128	0.21345	3.21	0.143
J102736.45+285917.6	156.90188	28.98824	0.25699	20.119	0.036	0.072	156.90168	28.98847	1.05674	1.46	0.144
J102755.32+180923.5	156.98052	18.15655	0.61436	19.497	0.026	0.081	156.98055	18.15661	0.23575	3.08	0.137
J102818.15+535113.6	157.07566	53.85378	0.51214	19.16	0.017	0.056	157.07567	53.85381	0.10571	2.3	0.149
J102834.03-023659.6	157.14182	-2.61657	0.47020	19.506	0.022	0.124	157.14182	-2.61655	0.05052	66.5	0.156
J102953.43+163739.2	157.47264	16.62758	0.44117	18.484	0.021	0.089	157.47272	16.62751	0.38820	2.02	0.132
J103027.97+300114.1	157.61656	30.02059	0.49727	19.399	0.018	0.061	157.61665	30.02063	0.33138	2.25	0.152
J103045.22+255522.1	157.68843	25.92281	0.69146	17.206	0.026	0.066	157.68848	25.92279	0.18065	47.56	0.143
J103100.66+444513.5	157.75275	44.75375	0.35626	20.967	0.045	0.053	157.75277	44.75376	0.08964	5.53	0.127
J103111.14+630545.6	157.79643	63.09600	0.11061	19.882	0.022	0.04	157.79638	63.09593	0.26534	3.35	0.146
J103246.80+391009.9	158.19501	39.16942	0.81654	19.256	0.017	0.047	158.19513	39.16948	0.38803	8.18	0.132
J103346.39+233220.0	158.44331	23.53891	0.46988	18.715	0.017	0.071	158.44320	23.53891	0.36641	9.2	0.137
J103853.09+203447.7	159.72123	20.57994	0.85004	20.368	0.03	0.086	159.72130	20.58009	0.58269	1.76	0.136
J103915.67+470541.0	159.81531	47.09474	0.03870	20.713	0.027	0.048	159.81512	47.09460	0.68503	358.25	0.146
J103925.56+490951.2	159.85650	49.16424	0.89057	18.287	0.023	0.036	159.85643	49.16419	0.22868	2.02	0.133
J104002.56+210900.1	160.01068	21.15003	0.89421	17.771	0.016	0.074	160.01070	21.1501	0.24865	7.16	0.147
J104011.18+452125.9	160.04658	45.35720	0.54650	17.668	0.014	0.064	160.04656	45.35709	0.38325	1.95	0.127
J104139.66+365925.6	160.41525	36.99046	0.80962	20.305	0.043	0.044	160.41503	36.99055	0.70052	1.2	0.113
J104539.86+520222.3	161.41610	52.03954	0.28382	20.673	0.042	0.048	161.41572	52.03956	0.82603	1.32	0.143
J104708.07+144557.7	161.78365	14.76603	0.70450	18.044	0.023	0.085	161.78364	14.76603	0.03214	1.15	0.152
J105232.73+612521.2	163.13641	61.42256	0.42101	16.745	0.013	0.045	163.13647	61.42234	0.80206	819.74	0.261
J105326.04+184203.3	163.35852	18.70092	0.66623	19.237	0.025	0.1	163.35856	18.70093	0.13777	65.8	0.149
J105327.92+375804.3	163.36636	37.96786	0.44621	20.801	0.042	0.05	163.36636	37.96792	0.21607	2.85	0.147
J105421.18+572544.6	163.58827	57.42906	0.20534	20.036	0.039	0.025	163.58849	57.42896	0.55976	1.44	0.134
J105435.30-015051.1	163.64708	-1.84753	0.93356	20.047	0.023	0.139	163.64698	-1.84755	0.37272	1.86	0.138
J105451.63+553736.5	163.71515	55.62681	0.92358	19.152	0.017	0.036	163.71517	55.62668	0.48052	2.95	0.142
J105458.86-023947.2	163.74526	-2.66311	0.15722	17.47	0.016	0.143	163.74517	-2.66306	0.35220	4.73	0.154
J105525.26+154433.8	163.85525	15.74273	0.81850	19.849	0.03	0.088	163.85524	15.74269	0.16642	2.98	0.149
J105642.50+242751.6	164.17712	24.46435	0.90470	19.544	0.031	0.052	164.17699	24.46433	0.41527	2.35	0.151
J105704.82+602405.1	164.27008	60.40142	0.81100	19.179	0.025	0.025	164.27006	60.40130	0.42301	3.57	0.15
J105939.03+205721.8	164.91266	20.95608	0.39261	19.602	0.021	0.057	164.91258	20.95608	0.26646	138.42	0.146
J105957.21+274150.7	164.98838	27.69742	0.24270	18.781	0.019	0.084	164.98856	27.69765	0.99372	1.07	0.15
J110145.37+460236.2	165.43907	46.04339	0.17836	17.632	0.024	0.036	165.43898	46.04353	0.55979	1.41	0.14
J110158.16+120531.1	165.49236	12.09199	0.12984	19.219	0.026	0.052	165.49238	12.09196	0.13010	1.63	0.143
J110505.47+251527.3	166.27281	25.25758	0.41208	19.692	0.027	0.053	166.27267	25.25754	0.46451	2.44	0.142
J110550.53+112702.0	166.46058	11.45058	0.14120	21.217	0.051	0.045	166.46052	11.45050	0.34309	2.53	0.144
J110648.32+480712.3	166.70135	48.12008	0.43486	19.123	0.022	0.079	166.70146	48.12007	0.26786	10.03	0.139
J110748.61+414539.4	166.95258	41.76095	0.71212	18.597	0.03	0.042	166.95270	41.76112	0.70052	37.47	0.149
J111432.14+632755.7	168.63395	63.46548	0.63084	19.514	0.022	0.037	168.63398	63.46528	0.71422	1.66	0.153
J111438.89+324133.5	168.66204	32.69263	0.18758	19.025	0.019	0.072	168.66212	32.69258	0.30832	106.07	0.119
J111504.22+251100.3	168.76759	25.18343	0.98061	17.458	0.02	0.05	168.76760	25.18347	0.14976	2.25	0.133
J111628.00+434505.8	169.11666	43.75162	0.80067	17.683	0.016	0.048	169.11671	43.75157	0.22247	7.0	0.134
J111706.25+201407.3	169.27605	20.23537	0.13798	17.019	0.025	0.065	169.27606	20.23540	0.09405	103.34	0.148
J111807.92+592844.1	169.53301	59.47892	0.39422	19.49	0.018	0.029	169.53312	59.47890	0.20738	6.01	0.14
J111908.67+211917.9	169.78616	21.32164	0.17569	14.395	0.016	0.075	169.78622	21.32159	0.27991	4.8	0.134
J111930.31+222649.3	169.87631	22.44704	0.41990	17.9	0.014	0.057	169.87632	22.44702	0.09815	90.58	0.147
J111952.42+165656.8	169.96842	16.94913	0.95114	19.194	0.018	0.067	169.96842	16.94908	0.18732	67.53	0.141
J112155.78-002852.0	170.48243	-0.48113	0.59220	19.455	0.022	0.126	170.48242	-0.48113	0.03671	63.28	0.157
J112529.14+224329.8	171.37145	22.72495	0.29419	18.388	0.027	0.051	171.37145	22.72488	0.24156	35.16	0.133
J112736.52+055532.0	171.90218	5.92557	0.75492	20.31	0.029	0.129	171.90222	5.925544	0.20109	214.11	0.152
J112825.60+402440.0	172.10669	40.41112	0.45203	19.616	0.014	0.059	172.10676	40.41113	0.21118	1.97	0.134
J112828.75+174637.2	172.11981	17.77702	0.48453	20.274	0.03	0.074	172.11986	17.77697	0.26067	1.75	0.128
J112847.12+564659.1	172.19636	56.78308	0.64333	20.004	0.028	0.053	172.19643	56.78288	0.72884	40.08	0.155
J112955.79+552706.3	172.48246	55.45176	0.97777	19.409	0.021	0.04	172.48226	55.45176	0.40870	1.36	0.152
J113020.40+422204.2	172.58501	42.36785	0.99149	18.48	0.016	0.063	172.58501	42.36780	0.18736	2.01	0.131
J113029.48+634620.7	172.62285	63.77244	0.07318	18.512	0.013	0.102	172.62270	63.77240	0.28195	7.25	0.181
J113128.00+484333.3	172.86670	48.72591	0.70153	19.524	0.018	0.042	172.86685	48.72593	0.36109	2.19	0.126
J113427.80+414722.0	173.61587	41.78946	0.81932	17.95	0.018	0.071	173.61584	41.78936	0.39174	3.34	0.15
J113439.09+622012.1	173.66290	62.33670	0.49983	19.86	0.023	0.03	173.66298	62.33654	0.58705	1.63	0.151
J113603.62+632744.2	174.01508	63.46228	0.75501	19.666	0.02	0.083	174.01563	63.46193	1.55841	18.34	0.159
J114054.82+625924.9	175.22844	62.99027	0.95490	19.314	0.023	0.086	175.22843	62.99010	0.62653	108.34	0.142
J114201.83+603030.4	175.50764	60.50846	0.71773	19.404	0.039	0.042	175.50767	60.50853	0.25646	1.0	0.148
J114249.75+082330.6	175.70730	8.39183	0.74011	19.762	0.022	0.074	175.70728	8.391803	0.15144	6.33	0.15
J114339.53+205921.1	175.91471	20.98920	0.75104	19.053	0.016	0.068	175.91466	20.98909	0.41505	2.16	0.144
J114710.22+250935.9	176.79260	25.15997	0.16816	19.283	0.024	0.093	176.79264	25.15997	0.14377	9.2	0.146
J114746.20+622214.5	176.94250	62.37069	0.38052	19.848	0.018	0.055	176.94265	62.37065	0.28070	6.31	0.15
J114749.80+492806.8	176.95751	49.46858	0.72978	20.661	0.043	0.053	176.95759	49.46859	0.18070	65.07	0.151
J114915.30+393325.4	177.31376	39.55707	0.62940	19.415	0.028	0.074	177.31378	39.55713	0.22301	2.33	0.141
J115106.03+404122.2	177.77516	40.68950	0.41515	21.122	0.046	0.065	177.77528	40.68964	0.59957	1.43	0.141
J115228.57+080626.1	178.11907	8.10725	0.57421	19.702	0.02	0.067	178.11924	8.107211	0.62319	8.4	0.14

J115338.83+055300.9	178.41183	5.88358	0.93033	20.001	0.026	0.04	178.41176	5.883575	0.22845	7.22	0.15
J115504.07+034850.3	178.76697	3.81397	0.76798	17.588	0.02	0.084	178.76712	3.814006	0.56009	2.91	0.146
J115557.11+211116.5	178.98796	21.18794	0.42339	20.511	0.075	0.106	178.98802	21.18796	0.21775	1.18	0.131
J115710.17+352426.0	179.29241	35.40723	0.78168	19.795	0.017	0.064	179.29250	35.40704	0.74750	1.47	0.148
J115727.60+431806.3	179.36502	43.30175	0.23033	18.35	0.027	0.044	179.36501	43.30188	0.44286	246.92	0.131
J115917.31+283814.4	179.82216	28.63736	0.21007	18.735	0.017	0.069	179.82214	28.63745	0.35199	2.22	0.154
J120329.85+480313.6	180.87437	48.05378	0.81698	16.349	0.012	0.077	180.87434	48.05376	0.12235	66.83	0.139
J120531.10+144827.9	181.37961	14.80775	0.97121	20.028	0.022	0.122	181.37959	14.80799	0.85120	51.34	0.137
J120713.48+470259.8	181.80617	47.04996	0.81224	18.94	0.021	0.052	181.80617	47.04998	0.07563	2.8	0.127
J120734.62+150643.7	181.89428	15.11214	0.75074	17.729	0.032	0.103	181.89423	15.11215	0.17648	2.14	0.132
J120751.79+604706.9	181.96579	60.78525	0.38521	17.926	0.02	0.054	181.96572	60.78514	0.43341	1.69	0.164
J120910.61+561109.2	182.29423	56.18591	0.45321	19.582	0.036	0.036	182.29452	56.18591	0.59702	1.98	0.154
J121113.97+464711.9	182.80823	46.78666	0.29430	19.074	0.022	0.043	182.80851	46.78632	1.39770	1.02	0.138
J121231.47+251429.1	183.13114	25.24142	0.84205	20.85	0.038	0.075	183.13128	25.24136	0.49883	1.01	0.142
J121413.55+052254.3	183.55648	5.38177	0.89841	17.362	0.018	0.06	183.5565	5.381825	0.19709	4.16	0.15
J121417.80+293143.4	183.57418	29.52872	0.06349	17.598	0.016	0.071	183.57422	29.52873	0.10986	64.55	0.115
J121834.44+484219.5	184.64351	48.70543	0.50122	20.338	0.023	0.046	184.6435	48.70538	0.19258	4.08	0.146
J121957.15+484926.8	184.98815	48.82413	0.82029	20.65	0.034	0.048	184.98808	48.82414	0.18443	6.92	0.135
J122006.84+065232.4	185.02853	6.87568	0.35376	20.857	0.039	0.066	185.02833	6.875714	0.72140	1.07	0.148
J122025.04+341445.7	185.10435	34.24605	0.87925	19.385	0.028	0.038	185.10442	34.24602	0.24618	11.33	0.147
J122118.00+465057.7	185.32502	46.84936	0.40070	20.653	0.035	0.05	185.32509	46.84943	0.30091	8.36	0.136
J122127.16+155624.8	185.36317	15.94023	0.39882	20.504	0.033	0.079	185.36319	15.94031	0.29789	15.2	0.151
J122243.19+293441.5	185.67998	29.57819	0.78610	19.234	0.039	0.09	185.68009	29.57820	0.32688	3.47	0.153
J122400.83+223615.1	186.00347	22.6042	0.41429	21.176	0.061	0.067	186.00345	22.60416	0.14008	3.58	0.145
J122449.90+062917.1	186.20791	6.48810	0.84574	20.61	0.035	0.075	186.20794	6.488169	0.26062	3.58	0.152
J123252.70+414322.4	188.21962	41.72290	0.79669	17.531	0.02	0.059	188.21955	41.72273	0.61115	2.64	0.13
J123338.65+422238.3	188.41106	42.37732	0.98080	18.707	0.067	0.066	188.41119	42.37753	0.82364	1.14	0.139
J123547.98+090801.0	188.94992	9.13363	0.31722	21.823	0.074	0.073	188.94992	9.1337	0.23802	2.11	0.133
J123640.35+563021.4	189.16813	56.50596	0.69752	19.628	0.016	0.06	189.16847	56.50625	1.24237	1.23	0.137
J123820.19+175039.1	189.58415	17.84420	0.45278	16.617	0.026	0.077	189.58417	17.84416	0.14975	3.79	0.144
J124009.12+242531.2	190.03800	24.42533	0.82937	17.026	0.02	0.05	190.03809	24.42529	0.32069	30.16	0.136
J124205.41+111728.4	190.52257	11.29124	0.40670	20.742	0.035	0.089	190.52255	11.29121	0.12066	4.71	0.132
J124251.69+101945.7	190.7154	10.32938	0.45732	19.909	0.026	0.066	190.71557	10.32936	0.63888	1.5	0.148
J124445.84+194054.7	191.19102	19.68186	0.64728	20.076	0.02	0.077	191.19093	19.68183	0.32018	1.68	0.134
J124511.25+335610.1	191.29691	33.93614	0.71132	16.881	0.027	0.048	191.29695	33.93617	0.16596	1.88	0.149
J124805.02+073352.3	192.02092	7.56453	0.76881	20.334	0.024	0.082	192.02089	7.564469	0.25973	1.41	0.151
J125235.36+471922.5	193.14735	47.32294	0.83179	19.702	0.057	0.039	193.14738	47.32289	0.18917	2.1	0.167
J125239.59+464044.7	193.16498	46.67910	0.72507	19.302	0.02	0.057	193.16506	46.67910	0.18538	12.37	0.151
J125249.86+112933.1	193.20778	11.49254	0.87417	17.2	0.02	0.126	193.20783	11.49249	0.24193	24.51	0.143
J125531.36+530912.9	193.88067	53.15358	0.48166	19.514	0.026	0.035	193.88066	53.15355	0.10756	1.4	0.149
J125627.23+120113.4	194.11347	12.02041	0.72711	20.359	0.026	0.103	194.11342	12.02033	0.35696	2.88	0.155
J125701.71+281230.0	194.25714	28.20835	0.30539	20.895	0.032	0.032	194.25689	28.20865	1.34283	1.15	0.16
J125745.32+480525.7	194.43885	48.09047	0.18164	18.652	0.139	0.051	194.43889	48.09036	0.40695	2.08	0.142
J125752.74+475020.6	194.46976	47.83906	0.52811	19.756	0.023	0.053	194.46975	47.83906	0.03013	80.63	0.188
J125915.13+072947.8	194.81308	7.49661	0.86521	20.116	0.028	0.108	194.81314	7.496597	0.23845	1.44	0.149
J125942.80+121312.5	194.92833	12.22016	0.72977	19.243	0.02	0.096	194.92832	12.22014	0.06367	2.0	0.136
J130003.48+121528.1	195.01450	12.25782	0.73321	20.728	0.161	0.096	195.01445	12.25779	0.20232	6.92	0.138
J130016.42+602903.6	195.06841	60.48433	0.55852	19.958	0.032	0.043	195.06806	60.48495	2.32304	4.69	0.147
J130055.53+040551.8	195.23141	4.09774	0.29463	19.672	0.023	0.087	195.23145	4.097781	0.20086	1.59	0.142
J130545.47+443328.4	196.43946	44.55789	0.50775	19.945	0.026	0.054	196.43944	44.55807	0.63252	1.91	0.131
J130630.53+462203.0	196.62722	46.36752	0.64513	19.706	0.028	0.039	196.62694	46.36738	0.85920	92.43	0.144
J130631.63+435100.4	196.63182	43.85012	0.75501	17.12	0.016	0.059	196.63191	43.85014	0.25796	2.9	0.132
J131150.88+420333.1	197.96202	42.05920	0.40525	20.761	0.03	0.042	197.96202	42.05920	0.01519	3.11	0.146
J131316.69+213202.1	198.31954	21.53393	0.97107	19.791	0.032	0.074	198.31953	21.53391	0.08561	8.82	0.155
J131526.31+535950.3	198.85962	53.99732	0.72430	18.324	0.021	0.087	198.85971	53.99733	0.19270	2.61	0.143
J131933.02+550808.5	199.88761	55.13572	0.32821	20.0	0.021	0.048	199.88753	55.13570	0.16549	3.25	0.15
J132052.19+574737.3	200.21749	57.79371	0.45673	17.832	0.021	0.04	200.21752	57.79360	0.40016	1.5	0.146
J132111.20+221612.1	200.29669	22.27003	0.94614	19.08	0.031	0.052	200.29670	22.27006	0.12557	383.55	0.151
J132146.53+265150.1	200.44387	26.86393	0.84450	17.165	0.013	0.072	200.44382	26.86388	0.22809	2.62	0.203
J132201.35+495835.0	200.50565	49.9764	0.97585	18.22	0.022	0.046	200.50639	49.97639	1.72735	1.2	0.137
J132401.53+032020.5	201.00638	3.33905	0.92690	19.988	0.023	0.081	201.00658	3.338986	0.77068	2.09	0.161
J132644.96+434804.5	201.68735	43.80126	0.74115	17.797	0.026	0.048	201.68741	43.80129	0.19445	7.7	0.132
J132749.91+191522.6	201.95797	19.25627	0.45898	20.125	0.035	0.065	201.95790	19.25628	0.23585	4.6	0.15
J132819.23+442432.9	202.08015	44.40914	0.36885	20.349	0.027	0.05	202.08023	44.409	0.54340	2.65	0.148
J133039.64+245432.9	202.66519	24.90916	0.72304	19.661	0.026	0.039	202.66512	24.90931	0.60823	5.81	1.038
J133245.23+472222.7	203.18848	47.37297	0.66877	17.744	0.019	0.073	203.18862	47.37295	0.33716	161.37	0.129
J133431.74+084748.8	203.63226	8.79690	0.76028	19.901	0.023	0.083	203.63228	8.796922	0.09118	1.13	0.138
J133749.32+594717.4	204.45551	59.78818	0.57983	20.244	0.028	0.044	204.45532	59.78805	0.57912	1.66	0.151
J133939.61+033109.8	204.91505	3.51940	0.24131	19.354	0.02	0.079	204.91495	3.519392	0.37401	2.22	0.145
J133942.71+182955.2	204.92798	18.49868	0.44650	18.539	0.028	0.063	204.92804	18.49861	0.31610	2.98	0.147
J133947.29+591210.3	204.94707	59.20288	0.38262	20.462	0.031	0.048	204.94719	59.20295	0.32587	2.9	0.142
J134151.07+083512.4	205.46282	8.58680	0.22685	20.919	0.032	0.096	205.46291	8.586675	0.55919	1.49	0.144
J134251.35+260555.2	205.71397	26.09867	0.76688	20.193	0.024	0.053	205.71395	26.09872	0.19076	30.09	0.146
J134300.17+284407.5	205.75074	28.73542	0.90686	17.232	0.019	0.042	205.75050	28.73528	0.89343	217.37	0.144
J134310.87+494604.6	205.79531	49.76797	0.50091	19.839	0.036	0.034	205.79537	49.76806	0.35606	1.64	0.175
J134701.56+640504.6	206.75653	64.08463	0.91479	19.528	0.016	0.057	206.75655	64.08456	0.24193	7.79	0.155
J135052.73+303453.5	207.71972	30.58155	0.71159	18.235	0.021	0.051	207.71972	30.58153	0.08280	309.71	0.151
J135302.39+335015.8	208.25999	33.83774	0.33175	21.298	0.039	0.058	208.26003	33.83769	0.19381	2.5	0.138
J135326.54+242413.5	208.36061	24.40376	0.52346	20.266	0.03	0.053	208.36071	24.40369	0.40700	1.12	0.143
J135335.28+080854.6	208.39704	8.14850	0.82256	19.613	0.029	0.089	208.397	8.148492	0.15705	16.49	0.146
J135607.37+413615.3	209.03071	41.60426	0.69566	16.889	0.019	0.015	209.03068	41.60426	0.08359	23.47	0.146
J135845.38+265808.4	209.68908	26.96902	0.33065	18.585	0.028	0.07	209.68916	26.96898	0.29617	1.82	0.153
J135938.49+223207.4	209.91038	22.53540	0.81114	19.313	0.015	0.067	209.91033	22.53542	0.15858	4.29	0.142
J140050.61+092655.7	210.21090	9.44881	0.92706	19.793	0.022	0.095	210.21107	9.448825	0.60169	1.11	0.17
J140307.59+320320.5	210.78165	32.05571	0.76515	19.604	0.022	0.053	210.78186	32.05586	0.84535	1.49	0.141
J140549.53+393946.0	211.45638	39.66279	0.66473	19.182	0.019	0.022	211.4565	39.66283	0.36083	2.1	0.126
J140718.49+535606.7	211.82707	53.9352	0.43218	20.805	0.037	0.042	211.82710	53.93512	0.27838	1.96	0.141
J140843.78+540751.4	212.18244	54.13097	0.91757	19.469	0.029	0.041	212.18249	54.13084	0.46618	14.44	0.15
J141058.58+354040.2	212.74411	35.67783	0.72192	19.607	0.02	0.044	212.74407	35.67775	0.33426	1.72	0.147
J141258.09+403216.4	213.24204	40.53789	0.70819	19.463	0.014	0.029	213.24200	40.53791	0.13329	3.57	0.139
J141911.28+351804.8	214.79702	35.30135	0.73038	19.476	0.018	0.046	214.79705	35.30146	0.41592	7.31	0.138
J141917.36+310923.2	214.82234	31.15645	0.84017	18.158	0.021	0.049	214.82235	31.15668	0.83206	1.12	0.136
J142129.75+474724.5	215.37395	47.79014	0.07259	15.06	0.02	0.058	215.37377	47.79019	0.47646	1.71	0.136
J142525.17+060930.1	216.35491	6.15836	0.70354	19.65	0.023	0.089	216.35493	6.158219	0.54069	1.17	0.143
J142548.09+523034.3	216.45037	52.50954	0.42005	18.832	0.021	0.027	216.45040	52.50950	0.14574	5.23	0.14
J142549.19+394655.0	216.45496	39.78194	0.50525	19.781	0.025	0.029	216.45512	39.78205	0.57921	7.47	0.144
J142726.29+375726.0	216.85955	37.95723	0.60525	20.474	0.023	0.038	216.85986	37.95733	0.93217	2.74	0.145
J142818.55+525826.9	217.07730	52.97415	0.74613	18.174	0.021	0.028	217.07732	52.974	0.54125	1.91	0.145
J142852.82+271042.5	217.22009	27.17847	0.44479	17.116	0.021	0.07	217.22012	27.17848	0.12741	1.28	0.137

J143157.94+341650.2	217.99145	34.28061	0.71543	17.2	0.021	0.054	217.99144	34.28063	0.05687	1.22	0.138
J143813.72+214432.6	219.55720	21.74239	0.55709	20.024	0.021	0.095	219.55721	21.74244	0.15537	5.48	0.144
J143952.91+392358.9	219.97049	39.39971	0.11185	18.336	0.026	0.031	219.97044	39.39982	0.42651	1.74	0.132
J144015.38+301752.0	220.06411	30.29779	0.64703	20.187	0.03	0.045	220.06410	30.29788	0.33623	2.41	0.151
J144356.89+250144.5	220.98705	25.02904	0.93974	19.729	0.02	0.125	220.9871	25.02903	0.16702	409.67	0.144
J144800.47+023916.2	222.00197	2.65450	0.89866	20.359	0.025	0.127	222.00186	2.654383	0.61625	2.63	0.132
J144815.81+390821.5	222.06587	39.13932	0.67252	19.563	0.022	0.039	222.06615	39.13956	1.16334	1.2	0.128
J145012.74+101543.9	222.55311	10.26221	0.69390	19.836	0.019	0.1	222.5531	10.26255	1.24298	1.04	0.147
J145559.45+492152.8	223.99773	49.36467	0.07587	18.062	0.026	0.065	223.9973	49.36455	1.09633	1.09	0.135
J145736.70+523454.6	224.40295	52.58184	0.63878	18.091	0.016	0.059	224.40304	52.58178	0.30321	2.95	0.142
J145941.18+071353.0	224.92159	7.23140	0.66644	19.451	0.029	0.092	224.92160	7.231389	0.07627	60.82	0.152
J150937.26-000714.0	227.40525	-0.12056	0.57931	20.278	0.023	0.187	227.40535	-0.12048	0.47481	2.2	0.15
J151112.73+163040.6	227.80306	16.51128	0.72988	18.974	0.02	0.09	227.80306	16.51133	0.18770	17.7	0.147
J151223.47+020904.0	228.09779	2.15111	0.95281	18.303	0.017	0.146	228.09764	2.151019	0.65908	2.48	0.245
J151228.20+370516.3	228.11752	37.08788	0.68438	20.185	0.03	0.049	228.11766	37.08780	0.49952	1.16	0.142
J151228.93+575051.8	228.12057	57.84774	0.42130	17.595	0.017	0.043	228.12065	57.84768	0.29318	2.92	0.144
J151436.63+445004.0	228.65263	44.83446	0.57182	19.244	0.022	0.082	228.65267	44.83446	0.10237	31.03	0.142
J151532.23+553326.9	228.88431	55.55749	0.25701	20.646	0.035	0.05	228.88431	55.55761	0.43571	7.45	0.142
J151548.25+472315.2	228.95105	47.38757	0.96439	19.883	0.024	0.115	228.95105	47.38757	0.01440	4.69	0.143
J151616.84+274122.9	229.07019	27.68970	0.74653	19.281	0.018	0.121	229.07019	27.68961	0.31040	4.02	0.132
J151923.50+271115.4	229.84792	27.18763	0.33364	19.906	0.027	0.113	229.84797	27.18761	0.15266	4.51	0.133
J152731.75+384307.7	231.88231	38.71881	0.39990	19.402	0.031	0.066	231.88223	38.7189	0.40413	1.43	0.138
J153110.33+430653.4	232.79307	43.11485	0.67707	19.924	0.025	0.093	232.79287	43.11492	0.58287	1.95	0.131
J153150.46+242317.7	232.96025	24.38826	0.39074	21.376	0.041	0.156	232.96031	24.38822	0.22374	2.24	0.204
J153655.73+290045.2	234.23221	29.01258	0.90813	19.7	0.017	0.099	234.23203	29.01254	0.57052	1.12	0.139
J154351.92+162422.1	235.96636	16.40615	0.84843	16.468	0.015	0.102	235.96635	16.40614	0.06065	12.48	0.136
J154930.05+202207.5	237.37522	20.36877	0.70732	19.862	0.021	0.174	237.37526	20.36893	0.61120	1.92	0.138
J155121.13+071357.7	237.83805	7.23271	0.67548	16.881	0.017	0.119	237.83806	7.232725	0.05597	55.59	0.149
J155131.53+611409.6	237.88139	61.23601	0.89716	19.25	0.023	0.035	237.88150	61.23615	0.55231	2.81	0.154
J155237.42+613644.3	238.15593	61.61232	0.67649	19.82	0.028	0.038	238.15592	61.61218	0.48241	2.41	0.146
J155257.78+104012.8	238.24077	10.67022	0.63862	20.512	0.029	0.196	238.24084	10.67025	0.24440	6.28	0.14
J155634.29+160021.1	239.14290	16.00588	0.81059	18.284	0.018	0.129	239.14291	16.00585	0.12367	2.51	0.159
J155732.74+232838.2	239.38644	23.47728	0.63346	19.898	0.022	0.21	239.38642	23.47736	0.30343	2.97	0.143
J160117.07+592046.1	240.32115	59.34616	0.63354	17.957	0.017	0.046	240.32108	59.34614	0.15371	1.7	0.157
J160134.81+070959.0	240.39505	7.16640	0.58744	19.475	0.016	0.141	240.39509	7.166486	0.33621	1.56	0.133
J160715.22+175330.0	241.81345	17.89167	0.5752	20.546	0.026	0.147	241.81353	17.89166	0.27863	5.09	0.15
J160839.47+253000.3	242.16448	25.50009	0.70320	19.781	0.018	0.171	242.16449	25.50011	0.07060	6.52	0.142
J160927.68+055138.3	242.36537	5.86065	0.58163	19.545	0.017	0.167	242.36535	5.860606	0.18205	2.87	0.155
J161217.24+391103.2	243.07185	39.18424	0.41768	19.542	0.065	0.028	243.07155	39.1842	0.82937	1.23	0.134
J161240.38+582255.7	243.16826	58.38213	0.95901	17.463	0.02	0.052	243.16849	58.38227	0.65265	1.42	0.137
J161346.35+072244.4	243.44315	7.37900	0.72300	19.851	0.023	0.184	243.44317	7.379044	0.16234	6.08	0.153
J161350.30+041917.6	243.45960	4.32155	0.98570	19.565	0.018	0.223	243.45973	4.321594	0.46361	46.57	0.154
J161603.77+463225.2	244.01571	46.54035	0.95025	19.668	0.018	0.034	244.01569	46.54036	0.06571	62.23	0.132
J161818.98+124111.5	244.57911	12.68653	0.19123	20.289	0.023	0.22	244.57895	12.68649	0.57081	1.65	0.134
J162052.59+540058.6	245.21914	54.01629	0.14561	18.346	0.013	0.041	245.21888	54.01633	0.55826	1.13	0.151
J162318.89+402258.6	245.82873	40.38296	0.90933	17.861	0.015	0.024	245.82884	40.38285	0.48425	8.63	0.14
J162420.69+514639.6	246.08623	51.77767	0.28394	19.91	0.025	0.062	246.08615	51.77763	0.20649	1.26	0.137
J162539.37+295149.5	246.41404	29.86376	0.89626	19.445	0.022	0.095	246.41403	29.86371	0.17264	3.3	0.148
J162542.15+411841.0	246.42566	41.31141	0.70390	19.414	0.017	0.021	246.42566	41.31141	0.01439	70.61	0.325
J163345.22+512748.4	248.43843	51.46345	0.62892	18.048	0.016	0.066	248.43853	51.46354	0.39743	7.52	0.139
J163600.37+432802.7	249.00157	43.46743	0.9401	17.432	0.017	0.03	249.00150	43.46728	0.57438	1.93	0.132
J163709.31+414030.8	249.28882	41.67523	0.76081	17.147	0.011	0.025	249.28885	41.67518	0.19409	7.34	0.157
J164027.47+113339.3	250.11447	11.56092	0.54374	19.884	0.017	0.18	250.11457	11.56090	0.35101	1.33	0.138
J164517.20+485540.2	251.32167	48.92784	0.12877	17.819	0.017	0.08	251.32195	48.92771	0.81574	1.58	0.142
J165050.82+503735.2	252.71177	50.62647	0.85373	18.847	0.021	0.081	252.71181	50.62650	0.14847	7.03	0.148
J170300.48+410835.8	255.75204	41.14329	0.89367	19.486	0.018	0.079	255.75199	41.14339	0.37603	1.4	0.131
J170617.47+280101.7	256.57279	28.01716	0.49080	19.2	0.016	0.415	256.57262	28.01708	0.58495	1.2	0.134
J170705.33+425824.8	256.77223	42.97356	0.57840	18.741	0.014	0.103	256.77212	42.97359	0.31453	1.33	0.138
J171145.75+350927.7	257.94064	35.15770	0.31602	20.112	0.025	0.092	257.94083	35.15764	0.60077	3.06	0.131
J171202.78+441337.0	258.01159	44.22696	0.87419	19.113	0.019	0.055	258.01156	44.22694	0.10213	135.73	0.148
J171749.62+253908.7	259.45675	25.65243	0.79692	19.388	0.012	0.139	259.45675	25.65225	0.65899	1.08	0.133
J172354.30+374841.3	260.97626	37.81147	0.82844	17.324	0.008	0.13	260.97613	37.81156	0.47808	1.69	0.148
J172414.19+330303.9	261.05914	33.05110	0.54805	20.785	0.03	0.146	261.05908	33.0511	0.17893	368.13	0.108
J172517.49+302640.8	261.32288	30.44468	0.98071	18.99	0.04	0.16	261.32293	30.44464	0.20255	112.53	0.137
J210722.65+064647.2	316.84438	6.77978	0.81766	19.969	0.018	0.24	316.84435	6.779914	0.47053	1.06	0.117
J211817.39+001316.7	319.57249	0.22132	0.46295	18.707	0.015	0.26	319.57252	0.221358	0.17102	95.48	0.131
J212229.80+043136.6	320.62418	4.52683	0.77271	19.579	0.023	0.312	320.62416	4.526783	0.20374	1.73	0.101
J212838.52-030310.2	322.16050	-3.05285	0.87548	19.067	0.015	0.193	322.16045	-3.05278	0.32600	3.9	0.376
J213613.74+005825.9	324.05728	0.97388	0.52792	19.75	0.019	0.217	324.05734	0.973939	0.30470	5.77	0.404
J213813.74-015107.3	324.55727	-1.85203	0.95956	18.573	0.016	0.155	324.55728	-1.85206	0.11275	30.08	0.15
J215712.85+101424.8	329.30356	10.24023	0.76119	19.682	0.021	0.243	329.30357	10.24019	0.16157	299.93	0.258
J221425.97-024134.1	333.60822	-2.69282	0.83609	19.858	0.023	0.288	333.60819	-2.69283	0.09817	2.67	0.147
J225243.74+061850.8	343.18229	6.31413	0.90892	19.913	0.027	0.254	343.18227	6.314078	0.21392	101.84	0.121
J225452.22+004631.3	343.71760	0.77537	0.09081	17.28	0.021	0.286	343.71771	0.775517	0.63754	1.05	0.111
J225954.06+120135.7	344.97525	12.02660	0.64333	18.966	0.025	0.472	344.97526	12.02657	0.10910	123.49	0.152
J230107.97-015804.6	345.28322	-1.96796	0.77719	19.248	0.019	0.203	345.28322	-1.96790	0.20633	254.93	0.138
J230815.61+124125.9	347.06507	12.69053	0.87546	19.491	0.025	0.323	347.06506	12.69052	0.05532	7.58	0.149
J230900.14+060226.5	347.25061	6.04071	0.43278	20.802	0.036	0.249	347.25052	6.040661	0.35119	2.28	0.122
J232143.44+101803.9	350.43104	10.30110	0.67606	19.502	0.033	0.22	350.43119	10.30114	0.55375	2.73	0.16
J232447.59+065314.0	351.19830	6.88722	0.43983	19.527	0.024	0.312	351.19824	6.887175	0.28197	2.68	0.132
J232714.61+103033.9	351.81090	10.50943	0.47416	19.504	0.028	0.199	351.81097	10.50953	0.42509	1.27	0.135
J233038.17+021450.5	352.65905	2.24737	0.69929	18.9	0.019	0.135	352.6591	2.247436	0.25696	36.07	0.106
J233419.71-012824.8	353.58213	-1.47358	0.79043	18.688	0.02	0.137	353.58208	-1.47363	0.27292	3.26	0.133
J234516.00+103936.3	356.31669	10.66010	0.91402	19.477	0.022	0.194	356.31674	10.66009	0.17013	2.35	0.152
J234724.32-031430.6	356.85137	-3.24185	0.88210	19.195	0.024	0.126	356.85122	-3.24183	0.54601	4.45	0.372
J235931.81-063943.4	359.88256	-6.66206	0.79864	18.098	0.016	0.111	359.88264	-6.66213	0.37636	64.63	0.3

Table A.3: FRII_{nc} sample. Same notation of table A.1

$\mathbf{FRII}_{nc}$ **AGN sample**											
SDSS ID	**RA**	**DEC**	**z**	m_g	Δm_g	A_g	$RA_{rl,1}$	$DEC_{rl,1}$	$Sep._1$	F_1	Rms_1
J000033.05+114049.6	0.13774	11.68045	0.73004	19.685	0.02	0.279	0.1351	11.67772	13.53528	5.15	0.146
J000929.11+074123.1	2.37132	7.68975	0.413001	19.724	0.016	0.475	2.38242	7.70518	68.21934	1.28	0.128
J003419.07+012000.4	8.57946	1.33345	0.850313	19.833	0.026	0.069	8.57870	1.33472	5.358001	107.02	0.134
J004947.04-024231.3	12.44603	-2.70871	0.664603	19.793	0.023	0.164	12.44757	-2.71230	14.04961	2.14	0.094
J014022.68+075357.0	25.09453	7.89917	0.899535	18.926	0.018	0.153	25.09574	7.89791	6.263414	19.59	0.113
J081703.10+162259.7	124.26294	16.38327	0.699275	19.307	0.019	0.114	124.26432	16.38550	9.319095	1.73	0.133
J081735.07+223717.7	124.39614	22.62159	0.981346	17.901	0.015	0.162	124.39582	22.62094	2.568911	42.17	0.156
J082133.86+425021.5	125.39109	42.83932	0.649144	20.3	0.024	0.209	125.38443	42.86984	111.2855	11.37	0.134
J082656.05+434333.0	126.73355	43.72585	0.456631	19.262	0.017	0.104	126.73057	43.72848	12.23812	34.97	0.142
J083144.49+451043.4	127.93538	45.17873	0.748255	19.437	0.021	0.083	127.97344	45.17091	100.5938	1.12	0.135
J084312.42+612943.8	130.80177	61.49552	0.854029	17.697	0.011	0.244	130.79682	61.49668	9.469177	310.2	0.167
J085234.22+421527.1	133.14259	42.25754	0.982065	19.474	0.019	0.09	133.14206	42.25517	8.644095	136.56	0.151
J085443.91+181156.0	133.68299	18.19889	0.719585	19.408	0.02	0.064	133.68437	18.20213	12.57237	14.33	0.146
J090240.95+483746.9	135.67063	48.62971	0.325613	19.928	0.022	0.076	135.66494	48.62556	20.16519	1.53	0.133
J090410.87+641012.0	136.04529	64.17002	0.71955	19.706	0.021	0.31	136.01816	64.19568	101.6987	1.14	0.14
J091011.14+542723.5	137.54643	54.45654	0.621961	17.312	0.025	0.058	137.53964	54.4588	16.36844	51.93	0.152
J091354.35+224843.3	138.47648	22.81203	0.709185	19.142	0.026	0.14	138.47790	22.83247	73.74082	7.4	0.145
J091634.67+195952.7	139.14447	19.99797	0.770704	19.681	0.053	0.122	139.14432	19.99719	2.845796	15.8	0.132
J092045.46+492721.6	140.18945	49.45602	0.797551	19.676	0.028	0.054	140.1829	49.46208	26.67410	3.62	0.147
J092433.48+365248.3	141.13951	36.88009	0.905531	16.955	0.019	0.04	141.13879	36.89550	55.49619	1.14	0.15
J092733.50+023449.3	141.88959	2.58038	0.73112	20.163	0.025	0.25	141.86898	2.57404	77.56735	7.92	0.143
J092953.43-013831.5	142.47263	-1.64209	0.709742	18.895	0.016	0.105	142.48849	-1.63207	67.51908	1.34	0.142
J093459.01-021909.8	143.74587	-2.31939	0.631745	18.529	0.017	0.115	143.7492	-2.31856	12.31296	14.27	0.157
J094647.39+193201.7	146.69749	19.53382	0.660044	19.273	0.017	0.087	146.69835	19.53765	14.09828	1.96	0.132
J095414.56+385503.9	148.56069	38.91775	0.688295	19.101	0.023	0.046	148.56993	38.92180	29.71126	18.42	0.15
J100620.50+543827.2	151.58542	54.64091	0.937855	19.554	0.016	0.03	151.59499	54.66773	98.57607	1.2	0.152
J101235.69-010823.2	153.14871	-1.13977	0.863513	19.33	0.024	0.139	153.14837	-1.15536	56.11895	5.89	0.145
J102734.02+135108.1	156.89176	13.85227	0.555539	19.408	0.028	0.12	156.89298	13.85666	16.37538	77.28	0.148
J103057.52+275602.3	157.73968	27.93397	0.978358	18.738	0.025	0.076	157.74168	27.93176	10.20359	390.12	0.149
J103354.28+501228.7	158.47620	50.20799	0.995289	19.62	0.032	0.048	158.47508	50.21876	38.87526	1.93	0.317
J103456.06+391042.9	158.73358	39.17859	0.528047	19.748	0.022	0.044	158.73326	39.17444	14.95947	7.25	0.146
J103932.15+263244.5	159.88398	26.54570	0.827965	19.125	0.027	0.091	159.88591	26.54184	15.21950	9.37	0.137
J105220.30+454322.2	163.08459	45.72285	0.240441	19.124	0.029	0.059	163.08319	45.72373	4.750937	2.06	0.14
J110837.66+385842.2	167.15692	38.97841	0.783552	19.913	0.021	0.056	167.15121	38.98174	19.97632	22.8	0.154
J111805.03+490218.8	169.52095	49.03856	0.577741	19.655	0.022	0.055	169.52397	49.01987	67.65499	1.12	0.13
J112412.22+432549.9	171.05095	43.43055	0.813505	19.578	0.031	0.048	171.05017	43.43146	3.851919	37.85	0.132
J112727.48+311039.1	171.86450	31.17753	0.251	20.299	0.028	0.06	171.88920	31.15455	112.4019	1.88	0.112
J112821.95+373137.9	172.09149	37.52721	0.977917	19.617	0.034	0.065	172.09169	37.51692	37.03778	8.85	0.145
J113823.70+252232.8	174.59877	25.37579	0.689621	19.312	0.027	0.097	174.59817	25.37533	2.584031	7.61	0.147
J114707.57+503053.4	176.78157	50.51485	0.520696	19.577	0.025	0.052	176.78011	50.51485	3.330730	16.07	0.141
J114847.83+105458.4	177.19929	10.91623	0.861026	17.739	0.021	0.14	177.20118	10.91681	6.979640	86.13	0.15
J115322.71+402622.8	178.34464	40.43968	0.726567	18.414	0.02	0.057	178.33695	40.43383	29.81104	1.41	0.202
J115825.22+113923.6	179.60510	11.65655	0.750849	19.128	0.026	0.073	179.61164	11.65634	23.05381	1.68	0.138
J121550.42+162649.0	183.96011	16.44696	0.718893	19.728	0.055	0.107	183.96110	16.44587	5.199984	16.18	0.148
J121628.03+035031.8	184.11679	3.84216	0.996753	19.366	0.018	0.06	184.11873	3.84082	8.499270	3.4	0.244
J122512.28+192720.9	186.30116	19.45582	0.857708	19.292	0.032	0.11	186.30163	19.45708	4.824243	9.31	0.138
J122521.37+033945.2	186.33904	3.66257	0.639341	20.508	0.032	0.053	186.34022	3.66259	4.246899	50.43	0.243
J122851.74+584444.2	187.21562	58.74563	0.806072	19.175	0.02	0.041	187.22313	58.74987	20.74953	6.02	0.153
J122921.46+520100.7	187.33943	52.01688	0.718572	19.11	0.026	0.056	187.35835	52.02228	46.20422	1.6	0.139
J123301.65+152457.9	188.25690	15.41610	0.75356	19.759	0.117	0.095	188.2563	15.41778	6.394146	2.87	0.187
J123455.23+573242.2	188.73013	57.54507	0.451342	19.525	0.026	0.033	188.73382	57.54261	11.37806	24.94	0.143
J124044.68+330349.8	190.18618	33.06384	0.81162	17.367	0.023	0.057	190.18578	33.06535	5.554545	6.84	0.135
J130543.00+334919.0	196.42918	33.82196	0.778512	20.153	0.026	0.035	196.41567	33.82428	41.26488	1.42	0.148
J130619.22+363150.4	196.58008	36.53069	0.604918	19.802	0.021	0.051	196.57866	36.53064	4.111171	17.39	0.139
J130952.28+494452.9	197.46785	49.74804	0.587259	19.654	0.029	0.039	197.47463	49.73752	41.04126	2.94	0.136
J132222.67+464535.2	200.59449	46.75979	0.374379	17.383	0.013	0.05	200.60377	46.75531	28.00932	1.34	0.147
J132942.49+454000.2	202.42704	45.66673	0.804769	19.15	0.02	0.051	202.42656	45.66520	5.628816	162.71	0.133
J134014.81+375201.1	205.06173	37.86699	0.809948	19.463	0.023	0.022	205.06703	37.87860	44.43561	1.07	0.136
J135651.49+554635.5	209.21455	55.77653	0.942052	19.28	0.021	0.029	209.23768	55.78878	64.30980	1.72	0.141
J135850.03+390413.4	209.70849	39.07041	0.808383	17.318	0.017	0.052	209.69955	39.06757	26.99379	282.86	0.241
J140227.27+520432.1	210.61365	52.07560	0.873284	19.72	0.026	0.045	210.61234	52.07224	12.44546	109.69	0.147
J142304.14+524630.3	215.76726	52.77508	0.997968	18.732	0.021	0.029	215.75842	52.77464	19.32088	1.15	0.135
J143744.19+285533.6	219.43415	28.92601	0.862699	19.78	0.024	0.048	219.43497	28.92673	3.678242	55.33	0.15
J143921.69+414923.5	219.84040	41.82321	0.981986	18.328	0.017	0.041	219.84385	41.82625	14.35312	15.26	0.135
J144811.15+142249.0	222.04649	14.38029	0.618897	19.728	0.019	0.072	222.05243	14.39282	49.65717	2.19	0.136
J151138.76+525154.4	227.91151	52.86513	0.34615	19.107	0.033	0.052	227.92045	52.85761	33.31549	2.02	0.143
J151427.97+323135.1	228.61656	32.52643	0.633022	19.38	0.02	0.059	228.61303	32.51785	32.69677	53.42	0.142
J152129.25+151255.8	230.37191	15.21551	0.652007	19.694	0.02	0.114	230.36762	15.20381	44.67416	3.85	0.188
J152834.45+472756.1	232.14356	47.46560	0.738527	19.347	0.02	0.061	232.15456	47.47264	36.86330	2.11	0.152
J152933.03+601552.5	232.38764	60.26459	0.798391	18.885	0.018	0.043	232.38418	60.25937	19.75487	1.56	0.142
J153308.88+074429.6	233.28704	7.74156	0.384221	19.87	0.018	0.146	233.29363	7.742242	23.65038	1.99	0.139
J153338.90+080821.8	233.41212	8.13939	0.617491	19.806	0.018	0.194	233.40880	8.139444	11.81520	20.47	0.152
J153533.22+491337.3	233.88845	49.22703	0.759097	19.564	0.016	0.055	233.90292	49.20913	72.86169	8.34	0.132
J155025.22+480723.0	237.60508	48.12307	0.962698	19.659	0.024	0.053	237.60855	48.12221	8.877311	2.18	0.14
J155127.31+481050.8	237.86380	48.18078	0.703513	19.244	0.022	0.052	237.86089	48.17826	11.44543	3.08	0.14
J160121.25+424548.1	240.33855	42.76338	0.957855	19.828	0.024	0.038	240.33752	42.76459	5.139983	14.18	0.148
J160902.41+610944.7	242.26005	61.16243	0.892948	19.489	0.018	0.04	242.24901	61.16741	26.25065	26.45	0.148
J161734.65+141132.2	244.39439	14.19230	0.845302	19.578	0.022	0.185	244.39340	14.19403	7.113800	223.47	0.155
J162951.87+150819.4	247.46614	15.13873	0.69512	20.496	0.03	0.19	247.46475	15.13828	5.107948	12.97	0.151
J163717.59+234258.6	249.32333	23.71629	0.875797	18.981	0.016	0.176	249.32260	23.71403	8.504771	221.32	0.143
J165105.17+503140.3	252.77156	50.52787	0.730099	18.971	0.022	0.076	252.7737	50.52735	5.225101	3.08	0.139
J170129.83+224553.6	255.37430	22.76490	0.635086	19.637	0.017	0.166	255.36705	22.76924	28.71109	3.12	0.137
J170224.93+374019.1	255.60391	37.67197	0.887879	19.749	0.019	0.083	255.60382	37.66081	40.16956	1.07	0.135
J170316.25+251215.1	255.81772	25.20420	0.673266	18.965	0.02	0.266	255.81890	25.19518	32.71976	1.06	0.132
J171716.38+382801.0	259.31829	38.46696	0.775526	21.07	0.062	0.207	259.31997	38.46696	4.735389	5.32	0.14
J173016.04+351237.6	262.56684	35.21046	0.579978	19.507	0.014	0.13	262.56162	35.21025	15.36931	36.1	0.143
J212939.40-000719.7	322.41418	-0.12215	0.553443	19.4	0.017	0.129	322.41544	-0.12431	9.004112	98.13	0.106
J213042.16+054927.6	322.67570	5.82435	0.85866	19.238	0.015	0.231	322.67718	5.82503	5.826997	43.74	0.104
J221719.98+011016.5	334.33328	1.17126	0.425443	20.187	0.027	0.181	334.35981	1.17636	97.23634	4.16	0.146
J222521.55+085613.9	336.33983	8.937201	0.668784	19.704	0.02	0.247	336.3398	8.9439	24.11663	12.6	0.106
J231007.94-030631.7	347.53312	-3.10880	0.673454	19.539	0.026	0.142	347.53236	-3.10948	3.649137	14.75	0.143
J235915.66+020654.5	359.81525	2.11516	0.569616	19.58	0.021	0.083	359.81360	2.11033	18.37105	29.28	0.111

Table A.4: Second part of table A.3.

FRII$_{nc}$ AGN sample						
$RA_{rl,2}$	$DEC_{rl,2}$	$Sep._2$	F_2	Rms_2	w	Ψ
0.14604	11.68217	29.90838	5.1	0.145	2.9082	145.411
2.3531	7.67620	81.27918	1.51	0.128	3.2462	162.313
8.58179	1.33013	14.58062	47.34	0.134	3.5150	177.709
12.45057	-2.714	25.05502	1.2	0.094	0.3524	170.674
25.09302	7.90036	6.896382	29.63	0.112	3.4471	172.355
124.26202	16.37797	19.33923	25.2	0.154	3.1445	157.225
124.39536	22.62470	11.48935	254.37	0.157	3.0810	176.897
125.36355	42.81581	111.5482	1.17	0.131	3.0678	153.390
126.72805	43.70022	93.38360	1.08	0.145	0.8350	172.419
127.89014	45.18797	119.5305	9.47	0.131	3.5989	179.949
130.80851	61.49223	16.57346	141.44	0.167	3.5064	179.410
133.14251	42.26047	10.55369	182.75	0.151	3.5339	176.697
133.68132	18.19473	16.03297	15.6	0.146	3.5795	178.978
135.66079	48.62619	26.62149	6.62	0.134	0.9001	164.663
135.9949	64.14585	117.5645	19.14	0.14	0.8094	161.950
137.5537	54.45446	16.94422	26.04	0.153	3.5790	178.952
138.49247	22.7879	101.8126	1.08	0.141	3.2803	164.015
139.14465	19.99952	5.613126	14.55	0.132	3.5447	177.237
140.20374	49.43336	88.15938	2.19	0.149	3.5506	177.534
141.10401	36.89406	113.9021	1.01	0.152	0.3503	152.331
141.91973	2.59341	118.0900	14.18	0.15	3.4642	173.211
142.44543	-1.66116	119.5425	1.12	0.131	3.5481	177.408
143.74040	-2.32017	19.88844	184.79	0.154	3.4870	174.354
146.70764	19.52862	39.17830	1.34	0.132	2.8638	146.574
148.54090	38.90695	67.71217	1.7	0.152	3.2038	160.190
151.56322	54.61040	119.1954	2.69	0.152	3.5437	177.187
153.13687	-1.12865	58.46910	13.34	0.147	2.6076	172.780
156.89059	13.84773	16.83569	90.66	0.148	3.5799	178.996
157.73779	27.93642	10.67185	94.42	0.149	3.5735	178.678
158.49402	50.22105	62.42078	2.16	0.318	0.2813	177.738
158.73305	39.18511	23.53415	5.45	0.146	3.5651	178.256
159.88041	26.54952	17.93374	6.39	0.136	3.5025	179.453
163.09009	45.71671	26.07548	1.27	0.142	0.8853	178.810
167.16482	38.97365	27.95725	8.99	0.155	0.8988	179.889
169.48270	49.03880	90.28525	3.11	0.129	3.1481	157.405
171.05245	43.42859	8.063876	17.58	0.132	3.5916	179.583
171.83447	31.19768	117.5478	1.23	0.1	3.5490	177.452
172.07863	37.55527	107.4631	5.59	0.15	3.5210	176.052
174.60052	25.38027	17.09093	18.47	0.147	0.7149	179.842
176.78351	50.51496	4.472292	35.1	0.141	3.4607	173.038
177.19674	10.91589	9.102559	42.12	0.149	3.3555	167.778
178.34890	40.45018	39.56362	1.76	0.214	3.3159	165.798
179.59670	11.65601	29.67800	2.19	0.138	3.4830	174.152
183.95799	16.45161	18.27883	38.07	0.149	3.4526	172.633
184.11556	3.84418	8.504511	1.53	0.243	3.2099	160.495
186.30014	19.45157	15.69539	12.63	0.139	3.5137	175.686
186.33699	3.66260	7.383679	198.85	0.243	3.5677	178.385
187.20532	58.74000	27.92897	2.75	0.154	3.5918	179.592
187.35284	52.02720	47.59665	11.85	0.139	0.7560	153.984
188.25862	15.41834	10.03290	1.95	0.187	0.8606	159.455
188.72487	57.56067	57.05497	1.05	0.146	3.5384	176.923
190.18778	33.05758	23.06547	36.05	0.133	0.8996	179.936
196.44827	33.81655	60.33725	1.4	0.147	3.5353	176.765
196.58132	36.53203	6.014883	9.66	0.139	0.8039	176.412
197.4564	49.77296	93.56564	1.26	0.135	0.8965	179.312
200.57259	46.77671	81.41812	1.06	0.144	3.5584	177.922
202.42902	45.67120	16.85336	39.42	0.133	3.5834	179.170
205.07706	37.86265	46.27066	1.13	0.132	3.2557	162.787
209.17	55.75807	112.0753	17.05	0.147	3.5200	176.004
209.69853	39.07080	27.89055	2.27	0.24	1.6908	159.935
210.61522	52.08150	21.51968	60.25	0.147	3.5895	179.475
215.75380	52.77065	33.37163	1.07	0.135	2.6585	156.735
219.43238	28.92373	9.923485	14.05	0.15	3.4170	170.853
219.83408	41.81827	24.55484	4.51	0.134	3.5660	178.303
222.04972	14.35542	90.22213	15.09	0.136	3.1865	159.327
227.87505	52.86957	80.82336	1.24	0.144	3.4518	172.594
228.64525	32.54713	114.6125	1.29	0.138	3.2686	163.434
230.35742	15.21759	50.88802	1.29	0.187	0.6618	146.882
232.17492	47.46132	77.85131	1.4	0.138	3.1957	169.363
232.34652	60.27087	76.82554	1.13	0.143	3.4202	171.011
233.27864	7.73913	31.21735	3.32	0.139	3.3410	167.054
233.41552	8.13923	12.15174	30.11	0.153	3.5647	178.237
233.89983	49.24932	84.57159	1.67	0.135	3.5104	175.522
237.58632	48.14275	83.96341	2.26	0.136	3.4950	174.752
237.86826	48.18210	11.72323	1.04	0.139	3.0626	179.776
240.33971	42.76183	6.357340	3.45	0.148	3.5935	179.676
242.27996	61.15783	38.32897	1.34	0.147	3.5592	178.856
244.40143	14.19638	28.64882	1.1	0.155	1.7995	141.340
247.46768	15.13854	5.391237	28.95	0.151	2.9083	145.417
249.32488	23.71921	11.67902	47.04	0.144	3.5217	178.596
252.76225	50.52843	21.39737	25.81	0.139	0.8734	176.981
255.39533	22.75149	84.86385	3.08	0.135	3.5904	179.522
255.62034	37.67802	51.63350	3.03	0.135	0.7009	140.180
255.81710	25.22045	58.50977	44.17	0.135	3.5806	179.034
259.31555	38.46731	7.816349	2.73	0.14	3.4708	173.541
262.57335	35.20987	19.27734	26.79	0.147	3.4375	173.948
322.41165	-0.11976	12.55477	124.3	0.106	3.2690	163.452
322.67415	5.82376	5.944758	28.14	0.105	3.4687	173.438
334.32014	1.14073	119.6691	1.08	0.146	2.3695	160.303
336.34015	8.92815	32.57518	4.05	0.107	3.5814	179.074
347.53252	-3.10607	10.07364	1.37	0.143	2.6152	149.588
359.81667	2.12033	19.28927	187.81	0.111	3.5211	176.057

Table A.5: FRII sample. Same notation of table A.1

FRII AGN sample											
SDSS ID	**RA**	**DEC**	**z**	m_g	Δm_g	A_g	RA_r	DEC_r	$Sep._r$	F_r	Rms_r
J001209.85+090249.3	3.0410	9.0470	0.7930	19.301	0.019	0.549	3.0410	9.0470	0.1018	4.55	0.11
J001741.45+082755.7	4.4227	8.4654	0.6785	19.433	0.022	0.651	4.4227	8.4654	0.1751	32.17	0.129
J010255.68+103702.9	15.7320	10.6174	0.9109	18.957	0.028	0.129	15.7321	10.6175	0.3479	5.09	0.15
J012141.59+114950.4	20.4233	11.8306	0.5713	19.713	0.028	0.106	20.4233	11.8306	0.1284	1197.68	0.777
J014239.99+073239.4	25.6666	7.5442	0.9064	19.625	0.025	0.144	25.6666	7.5444	0.4699	3.65	0.129
J015635.70+014816.1	29.1487	1.8044	0.8641	19.48	0.021	0.087	29.1487	1.8044	0.3551	4.86	0.085
J020714.36+011806.3	31.8098	1.3017	0.9735	19.134	0.021	0.087	31.8098	1.3019	0.6454	3.81	0.153
J021008.48+011839.6	32.5353	1.3110	0.8652	18.482	0.029	0.095	32.5354	1.3111	0.7716	6.73	0.151
J023322.16-045506.8	38.3423	-4.9185	0.7804	17.155	0.052	0.079	38.3423	-4.9185	0.1779	83.88	0.146
J024500.70-074736.4	41.2529	-7.7934	0.8870	19.747	0.025	0.097	41.2527	-7.7928	2.4164	1.13	0.141
J025509.76+025345.6	43.7906	2.8960	0.6626	19.363	0.023	0.344	43.7907	2.896	0.1927	626.9	0.254
J075244.19+455657.4	118.1841	45.9492	0.0514	17.4	0.013	0.272	118.1841	45.9491	0.3423	40.56	0.13
J081336.06+481302.6	123.4002	48.2174	0.8704	18.194	0.014	0.191	123.4001	48.2171	0.8925	7709.03	1.182
J081646.06+401324.8	124.1919	40.2235	0.9786	20.259	0.023	0.175	124.1919	40.2235	0.0168	2.64	0.149
J082014.21+154519.3	125.0592	15.7553	0.9424	17.728	0.016	0.119	125.0592	15.7553	0.1458	17.45	0.149
J083052.08+241059.8	127.7170	24.1832	0.9406	17.37	0.022	0.111	127.7169	24.1832	0.1352	835.48	0.148
J083133.06+163023.4	127.8877	16.5065	0.8928	20.145	0.02	0.088	127.8877	16.5065	0.2384	63.62	0.135
J085556.18+371342.5	133.9840	37.2284	0.7115	18.955	0.095	0.119	133.9840	37.2284	0.1377	13.32	0.143
J085820.33+461722.1	134.5847	46.2894	0.9644	19.358	0.05	0.075	134.5847	46.2895	0.3583	2.09	0.141
J091751.28+115258.9	139.4637	11.8830	0.5288	20.209	0.034	0.088	139.4636	11.8830	0.3608	1.3	0.139
J092351.52+281525.1	140.9646	28.2569	0.7445	19.252	0.027	0.063	140.9646	28.2569	0.1931	169.59	0.146
J093301.58+495029.9	143.2566	49.8416	0.6157	18.315	0.03	0.037	143.2567	49.8415	0.4298	9.61	0.134
J093348.07+511405.6	143.4502	51.2348	0.5765	17.976	0.025	0.047	143.4497	51.2351	1.6088	3.55	0.14
J094203.33+593709.5	145.5139	59.6193	0.5355	20.933	0.037	0.062	145.5138	59.6193	0.1276	17.63	0.148
J094558.42+135650.8	146.4934	13.9474	0.5696	18.742	0.025	0.109	146.4934	13.9474	0.1059	5.42	0.151
J094645.73-014049.4	146.6905	-1.6804	0.7465	19.221	0.018	0.14	146.6906	-1.6804	0.1622	30.21	0.151
J095649.88+251516.0	149.2078	25.2544	0.7076	17.957	0.013	0.124	149.2078	25.2544	0.1328	1041.77	0.172
J100943.55+052953.8	152.4314	5.4982	0.9423	17.196	0.016	0.074	152.4314	5.4982	0.0751	25.09	0.154
J102059.85+520918.2	155.2494	52.1550	0.8105	19.384	0.03	0.045	155.2493	52.1550	0.1411	1.36	0.144
J102106.04+452331.8	155.2751	45.3921	0.3640	18.218	0.019	0.034	155.2751	45.3921	0.2981	39.41	0.145
J103024.95+551622.7	157.6039	55.2729	0.4348	17.013	0.025	0.032	157.6042	55.2728	0.6926	11.4	0.139
J103822.46+134657.3	159.5936	13.7826	0.9465	17.685	0.014	0.122	159.5936	13.7826	0.1016	45.6	0.153
J103848.12+372924.5	159.7005	37.4901	0.7297	17.407	0.016	0.056	159.7006	37.4901	0.2663	17.47	0.137
J105829.60+013358.8	164.6233	1.5663	0.8927	18.309	0.015	0.087	164.6231	1.5662	0.7218	3314.16	0.819
J110436.33+212417.8	166.1513	21.4049	0.1876	17.268	0.015	0.057	166.1514	21.4050	0.4684	11.04	0.139
J110655.96+624800.1	166.7331	62.8000	0.8437	18.441	0.021	0.027	166.7330	62.7998	0.6872	6.69	0.154
J111506.83+302618.3	168.7784	30.4384	0.9391	18.262	0.019	0.047	168.7784	30.4384	0.1939	3.25	0.144
J112946.01-012140.5	172.4417	-1.3612	0.7263	17.65	0.021	0.1	172.4417	-1.3611	0.2846	6.84	0.14
J112956.02+402514.4	172.4834	40.4206	0.7586	20.247	0.032	0.08	172.4833	40.4207	0.2330	2.28	0.158
J114603.76+334551.9	176.5156	33.7644	0.7610	19.807	0.024	0.058	176.5156	33.7645	0.2069	3.06	0.142
J114803.17+565411.6	177.0132	56.9032	0.4514	17.72	0.016	0.03	177.0132	56.9031	0.2900	24.24	0.152
J115159.93+495056.1	177.9997	49.8489	0.8911	18.53	0.029	0.056	177.9996	49.8488	0.3287	3.83	0.146
J115318.07+234113.5	178.3253	23.6870	0.9901	19.798	0.02	0.092	178.3255	23.6869	0.8329	1.86	0.145
J120951.76+181006.8	182.4656	18.1685	0.8448	18.933	0.017	0.103	182.4657	18.1685	0.1357	62.69	0.142
J122106.86+454852.1	185.2786	45.8144	0.5248	17.088	0.022	0.039	185.2785	45.8144	0.1590	21.46	0.15
J124012.46+533437.2	190.0519	53.5770	0.2925	20.613	0.034	0.064	190.0520	53.5770	0.3525	4.42	0.15
J124145.80+262226.7	190.4408	26.3741	0.7464	18.766	0.015	0.045	190.4408	26.3741	0.0731	1.2	0.145
J125542.55+311048.5	193.9273	31.1801	0.3022	18.842	0.026	0.062	193.9273	31.1801	0.2049	5.19	0.139
J130554.16+014929.9	196.4756	1.8249	0.7332	17.594	0.03	0.106	196.4756	1.8249	0.1593	41.46	0.153
J132029.67+491647.1	200.1236	49.2797	0.6844	19.064	0.018	0.026	200.1237	49.2797	0.2327	1.57	0.138
J132512.19+511933.3	201.3008	51.3259	0.7885	19.101	0.031	0.037	201.3015	51.3257	1.7638	9.0	0.13
J134751.58+283629.7	206.9649	28.6082	0.7405	17.531	0.317	0.049	206.9649	28.6083	0.3120	34.97	0.157
J135335.92+263147.5	208.3996	26.5298	0.3079	16.832	0.021	0.05	208.3996	26.5298	0.0508	22.35	0.137
J140232.37+461233.6	210.6348	46.2093	0.5574	19.611	0.023	0.029	210.6349	46.2093	0.2364	7.83	0.13
J140626.60+250921.0	211.6108	25.1558	0.8668	16.886	0.015	0.062	211.6108	25.1559	0.2490	67.5	0.136
J142242.49+041439.1	215.6770	4.24419	0.9725	17.427	0.019	0.097	215.6771	4.2442	0.2102	66.69	0.144
J142457.80+124749.5	216.2408	12.7970	0.7726	19.293	0.02	0.077	216.2407	12.7971	0.3852	3.98	0.149
J145359.73+091543.3	223.4988	9.2620	0.2792	18.995	0.017	0.1	223.4989	9.2620	0.3996	118.06	0.143
J150532.63+202810.1	226.3859	20.4694	0.7792	19.243	0.018	0.114	226.3859	20.4695	0.2753	2.46	0.148
J153036.32+235236.7	232.6513	23.8768	0.9548	17.036	0.015	0.171	232.6514	23.8769	0.4550	19.26	0.267
J153057.78+102216.0	232.7407	10.3711	0.4763	19.902	0.025	0.118	232.7410	10.3711	1.1452	1.32	0.15
J160226.89+274141.9	240.6120	27.6949	0.9371	17.973	0.017	0.138	240.6120	27.6948	0.4218	15.86	0.148
J160303.65+385143.9	240.7652	38.8622	0.2815	21.225	0.053	0.04	240.7650	38.8624	1.1252	8.5	0.156
J163745.13+471733.8	249.4380	47.2927	0.7354	19.314	0.016	0.074	249.4379	47.2927	0.1548	601.81	0.157
J164504.76+180623.9	251.2698	18.1066	0.6514	19.392	0.021	0.266	251.2702	18.1065	1.5222	5.14	0.112
J170634.12+361508.0	256.6422	36.2522	0.9172	18.128	0.019	0.095	256.6423	36.2522	0.3573	18.85	0.14
J170726.31+334513.5	256.8596	33.7537	0.6306	19.391	0.047	0.082	256.8598	33.7537	0.5029	6.25	0.14
J172109.49+354216.0	260.2895	35.7044	0.2832	18.228	0.02	0.137	260.2896	35.7043	0.4899	386.51	0.248
J213004.76-010244.4	322.5198	-1.0456	0.7044	18.141	0.023	0.177	322.5199	-1.0460	1.3823	36.98	0.152
J213344.19-015716.4	323.4341	-1.9545	0.8028	19.478	0.017	0.176	323.4341	-1.9545	0.1723	4.1	0.264
J213552.50+011815.7	323.9687	1.30438	0.7796	19.724	0.025	0.202	323.9687	1.3043	0.0274	835.97	0.14
J221428.08-032349.1	333.6170	-3.3969	0.6574	18.893	0.02	0.286	333.6169	-3.3969	0.2296	9.86	0.231
J223458.73-022419.0	338.7447	-2.4053	0.5494	18.566	0.021	0.175	338.7448	-2.4052	0.3033	6.56	0.15
J224001.10-031601.6	340.0046	-3.2671	0.8585	18.471	0.021	0.165	340.0045	-3.2671	0.1537	1.96	0.135
J235451.67-040503.4	358.7153	-4.0843	0.7218	18.238	0.024	0.11	358.7153	-4.0842	0.3426	304.83	0.18
J235737.96+003227.8	359.4081	0.5410	0.9536	19.209	0.016	0.117	359.4082	0.5412	0.8610	1.33	0.107

Table A.6: Second part of table A.5.

FRII AGN sample											
$RA_{rl,1}$	$DEC_{rl,1}$	$Sep._1$	F_1	Rms_1	$RA_{rl,2}$	$DEC_{rl,2}$	$Sep._2$	F_2	Rms_2	w	Ψ
3.0481	9.0418	31.4749	5.51	0.11	3.0254	9.0631	80.2257	3.74	0.108	3.4012	170.0630
4.4123	8.4641	37.3159	9.75	0.128	4.4481	8.4698	91.9438	1.42	0.13	0.2217	179.8638
15.7306	10.6108	24.3788	9.53	0.151	15.7355	10.6255	31.4668	11.55	0.15	3.3612	168.0610
20.4072	11.8294	56.6939	6.05	0.777	20.4309	11.8498	74.0233	6.36	0.781	2.2402	179.0008
25.6700	7.5449	12.5255	11.17	0.129	25.6595	7.5448	25.2581	6.98	0.129	3.3036	165.1840
29.1434	1.8048	19.1190	3.95	0.085	29.1550	1.8029	23.4338	13.92	0.084	3.4060	170.3011
31.8113	1.3041	10.1886	5.19	0.153	31.8072	1.2988	14.2002	59.74	0.153	3.3899	169.4972
32.5371	1.3174	23.8879	1.01	0.151	32.5289	1.3157	28.8996	1.01	0.151	1.3653	174.4579
38.3332	-4.9169	32.9989	9.66	0.144	38.3519	-4.9179	34.6438	31.34	0.149	3.3201	166.0061
41.2527	-7.7943	3.2381	1.09	0.14	41.2532	-7.7912	7.9291	10.37	0.141	3.5534	177.6740
43.7866	2.8836	46.7465	2.29	0.255	43.7986	2.8855	47.5146	3.14	0.255	1.0953	179.8158
118.1751	45.9438	29.7394	7.63	0.13	118.1959	45.9574	41.7289	6.72	0.132	3.4539	172.6968
123.3805	48.2172	47.2379	20.69	1.174	123.3870	48.2313	59.3844	12.2	1.185	0.4993	178.7004
124.1859	40.2227	16.5736	2.74	0.149	124.1995	40.2240	21.1349	1.04	0.148	3.4369	171.8450
125.0586	15.7582	10.7125	42.52	0.149	125.0597	15.7515	13.9188	21.23	0.149	3.5565	177.8266
127.7147	24.1867	14.7387	1.6	0.148	127.7195	24.1871	16.0619	1.59	0.149	0.7883	175.7169
127.8727	16.5083	52.2773	1.26	0.135	127.9138	16.4901	107.492	4.81	0.135	3.2379	161.8982
133.9777	37.2254	21.3151	20.6	0.144	133.9901	37.2334	24.8458	2.68	0.143	2.8498	142.4901
134.5758	46.2936	26.8578	7.1	0.14	134.5967	46.2843	35.0410	1.57	0.142	3.5874	179.3734
139.4579	11.8822	20.3278	2.92	0.139	139.4849	11.8836	74.8089	5.15	0.139	0.8634	172.6995
140.9652	28.2538	11.2303	4.97	0.146	140.9643	28.2601	11.4787	50.57	0.145	3.5790	178.9521
143.2735	49.8418	39.3029	1.08	0.134	143.2335	49.8406	53.7527	3.84	0.134	0.8842	176.9226
143.4436	51.2380	18.7092	21.71	0.14	143.4627	51.2293	34.5096	22.72	0.139	3.5936	179.6827
145.5126	59.6150	15.6667	4.28	0.147	145.5155	59.6264	25.7798	1.1	0.149	3.5916	179.5835
146.4951	13.9477	6.0422	1.18	0.151	146.4846	13.9465	30.9918	12.07	0.151	0.8826	179.2283
146.6926	-1.6782	10.8836	8.58	0.151	146.6876	-1.6833	14.7894	8.24	0.152	3.5585	177.9298
149.2136	25.2527	19.9009	2.3	0.172	149.1998	25.2539	26.1768	1.53	0.172	3.2502	162.5117
152.4339	5.5022	16.8412	1.56	0.154	152.4292	5.4936	18.4266	1.05	0.154	3.4700	174.4850
155.2450	52.1507	18.2538	2.9	0.144	155.2552	52.1615	26.7863	1.75	0.143	3.5763	179.7490
155.2748	45.3898	8.3959	2.25	0.146	155.2745	45.3965	15.8859	3.44	0.145	0.8861	179.2413
157.6020	55.2712	7.3522	19.1	0.138	157.6093	55.2751	13.5777	73.13	0.139	3.2286	161.4346
159.6010	13.7734	41.7222	2.02	0.153	159.5829	13.7959	60.7506	2.33	0.152	3.5973	179.8652
159.7007	37.4843	20.9321	1.07	0.137	159.7029	37.4979	28.7594	1.74	0.136	3.5094	175.4700
164.6224	1.5691	10.7384	19.63	0.82	164.6230	1.5616	16.9406	50.45	0.818	3.1930	159.6500
166.1491	21.4032	9.7421	5.86	0.138	166.152	21.4077	10.1732	5.32	0.139	2.6657	133.2865
166.7140	62.7857	60.5490	7.53	0.154	166.7586	62.8210	86.4400	2.21	0.153	3.5865	179.3293
168.7785	30.4318	23.8547	6.56	0.142	168.7828	30.4576	70.5730	1.63	0.147	3.5190	175.9519
172.4485	-1.3549	33.4136	65.94	0.139	172.4306	-1.3703	51.7138	130.76	0.142	3.5318	176.5907
172.4616	40.4313	70.8774	2.96	0.157	172.5112	40.4044	96.0047	13.95	0.157	3.5778	178.8910
176.5262	33.7545	47.7811	35.56	0.144	176.5020	33.7785	65.0096	3.82	0.141	3.5866	179.3335
177.0165	56.8989	16.8555	1.9	0.152	177.0114	56.9093	22.3241	1.38	0.152	3.5672	179.4043
178.0046	49.8560	28.2795	27.74	0.145	177.9935	49.8406	32.9771	3.41	0.146	3.5904	179.5249
178.3284	23.6872	10.1798	2.48	0.145	178.3218	23.6868	11.3478	2.36	0.145	3.5548	177.7437
182.4730	18.1664	26.5677	2.96	0.142	182.4475	18.1732	64.2737	3.39	0.145	3.5777	178.8854
185.2825	45.8188	18.6823	12.82	0.15	185.2728	45.8107	19.7212	53.69	0.15	3.4275	178.0647
190.0422	53.5775	20.8195	2.47	0.15	190.0401	53.5747	26.4064	3.92	0.15	1.4333	170.6286
190.4389	26.3712	11.8491	1.07	0.148	190.4321	26.3818	39.7593	7.87	0.146	3.0726	153.6323
193.9298	31.1842	16.8153	1.25	0.139	193.9235	31.1756	19.9991	1.93	0.138	3.5112	175.5601
196.4728	1.8189	23.9085	85.01	0.152	196.5053	1.8246	106.818	30.8	0.153	2.1907	179.3057
200.1362	49.2746	34.9625	1.11	0.137	200.1098	49.2835	35.1112	1.46	0.138	3.5615	178.0767
201.2964	51.3273	11.1035	7.26	0.13	201.3058	51.3243	12.6983	15.52	0.13	3.5940	179.7027
206.9673	28.6081	7.6579	19.0	0.157	206.9576	28.6052	25.3429	80.74	0.157	2.1830	141.6639
208.3956	26.5088	76.8295	2.92	0.138	208.3990	26.5523	80.7648	7.42	0.137	3.5334	176.6700
210.6388	46.2084	10.4066	9.33	0.13	210.6296	46.2098	13.2345	14.8	0.13	3.5152	175.7634
211.6092	25.1571	7.0632	28.43	0.136	211.6255	25.1495	52.9833	2.78	0.137	0.3890	179.3994
215.6764	4.2414	10.1019	47.6	0.144	215.6750	4.2466	11.5730	20.91	0.145	2.7255	136.2770
216.2375	12.7980	11.9594	3.87	0.149	216.2442	12.7966	11.9859	2.29	0.149	3.4486	172.4320
223.5005	9.2592	11.6347	1.41	0.143	223.4998	9.2823	73.0075	1.01	0.146	0.3539	166.8721
226.3864	20.4725	11.0607	1.9	0.148	226.3884	20.4605	33.2138	1.23	0.149	3.4565	172.8294
232.6603	23.8800	31.7943	3.4	0.28	232.6407	23.8726	37.9411	2.34	0.253	3.3706	168.5342
232.7397	10.3637	26.8531	1.38	0.15	232.7404	10.3796	30.6133	38.66	0.15	3.4684	173.4203
240.6122	27.6911	13.6957	87.81	0.148	240.6151	27.7073	45.4306	1.23	0.148	0.8830	176.6049
240.7654	38.8580	14.8477	4.49	0.156	240.7648	38.8667	16.3253	19.05	0.156	3.5946	179.8587
249.4356	47.2885	16.1954	1.59	0.157	249.4390	47.2974	17.0158	174.99	0.157	3.5708	179.4389
251.2726	18.1038	13.7638	13.15	0.111	251.2639	18.1118	27.4920	2.56	0.114	3.5752	179.6363
256.6411	36.2706	66.4307	2.24	0.142	256.6327	36.2325	76.0094	2.47	0.138	3.5300	176.5048
256.8634	33.7549	12.1672	11.22	0.14	256.8543	33.7513	18.1518	3.66	0.14	2.7717	144.3444
260.2901	35.6942	37.0020	27.66	0.247	260.2848	35.7183	51.9330	5.01	0.246	3.5710	179.8415
322.5203	-1.0495	14.0607	41.83	0.152	322.5192	-1.0415	15.1317	114.29	0.152	3.5820	179.1026
323.4379	-1.9582	18.8880	12.88	0.265	323.4268	-1.9474	36.7790	10.0	0.261	3.5957	179.7871
323.9967	1.3115	103.816	1.16	0.139	323.9458	1.3234	107.174	1.04	0.14	2.5668	167.5929
333.6118	-3.4053	35.3550	3.42	0.236	333.6247	-3.3869	45.6282	2.47	0.232	3.5165	175.8296
338.7388	-2.3907	56.3995	3.17	0.147	338.7624	-2.4163	74.9682	1.92	0.158	2.7110	179.6274
340.0322	-3.2520	113.333	1.03	0.131	339.9775	-3.2490	116.941	1.4	0.14	2.2899	168.3400
358.7155	-4.0792	18.2420	2.27	0.18	358.7151	-4.0894	18.3625	2.52	0.179	3.5821	179.5104
359.4051	0.5369	18.3345	4.35	0.107	359.4104	0.5458	19.1558	24.12	0.109	3.3716	168.5831

Table A.7: Partially resolved CD sample and the kellerman parameter associated. *Note.* F_b: SDSS source density flux corrected for galactic extinction and K-correction (mJy). ΔF_b: error associated to F_b (mJy). F_r: radio core FIRST source peak density flux corrected for K-correction (mJy). ΔF_r: error associated to F_r (mJy). F_{tot}: sum of all the radio components density flux (mJy). ΔF_{tot}: error associated to F_{tot}. $logR_K$: Kellerman parameter base 10 logarithm. $\Delta logR_K$: error associated to $logR_K$.

Partially resolved CD AGN						
SDSS ID	F_b (mJy)	ΔF_b (mJy)	F_r (mJy)	ΔF_r (mJy)	$logR_K$	$\Delta logR_K$
J170717.75+453610.5	0.78719	0.00598	965.09417	0.21957	3.08848	0.00782
J163116.54+492739.5	0.06452	0.00046	206.64086	0.17410	3.50551	0.00804
J162637.91+523804.5	0.15744	0.00157	36.58614	0.18978	2.36619	0.01518
J161706.32+410647.0	0.13712	0.00115	65.61906	0.16401	2.67992	0.01089
J153934.80+473531.2	2.11186	0.02365	60.22694	0.20891	1.45512	0.01466
J153145.14+431933.8	0.06346	0.00053	11.87954	0.19999	2.27225	0.02523
J152548.29+582851.3	0.03100	0.00033	76.87004	0.16069	3.39436	0.01289
J152039.69+421111.1	0.08116	0.00090	70.72415	0.17803	2.94018	0.01371
J150725.62+112635.6	0.09629	0.00077	29.55540	0.20086	2.48704	0.01479
J145922.15+152654.7	0.08349	0.00066	117.99256	0.18570	3.15018	0.00957
J141927.40+283537.9	0.09239	0.00066	26.69991	0.21392	2.46088	0.01521
J141324.26+530527.2	0.02638	0.00031	68.99034	0.43053	3.41737	0.01824
J141238.66+484447.1	0.19701	0.00157	82.97751	0.22146	2.62445	0.01066
J141159.73+423950.3	0.87132	0.00453	110.98125	0.22143	2.10507	0.00719
J135222.05+420313.4	0.09702	0.00069	11.53122	0.20074	2.07499	0.02460
J133152.22+111649.6	0.11911	0.00090	2.70935	0.15618	1.35691	0.06524
J124557.17+215616.1	0.12579	0.00110	9.32901	0.21617	1.87018	0.03197
J115324.46+493108.7	0.50210	0.00401	670.57393	0.18718	3.12564	0.00827
J111018.12+104619.5	0.09604	0.00119	82.40595	0.29654	2.93348	0.01599
J111006.79+405000.7	0.09155	0.00062	1.48282	0.20674	1.20940	0.14622
J102329.79+441414.2	0.59484	0.00309	11.99129	0.20873	1.30445	0.02260
J101326.05-000136.4	0.06187	0.00047	1.41869	0.17704	1.36035	0.13239
J095753.84+121606.7	0.12303	0.00068	58.69828	0.21133	2.67860	0.00920
J095637.65+155125.0	0.10743	0.00094	30.12177	0.20609	2.44771	0.01564
J095427.81+301912.9	0.52867	0.00465	31.17208	0.18344	1.77057	0.01468
J083928.53+260614.3	0.11583	0.00074	15.77848	0.21785	2.13420	0.02020
J082753.69+521758.6	0.05734	0.00048	167.94550	0.17653	3.46666	0.00945
J020514.77-045639.7	0.03467	0.00049	5.94687	0.19615	2.23430	0.04738
J014756.74+124912.5	0.10707	0.00111	15.75475	0.38498	2.16771	0.03483
J014540.95+073217.2	0.05624	0.00053	1.53232	0.19081	1.43528	0.13412
J005327.77-065651.2	0.08310	0.00079	8.92434	0.31828	2.03096	0.04526

Table A.8: Unresolved CD sample and kellerman parameter associated. Same notation of table A.7.

Unresolved CD AGN													
SDSS ID	F_b	ΔF_b	F_1	ΔF_1	$logR_K$	$\Delta logR_K$	**SDSS ID**	F_b	ΔF_b	F_1	ΔF_1	$logR_K$	$\Delta logR_K$
J000652.00+061509.2	0.27087	0.00325	4.59229	0.20013	1.22926	0.05558	J114915.30+393325.4	0.09376	0.00105	3.27925	0.19844	1.54373	0.07171
J000727.89+055701.3	0.17318	0.00152	12.51424	0.16996	1.85889	0.02238	J115106.03+404122.2	0.01748	0.00032	1.82347	0.17979	2.01810	0.11700
J000804.16-012917.0	0.03484	0.0004	2.29998	0.17431	1.81952	0.08738	J115228.57+080626.1	0.06981	0.00055	11.54046	0.19234	2.21825	0.02466
J001932.63-070302.6	0.11165	0.00093	1.52346	0.20910	1.13497	0.14565	J115338.83+055300.9	0.05964	0.00062	11.44142	0.23770	2.28291	0.03117
J002312.69+072455.4	0.34690	0.00374	4.03615	0.17970	1.06575	0.05532	J115504.07+034850.3	0.53909	0.00431	4.33639	0.21756	0.90546	0.05817
J002554.26+083711.3	0.33939	0.0023	208.47836	0.17449	2.78836	0.00763	J115557.11+211116.5	0.03201	0.00096	1.51080	0.16772	1.67385	0.14101
J003706.29-050111.3	0.10969	0.00127	6.55872	0.24978	1.77661	0.04968	J115710.17+352426.0	0.06969	0.00047	2.20241	0.22173	1.49969	0.10748
J003848.49+075059.6	0.08269	0.00069	2.50431	0.15924	1.48119	0.07198	J115727.60+431806.3	0.19982	0.00215	285.47734	0.15145	3.15492	0.01133
J004428.66+090959.4	0.10245	0.00094	7.36092	0.18402	1.85640	0.03420	J115917.31+283814.4	0.14177	0.00096	2.537	0.17599	1.25272	0.07616
J010123.42+005013.3	0.03091	0.00038	2.89755	0.18544	1.97180	0.07640	J120329.85+480313.6	1.70911	0.0082	101.51184	0.21113	1.77374	0.00687
J010352.47+003739.7	0.50677	0.00547	3.07838	0.15537	0.78351	0.06127	J120531.10+144827.9	0.06367	0.00056	82.55984	0.22030	3.11282	0.01146
J010717.05+074446.4	0.09223	0.00084	1.77569	0.19158	1.28447	0.11709	J120713.48+470259.8	0.15331	0.00128	4.24531	0.19255	1.44233	0.05375
J010927.10-031714.4	0.18638	0.00186	10.76286	0.20134	1.76150	0.02870	J120734.62+150643.7	0.47850	0.00612	3.16716	0.19535	0.82078	0.07448
J011239.13-032842.8	0.20506	0.00164	184.63436	0.19848	2.95441	0.00907	J120751.79+604706.9	0.32380	0.00259	2.12299	0.20601	0.81666	0.10504
J011533.41+101456.5	0.17912	0.0015	2.66082	0.19923	1.17187	0.08327	J120910.61+561109.2	0.07165	0.00103	2.57215	0.20005	1.55503	0.09217
J012209.02+102020.0	0.21405	0.00179	1.51520	0.20202	0.84995	0.14173	J121113.97+464711.9	0.10618	0.00093	1.22187	0.16531	1.06097	0.14409
J013034.90+111803.9	0.15724	0.00106	15.56805	0.21336	1.99565	0.02050	J121231.47+251429.1	0.02727	0.00041	1.54893	0.21777	1.75429	0.15579
J013224.25+080103.1	0.07990	0.00079	7.67250	0.18970	1.98236	0.03472	J121413.55+052254.3	0.68249	0.00491	6.51579	0.23494	0.97986	0.04325
J013427.29-013350.3	0.29338	0.00176	14.35903	0.19955	1.68968	0.01989	J121417.80+293143.4	0.36977	0.00236	67.39255	0.12006	2.26067	0.00818
J013908.45+044911.7	0.11908	0.00081	3.35748	0.17608	1.45015	0.05924	J121834.44+484219.5	0.03687	0.00033	5.42216	0.19402	2.16743	0.04498
J014738.38-082718.0	0.08672	0.0009	125.29783	0.22844	3.15979	0.01222	J121957.15+484926.8	0.03171	0.00043	10.52458	0.20532	2.52087	0.03310
J014817.84-054404.1	0.06855	0.00139	3.00450	0.14509	1.64172	0.06869	J122006.84+065232.4	0.02166	0.00033	1.3227	0.18295	1.78575	0.15391
J015646.33+115644.3	0.33219	0.00279	20.35998	0.27431	1.78737	0.02187	J122025.04+341445.7	0.10304	0.00115	17.62056	0.22861	2.23300	0.02417
J020350.85-020651.1	0.11975	0.00172	3.66266	0.24096	1.48550	0.08018	J122118.00+465057.7	0.02637	0.00036	10.58396	0.17217	2.60338	0.03026
J020809.63-053839.1	0.14388	0.00212	7.38662	0.24339	1.71044	0.04775	J122127.16+155624.8	0.03104	0.00041	19.22549	0.19099	2.79181	0.02313
J021640.73-044404.8	1.65434	0.02051	148.71851	0.24372	1.95373	0.01403	J122243.19+293441.5	0.11988	0.00187	5.20792	0.22962	1.63790	0.05969
J021705.52-042253.5	0.09871	0.00106	102.90316	0.23885	3.01806	0.01312	J122400.83+223615.1	0.01666	0.0004	4.56309	0.18481	2.43745	0.06490
J021859.74-040237.1	0.06284	0.00105	2.03759	0.16847	1.51082	0.09948	J122449.90+062917.1	0.03406	0.00047	5.49797	0.23343	2.20785	0.05645
J022508.07+001707.2	0.18598	0.00185	368.02552	0.13569	3.29639	0.01036	J123252.70+414322.4	0.56151	0.00449	3.97865	0.19591	0.85037	0.05724
J022712.98-044636.4	0.37976	0.00243	7.84367	0.17753	1.31501	0.02903	J123338.65+422238.3	0.20483	0.00548	1.83947	0.22428	0.95327	0.14872
J022845.62-050232.0	0.02998	0.00039	4.00715	0.13631	2.12592	0.04721	J123547.98+090801.0	0.00878	0.00026	2.55884	0.16129	2.46425	0.09263
J023313.12-033924.0	0.13498	0.00151	12.83127	0.21269	1.9779	0.02777	J123640.35+563021.4	0.07828	0.0005	1.78146	0.19842	1.35707	0.11778
J023859.18-000158.1	0.19448	0.00163	1.65304	0.14558	0.92940	0.09647	J123820.19+175039.1	1.14174	0.01187	4.92244	0.18702	0.63461	0.04839
J024706.65+002318.1	0.10144	0.00081	2.16147	0.13291	1.36196	0.09633	J124009.12+242531.2	0.89792	0.00718	46.03031	0.20756	1.70981	0.12509
J024817.69+024128.4	0.11829	0.00099	1.9647	0.19042	1.22031	0.10532	J124205.41+111728.4	0.02527	0.00035	5.98085	0.16762	2.37419	0.42025
J071933.35+403253.0	0.17280	0.00110	1.993	0.17923	1.06196	0.09633	J124251.69+101945.7	0.05461	0.00056	1.95245	0.19264	1.55326	0.10906
J072729.35+413632.9	0.05557	0.00048	2.48247	0.15869	1.65001	0.07272	J124445.84+194054.7	0.05154	0.00041	2.38257	0.19003	1.66488	0.08776
J073638.86+435316.6	0.17832	0.00128	4.94979	0.14558	1.44338	0.03661	J124511.25+335610.1	0.97759	0.01055	2.73836	0.21702	0.44733	0.09005
J073945.16+215636.1	0.05541	0.00044	36.53163	0.22243	2.81900	0.01408	J124805.02+073352.3	0.04291	0.00041	2.10182	0.22508	1.68999	0.11669
J074026.41+365534.4	0.16651	0.00146	4.17470	0.20082	1.39917	0.05690	J125235.36+471922.5	0.07565	0.00172	3.20798	0.25511	1.62739	0.10232
J074140.45+365544.6	0.12789	0.00081	4.69366	0.18669	1.56464	0.04617	J125239.59+464044.7	0.10660	0.00085	18.11905	0.22117	2.23034	0.02020
J074559.61+450434.3	0.09429	0.00083	5.95424	0.15481	1.80033	0.03480	J125249.86+112933.1	0.83443	0.00667	38.04605	0.22197	1.65891	0.01383
J074630.61+440433.5	0.15368	0.00147	1.35827	0.15054	0.94635	0.12043	J125531.36+530912.9	0.07725	0.0008	1.84354	0.19620	1.37770	0.11682
J075001.55+442845.1	0.02374	0.00031	2.47684	0.16087	2.01838	0.07815	J125627.23+120113.4	0.04204	0.00043	4.22199	0.22722	2.00176	0.06421
J075052.04+480345.6	0.09984	0.00083	1.66000	0.22291	1.22076	0.14268	J125701.71+281230.0	0.01976	0.00025	1.38585	0.19281	1.84587	0.15193
J075244.63+434105.3	0.04878	0.00048	12.01317	0.14034	2.39135	0.02168	J125745.32+480525.7	0.14803	0.00823	2.33778	0.15959	1.19843	0.12386
J075659.58+452830.5	0.01770	0.00028	5.88076	0.14701	2.52142	0.04099	J125752.74+475020.6	0.06422	0.00059	108.49394	0.25296	3.22767	0.01153
J075813.13+524451.2	0.11700	0.00074	44.94530	0.19891	2.58446	0.01082	J125915.13+072947.8	0.05576	0.00062	2.22777	0.23051	1.60153	0.11467
J080037.62+461257.9	0.16456	0.00111	2.27697	0.15450	1.14102	0.07465	J125942.80+121312.5	0.11690	0.00093	2.93510	0.19958	1.39980	0.07600
J080424.20+065456.9	0.03312	0.00042	2.78219	0.20969	1.92426	0.08816	J130003.48+121528.1	0.02981	0.00192	10.16957	0.20280	2.53287	0.08434
J081209.24+560038.1	0.09579	0.00072	2.87004	0.19600	1.47652	0.07589	J130016.42+602903.6	0.05357	0.00068	6.39840	0.20054	2.07714	0.04414
J081305.92+371958.0	0.03650	0.00038	7.15446	0.17919	2.29226	0.03544	J130055.53+040551.8	0.06375	0.00058	1.90502	0.17013	1.47537	0.09850
J081347.53+534754.0	0.30028	0.0024	112.34586	0.28201	2.57302	0.01051	J130545.47+443328.4	0.05351	0.00055	2.54603	0.17462	1.67740	0.07898
J081425.89+294115.6	0.23627	0.00151	6.03306	0.18111	1.40712	0.03642	J130630.53+462203.0	0.06991	0.00078	130.96457	0.20403	3.27258	0.01275
J081516.86+460430.8	0.94674	0.00757	5.62592	0.15530	0.77396	0.03560	J130631.63+435100.4	0.80653	0.00516	4.29926	0.19569	0.72677	0.05191
J081929.48+522345.2	0.09259	0.00077	3.67836	0.29342	1.59907	0.08817	J131150.88+420333.1	0.02376	0.00028	3.94628	0.18525	2.22033	0.05894
J082149.22+245159.5	0.10000	0.00084	5.52213	0.20291	1.74209	0.04514	J131316.69+213202.1	0.07577	0.00097	14.18273	0.24924	2.27224	0.03037
J082311.26+435318.5	0.15971	0.0037	2.29381	0.16191	1.15720	0.09378	J131526.31+535950.3	0.26968	0.00226	3.82181	0.20939	1.15141	0.06318
J082456.93+215539.4	0.60713	0.00315	2.09823	0.18282	0.53857	0.09233	J131933.02+550808.5	0.04629	0.00038	3.96433	0.18296	1.93265	0.05455
J082808.65+394816.2	0.11434	0.00091	60.22231	0.22328	2.72155	0.01170	J132052.19+574737.3	0.36107	0.00303	1.95189	0.18998	0.73286	0.10573
J082826.20+394436.8	0.08552	0.00116	1.88648	0.22606	1.34355	0.13343	J132111.20+221612.1	0.14166	0.00175	611.28558	0.24065	3.63499	0.01279
J082911.95+341055.8	0.05776	0.00073	1.80236	0.19840	1.49416	0.12287	J132146.53+265150.1	0.81085	0.00421	4.02177	0.31161	0.69547	0.08268
J083307.86+501000.3	0.26074	0.00198	4.53172	0.14932	1.24005	0.04055	J132201.35+495835.0	0.31437	0.00276	1.93290	0.22067	0.78875	0.12296

J083354.46+565816.1	0.39409	0.00362	15.47884	0.22884	1.59413	0.02398	J132401.53+032020.5	0.06260	0.00057	3.30787	0.25481	1.72292	0.08623
J083413.91+511214.6	0.00599	0.00026	2.77643	0.17430	2.66547	0.10678	J132644.96+434804.5	0.42560	0.00442	11.35209	0.19460	1.42606	0.02754
J083431.37+582425.7	0.09603	0.01060	2.33906	0.19247	1.38661	0.19268	J132749.91+191522.6	0.04475	0.00062	5.99229	0.19540	2.12673	0.04660
J083522.77+424258.3	0.40606	0.00276	1.93634	0.20876	0.67838	0.11461	J132819.23+442432.9	0.03434	0.00037	3.30138	0.18437	1.98282	0.06664
J083525.97+435211.2	0.49234	0.00256	2.34229	0.18217	0.67736	0.08297	J133039.64+245432.9	0.07527	0.00078	8.50321	1.51916	2.05294	0.18905
J083537.33+284712.9	0.04643	0.00053	1.73923	0.18036	1.57350	0.11530	J133245.23+472222.7	0.44392	0.00337	230.94110	0.18461	2.71619	0.00839
J083558.43+261444.4	0.04191	0.00058	5.88932	0.21934	2.14766	0.05124	J133431.74+084748.8	0.06378	0.00058	1.67874	0.20501	1.42025	0.13132
J084348.64+620626.6	0.13970	0.00106	2.01085	0.24473	1.15816	0.12930	J133749.32+594717.4	0.04159	0.00046	2.28631	0.20797	1.74008	0.10216
J084515.98+391412.1	0.14841	0.00124	3.00943	0.19489	1.30699	0.07316	J133939.61+033109.8	0.08236	0.00065	2.58267	0.16868	1.49632	0.07331
J084744.55+442610.6	0.08345	0.00116	8.22021	0.16335	1.99342	0.03387	J133942.71+182955.2	0.19135	0.00214	3.85869	0.19034	1.30458	0.06052
J085031.81+163913.0	0.03258	0.00039	2.16612	0.19808	1.82261	0.10344	J133947.29+591210.3	0.03111	0.00038	3.63824	0.17814	2.06797	0.06136
J085106.74+582656.5	0.11796	0.00117	2.46170	0.16509	1.31949	0.07706	J134151.07+083512.4	0.01963	0.00025	1.71925	0.16615	1.94236	0.10944
J085206.15+465050.5	0.16318	0.00156	1.87254	0.17485	1.05975	0.10297	J134251.35+260555.2	0.04754	0.00045	44.81961	0.21746	2.97439	0.01445
J085726.27+484518.8	0.03951	0.00042	17.0981	0.18024	2.63614	0.02134	J134300.17+284407.5	0.75901	0.00576	341.52596	0.22624	2.65317	0.00826
J085943.79+155232.8	0.30536	0.00171	104.92528	0.20433	2.53606	0.00754	J134310.87+494604.6	0.05773	0.00083	2.17918	0.23253	1.57681	0.12110
J090245.60+111619.9	0.12843	0.00087	4.69967	0.20975	1.56338	0.05143	J134701.56+640504.6	0.09313	0.00059	12.27503	0.24424	2.11991	0.02629
J090508.17+523527.5	0.04355	0.00043	1.40683	0.18985	1.50921	0.14495	J135052.73+303453.5	0.28171	0.00236	451.16629	0.21996	3.20452	0.00888
J090512.95+233139.6	0.04307	0.00044	6.91198	0.18493	2.20538	0.03715	J135302.39+335015.8	0.01416	0.00022	3.05517	0.16864	2.33391	0.07079
J090712.21+091056.4	0.09623	0.00073	12.28877	0.22513	2.10619	0.02592	J135326.54+242413.5	0.04006	0.00048	1.50383	0.19200	1.57439	0.13967
J090745.28+532421.4	0.59490	0.00594	12.27255	0.20551	1.31448	0.02674	J135335.28+080854.6	0.08568	0.00099	25.10143	0.22224	2.46679	0.02045
J090858.81+472617.2	0.15601	0.00131	2.28811	0.19633	1.16630	0.09420	J135607.37+413615.3	0.93532	0.0071	33.96651	0.21129	1.56008	0.01382
J091542.24+251939.0	0.40725	0.00374	163.64214	0.20834	2.60403	0.01047	J135845.38+265808.4	0.17412	0.00195	2.22288	0.18686	1.10604	0.09526
J092058.62+232317.0	0.02466	0.00029	2.58709	0.18700	2.02079	0.08428	J135938.49+223207.4	0.11020	0.00066	6.50167	0.21520	1.77083	0.03910
J092206.67+630334.9	0.04401	0.00044	6.07792	0.32954	2.14015	0.06421	J140050.61+092655.7	0.07590	0.00066	1.75691	0.26907	1.36449	0.16195
J092518.10+044529.8	0.16165	0.00129	3.24047	0.22490	1.30201	0.07740	J140307.59+320320.5	0.08172	0.00071	2.21785	0.20987	1.43356	0.10343
J092551.85+361235.6	0.13392	0.00101	334.12726	0.24352	3.39703	0.00832	J140549.53+393946.0	0.11245	0.00085	3.00026	0.18001	1.42619	0.06760
J092708.11+143413.5	0.05411	0.00052	6.47683	0.19855	2.07803	0.04025	J140718.49+535606.7	0.02312	0.00034	2.52031	0.18130	2.03743	0.08673
J092725.19+043851.5	0.20458	0.00122	1.55966	0.20984	0.88216	0.14054	J140843.78+540751.4	0.09699	0.00112	22.77687	0.23660	2.37074	0.02198
J093230.89+405720.2	0.00462	0.0002	6.80113	0.23465	3.16729	0.07810	J141058.58+354040.2	0.07943	0.00063	2.51615	0.21504	1.50070	0.09346
J093509.47+481910.6	0.27553	0.00264	2.13072	0.16009	0.88834	0.08473	J141258.09+403216.4	0.08896	0.00049	5.19330	0.20220	1.76624	0.04453
J093601.69+193850.2	0.46628	0.00242	1.91928	0.20114	0.61448	0.10999	J141911.28+351804.8	0.09010	0.00064	10.73044	0.20257	2.07589	0.02607
J093712.32+500852.1	0.06361	0.00043	195.19839	0.18733	3.48688	0.00775	J141917.36+310923.2	0.31756	0.00266	1.71640	0.20842	0.73279	0.12982
J094033.75+462315.0	0.50452	0.00645	2.10001	0.18393	0.61934	0.10038	J142129.75+474724.5	3.80653	0.03045	1.79597	0.14283	-0.3262	0.08753
J094100.81+143614.4	0.03691	0.00039	9.27751	0.17701	2.40021	0.02987	J142525.17+060930.1	0.07899	0.00072	1.69876	0.20762	1.33255	0.13142
J094248.08+112934.3	0.07986	0.00092	4.07914	0.20395	1.70819	0.06160	J142548.09+523034.3	0.13952	0.00117	6.68519	0.17895	1.68047	0.03516
J094406.99+321444.6	0.05222	0.00075	2.28448	0.16047	1.64092	0.08464	J142549.19+394655.0	0.06075	0.0006	9.94599	0.19172	2.21409	0.02927
J094804.86+270042.0	0.03796	0.00047	3.78477	0.18252	1.99862	0.06062	J142726.29+375726.0	0.03384	0.00031	3.81619	0.20195	2.05212	0.06211
J095150.49-025545.5	0.23945	0.00153	13.14730	0.23690	1.73961	0.02441	J142818.55+525826.9	0.29585	0.00248	2.82155	0.21420	0.97940	0.08431
J095633.93+562216.0	0.43055	0.00275	3.67339	0.25166	0.93104	0.07491	J142852.82+271042.5	0.71365	0.00599	1.65605	0.17724	0.36558	0.11543
J095738.18+552257.7	0.39893	0.00494	4400.23913	0.86933	4.04257	0.01259	J143157.94+341650.2	0.73398	0.00616	1.78000	0.20134	0.38473	0.12151
J095746.55+474549.4	0.03819	0.00036	17.35714	0.18500	2.65742	0.02025	J143813.72+214432.6	0.05285	0.00044	7.47136	0.19632	2.15035	0.03467
J100256.22+475027.7	0.08469	0.00091	2.35544	0.15870	1.44421	0.07817	J143952.91+392358.9	0.18632	0.00193	1.87405	0.14216	1.00252	0.08626
J100432.83+124831.4	0.04901	0.00033	2.61386	0.19829	1.72692	0.08266	J144015.38+301752.0	0.04517	0.00054	3.41750	0.21412	1.87879	0.07465
J100458.31+202449.2	0.30193	0.00193	10.91990	0.21587	1.55830	0.02616	J144356.89+250144.5	0.08314	0.00066	651.41124	0.22897	3.89400	0.00835
J100507.89+341424.1	0.34709	0.0036	3.77663	0.15884	1.03665	0.05245	J144800.47+023916.2	0.04593	0.00045	4.11974	0.20677	1.95272	0.06019
J100603.11+195917.4	0.16466	0.00144	1.77614	0.21455	1.03288	0.12959	J144815.81+390821.5	0.08068	0.00071	1.72005	0.18347	1.32875	0.11546
J100651.13+565654.6	0.08753	0.00066	5.53902	0.21474	1.80124	0.04637	J145012.74+101543.9	0.06696	0.0005	1.50402	0.21258	1.35140	0.14894
J100933.22+255901.1	0.00425	0.00017	1.51139	0.18486	2.55075	0.16271	J145559.45+492152.8	0.24180	0.00251	1.14725	0.14209	0.67620	0.13425
J101425.63+031434.5	0.20014	0.00192	1.57204	0.18864	0.89511	0.12960	J145736.70+523454.6	0.31433	0.00201	4.16857	0.20065	1.12259	0.05453
J101643.72+455051.1	0.05073	0.00067	17.36103	0.15893	2.53426	0.02235	J145941.18+071353.0	0.09368	0.00108	86.956	0.21731	2.96762	0.01409
J101857.98+103625.6	0.06126	0.00061	103.71238	0.20671	3.22860	0.01199	J150937.26-000714.0	0.04597	0.00042	3.02936	0.20654	1.81879	0.07738
J101931.79+262643.2	0.17774	0.00149	1.30916	0.16364	0.86719	0.13340	J151112.73+163040.6	0.14894	0.00119	25.97679	0.21573	2.24154	0.01630
J101952.59+073050.8	0.07405	0.00077	1.94669	0.19064	1.41974	0.10833	J151223.47+020904.0	0.31673	0.00215	3.96200	0.39140	1.09722	0.10559
J102009.69-012758.7	0.09213	0.00073	3.75746	0.21493	1.61048	0.06520	J151228.20+370516.3	0.04614	0.00055	1.67096	0.20454	1.55883	0.13441
J102011.66+281635.8	0.09772	0.00093	8.52867	0.19924	1.94089	0.03296	J151228.93+575051.8	0.44269	0.00301	3.73477	0.18418	0.92615	0.05611
J102041.14+395811.2	0.19194	0.00145	4.13164	0.25613	1.33294	0.06959	J151436.63+445004.0	0.10782	0.00094	42.58573	0.19488	2.59655	0.01337
J102144.05+233738.6	0.08292	0.00089	1.45165	0.16217	1.24318	0.12251	J151532.23+553326.9	0.02461	0.00034	8.74370	0.16665	2.55053	0.03306
J102152.49+131146.4	0.10162	0.00134	3.48040	0.20121	1.53461	0.07101	J151548.25+472315.2	0.07212	0.00069	7.52372	0.22940	2.01834	0.04009
J102222.61+495216.4	0.08948	0.00078	4.60269	0.20504	1.71127	0.05334	J151616.84+274122.9	0.11629	0.00083	5.93950	0.19502	1.70819	0.04003
J102736.45+285917.6	0.04080	0.00058	1.71350	0.16900	1.62312	0.11303	J151923.50+271115.4	0.05374	0.00058	5.51702	0.16269	2.01134	0.04029
J102755.32+180923.5	0.08694	0.0009	4.30677	0.19156	1.69492	0.05488	J152731.75+384307.7	0.08470	0.00105	1.80969	0.17464	1.32970	0.10890
J102818.15+535113.6	0.11069	0.00075	3.07215	0.19902	1.44330	0.07158	J153110.33+430653.4	0.06092	0.0006	2.80040	0.18812	1.66240	0.07717
J102834.03-023659.6	0.08402	0.00073	87.09358	0.20430	3.01559	0.01114	J153150.46+242317.7	0.01486	0.00024	2.82176	0.25698	2.27822	0.10747

J102953.43+163739.2	0.20565	0.00172	2.60887	0.17048	11.0332	0.07374	J153655.73+290045.2	0.08242	0.00056	1.76053	0.21849	1.32959	0.13090
J103027.97+300114.1	0.08862	0.00063	2.98464	0.20162	1.52735	0.07475	J154351.92+162422.1	1.58631	0.00951	19.18569	0.20907	1.08258	0.01689
J103045.22+255522.1	0.73081	0.0076	68.71089	0.20659	1.97321	0.01340	J154930.05+202207.5	0.07037	0.00059	2.79204	0.20067	1.59847	0.08027
J103100.66+444513.5	0.01936	0.00034	6.84490	0.15719	2.54829	0.04096	J155121.13+071357.7	1.02830	0.00699	79.78008	0.21383	1.88977	0.00948
J103111.14+630545.6	0.04519	0.00039	3.60527	0.15712	1.90181	0.05238	J155131.53+611409.6	0.11713	0.00107	4.39926	0.24109	1.57468	0.06400
J103246.80+391009.9	0.11426	0.00077	12.42297	0.20046	2.03632	0.02293	J155237.42+613644.3	0.06372	0.00071	3.46017	0.20962	1.73479	0.07178
J103346.39+233220.0	0.16577	0.00112	12.04718	0.17939	1.86136	0.02169	J155257.78+104012.8	0.03834	0.00044	8.87352	0.19781	2.36433	0.03389
J103853.09+203447.7	0.04307	0.00051	2.70732	0.20920	1.79828	0.08927	J155634.29+160021.1	0.30095	0.00216	3.80320	0.24091	1.10164	0.07054
J103915.67+470541.0	0.02021	0.00021	367.90156	0.14993	4.26015	0.01120	J155732.74+232838.2	0.06823	0.0006	4.18729	0.20161	1.78793	0.05694
J103925.56+490951.2	0.28394	0.00261	3.15476	0.20771	1.04572	0.07504	J160117.07+592046.1	0.35060	0.00238	2.39685	0.22135	0.83482	0.09915
J104002.56+210900.1	0.47361	0.00303	11.19730	0.22988	1.37368	0.02693	J160134.81+070959.0	0.09266	0.00059	2.15582	0.18379	1.36669	0.09165
J104011.18+452125.9	0.44768	0.0025	2.64593	0.17232	0.77160	0.07072	J160715.22+175330.0	0.03455	0.00035	6.99604	0.20617	2.30629	0.03986
J104139.66+365925.6	0.04324	0.00074	1.81757	0.17115	1.62355	0.11136	J160839.47+253000.3	0.07549	0.00054	9.46530	0.20614	2.09822	0.02897
J104539.86+520222.3	0.02432	0.0004	1.57227	0.17032	1.81054	0.12513	J160927.68+055138.3	0.08875	0.0006	3.95599	0.21365	1.64905	0.06080
J104708.07+144557.7	0.34557	0.00317	1.67038	0.22078	0.68427	0.14137	J161217.24+391103.2	0.07253	0.00188	1.57040	0.17108	1.33547	0.13494
J105232.73+612521.2	0.97016	0.00504	1048.32215	0.33377	3.03365	0.00551	J161240.38+582255.7	0.63103	0.00504	2.27360	0.21935	0.55666	0.10447
J105326.04+184203.3	0.11493	0.00114	94.06786	0.21301	2.91299	0.01226	J161346.35+072244.4	0.07221	0.00066	8.89824	0.22391	2.09067	0.03436
J105327.92+375804.3	0.02353	0.00039	3.68984	0.19031	2.19521	0.06837	J161350.30+041917.6	0.10758	0.00077	75.27424	0.24892	2.84488	0.01050
J105421.18+572544.6	0.04096	0.00063	1.64111	0.15271	1.60273	0.10865	J161603.77+463225.2	0.08118	0.00058	99.32604	0.21068	3.08757	0.00932
J105435.30-015051.1	0.06270	0.00057	2.95096	0.21894	1.67268	0.08339	J161818.98+124111.5	0.03851	0.00035	1.86501	0.15146	1.68505	0.09041
J105451.63+553736.5	0.12956	0.00088	4.66337	0.22447	1.55619	0.05493	J162052.59+540058.6	0.19026	0.00098	1.24280	0.16607	0.81505	0.13882
J105458.86-023947.2	0.47164	0.00301	5.23904	0.17057	1.04563	0.03895	J162318.89+402258.6	0.41864	0.00251	13.57149	0.22016	1.51078	0.02222
J105525.26+154433.8	0.06877	0.00082	4.52914	0.22645	1.81859	0.06200	J162420.69+514639.6	0.04975	0.00049	1.50090	0.16319	1.47954	0.11873
J105642.50+242751.6	0.09101	0.00112	3.68932	0.23705	1.60784	0.07665	J162539.37+295149.5	0.10340	0.00091	5.16467	0.23162	1.69848	0.05364
J105704.82+602405.1	0.11994	0.00119	5.41017	0.22731	1.65424	0.05201	J162542.15+411841.0	0.09222	0.00062	102.53646	0.47194	3.04603	0.01140
J105939.03+205721.8	0.06961	0.00058	174.53395	0.18409	3.39917	0.00945	J163345.22+512748.4	0.32776	0.00209	10.58151	0.19558	1.50899	0.02488
J105957.21+274150.7	0.14037	0.00106	1.24577	0.17464	0.94815	0.14778	J163600.37+432802.7	0.63198	0.00429	3.06926	0.20991	0.68633	0.07519
J110145.37+460236.2	0.37283	0.00357	1.58166	0.15704	0.62759	0.10889	J163709.31+414030.8	0.76423	0.00336	10.90673	0.23329	1.15446	0.02578
J110158.16+120531.1	0.08518	0.00088	1.77541	0.15575	1.31896	0.09813	J164027.47+113339.3	0.06462	0.00043	1.80241	0.18701	1.44542	0.11055
J110505.47+251527.3	0.06446	0.00069	3.10665	0.18079	1.68296	0.06899	J164517.20+485540.2	0.31713	0.00215	1.71981	0.15456	0.73423	0.09667
J110550.53+112702.0	0.01353	0.00027	2.77507	0.15794	2.31189	0.07731	J165050.82+503735.2	0.17428	0.00146	10.82901	0.22797	1.79332	0.02945
J110648.32+480712.3	0.11277	0.00099	12.91425	0.17897	2.05887	0.02265	J170300.48+410835.8	0.09802	0.0007	2.18897	0.20482	1.34890	0.10077
J110748.61+414539.4	0.20021	0.0024	54.59568	0.21710	2.43565	0.01597	J170617.47+280101.7	0.14703	0.00094	1.58699	0.17721	1.03315	0.11806
J111432.14+632755.7	0.08277	0.00072	2.33774	0.21546	1.45088	0.10096	J170705.33+425824.8	0.17521	0.00098	1.83064	0.18994	1.01902	0.10935
J111438.89+324133.5	0.10742	0.00081	119.63453	0.13421	3.04676	0.00872	J171145.75+350927.7	0.04320	0.00043	3.70857	0.15876	1.93369	0.05281
J111504.22+251100.3	0.63765	0.0051	3.63029	0.21459	0.75535	0.06711	J171202.78+441337.0	0.13421	0.00102	210.69078	0.22973	3.19584	0.00869
J111628.00+434505.8	0.48398	0.00309	10.56580	0.20225	1.33907	0.02554	J171749.62+253908.7	0.10929	0.00052	1.62777	0.20045	1.17299	0.12794
J111706.25+201407.3	0.65723	0.00657	113.12662	0.16201	2.23584	0.01143	J172354.30+374841.3	0.73431	0.00234	2.57835	0.22579	0.54546	0.09077
J111807.92+592844.1	0.07527	0.00054	7.58417	0.17666	2.00324	0.03049	J172414.19+330303.9	0.02737	0.00032	499.86469	0.14664	4.26157	0.01229
J111908.67+211917.9	7.6073	0.04868	5.37583	0.15007	-0.1507	0.03431	J172517.49+302640.8	0.17210	0.00275	181.56951	0.22105	3.02324	0.01721
J111930.31+222649.3	0.33838	0.00189	115.77468	0.18788	2.53420	0.00722	J210722.65+064647.2	0.07080	0.00051	1.61051	0.17776	1.35687	0.11757
J111952.42+165656.8	0.12954	0.00093	107.81998	0.22512	2.92027	0.00928	J211817.39+001316.7	0.19810	0.00118	124.61608	0.17097	2.79868	0.00737
J112155.78-002852.0	0.09328	0.00082	87.63253	0.21741	2.97284	0.01128	J212229.80+043136.6	0.10648	0.00098	2.58281	0.15078	1.38481	0.06758
J112529.14+224329.8	0.20119	0.00217	42.11615	0.15931	2.32082	0.01458	J212838.52-030310.2	0.15907	0.00095	6.05681	0.58393	1.58063	0.10241
J112736.52+055532.0	0.04556	0.00052	317.40805	0.22533	3.84301	0.01230	J213613.74+005825.9	0.07511	0.00057	7.76332	0.54356	2.01434	0.07761
J112825.60+402440.0	0.07089	0.00039	2.55770	0.17397	1.55723	0.07362	J213813.74-015107.3	0.24965	0.00159	48.17147	0.24021	2.28545	0.01138
J112828.75+174637.2	0.03982	0.00047	2.30755	0.16878	1.76301	0.08514	J215712.85+101424.8	0.09046	0.00076	445.74324	0.38342	3.69259	0.00926
J112847.12+564659.1	0.05378	0.0006	56.74599	0.21945	3.02330	0.01506	J221425.97-024134.1	0.08255	0.00076	4.08543	0.22492	1.69448	0.06425
J112955.79+552706.3	0.10465	0.00087	2.19211	0.24500	1.32111	0.12016	J225243.74+061850.8	0.07815	0.00084	160.12898	0.19025	3.31149	0.01198
J113020.40+422204.2	0.25272	0.00161	3.25552	0.21217	1.10996	0.07157	J225452.22+004631.3	0.61496	0.00516	1.11587	0.11796	0.25876	0.11411
J113029.48+634620.7	0.16500	0.00085	7.61745	0.19017	1.66431	0.03016	J225954.06+120135.7	0.20579	0.00205	174.83985	0.21520	2.92920	0.01123
J113128.00+484333.3	0.08488	0.00061	3.17711	0.18279	1.57321	0.06473	J230107.97-015804.6	0.13087	0.00099	381.27221	0.20639	3.46439	0.00814
J113427.80+414722.0	0.38936	0.0028	5.07788	0.22804	1.11532	0.05211	J230815.61+124125.9	0.12133	0.00121	11.77187	0.23139	1.98684	0.02965
J113439.09+622012.1	0.05639	0.00051	2.16479	0.20054	1.58416	0.10183	J230900.14+060226.5	0.02806	0.0004	2.93265	0.15692	2.01910	0.06790
J113603.62+632744.2	0.07903	0.00063	27.18916	0.23571	2.53657	0.01666	J232143.44+101803.9	0.10097	0.00133	3.91892	0.22968	1.58893	0.07180
J114054.82+625924.9	0.11819	0.00108	173.21177	0.22702	3.16596	0.01051	J232447.59+065314.0	0.09657	0.00092	3.45902	0.17036	1.55410	0.05885
J114201.83+603030.4	0.09543	0.00148	1.46038	0.21613	1.18477	0.16360	J232714.61+103033.9	0.09036	0.00101	1.66642	0.17714	1.26577	0.11749
J114249.75+082330.6	0.07132	0.00062	9.32843	0.22105	2.11657	0.03249	J233038.17+021450.5	0.16414	0.00124	52.27988	0.15363	2.50311	0.01053
J114339.53+205921.1	0.13687	0.00087	3.19714	0.21314	1.36842	0.07306	J233419.71-012824.8	0.20734	0.00165	4.90103	0.19995	1.37359	0.04879
J114710.22+250935.9	0.08536	0.00081	10.25745	0.16278	2.07976	0.02546	J234516.00+103936.3	0.11071	0.00097	3.70195	0.23944	1.52424	0.07348
J114746.20+622214.5	0.05506	0.00039	7.90789	0.18798	2.15720	0.03097	J234724.32-031430.6	0.13325	0.00127	6.92804	0.57915	1.71593	0.09319
J114749.80+492806.8	0.03043	0.00052	95.49398	0.22160	3.49655	0.01952	J235931.81-063943.4	0.34969	0.00223	97.47542	0.45246	2.44520	0.01104

Table A.11: FRII_{nc} sample and R_K parameter associated. Same notation of table A.7.

$\mathbf{FRII}_{nc}$ **AGN**						
SDSS ID	F_b	ΔF_b	F_{tot}	ΔF_{tot}	$logR_K$	$\Delta logR_K$
J000033.05+114049.6	0.09210	0.00073	10.25	0.291	2.04645	0.03639
J000929.11+074123.1	0.09236	0.00059	2.79	0.256	1.48007	0.09815
J003419.07+012000.4	0.06942	0.00072	154.36	0.268	3.34703	0.01213
J004947.04-024231.3	0.07300	0.00067	3.34	0.188	1.66040	0.06548
J014022.68+075357.0	0.17614	0.00126	49.22	0.225	2.44626	0.01177
J081703.10+162259.7	0.11066	0.00084	26.93	0.287	2.38622	0.01825
J081735.07+223717.7	0.47021	0.00282	296.54	0.313	2.79978	0.00705
J082133.86+425021.5	0.04739	0.00045	12.54	0.265	2.42259	0.03073
J082656.05+434333.0	0.10260	0.00069	36.05	0.287	2.54573	0.01476
J083144.49+451043.4	0.09733	0.00081	10.59	0.266	2.03664	0.03351
J084312.42+612943.8	0.58412	0.00257	451.64	0.334	2.88828	0.00513
J085234.22+421527.1	0.10337	0.00078	319.31	0.302	3.48980	0.00854
J085443.91+181156.0	0.09710	0.00077	29.93	0.292	2.48888	0.01775
J090240.95+483746.9	0.05068	0.00044	8.15	0.267	2.20623	0.04156
J090410.87+641012.0	0.09255	0.00077	20.28	0.28	2.34065	0.02220
J091011.14+542723.5	0.63893	0.00638	77.97	0.305	2.08647	0.01391
J091354.35+224843.3	0.13248	0.00137	8.48	0.286	1.80621	0.04412
J091634.67+195952.7	0.08130	0.00172	30.35	0.264	2.57203	0.02989
J092045.46+492721.6	0.07753	0.00086	5.81	0.296	1.87467	0.06214
J092433.48+365248.3	0.97732	0.00742	2.15	0.302	0.34240	0.14806
J092733.50+023449.3	0.05776	0.00057	22.1	0.293	2.58273	0.02325
J092953.43-013831.5	0.16109	0.00103	2.46	0.273	1.18385	0.11737
J093459.01-021909.8	0.22043	0.00149	199.06	0.311	2.95570	0.00836
J094647.39+193201.7	0.10957	0.00074	3.3	0.264	1.47880	0.08679
J095414.56+385503.9	0.12509	0.00115	20.12	0.302	2.20638	0.02420
J100620.50+543827.2	0.08944	0.00057	3.89	0.304	1.63839	0.08454
J101235.69-010823.2	0.11826	0.00113	19.23	0.292	2.21112	0.02478
J102734.02+135108.1	0.09531	0.00106	167.94	0.296	3.24601	0.01296
J103057.52+275602.3	0.20074	0.00200	484.54	0.298	3.38269	0.01061
J103354.28+501228.7	0.08734	0.00111	4.09	0.635	1.67049	0.16805
J103456.06+391042.9	0.06416	0.00056	12.7	0.292	2.29648	0.03179
J103932.15+263244.5	0.13483	0.00145	15.76	0.273	2.06775	0.02812
J105220.30+454322.2	0.09989	0.00115	3.33	0.282	1.52291	0.09628
J110837.66+385842.2	0.06210	0.00052	31.79	0.309	2.70916	0.01812
J111805.03+490218.8	0.07221	0.00063	4.23	0.259	1.76768	0.07002
J112412.22+432549.9	0.08491	0.00105	55.43	0.264	2.81475	0.01716
J112727.48+311039.1	0.03408	0.00038	3.11	0.212	1.96025	0.07936
J112821.95+373137.9	0.08842	0.00120	14.44	0.295	2.21299	0.03402
J113823.70+252232.8	0.10801	0.00116	26.08	0.294	2.38282	0.02207
J114707.57+503053.4	0.07541	0.00075	51.17	0.282	2.83155	0.01551
J114847.83+105458.4	0.51197	0.00430	128.25	0.299	2.39880	0.01073
J115322.71+402622.8	0.24168	0.00193	3.17	0.416	1.11780	0.13923
J115825.22+113923.6	0.12832	0.00133	3.87	0.276	1.47941	0.08171
J121550.42+162649.0	0.07521	0.00165	54.25	0.297	2.85809	0.02747
J121628.03+035031.8	0.11164	0.00080	4.93	0.487	1.64499	0.10598
J122512.28+192720.9	0.11899	0.00152	21.94	0.277	2.26572	0.02542
J122521.37+033945.2	0.03375	0.00043	249.28	0.486	3.86839	0.01474
J122851.74+584444.2	0.12193	0.00097	8.77	0.307	1.85685	0.04300
J122921.46+520100.7	0.12677	0.00131	13.45	0.278	2.02567	0.03106
J123301.65+152457.9	0.07331	0.00343	4.82	0.374	1.81787	0.12439
J123455.23+573242.2	0.07524	0.00078	25.99	0.289	2.53834	0.02151
J124044.68+330349.8	0.65565	0.00603	42.89	0.268	1.81568	0.01544
J130543.00+334919.0	0.04873	0.00050	2.82	0.295	1.76238	0.11500
J130619.22+363150.4	0.06359	0.00053	27.05	0.278	2.62872	0.01867
J130952.28+494452.9	0.07152	0.00082	4.2	0.271	1.76876	0.07612
J132222.67+464535.2	0.52905	0.00275	2.40	0.291	0.65671	0.12645
J132942.49+454000.2	0.12586	0.00100	202.13	0.266	3.20570	0.00931
J134014.81+375201.1	0.09204	0.00084	2.2	0.268	1.37843	0.13101
J135651.49+554635.5	0.11518	0.00096	18.77	0.288	2.21205	0.02374
J135850.03+390413.4	0.68191	0.00463	285.13	0.481	2.62131	0.00848
J140227.27+520432.1	0.07600	0.00079	169.94	0.294	3.34944	0.01213
J142304.14+524630.3	0.19464	0.00163	2.22	0.27	1.05711	0.13002
J143744.19+285533.6	0.07183	0.00068	69.38	0.3	2.98490	0.01392
J143921.69+414923.5	0.28392	0.00193	19.77	0.269	1.84280	0.02040
J144811.15+142249.0	0.06983	0.00053	17.28	0.272	2.39346	0.02334
J151138.76+525154.4	0.10675	0.00140	3.26	0.287	1.48482	0.10123
J151427.97+323135.1	0.09565	0.00076	54.71	0.28	2.75734	0.01311
J152129.25+151255.8	0.07596	0.00060	5.14	0.375	1.83032	0.08095
J152834.45+472756.1	0.10321	0.00082	3.51	0.29	1.53155	0.09062
J152933.03+601552.5	0.15909	0.00114	2.69	0.285	1.22810	0.11314
J153308.88+074429.6	0.05878	0.00042	5.31	0.278	1.95582	0.05955
J153338.90+080821.8	0.07268	0.00052	50.58	0.305	2.84256	0.01323
J153533.22+491337.3	0.08474	0.00054	10.01	0.267	2.07230	0.03307
J155025.22+480723.0	0.08368	0.00080	4.44	0.276	1.72475	0.07176
J155127.31+481050.8	0.11096	0.00097	4.12	0.279	1.56972	0.07651
J160121.25+424548.1	0.07051	0.00067	17.63	0.296	2.39797	0.02638
J160902.41+610944.7	0.09428	0.00067	27.79	0.295	2.46946	0.01781
J161734.65+141132.2	0.09751	0.00085	224.57	0.31	3.36227	0.01018
J162951.87+150819.4	0.03963	0.00047	41.92	0.302	3.02435	0.01920
J163717.59+234258.6	0.16953	0.00108	268.36	0.287	3.19946	0.00746
J165105.17+503140.3	0.14746	0.00129	28.89	0.278	2.29207	0.01842
J170129.83+224553.6	0.08338	0.00056	6.2	0.272	1.87128	0.05067
J170224.93+374019.1	0.07705	0.00058	4.1	0.27	1.72597	0.07345
J170316.25+251215.1	0.17255	0.00138	45.23	0.267	2.41850	0.01390
J171716.38+382801.0	0.02451	0.00060	8.05	0.28	2.51644	0.05958
J173016.04+351237.6	0.08877	0.00049	62.89	0.290	2.85029	0.01021
J212939.40-000719.7	0.09672	0.00065	222.43	0.212	3.36166	0.00775
J213042.16+054927.6	0.13985	0.00083	71.88	0.209	2.71094	0.00890
J221719.98+011016.5	0.04627	0.00049	5.24	0.292	2.05394	0.06652
J222521.55+085613.9	0.08568	0.00068	16.65	0.213	2.28850	0.02079
J231007.94-030631.7	0.09073	0.00094	16.12	0.286	2.24960	0.02814
J235915.66+020654.5	0.07911	0.00066	217.09	0.222	3.43835	0.00942

Table A.12: FRII sample and kellerman parameter associated. Same notation of table A.7.

FRII AGN								
SDSS ID	F_b	ΔF_b	F_1	ΔF_1	F_{tot}	ΔF_{tot}	$logR_K$	$\Delta logR_K$
J021008.48+011839.6	0.24816	0.00287	10.41186	0.23360	12.43186	0.53560	1.69979	0.05468
J100943.55+052953.8	0.81857	0.00523	39.93307	0.24510	42.54307	0.55310	1.71577	0.01940
J103848.12+372924.5	0.61123	0.00391	25.63764	0.20105	28.44764	0.47405	1.66783	0.02306
J110436.33+212417.8	0.53446	0.00320	12.45268	0.15678	23.63268	0.43378	1.64559	0.02435
J111506.83+302618.3	0.29878	0.00227	5.16675	0.22892	13.35675	0.51792	1.65033	0.04637
J124145.80+262226.7	0.17423	0.00104	1.77294	0.21423	10.71294	0.50823	1.78876	0.05344
J132029.67+491647.1	0.12686	0.00091	2.26164	0.19879	4.83164	0.47379	1.58074	0.10526
J135335.92+263147.5	0.84885	0.00713	26.97037	0.16532	37.31037	0.44032	1.64299	0.02020
J150532.63+202810.1	0.12122	0.00087	3.68220	0.22153	6.81220	0.51853	1.74968	0.08331
J153036.32+235236.7	1.04186	0.00625	30.79228	0.42687	36.53228	0.95987	1.54486	0.03227
J224001.10-031601.6	0.26671	0.00224	3.02462	0.20832	5.45462	0.47932	1.31072	0.09627
J001209.85+090249.3	0.17248	0.00131	6.84746	0.16554	16.09746	0.38354	1.97001	0.03142
J001741.45+082755.7	0.16020	0.00140	46.22851	0.18537	57.39851	0.44337	2.55421	0.01652
J010255.68+103702.9	0.16815	0.00188	8.00936	0.23603	29.08936	0.53703	2.23802	0.02966
J012141.59+114950.4	0.07155	0.00080	1643.33110	1.06611	1655.74110	2.62411	4.36438	0.01278
J014239.99+073239.4	0.09199	0.00091	5.73381	0.20264	23.88381	0.46064	2.41432	0.02928
J015635.70+014816.1	0.09821	0.00082	7.51586	0.13145	25.38586	0.30045	2.41242	0.02023
J020714.36+011806.3	0.14057	0.00118	6.13190	0.24624	71.06190	0.55224	2.70374	0.01617
J023322.16-045506.8	0.80350	0.01671	125.60914	0.21863	166.60914	0.51163	2.31670	0.02387
J024500.70-074736.4	0.07817	0.00078	1.76249	0.21992	13.22249	0.50092	2.22823	0.04788
J025509.76+025345.6	0.12793	0.00117	894.88357	0.36257	900.31357	0.87257	3.84739	0.01016
J075244.19+455657.4	0.52975	0.00275	42.00982	0.13464	56.35982	0.39664	2.02689	0.01223
J081336.06+481302.6	0.35414	0.00198	11949.67226	1.83220	11982.56226	4.19120	4.52936	0.00594
J081646.06+401324.8	0.05418	0.00049	4.25663	0.24024	8.03663	0.53724	2.17118	0.07604
J082014.21+154519.3	0.52271	0.00334	27.774	0.23715	91.524	0.53515	2.24326	0.01224
J083052.08+241059.8	0.72109	0.00634	1328.93856	0.23541	1332.12856	0.53241	3.26655	0.00919
J083133.06+163023.4	0.05385	0.00043	99.44174	0.21101	105.51174	0.48101	3.29209	0.01255
J085556.18+371342.5	0.15452	0.00587	19.40329	0.20830	42.68329	0.49530	2.44126	0.04960
J085820.33+461722.1	0.11274	0.00225	3.35282	0.22619	12.02282	0.50819	2.02791	0.06226
J091751.28+115258.9	0.04371	0.00059	1.74983	0.18709	9.81983	0.46509	2.35142	0.06096
J092351.52+281525.1	0.11313	0.00122	250.36799	0.21554	305.90799	0.50654	3.43198	0.01245
J093301.58+495029.9	0.24813	0.00297	13.44581	0.18748	18.36581	0.45548	1.86932	0.03680
J093348.07+511405.6	0.33637	0.00336	4.88230	0.19254	49.31230	0.47154	2.16613	0.01956
J094203.33+593709.5	0.02197	0.00032	23.80334	0.19982	29.18334	0.49582	3.12312	0.03178
J094558.42+135650.8	0.17534	0.00175	7.43135	0.20703	20.68135	0.50903	2.07168	0.03461
J094645.73-014049.4	0.12506	0.00090	44.63481	0.22310	61.45481	0.52610	2.69140	0.01576
J095649.88+251516.0	0.38859	0.00202	1515.11539	0.25015	1518.94539	0.59415	3.59204	0.00559
J102059.85+520918.2	0.10113	0.00121	2.06067	0.21818	6.71067	0.50518	1.82186	0.08728
J102106.04+452331.8	0.24032	0.00182	48.97651	0.18019	54.66651	0.47119	2.35691	0.01621
J103024.95+551622.7	0.75402	0.00754	14.67785	0.17896	106.90785	0.45596	2.15162	0.01426
J103822.46+134657.3	0.54614	0.00305	72.68555	0.24387	77.03555	0.54887	2.14938	0.01272
J105829.60+013358.8	0.29187	0.00175	5180.18769	1.28013	5250.26769	2.91813	4.25498	0.00655
J110655.96+624800.1	0.24011	0.00201	10.26654	0.23633	20.00654	0.54333	1.92074	0.03555
J112946.01-012140.5	0.50818	0.00426	10.02424	0.20517	206.72424	0.48617	2.60936	0.01075
J112956.02+402514.4	0.04622	0.00059	3.38495	0.23457	20.29495	0.54857	2.64254	0.03982
J114603.76+334551.9	0.06799	0.00065	4.54735	0.21102	43.92735	0.49602	2.81027	0.02089
J114803.17+565411.6	0.39563	0.00253	31.46271	0.19729	34.74271	0.50129	1.94357	0.02082
J115159.93+495056.1	0.23128	0.00268	5.98292	0.22806	37.13292	0.51906	2.20561	0.02557
J115318.07+234113.5	0.07706	0.00061	3.01112	0.23473	7.85112	0.52473	2.00809	0.07483
J120951.76+181006.8	0.16375	0.00111	96.24257	0.21800	102.59257	0.50500	2.79692	0.01172
J122106.86+454852.1	0.73908	0.00650	28.83338	0.20153	95.34338	0.50153	2.11059	0.01406
J124012.46+533437.2	0.02620	0.00035	5.28986	0.17952	11.67986	0.47952	2.64898	0.05465
J125542.55+311048.5	0.13436	0.00139	6.24370	0.16722	9.42370	0.44422	1.84591	0.05753
J130554.16+014929.9	0.53954	0.00647	60.93038	0.22485	176.74038	0.52985	2.51530	0.01499
J132512.19+511933.3	0.12917	0.00160	13.52067	0.19529	36.30067	0.45529	2.44873	0.02494
J134751.58+283629.7	0.54413	0.06899	51.54404	0.23141	151.28404	0.54541	2.44408	0.13040
J140232.37+461233.6	0.07276	0.00066	10.67691	0.17726	34.80691	0.43726	2.67975	0.02176
J140626.60+250921.0	1.04759	0.00628	104.48939	0.21052	135.69939	0.48352	2.11238	0.00956
J142242.49+041439.1	0.68319	0.00519	107.29429	0.23167	175.80429	0.52067	2.41048	0.01056
J142457.80+124749.5	0.11160	0.00089	5.94190	0.22244	12.10190	0.52044	2.03518	0.05100
J145359.73+091543.3	0.11936	0.00081	140.26873	0.16990	142.68873	0.45890	3.07750	0.01001
J153057.78+102216.0	0.05819	0.00058	1.73385	0.19702	41.77385	0.49702	2.85603	0.02189
J160226.89+274141.9	0.42368	0.00288	25.19558	0.23511	114.23558	0.53111	2.43075	0.01144
J160303.65+385143.9	0.01450	0.00030	10.11204	0.18558	33.65204	0.49758	3.36556	0.03598
J163745.13+471733.8	0.10754	0.00068	885.20175	0.23093	1061.78175	0.54493	3.99442	0.00691
J164504.76+180623.9	0.11538	0.00096	7.30256	0.15912	23.01256	0.38412	2.29982	0.02509
J170634.12+361508.0	0.35050	0.00266	29.72896	0.22079	34.43896	0.50079	1.99235	0.02214
J170726.31+334513.5	0.09662	0.00181	8.80106	0.19714	23.68106	0.47714	2.38931	0.03894
J172109.49+354216.0	0.25086	0.00200	460.23693	0.29530	492.90693	0.78830	3.29331	0.00959
J213004.76-010244.4	0.34398	0.00316	53.71324	0.22077	209.83324	0.52477	2.78533	0.01170
J213344.19-015716.4	0.10432	0.00070	6.19373	0.39881	29.07373	0.92481	2.44510	0.03860
J213552.50+011815.7	0.08442	0.00084	1251.46564	0.20958	1253.66564	0.48858	4.17172	0.01038
J221428.08-032349.1	0.18656	0.00149	14.04388	0.32902	19.93388	0.79702	2.02875	0.04798
J223458.73-022419.0	0.21714	0.00182	8.91301	0.20380	14.00301	0.50880	1.80947	0.04473
J235451.67-040503.4	0.29786	0.00285	445.90906	0.26330	450.69906	0.62230	3.17987	0.01098
J235737.96+003227.8	0.13391	0.00085	2.12544	0.17099	30.59544	0.38699	2.35883	0.01904

Table A.13: Intermediate CD$_j$ AGN R$_{FeII}$ and Hβ FWHM measures.

intermediate CD$_j$ AGN					
SDSS ID	**Plate**	**MJD**	**Fiber**	**FWHM(Hβ)** (Å)	R_{FeII} (km/s)
J111006.79+405000.7	4620	55652	0232	3290.8	~ 0
J153934.80+473531.2	6729	56419	0258	6097.0	~ 0
J102329.79+441414.2	4692	55644	0150	8461.5	~ 0
J095427.81+301912.9	5800	56279	0568	11316.9	~ 0
J014540.95+073217.2	4532	55559	0334	6450.9	0.524

Table A.14: Loud CD$_j$ AGN R$_{FeII}$ and Hβ FWHM measures.

Loud CD$_j$ AGN					
SDSS ID	**Plate**	**MJD**	**Fiber**	**FWHM(Hβ)** (km/s)	R_{FeII}
J083928.53+260614.3	4460	55533	0994	4035.8	~ 0
J014756.74+124912.5	4659	55587	0588	5442.0	~ 0
J095753.84+121606.7	5323	55957	0026	4458.9	~ 0
J095637.65+155125.0	5326	56002	0348	4515.6	~ 0
J111018.12+104619.5	5361	55973	0970	6198.1	~ 0
J124557.17+215616.1	5988	56072	0618	5583.2	~ 0
J170717.75+453610.5	6025	56098	0118	4334.3	~ 0
J141159.73+423950.3	6059	56093	0592	7006.0	~ 0
J162637.91+523804.5	6313	56460	0835	7308.2	~ 0
J115324.46+493108.7	6677	56385	0646	4151.8	~ 0
J141238.66+484447.1	6746	56386	0142	5320.5	~ 0
J005327.77-065651.2	7155	56629	0845	5911.9	~ 0
J020514.77-045639.7	7238	56660	0724	4590.9	~ 0
J082753.69+521758.6	7301	56746	0032	4449.7	~ 0
J150725.62+112635.6	5485	56063	0680	11773.3	0.391
J153145.14+431933.8	6041	56102	0406	12895.8	0.202
J152039.69+421111.1	5164	56067	0766	19550.3	~ 0

Table A.15: Detected CD AGN R$_{FeII}$ and Hβ FWHM measures.

Detected CD AGN					
SDSS ID	**Plate**	**MJD**	**Fiber**	**FWHM(Hβ)** (km/s)	R_{FeII}
J143157.94+341650.2	3860	55269	0264	3683.1	~ 0
J082456.93+215539.4	4483	55587	0702	3021.9	~ 0
J101425.63+031434.5	4801	55653	0170	2740.1	~ 0
J132201.35+495835.0	6754	56414	0840	2185.6	~ 0
J225452.22+004631.3	4206	55471	0864	1827.9	0.764
J123252.70+414322.4	4702	55618	0532	2769.1	0.851
J092725.19+043851.5	4796	55924	0318	2371.9	0.769
J120734.62+150643.7	5392	56010	0480	2933.1	0.875
J093601.69+193850.2	5766	56248	0732	1483.8	0.533
J162052.59+540058.6	6309	56485	0308	1971.6	0.533
J111908.67+211917.9	6430	56299	0516	3639.3	0.545
J105957.21+274150.7	6446	56363	0113	1290.1	0.957
J145559.45+492152.8	6726	56394	0296	1428.3	0.944
J161240.38+582255.7	6786	56448	0958	3559.7	0.581
J094033.75+462315.0	7316	56710	0846	2611.2	0.961
J124511.25+335610.1	3971	55322	0210	3446.9	1.281
J132146.53+265150.1	5997	56309	0138	2770.3	1.157
J130631.63+435100.4	6621	56366	0274	2381.1	1.107
J104011.18+452125.9	7391	56781	0396	2854.8	1.281
J095633.93+562216.0	5743	56011	0868	3149.6	1.951
J012209.02+102020.0	4552	55884	0522	5188.5	~ 0
J172354.30+374841.3	4990	55743	0110	7456.2	~ 0
J104708.07+144557.7	5350	56009	0896	5429.6	~ 0
J142129.75+474724.5	6751	56368	0946	6315.3	~ 0
J132052.19+574737.3	6829	56453	0524	7906.4	~ 0
J120751.79+604706.9	6972	56426	0340	5329.7	~ 0
J142818.55+525826.9	7032	56471	0780	5831.7	~ 0
J010352.47+003739.7	4226	55475	0600	11119.6	~ 0
J123338.65+422238.3	4705	55705	0106	9435.9	~ 0
J115504.07+034850.3	4765	55674	0112	6759.3	~ 0
J121413.55+052254.3	4832	55680	0464	9139.9	~ 0
J142852.82+271042.5	6018	56067	0338	8732.8	~ 0
J101931.79+262643.2	6465	56279	0824	9405.1	~ 0
J023859.18-000158.1	6782	56572	0559	8523.2	~ 0
J093509.47+481910.6	7298	56661	0415	9528.4	~ 0
J123820.19+175039.1	5854	56035	0732	7659.7	0.522
J111504.22+251100.3	6413	56336	0184	5726.9	0.545
J083525.97+435211.2	4683	55924	0683	5571.5	1.231

Table A.16: Intemediate CD AGN R_{FeII} and Hβ FWHM measures

Intermediate CD AGN											
SDSS ID	**Plate**	**MJD**	**Fiber**	**FWHM(Hβ)** (km/s)	R_{FeII}	**SDSS ID**	**Plate**	**MJD**	**Fiber**	**FWHM(Hβ)** (km/s)	R_{FeII}
J133939.61+033109.8	4786	55651	0296	3285.3	~ 0	J090745.28+532421.4	5728	56334	0162	7499.4	~ 0
J081209.24+560038.1	5149	55944	0294	3406.8	~ 0	J090858.81+472617.2	5736	55984	0794	5596.2	~ 0
J083431.37+582425.7	5152	56010	0972	1567.1	~ 0	J100458.31+202449.2	5784	56029	0050	7709.1	~ 0
J090508.17+523527.5	5155	55946	0996	2995.4	~ 0	J232714.61+103033.9	6156	56239	0230	4589.0	~ 0
J100603.11+195917.4	5882	56029	0844	2107.9	~ 0	J165050.82+503735.2	6311	56447	0180	4425.6	~ 0
J102755.32+180923.5	5884	56046	0180	3875.5	~ 0	J110505.47+251527.3	6412	56358	0173	4832.6	~ 0
J112828.75+174637.2	5890	56037	0850	4089.5	~ 0	J132644.96+434804.5	6622	56365	0680	5772.5	~ 0
J024706.65+002318.1	6782	56273	0979	4640.2	~ 0	J120713.48+470259.8	6641	56383	0748	7813.9	~ 0
J155237.42+613644.3	6802	56456	0780	4317.1	~ 0	J001932.63-070302.6	7150	56597	0812	6103.7	~ 0
J120329.85+480313.6	7426	56771	0652	4035.8	~ 0	J121113.97+464711.9	7426	56771	0550	4009.3	~ 0
J105458.86-023947.2	3772	55277	0167	1536.8	0.843	J074140.45+365544.6	3662	55182	0966	11915.2	~ 0
J232447.59+065314.0	4408	55888	0746	1775.5	0.812	J075052.04+480345.6	3675	55183	0238	8800.7	~ 0
J143952.91+392358.9	5171	56038	0520	2381.8	0.627	J151616.84+274122.9	3851	55302	0438	8227.1	~ 0
J140050.61+092655.7	5447	55958	0872	1902.6	0.951	J140307.59+320320.5	3862	55276	0656	10564.5	~ 0
J133942.71+182955.2	5862	56045	0204	1917.4	0.838	J164027.47+113339.3	4075	55352	0132	9361.9	~ 0
J124009.12+242531.2	5984	56337	0242	3639.3	0.843	J010927.10-031714.4	4373	55811	0208	9522.3	~ 0
J135845.38+265808.4	6009	56313	0376	2090.7	0.705	J081425.89+294115.6	4447	55542	0326	8332.1	~ 0
J170705.33+425824.8	6062	56091	0371	3053.4	0.655	J003848.49+075059.6	4541	55882	0858	9435.9	~ 0
J103027.97+300114.1	6456	56339	0806	3647.3	0.511	J010717.05+074446.4	4550	55894	0900	8418.3	~ 0
J115917.31+283814.4	6475	56337	0502	3333.4	0.478	J102041.14+395811.2	4558	55569	0489	10058.8	~ 0
J130545.47+443328.4	6621	56366	0690	1687.3	0.730	J113427.80+414722.0	4699	55684	0144	9411.2	~ 0
J133749.32+594717.4	6810	56447	0814	2249.8	0.731	J152731.75+384307.7	4979	56045	0080	9442.1	~ 0
J085206.15+465050.5	7327	56715	0080	3446.9	0.587	J170617.47+280101.7	5013	55723	0031	9984.8	~ 0
J125745.32+480525.7	7416	56810	0968	3129.9	0.521	J133431.74+084748.8	5433	55981	0938	11946.0	~ 0
J071933.35+403253.0	3655	55240	0630	3552.3	1.241	J104002.56+210900.1	5874	56039	0770	8942.5	~ 0
J095150.49-025545.5	3768	55564	0378	2582.2	1.157	J135938.49+223207.4	6004	56066	0256	10120.5	~ 0
J024817.69+024128.4	4259	55501	0722	1310.5	1.255	J163709.31+414030.8	6036	56093	0220	8072.9	~ 0
J114915.30+393325.4	4654	55659	0080	1692.9	1.235	J162318.89+402258.6	6045	56072	0384	11212.1	~ 0
J171749.62+253908.7	5016	55709	0580	2028.4	1.428	J153110.33+430653.4	6049	56091	0936	9602.4	~ 0
J094248.08+112934.3	5316	55955	0864	1492.4	1.166	J162420.69+514639.6	6313	56460	0277	11477.3	~ 0
J121231.47+251429.1	5975	56334	0556	3446.9	1.104	J122243.19+293441.5	6474	56362	0498	9176.9	~ 0
J170300.48+410835.8	6063	56098	0802	3138.5	1.633	J135607.37+413615.3	6630	56358	0581	8011.3	~ 0
J163345.22+512748.4	6314	56191	0608	3632.5	1.238	J102222.61+495216.4	6658	56606	0748	12223.5	~ 0
J080037.62+461257.9	7379	56713	0536	2017.9	1.266	J100256.22+475027.7	6663	56338	0756	9281.7	~ 0
J141058.58+354040.2	3855	55268	0284	2057.4	1.782	J125235.36+471922.5	6666	56371	0072	9657.9	~ 0
J101952.59+073050.8	5339	55922	0365	1595.4	1.551	J103925.56+490951.2	6702	56381	0452	11187.4	~ 0
J114339.53+205921.1	6432	56309	0594	1903.2	1.611	J105451.63+553736.5	7094	56660	0092	10576.9	~ 0
J102818.15+535113.6	6696	56398	0118	1717.5	1.592	J111432.14+632755.7	7109	56658	0668	8868.5	~ 0
J120910.61+561109.2	6838	56429	0297	1643.5	1.909	J083354.46+565816.1	7374	56751	0666	9738.1	~ 0
J114201.83+603030.4	7107	56740	0172	2543.3	1.954	J074026.41+365534.4	3662	55182	0930	13648.2	~ 0
J081929.48+522345.2	3690	55182	0316	2381.8	2.089	J082149.22+245159.5	4461	55888	0300	15227.1	~ 0
J123640.35+563021.4	6832	56426	0650	2466.9	2.231	J113020.40+422204.2	4699	55684	0696	13105.5	~ 0
J082826.20+394436.8	3761	55272	0854	5969.3	~ 0	J085106.74+582656.5	5148	56220	0118	11822.7	~ 0
J102009.69-012758.7	3770	55234	0530	5113.9	~ 0	J102144.05+233738.6	6424	56272	0712	13950.4	~ 0
J212229.80+043136.6	4081	55365	0285	6210.4	~ 0	J125531.36+530912.9	6679	56401	0244	14018.2	~ 0
J013908.45+044911.7	4274	55508	0832	7388.4	~ 0	J113128.00+484333.3	6685	56412	0192	12198.9	~ 0
J013427.29-013350.3	4351	55538	0754	6802.5	~ 0	J003706.29-050111.3	7040	56574	0450	13993.6	~ 0
J233419.71-012824.8	4358	55833	0916	5326.0	~ 0	J105704.82+602405.1	7103	56661	0580	12365.4	~ 0
J212838.52-030310.2	4384	56105	0299	6833.3	~ 0	J154930.05+202207.5	3936	55302	0334	17953.1	~ 0
J020809.63-053839.1	4398	55946	0988	5765.8	~ 0	J113439.09+622012.1	7107	56740	0668	17219.1	~ 0
J002312.69+072455.4	4539	55865	0516	4753.7	~ 0	J155634.29+160021.1	3926	55327	0046	5686.8	0.594
J112825.60+402440.0	4651	56008	0260	4421.3	~ 0	J154351.92+162422.1	3932	55337	0246	5472.2	0.511
J011533.41+101456.5	4667	55868	0164	7813.9	~ 0	J155732.74+232838.2	3941	55321	0024	4415.7	0.636
J111628.00+434505.8	4686	56013	0594	4204.2	~ 0	J210722.65+064647.2	4079	55363	0422	5500.6	0.581
J130055.53+040551.8	4758	55682	0391	5229.8	~ 0	J000652.00+061509.2	4415	55831	0914	4484.2	0.673
J132401.53+032020.5	4761	55633	0136	4563.8	~ 0	J142525.17+060930.1	4861	55710	0058	4533.5	0.888
J160927.68+055138.3	4895	55708	0274	7419.2	~ 0	J160134.81+070959.0	4893	55709	0233	4693.3	0.666
J140549.53+393946.0	5169	56045	0454	7746.1	~ 0	J102152.49+131146.4	5338	56002	0748	7696.7	0.583
J141258.09+403216.4	5169	56045	0858	7672.1	~ 0	J232143.44+101803.9	6156	56239	0300	6784.1	0.508
J144815.81+390821.5	5172	56071	0168	4779.0	~ 0	J142548.09+523034.3	7032	56471	0275	6592.8	0.622
J161217.24+391103.2	5189	56074	0432	6144.4	~ 0	J105642.50+242751.6	6418	56354	0606	16725.7	0.625
J090245.60+111619.9	5296	55922	0786	7240.4	~ 0	J234724.32-031430.6	4356	55829	0178	5020.7	1.239
J102953.43+163739.2	5342	56003	0270	4423.1	~ 0	J083537.33+284712.9	4454	55536	0622	4070.4	1.331
J124251.69+101945.7	5406	55955	0994	7918.8	~ 0	J145736.70+523454.6	6719	56390	0072	4457.1	1.485
J125249.86+112933.1	5412	55981	0176	6543.5	~ 0						

Table A.17: Loud CD AGN R_{FeII} and Hβ FWHM measures.

Loud CD AGN					
SDSS ID	**Plate**	**MJD**	**Fiber**	**FWHM(Hβ)** (km/s)	R_{FeII}
J215712.85+101424.8	4095	55497	0854	2453.9	~ 0
J211817.39+001316.7	4192	55469	0694	1808.2	~ 0
J000804.16-012917.0	4365	55539	0670	2104.2	~ 0
J023313.12-033924.0	4386	55540	0718	3577.1	~ 0
J110748.61+414539.4	4620	55652	0688	2209.7	~ 0
J172517.49+302640.8	5002	55710	0366	3020.1	~ 0
J120531.10+144827.9	5387	56009	0028	2034.5	~ 0
J144356.89+250144.5	6022	56076	0322	2126.4	~ 0
J162542.15+411841.0	6045	56072	0732	3477.1	~ 0
J171202.78+441337.0	6062	56091	0886	3406.8	~ 0
J122118.00+465057.7	6640	56385	0813	1941.4	~ 0
J115727.60+431806.3	6642	56396	0248	3498.1	~ 0
J121834.44+484219.5	6671	56388	0376	1860.1	~ 0
J125239.59+464044.7	7416	56810	0250	2760.4	~ 0
J151923.50+271115.4	3851	55302	0262	2816.6	0.603
J233038.17+021450.5	4284	55863	0973	3105.2	0.803
J081347.53+534754.0	4529	55563	0276	4791.9	0.721
J225954.06+120135.7	5051	56214	0944	3023.8	0.782
J085943.79+155232.8	5295	55978	0759	3644.8	0.552
J105525.26+154433.8	5355	56009	0794	2629.1	0.901
J143813.72+214432.6	5904	56046	0567	2621.1	0.806
J122400.83+223615.1	5982	56074	0552	3563.4	0.655
J112529.14+224329.8	6421	56274	0468	1871.7	0.671
J135052.73+303453.5	6494	56363	0572	3406.8	0.525
J084744.55+442610.6	6783	56284	0938	3555.4	0.785
J010123.42+005013.3	3735	55209	0590	1477.1	1.391
J142549.19+394655.0	5170	56063	0106	2175.2	1.214
J103346.39+233220.0	6425	56298	0820	1674.4	1.208
J132819.23+442432.9	6627	56369	0434	2011.1	1.458
J083558.43+261444.4	4460	55533	0854	2532.2	1.884
J075813.13+524451.2	3682	55244	0330	6777.8	~ 0
J112155.78-002852.0	3838	55588	0021	6728.5	~ 0
J230107.97-015804.6	4362	55828	0816	5482.7	~ 0
J160839.47+253000.3	4724	55742	0082	6028.5	~ 0
J145941.18+071353.0	4857	55711	0962	6537.3	~ 0
J155121.13+071357.7	4877	55707	0666	6028.5	~ 0
J124205.41+111728.4	5409	55957	0299	7172.5	~ 0
J151112.73+163040.6	5484	56039	0120	4454.6	~ 0
J095738.18+552257.7	5743	56011	0160	3882.9	~ 0
J090512.95+233139.6	5776	56010	0860	5499.3	~ 0
J091542.24+251939.0	5777	56280	0316	6888.8	~ 0
J105939.03+205721.8	5876	56042	0839	5210.7	~ 0
J161603.77+463225.2	6323	56189	0066	4449.7	~ 0
J111930.31+222649.3	6420	56304	0254	6156.1	~ 0
J102011.66+281635.8	6463	56340	0586	7887.9	~ 0
J103045.22+255522.1	6464	56309	0878	5537.0	~ 0
J131933.02+550808.5	6760	56425	0992	7197.2	~ 0
J011239.13-032842.8	7045	56577	0704	4092.6	~ 0
J105232.73+612521.2	7096	56683	0930	7659.7	~ 0
J111807.92+592844.1	7108	56686	0310	6543.5	~ 0
J235931.81-063943.4	7147	56574	0802	4948.6	~ 0
J021640.73-044404.8	7236	56605	0538	5966.2	~ 0
J021705.52-042253.5	7236	56605	0530	7832.4	~ 0
J140843.78+540751.4	7339	56799	0543	5152.1	~ 0
J133245.23+472222.7	7406	56805	0234	4137.6	~ 0
J125239.59+464044.7	7416	56810	0250	6728.5	~ 0
J102834.03-023659.6	3785	55273	0424	8184.0	~ 0
J213613.74+005825.9	4195	55452	0566	10626.2	~ 0
J000727.89+055701.3	4415	55831	0934	8677.3	~ 0
J103246.80+391009.9	4633	55620	0422	11440.3	~ 0
J090712.21+091056.4	5299	55927	0729	8671.2	~ 0
J092708.11+143413.5	5310	55983	0336	8455.3	~ 0
J114249.75+082330.6	5377	55957	0876	10194.5	~ 0
J115228.57+080626.1	5382	55982	0198	8893.2	~ 0
J125627.23+120113.4	5419	55983	0520	11958.3	~ 0
J085726.27+484518.8	5735	55980	0610	9880.1	~ 0
J095746.55+474549.4	5739	55976	0104	8523.2	~ 0
J092058.62+232317.0	5774	56002	0480	11767.2	~ 0
J094804.86+270042.0	5795	56298	0060	9152.27	~ 0
J134300.17+284407.5	6003	56311	0944	10132.8	~ 0
J125701.71+281230.0	6480	56340	0940	7197.2	~ 0
J151548.25+472315.2	6734	56386	0780	10299.3	~ 0
J112847.12+564659.1	7092	56683	0560	11286.1	~ 0
J114746.20+622214.5	7106	56663	0440	10194.5	~ 0
J114054.82+625924.9	7113	56711	0100	10897.6	~ 0
J130630.53+462203.0	7414	56748	0730	8825.4	~ 0
J161350.30+041917.6	4807	55687	0934	17132.7	~ 0
J134251.35+260555.2	6002	56104	0740	14530.1	~ 0
J130016.42+602903.6	6967	56447	0416	15701.9	~ 0
J144800.47+023916.2	4018	55622	0680	7110.8	0.764
J073945.16+215636.1	4480	55591	0760	4980.1	0.718
J002554.26+083711.3	4539	55865	0582	3868.1	0.571
J013224.25+080103.1	4553	55584	0812	6549.6	0.527
J092551.85+361235.6	4576	55592	0440	6083.4	0.624
J110648.32+480712.3	7380	56753	0035	6167.3	0.722
J004428.66+090959.4	4542	55833	0118	8584.8	0.611
J230815.61+124125.9	6146	56265	0146	9158.4	0.744
J113603.62+632744.2	7113	56711	0234	10897.6	0.655
J022508.07+001707.2	6780	56267	0534	11674.6	0.527
J141911.28+351804.8	3859	55246	0700	4136.4	1.181

Table A.18: Intermediate FRII$_{nc}$ AGN R$_{FeII}$ and Hβ FWHM measures.

Intermediate FRII$_{nc}$ AGN					
SDSS ID	**Plate**	**MJD**	**Fiber**	**FWHM(Hβ)** (km/s)	R_{FeII}
J004947.04-024231.3	4371	55830	0428	2734.5	~ 0
J094647.39+193201.7	5783	56017	0812	3352.5	~ 0
J152933.03+601552.5	6799	56478	0608	2706.8	~ 0
J142304.14+524630.3	7339	56722	0023	3781.7	~ 0
J130543.00+334919.0	6488	56364	0874	3132.3	0.434
J151138.76+525154.4	6713	56402	0402	2866.5	0.512
J155025.22+480723.0	6730	56425	0602	3618.3	0.773
J130952.28+494452.9	6755	56413	0066	3038.0	0.864
J092953.43-013831.5	3767	55214	0530	4589.0	~ 0
J134014.81+375201.1	3987	55590	0778	7203.4	~ 0
J115825.22+113923.6	5388	55983	0606	5923.0	~ 0
J111805.03+490218.8	6692	56390	0150	5657.8	~ 0
J152834.45+472756.1	6735	56397	0656	5604.2	~ 0
J000929.11+074123.1	4533	55855	0646	9485.3	~ 0
J155127.31+481050.8	6730	56425	0648	7376.0	~ 0
J105220.30+454322.2	7391	56781	0017	11520.5	~ 0
J115322.71+402622.8	4697	55660	0610	7061.5	0.562
J100620.50+543827.2	7084	56624	0376	5326.6	0.932

Table A.19: Loud FRII$_{nc}$ AGN R$_{FeII}$ and Hβ FWHM measures

Loud FRII$_{nc}$ AGN					
SDSS ID	**Plate**	**MJD**	**Fiber**	**FWHM(Hβ)** (km/s)	R_{FeII}
J132942.49+454000.2	6627	56369	0632	2643.5	~ 0
J153533.22+491337.3	6729	56419	0632	2281.	~ 0
J123455.23+573242.2	6837	56442	0260	3398.1	~ 0
J101235.69-010823.2	3769	55240	0910	3516.5	0.717
J083144.49+451043.4	6395	56354	0389	2150.5	0.522
J140227.27+520432.1	6741	56394	0796	3868.7	0.801
J170129.83+224553.6	4178	55653	0952	3136.6	1.161
J221719.98+011016.5	4321	55504	0118	1435.1	1.487
J152129.25+151255.8	5491	56034	0736	3335.2	1.261
J161734.65+141132.2	4070	55681	0920	5310.0	~ 0
J170316.25+251215.1	4177	55688	0650	5748.5	~ 0
J163717.59+234258.6	4186	55691	0448	6158.6	~ 0
J235915.66+020654.5	4278	55505	0500	6660.6	~ 0
J081735.07+223717.7	4479	55592	0728	6457.1	~ 0
J014022.68+075357.0	4549	55556	0124	7283.5	~ 0
J095414.56+385503.9	4570	55623	0652	4598.3	~ 0
J112821.95+373137.9	4617	55617	0480	5232.9	~ 0
J135850.03+390413.4	4711	55737	0506	6463.3	~ 0
J092733.50+023449.3	4742	55660	0502	6222.8	~ 0
J153308.88+074429.6	5209	56002	0126	7271.2	~ 0
J085443.91+181156.0	5292	55926	0830	5393.9	~ 0
J102734.02+135108.1	5340	56011	0196	7295.9	~ 0
J084312.42+612943.8	5709	56571	0608	6265.9	~ 0
J090410.87+641012.0	5718	56693	0516	4437.3	~ 0
J091011.14+542723.5	5728	56334	0107	4946.7	~ 0
J091354.35+224843.3	5775	56009	0266	7252.7	~ 0
J121550.42+162649.0	5849	56033	0320	6734.6	~ 0
J122512.28+192720.9	5850	56042	0220	7314.4	~ 0
J082656.05+434333.0	6380	56340	0640	6142.6	~ 0
J113823.70+252232.8	6415	56310	0910	3435.1	~ 0
J112727.48+311039.1	6436	56363	0428	4754.3	~ 0
J103932.15+263244.5	6439	56358	0788	4896.2	~ 0
J103057.52+275602.3	6457	56330	0638	6198.1	~ 0
J124044.68+330349.8	6482	56358	0704	5611.6	~ 0
J122921.46+520100.7	6675	56415	0944	7191.1	~ 0
J114707.57+503053.4	6683	56416	0456	5718.3	~ 0
J093459.01-021909.8	3767	55214	0224	8221.01	~ 0
J162951.87+150819.4	4056	55357	0144	8153.1	~ 0
J213042.16+054927.6	4084	55447	0735	8147.1	~ 0
J003419.07+012000.4	4302	55531	0130	8325.8	~ 0
J085234.22+421527.1	4604	55983	0620	9960.1	~ 0
J110837.66+385842.2	4621	55649	0660	10404.2	~ 0
J222521.55+085613.9	5057	56209	0678	9109.1	~ 0
J153338.90+080821.8	5209	56002	0104	8072.9	~ 0
J123301.65+152457.9	5404	56013	0274	10509.1	~ 0
J165105.17+503140.3	6311	56447	0122	10040.3	~ 0
J122851.74+584444.2	6968	56443	0250	8732.8	~ 0
J090240.95+483746.9	7513	56780	0116	8134.7	~ 0
J212939.40-000719.7	4193	55476	0620	15294.9	~ 0
J081703.10+162259.7	4498	55615	0640	12982.1	~ 0
J151427.97+323135.1	4720	55691	0188	15134.5	~ 0
J122521.37+033945.2	4751	55646	0116	15510.7	~ 0
J173016.04+351237.6	4995	55739	0580	14289.6	~ 0
J091634.67+195952.7	5768	56017	0800	17730.9	~ 0
J143921.69+414923.5	6061	56076	0310	16170.6	~ 0
J115322.71+402622.8	4697	55660	0610	7043.0	0.536
J000033.05+114049.6	6182	56190	0693	9966.3	0.511

Table A.20: Intermiediate FRII AGN R_{FeII} and Hβ FWHM measures.

intermediate FRII AGN					
SDSS ID	**Plate**	**MJD**	**Fiber**	**FWHM(Hβ)** (km/s)	R_{FeII}
J021008.48+011839.6	4269	55502	0163	6845.7	~ 0
J103848.12+372924.5	4634	55626	0414	6247.4	~ 0
J100943.55+052953.8	4801	55653	0584	6888.8	~ 0
J124145.80+262226.7	5968	56356	0322	6376.9	~ 0
J110436.33+212417.8	6428	56279	0260	5564.1	0.2176
J150532.63+202810.1	3956	55656	0536	10379.5	~ 0
J224001.10-031601.6	4363	55537	0445	8412.1	~ 0
J135335.92+263147.5	6006	56105	0084	8436.8	~ 0
J132029.67+491647.1	6743	56385	0542	9238.6	~ 0
J111506.83+302618.3	6441	56364	0856	6161.7	0.8408

Table A.21: Loud FRII AGN R$_{FeII}$ and Hβ FWHM measures.

Loud FRII AGN					
SDSS ID	**Plate**	**MJD**	**Fiber**	**FWHM(Hβ)** (km/s)	**R**$_{FeII}$
J094645.73-014049.4	3782	55244	0896	2946.7	~ 0
J025509.76+025345.6	4257	55480	0728	3710.8	0.3280
J170634.12+361508.0	4988	55825	0856	3321.7	~ 0
J153057.78+102216.0	5493	56009	0063	3836.0	~ 0
J095649.88+251516.0	6467	56270	0466	3017.0	0.2176
J125542.55+311048.5	6485	56342	0082	3535.0	0.2635
J103024.95+551622.7	6696	56398	0931	2287.4	~ 0
J235451.67-040503.4	7033	56565	0791	3460.4	0.5159
J112946.01-012140.5	3789	55269	0712	7215.7	~ 0
J130554.16+014929.9	4007	55327	0496	6432.4	0.8408
J164504.76+180623.9	4062	55383	0080	6722.3	~ 0
J221428.08-032349.1	4378	55853	0284	6450.9	~ 0
J082014.21+154519.3	4498	55615	0820	4278.2	~ 0
J001741.45+082755.7	4538	55860	0485	6981.3	~ 0
J010255.68+103702.9	4547	55893	0871	4858.5	0.2176
J112956.02+402514.4	4655	55620	0397	6636.0	~ 0
J160226.89+274141.9	4724	55742	0622	5326.0	~ 0
J142242.49+041439.1	4782	55654	0008	4553.3	~ 0
J170726.31+334513.5	4993	55738	0736	4698.8	~ 0
J172109.49+354216.0	4994	55739	0945	4581.0	0.8408
J094558.42+135650.8	5320	55999	0404	5826.2	~ 0
J103822.46+134657.3	5345	56010	0135	5322.9	~ 0
J145359.73+091543.3	5476	55986	0848	4100.6	~ 0
J120951.76+181006.8	5848	56029	0442	4497.8	0.4770
J140626.60+250921.0	6008	56093	0144	7172.5	~ 0
J163745.13+471733.8	6318	56186	0415	5395.7	~ 0
J134751.58+283629.7	6493	56338	0086	5205.8	~ 0
J102059.85+520918.2	6668	56605	0830	6290.6	~ 0
J115159.93+495056.1	6677	56385	0586	6370.8	~ 0
J023322.16-045506.8	7235	56603	0078	4843.1	~ 0
J093301.58+495029.9	7298	56661	0548	4501.5	~ 0
J102106.04+452331.8	7385	56710	0214	6407.8	~ 0
J122106.86+454852.1	7425	56777	0272	4951.7	~ 0
J015635.70+014816.1	4271	55507	0393	9571.6	~ 0
J223458.73-022419.0	4381	55824	0380	8714.3	~ 0
J213004.76-010244.4	4384	56105	0840	11514.3	~ 0
J001209.85+090249.3	4536	55857	0620	11952.2	~ 0
J012141.59+114950.4	4669	55831	0694	9312.6	~ 0
J091751.28+115258.9	5306	55926	0586	9479.1	~ 0
J140232.37+461233.6	6629	56365	0902	9349.6	~ 0
J132512.19+511933.3	6754	56414	0994	10909.9	~ 0
J024500.70-074736.4	7057	56593	0856	9923.1	~ 0
J114803.17+565411.6	7091	56658	0452	8227.1	~ 0
J110655.96+624800.1	7104	56711	0070	9503.8	~ 0
J213344.19-015716.4	4384	56105	0978	13352.2	~ 0
J114603.76+334551.9	4646	55622	0207	14918.6	~ 0
J094203.33+593709.5	5716	56684	0120	15085.2	~ 0
J115318.07+234113.5	6404	56330	0375	17749.4	~ 0
J093348.07+511405.6	7448	56739	0330	14234.1	~ 0
J014239.99+073239.4	4532	55559	0462	18945.9	~ 0

APPENDIX B

Specfit fitting models

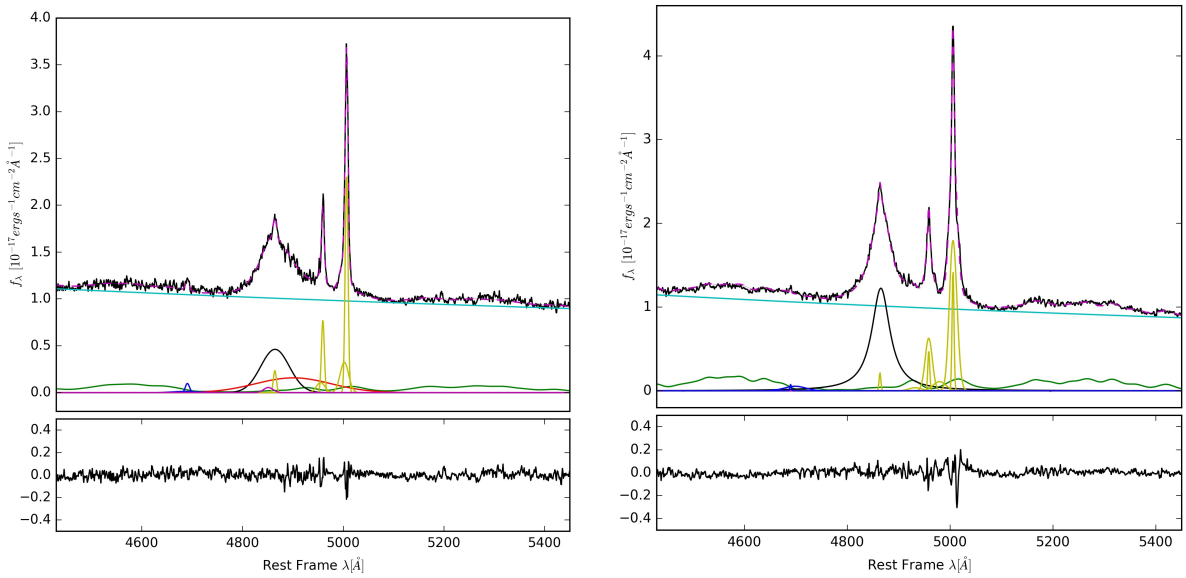

Figure B.1: Spectra of Hβ for spectral type B1 partially resolved loud CD AGN (left) and A1 unresolved detected CD AGN (right). For more details refer to section 2.3.2 and 3.

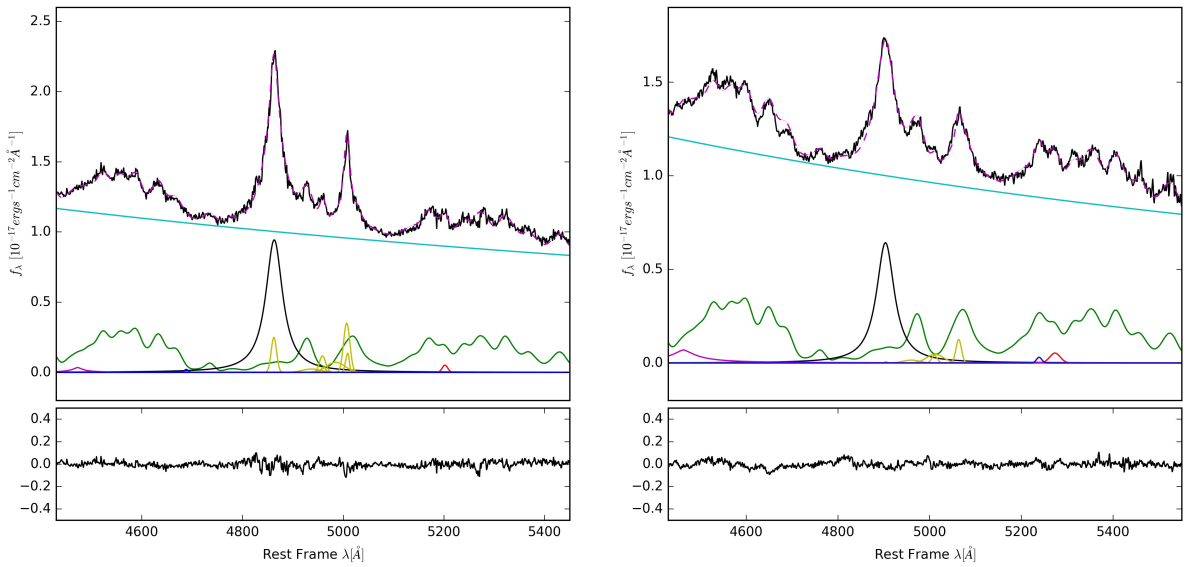

Figure B.2: Spectra of Hβ for spectral type A2 unresolved detected CD AGN (left) and A3 unresolved detected CD AGN (right).

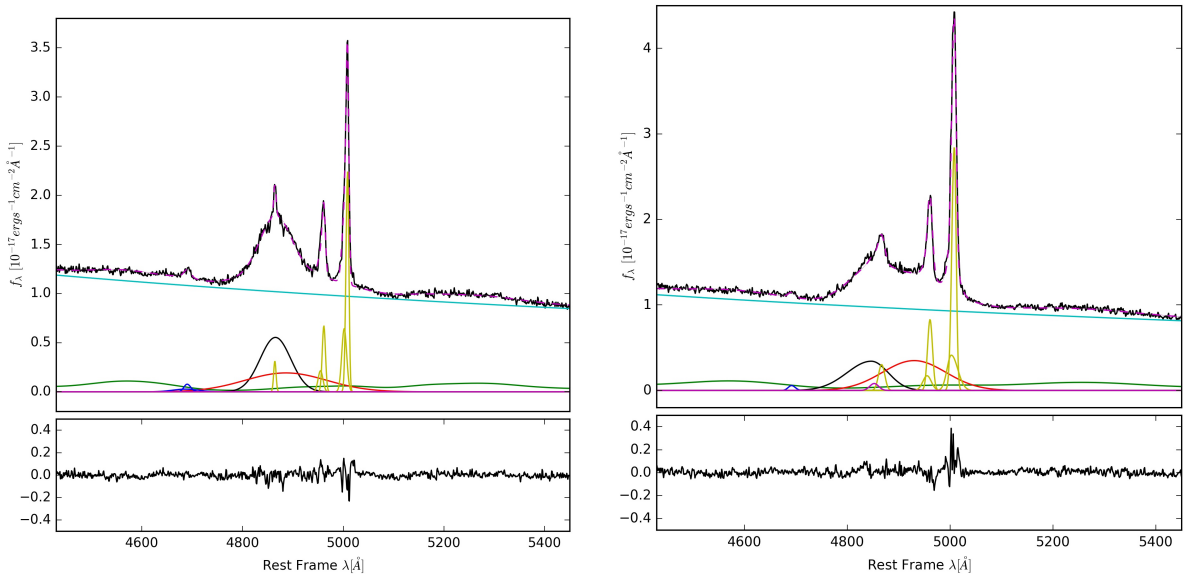

Figure B.3: Spectra of Hβ for spectral type B1 unresolved detected CD AGN (left) and B1+ unresolved detected CD AGN (right).

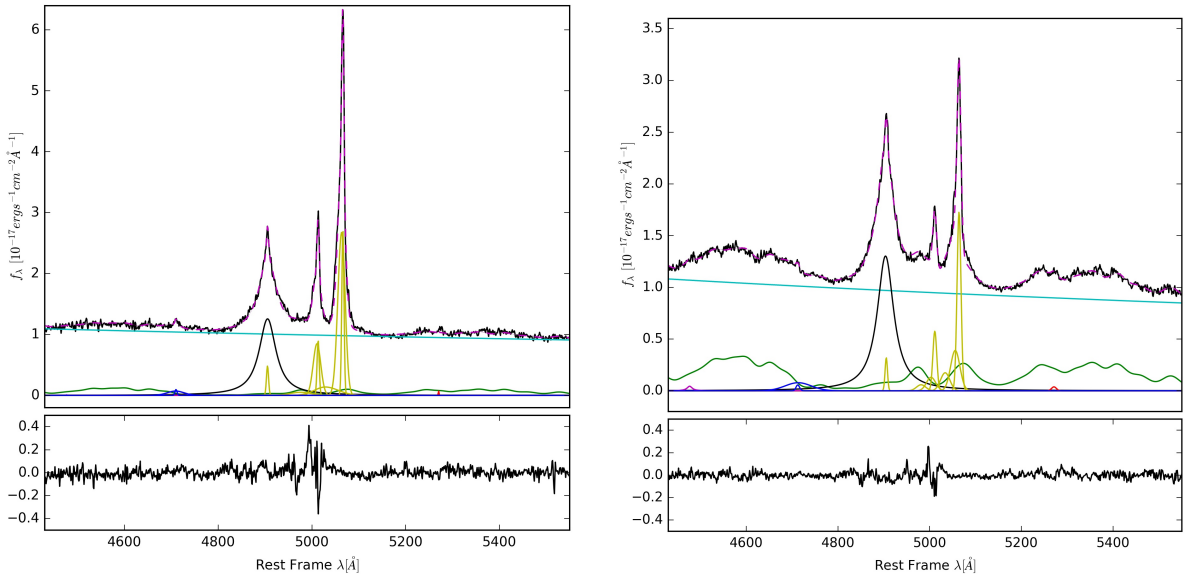

Figure B.4: Spectra of Hβ for spectral type A1 unresolved intermediate CD AGN (left) and A2 unresolved intermediate CD AGN (right).

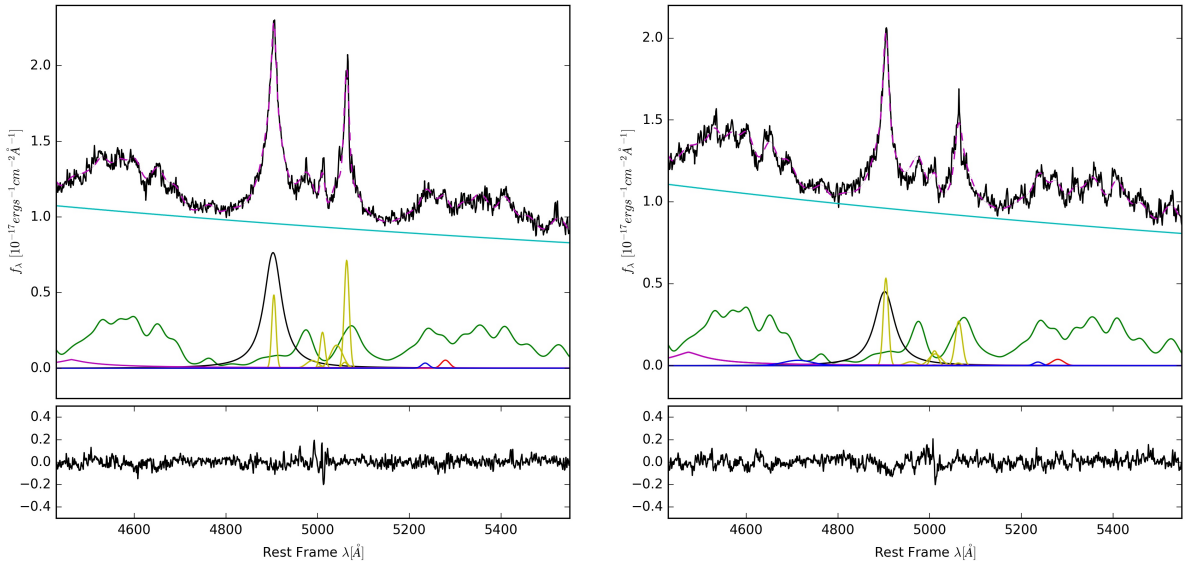

Figure B.5: Spectra of Hβ for spectral type A3 unresolved intermediate CD AGN (left) and A4 unresolved intermediate CD AGN (right).

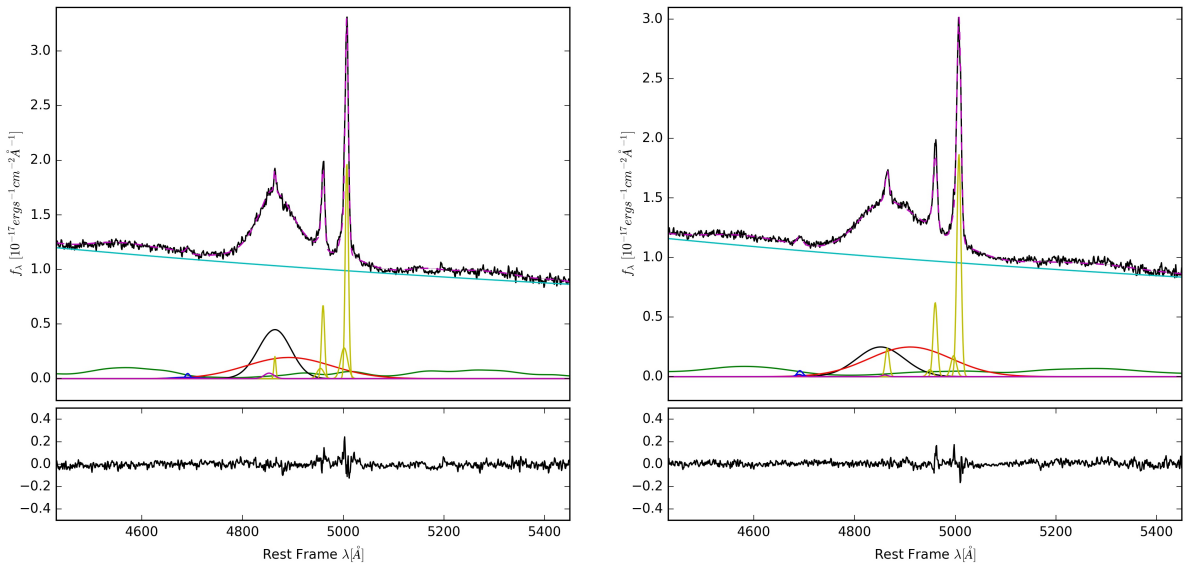

Figure B.6: Spectra of Hβ for spectral type B1 unresolved intermediate CD AGN (left) and B1+ unresolved intermediate CD AGN (right).

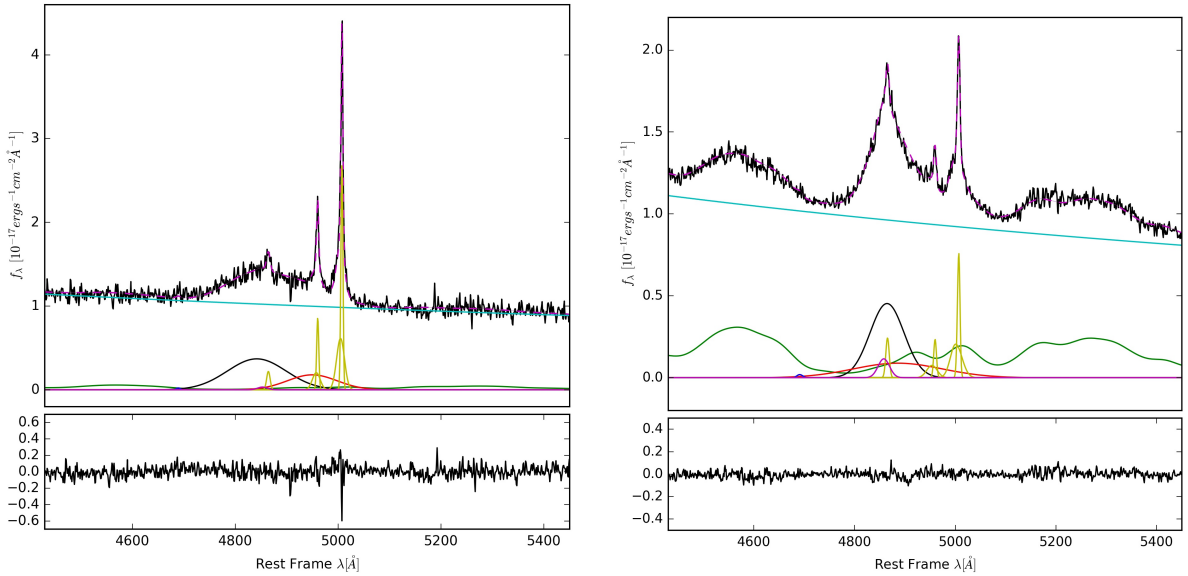

Figure B.7: Spectra of Hβ for spectral type B1++ unresolved intermediate CD AGN (left) and B2 unresolved intermediate CD AGN (right).

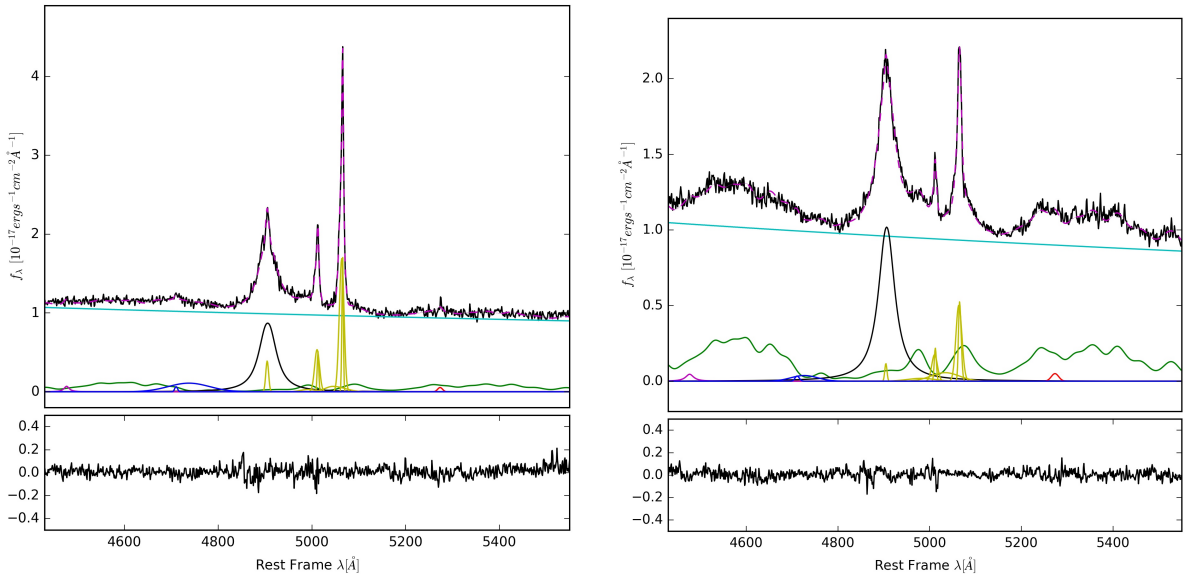

Figure B.8: Spectra of Hβ for spectral type A1 unresolved loud CD AGN (left) and A2 unresolved loud CD AGN (right).

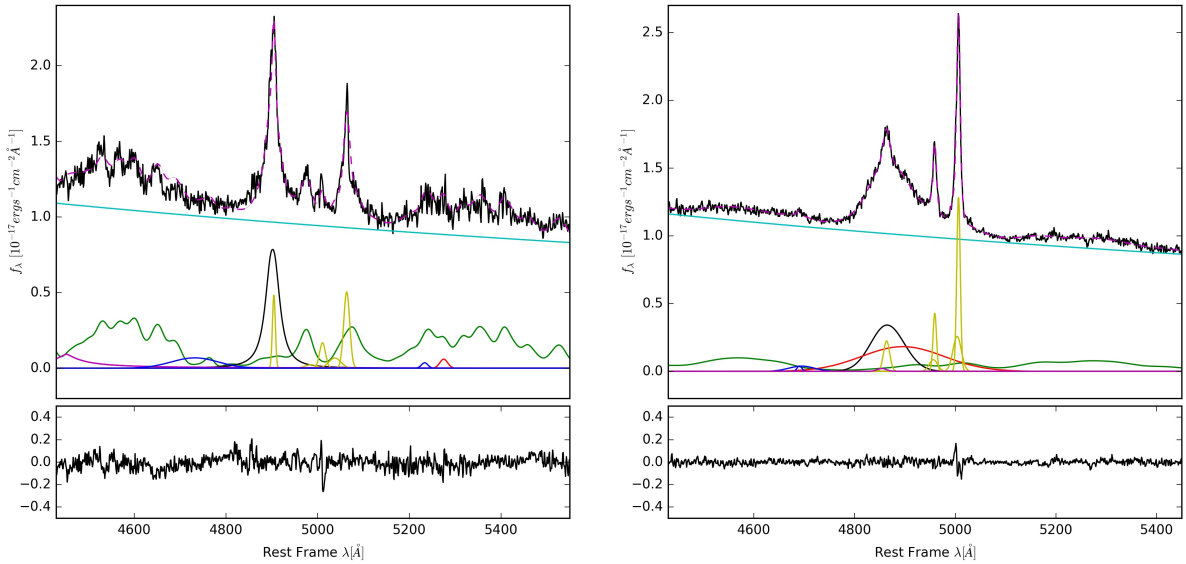

Figure B.9: Spectra of Hβ for spectral type A3 unresolved loud CD AGN (left) and B1 unresolved loud CD AGN (right).

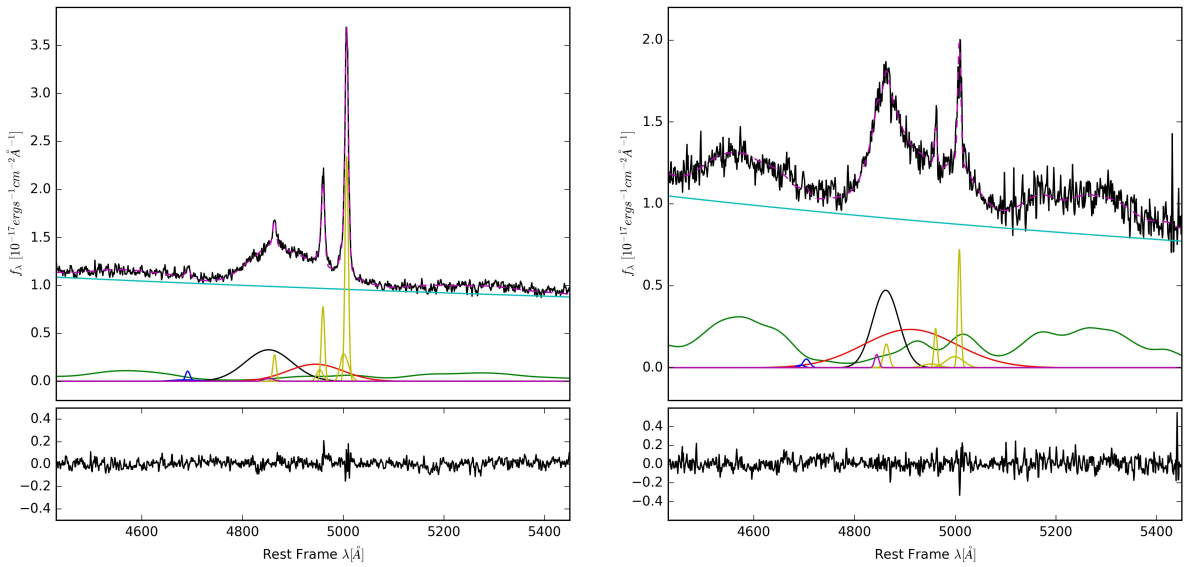

Figure B.10: Spectra of Hβ for spectral type B1+ unresolved loud CD AGN (left) and B2 unresolved loud CD AGN (right).

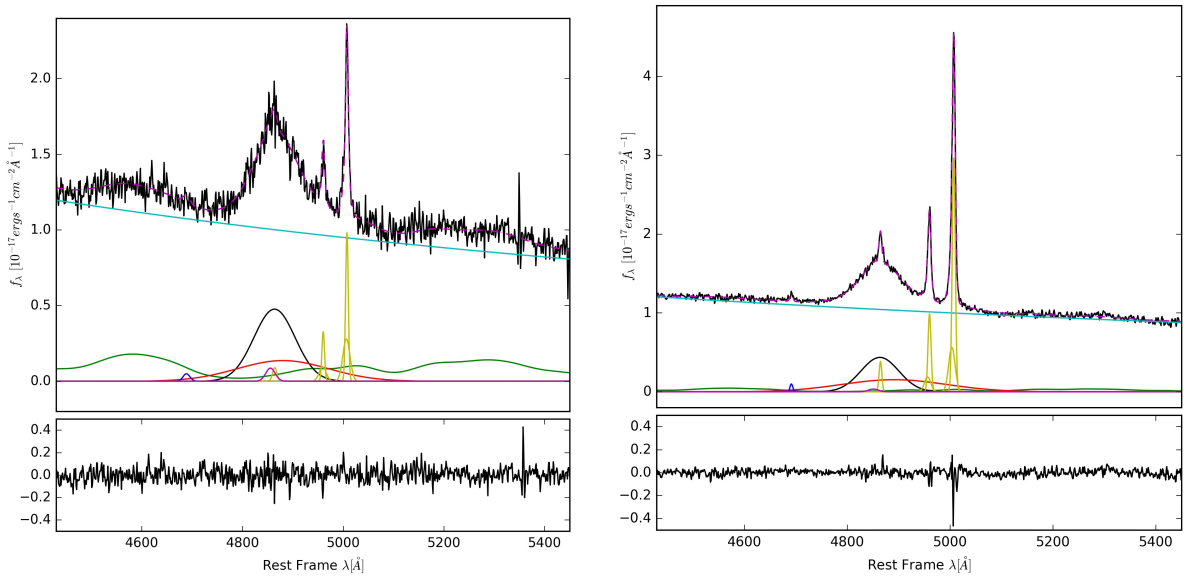

Figure B.11: Spectra of Hβ for spectral type B1 intermediate FRII$_{nc}$ AGN (left) and B1 loud FRII$_{nc}$ AGN (right).

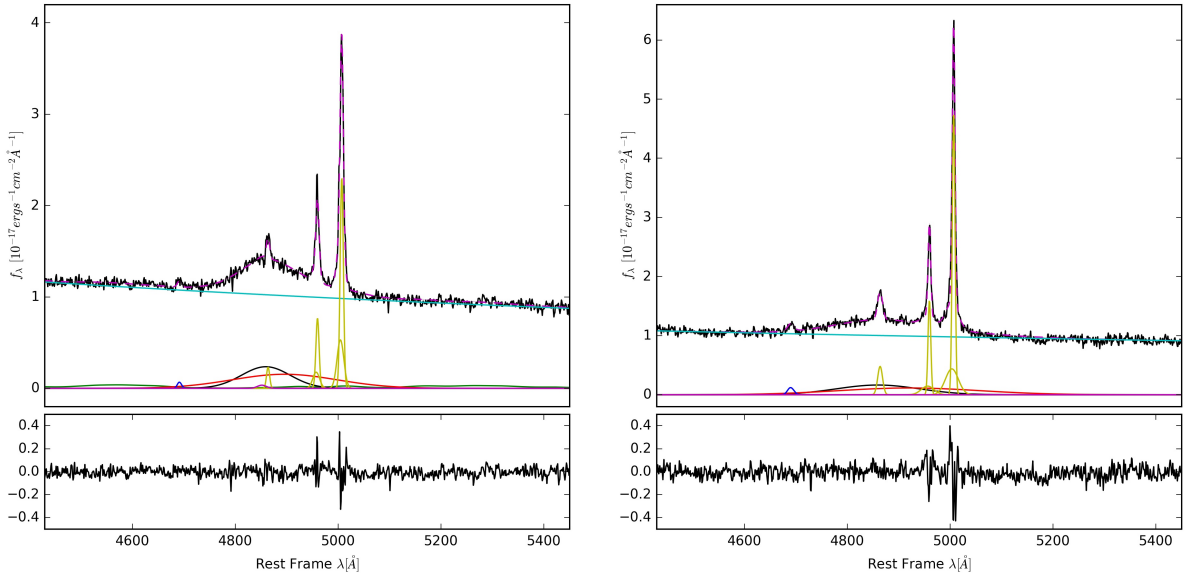

Figure B.12: Spectra of Hβ for spectral type B1+ loud FRII$_{nc}$ AGN (left) and B1++ loud FRII$_{nc}$ AGN (right).

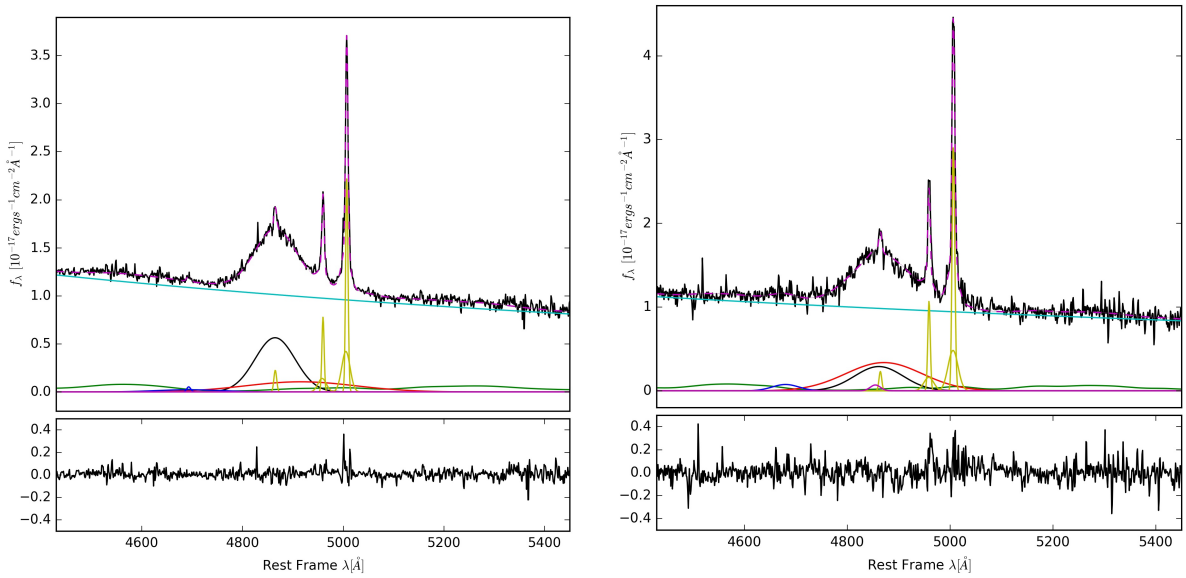

Figure B.13: Spectra of Hβ for spectral type B1 intermediate FRII AGN (left) and B1+ intermediate FRII AGN (right).

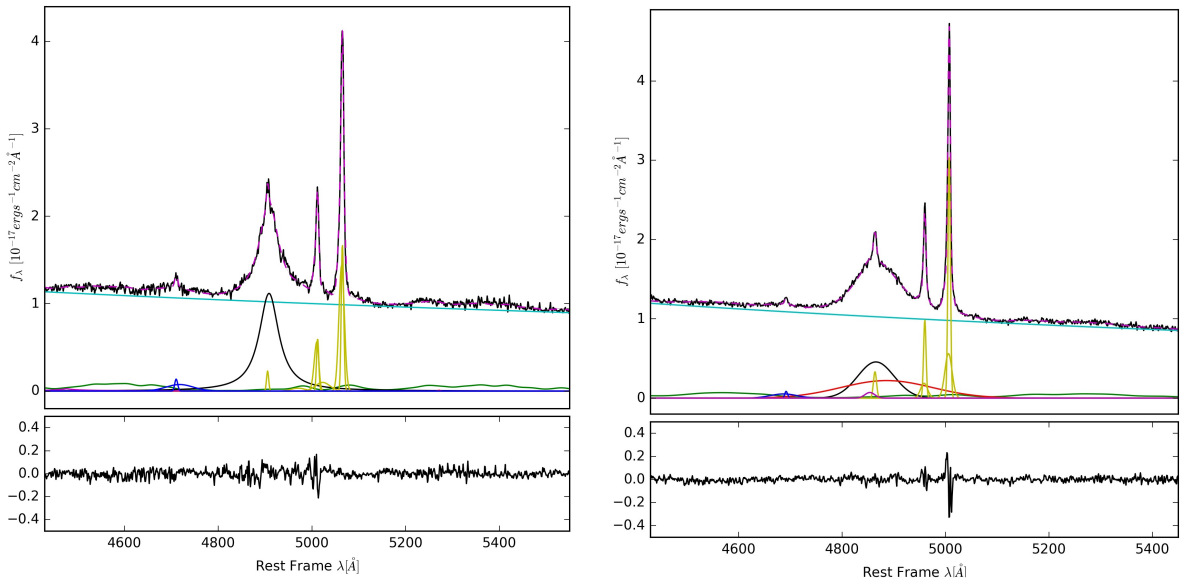

Figure B.14: Spectra of Hβ for spectral type A1 loud FRII AGN (left) and B1 loud FRII AGN (right).

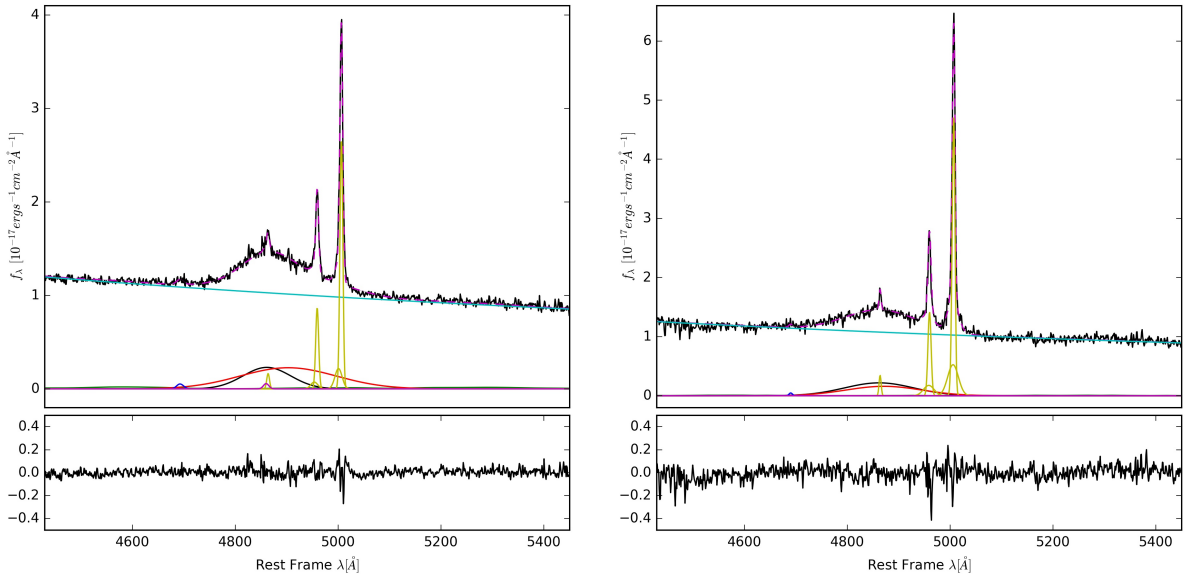

Figure B.15: Spectra of Hβ for spectral type B1+ loud FRII AGN (left) and B1++ loud FRII AGN (right).

List of Figures

List of Tables

Bibliography

[1] Abramowicz M. A., Czerny B., Lasota J. P., Szuszkiewicz E., *Slim accretion disks*, Astrophysical Journal, Part 1 (ISSN 0004-637X), vol. 332, 1988.

[2] Ackermann M., Ajello M., Allafort A., Baldini L., Ballet J., Barbiellini G., Bastieri D., Bechtol K., et al., *Search for Gamma-ray Emission from X-Ray-selected Seyfert Galaxies with Fermi-LAT*, Astrophys J 747: 104. doi:10.1088/0004-637X/747/2/104, 2012.

[3] Aharonian F.A., *TeV gamma rays from BL Lac objects due to synchrotron radiation of extremely high energy protons*, New Astron., 5, 377395, doi:10.1016/S1384-1076(00)00039-7, 2000.

[4] Antonucci R., *Unified models for active galactic nuclei and quasars*, Annual review of astronomy and astrophysics. Vol. 31 (A94-12726 02-90), p. 473-521, 1993.

[5] Balbus A., Hawley F., *A powerful local shear instability in weakly magnetized disks. I - Linear analysis. II - Nonlinear evolution*, Astrophysical Journal, Part 1 (ISSN 0004-637X), vol. 376, July 20, p. 214-233, 1991.

[6] Baldwin J. A., Ferland G. J., Korista K. T., Carswell R. F., Hamann F., Phillips M. M. et al., *Very High Density Clumps and Outflowing Winds in QSO Broad-Line Regions*, Astroph. J. 461, 664+. doi:10.1086/177093, 1996.

[7] Baldwin J. A., Ferland G. J., Korista K. T., Carswell R. F., Hamann F., Phillips M. M. et al., *Emission-line properties of optically and radio-selected complete quasar samples*, Astroph. J., 338:630-653, 1989.

[8] Bardeen J. M., Bond J. R., Kaiser N. and Szalay A. S., *The statistics of peaks of Gaussian random fields*, Astrophys. J. 304, 15-61, 1986.

[9] Barvainis R., *Hot dust and the near-infrared bump in the continuum spectra of quasars and active galactic nuclei*, Astrophys J 320: 537-544. doi:10.1086/165571, 1987.

[10] Beckmann V. and Shrader C., *Active Galactic Nuclei*, WILEY-VCH Verlag GmbH e Co. KGaA, 2012.

[11] Begelman, M.C., Hatchett, S.P., McKee, C.F., Sarazin, C.L., Arons, J., *eam models for SS 433*, ApJ 238, 722730, 1980.

[12] Berton M. et al., *An orientation-based unification of young jetted AGN: the case of 3C 286*, arXiv:1705.07905v2 [astro-ph.GA] 26 Jul 2017.

[13] Beloborodov A. M., *High Energy Processes in Accreting Black Holes*, ASP Conference Series 161, 1999.

[14] Bisnovatyi-Kogan G.S., Ruzmaikin A.A., *The accretion of matter by a collapsing star in the presence of a magnetic field*, Astrophysics and Space Science, Volume 28, Issue 1, pp.45-59, 1974.

[15] Blandford R.D. and Znajek R.L. , *Electromagnetic extraction of energy from Kerr black holes*, Mon. Not. R. astr. Soc. (1977) 179, 433-456, 1977.

[16] Blandford, R. D.; Konigl, A., *Relativistic jets as compact radio sources*, Astrophysical Journal, Part 1, vol. 232, p. 34-48, 1979.

[17] Bogdanovic, Tamara; Reynolds, C. S.; Balbus, S. A.; Parrish, I. J., *Cooling or Boiling? Cooling Flow Problem and MHD Instabilities in Galaxy Clusters*, American Astronomical Society, HEAD meeting n.11, id.4.04; Bulletin of the American Astronomical Society, Vol. 41, p.656, 2010.

[18] Boller T., Brandt W. N. and Fink H., *Soft X-ray properties of narrow-line Seyfert 1 galaxies*, 1Astron. Astroph. 305, 53, 1996.

[19] Bondi H., *On sperichally symmetrical accretion*, 1952MNRAS.112..195B, 1952.

[20] Bonzini M. et al., *Star formation properties of sub-mJy radio sources*, arXiv:1508.01905v1 [astro-ph.GA] 8 Aug 2015.

[21] Boroson T. A. and Green R. F., *The emission-line properties of low-redshift quasi-stellar objects*, Astrophys. J. Supp. 80, 109-135, 1992.

[22] Boroson T. A., *Black Hole Mass and Eddington Ratio as Drivers for the Observable Properties of Radio-loud and Radio-quiet QSOs*, ApJ 565, 7885. doi:10.1086/324486, 2002

[23] Bottcher M., Reimer A., Sweeney K. and Prakash A., *Leptonic and Hadronic Modeling of Fermi-detected Blazars*, Astrophys J 768: 54. doi:10.1088/0004-637X/768/1/54, 2013.

[24] Broderick J.W. and Fender R.P., *Is there really a dichotomy in active galactic nucleus jet power?*, Mon. Not. R. Astron. Soc., 417, 184197, doi:10.1111/j.1365-2966.2011.19060.x, 2011.

[25] Browne, I. W. A.; Wright, A. E., *Relativistic beaming and the optical magnitudes of QSOs*, Monthly Notices of the Royal Astronomical Society (ISSN 0035-8711), vol. 213, p. 97-102, 1985.

[26] Caccianiga A. et al., *SDSS J143244.91+301435.3: a link between radio-loud narrow-line Seyfert 1 galaxies and compact steep-spectrum radio sources?*, Monthly Notices of the Royal Astronomical Society, Volume 441, Issue 172, p. 172186, 2014.

[27] Caccianiga A. et al., *WISE colours and star-formation in the host galaxies of radio-loud narrow-line Seyfert 1*, arXiv:1504.07068v1 [astro-ph.GA] 27 Apr 2015.

[28] Calzetti D., *Star formation rate indicators*, arXiv:1208.2997v1 [astro-ph.CO] 15 Aug 2012.

[29] Capellupo D. M., Netzer H., Lira P., Trakhtenbrot B., *Active galactic nuclei at z $\sim$ 1.5 - I. Spectral energy distribution and accretion discs*, Monthly Notices of the Royal Astronomical Society, Volume 446, Issue 4, p.3427-3446, 2015.

[30] Capetti A., *Revisiting the census of lowluminosity AGN*, Astron. Astrophys., 535, A28, doi:10.1051/0004-6361/201117937, 2011.

[31] Castignani G. and De Zotti G., *AGN torus emission for a homogeneous sample of bright flat-spectrum radio quasars*, Astronomy and Astrophysics, Volume 573, A125, 2015.

[32] Chandrasekhar S., *Mathematical Theory of Black Holes*, Oxford University Press. ISBN 0-19-850370-9, 1999.

[33] Clark D. H., Caswell J. L., *A study of galactic supernova remnants, based on Molonglo-Parkes observational data*, Monthly Notices of the Royal Astronomical Society, vol. 174, p. 267-305, 1976.

[34] Comastri A., Gilli R., Hasinger G., *Rolling down from the 30 keV peak: Modelling the Hard X-Ray and -Ray Backgrounds*, Astronomy 20: 41-47. doi:10.1007/s10686-006-9041-6, 2005.

[35] Comparat J. et al., *Measuring galaxy [OII] emission line doublet with future ground-based wide-field spectroscopic surveys*, arXiv:1310.0615 [astro-ph.IM], 2013.

[36] Condon J. J., Helou G., Sanders D. B., Soifer B. T., *A 1.49 GHz atlas of the IRAS Bright Galaxy Sample*, Astrophysical Journal Supplement Series (ISSN 0067-0049), vol. 73, p. 359-400, 1990.

[37] Condon J. J., Huang Z.-P., Yin Q. F., Thuan T. X., *Compact starbursts in ultraluminous infrared galaxies*, Astrophysical Journal, Part 1 (ISSN 0004-637X), vol. 378, p. 65-76, 1991.

[38] Condon J. J., *Radio emission from normal galaxies*, Annu. Rev. Astron. Astrophys. 30:575-611, 1992.

[39] Condon J. J., Kellermann K. I., Kimball A. E., Ivezic Z., Perley R. A., *Active Galactic Nucleus and Starburst Radio Emission from Optically Selected Quasi-stellar Objects*, Astrophys J 768:37.doi:10.1088/0004-637X/768/1/37, 2013.

[40] Contopoulos I., Kazanas D., *A Cosmic Battery*, The Astrophysical Journal, Volume 508, Number 2, 1998.

[41] Czerny B. et al., *Accretion Disk Model of Short-Timescale Intermittent Activity in Young Radio Sources*, The Astrophysical Journal, Volume 698, Issue 1, pp. 840-851, 2009.

[42] Czerny B. and Hryniewicz K., *The origin of the broad line region in active galactic nuclei*, Astronomy and Astrophysics Volume 525 L8, 2011.

[43] Czerny B. and You B., *Accretion in active galactic nuclei and disk-jet coupling*, arXiv:1507.05852v2 [astro-ph.HE] 15 Oct 2015.

[44] De Vries W. H., Becker R. H. and White R. L., *Double-lobed radio quasars from the Sloan digital sky survey*, The Astronomical Journal, 131:666679, 2006.

[45] Dickey J. M., Salpeter E. E., *1.4 GHz continuum sources in the Hercules cluster*, Astrophysical Journal, Part 1 (ISSN 0004-637X), vol. 284, p. 461-470, 1984.

[46] Dicken D., Tadhunter C., Axon D. et al., *The origin of the infrared emission in radio galaxies. II. Analysis of midto far-infrared Spitzer observations of the 2 Jy sample*, Astrophys. J., 694, 268285, doi:10.1088/0004-637X/694/1/268, 2009.

[47] Doi A. et al., *Kiloparsec-scale radio structures in narrow-line seyfert 1 galaxies*, The Astrophysical Journal, Volume 760, Number 1, 2012.

[48] Done C., Davis S. W., Jin C., Blaes O., and Ward M., *Intrinsic disc emission and the soft X-ray excess in active galactic nuclei*, Mon. Not. R. Astron. Soc. 420, 18481860. doi:10.1111/j.1365-2966. 2011.19779.x, 2012.

[49] Duras F. et al., *The WISSH quasars project II. Giant star nurseries in hyper-luminous quasars*, A& A 604, A67, 2017.

[50] Evans D. A., Worrall D. M., Hardcastle M. J., Kraft R. P., Birkinshaw M., *Chandra and XMM-Newton Observations of a Sample of Low-Redshift FR I and FR II Radio Galaxy Nuclei*, Astrophys J 642: 96-112. doi:10.1086/500658, 2006.

[51] Fanti, C.; Fanti, R.; Dallacasa, D.; Schilizzi, R. T.; Spencer, R. E.; Stanghellini, C., *Are compact steep-spectrum sources young?*, Astronomy and Astrophysics, v.302, p.317, 1995.

[52] Ferrarese, Laura; Merritt, David, *A Fundamental Relation between Supermassive Black Holes and Their Host Galaxies*, The Astrophysical Journal, Volume 539, Issue 1, pp. L9-L12, 2000.

[53] Franceschini A., Vercellone S. and Fabian A.C., *Supermassive black holes in early-type galaxies: Relationship with radio emission and constraints on the black hole mass function*, Mon. Not. R. Astron. Soc., 297, 817824, doi:10.1046/j.1365-8711.1998.01534.x, 1998.

[54] Fraix-Burnet D., Marziani P., DOnofrio M. and Dultzin D., *The phylogeny of quasars and the ontogeny of their central black holes*, arXiv:1702.02468v1 [astro-ph.GA] 8 Feb 2017.

[55] Fukugita M., Ichikawa T., Gunn J. E. et al., *The Sloan Digital Sky Survey Photometric System*, The Astronomical Journal, 111, 1748, 1996.

[56] Garofalo D., *Signatures of vlack hole spin in galaxy evoltion*, The Astrophysical Journal Letters, Volume 699, Number 1, 2009.

[57] C. Martin Gaskell, *Galactic mergers, starburst galaxies, quasar activity and massive binary black holes*, Nature volume 315, page 386 (30 May 1985).

[58] Gendre M. A., Best P. N., Wall J. V., Ker L. M., *The relation between morphology, accretion modes and environmental factors in local radio AGN*, MNRAS 430: 3086-3101.doi:10.1093/mnras/stt116, 2013.

[59] Gehrz R. D., Sramek R. A., Weedman D. W., *Star bursts and the extraordinary galaxy NGC 3690*, Astrophysical Journal, Part 1 (ISSN 0004-637X), vol. 267, p. 551-562, 1983.

[60] Ghisellini G., *Gamma ray bursts: some facts and ideas*, arXiv:astro-ph/0111584v1, 2001.

[61] Giroletti, M.; Polatidis, A., *Samples and statistics of CSS and GPS sources*, Astronomische Nachrichten, Vol.330, Issue 2, p.193, 2009.

[62] Giveon U., Maoz D., Kaspi S., Netzer H., and Smith P. S., *Long-term optical variability properties of the Palomar-Green quasars*, MNRAS 306, 637654. doi:10.1046/j.1365-8711.1999.02556.x, 1999.

[63] Gu Q. and Huang J., *Seyfert 2 galaxies with spectropolarimetric observations*, Astrophys. J., 579, 205213, doi:10.1086/342703, 2002.

[64] Gunn J. E., Siegmund W. A., Mannery E. J. et al., *The 2.5 m Telescope of the Sloan Digital Sky Survey*, Astrophys. J., 131, 2332, 2006.

[65] Haardt F. and Maraschi L. , *A twophase model for the X-ray emission from Seyfert galaxies*, Astrophys. J. Lett., 380, L51L54, doi:10.1086/186171, 1991.

[66] Haardt F. and Maraschi L. , *X-ray spectra from two-phase accretion disks*, Astrophys. J., 413, 507517, doi:10.1086/173020, 1993.

[67] Hatziminaoglou E., Omont A., Stevens J. A., et al., *HerMES: Far infrared properties of known AGN in the HerMES fields*, Astron Astrophys 518:L33. doi:10.1051/0004-6361/201014679, 2010.

[68] Heckman H.T., Philiph N.B., *The Co-Evolution of Galaxies and Supermassive Black Holes: Insights from Surveys of the Contemporary Universe*, arXiv:1403.4620v1 [astro-ph.GA], 2014.

[69] Helfand D. J., White R. L. and Becker R. H., *The last of FIRST: the final catalog and source identifications*, ApJ, 801, 26, 2015.

[70] Hine R.G., Longair M. S., *Optical spectra of 3CR radio galaxies*, MNRAS, 188, 111, 1978.

[71] Ho L.C., *On the relationship between radio emission and black hole mass in galactic nuclei*, Astrophys. J., 564, 120132, doi:10.1086/324399, 2002.

[72] Hogg D. W., Finkbeiner D. P., Schlegel D. J. and Gunn J. E., *A Photometricity and Extinction Monitor at the Apache Point Observatory*, AJ, 122, 2129, 2001. 2002.

[73] Hopkins F. et al., *Black Holes in Galaxy Mergers: Evolution of Quasars*, The Astrophysical Journal, Volume 630, Issue 2, pp. 705-715, 2005.

[74] Ichimaru S., *Bimodal behavior of accretion disks - Theory and application to Cygnus X-1 transitions*, Astrophysical Journal, Part 1, vol. 214, p. 840-855, 1977.

[75] D. Ilic and L. C. Popovic, *Supermassive black holes and spectral emission lines*, Journal of Physics: Conference Series 548, 012002, 2014.

[76] Jackson N. and Browne I.W.A., *Spectral differences between radio galaxies and quasars*, Nature, 343, 4345, doi:10.1038/343043a0, 1990.

[77] Jian-Min Wang, Pu Du1, David Valls-Gabaud, Chen Hu1 and Hagai Netzer, *Super-Eddington accreting massive black holes as long-lived cosmological standards*, arXiv:1301.4225v1 [astro-ph.CO] 17 Jan 2013.

[78] Kaastra J.S., Petrucci P.O., Cappi M. et al., *Multiwavelength campaign on Mrk 509. I. Variability and spectral energy distribution*, Astron. Astrophys., 534, A36, doi:10.1051/0004-6361/201116869, 2011.

[79] Kellermann K. I., Sramek R., Schmidt M., Shaffer D. B., Green R., *VLA observation of objects in the Palomar bright quasar survey*, Astronomical Journal (ISSN 0004-6256), vol. 98, p. 1195-1207, 1989.

[80] Kennicutt R. C. Jr., *The rate of star formation in normal disk galaxies*, Astrophysical Journal, Part 1 (ISSN 0004-637X), vol. 272, p. 54-67, 1983.

[81] Khokhlov A. M. et al., *Jet-induced Explosions of Core Collapse Supernovae*, The Astrophysical Journal Letters, Volume 524, Number 2, 1999.

[82] King A., *Disc accretion in active galactic nuclei*, New Astron. Rev., 52, 253256, doi:10.1016/j.newar.2008.06.006, 2008.

[83] Klein U., Wielebinsky R., Morsi H. W., *Radio continuum observations of M82*, Astronomy and Astrophysics (ISSN 0004-6361), vol. 190, no. 1-2, p. 41-46, 1988.

[84] Koide S., Shibata K., Kudoh T., *General Relativistic Magnetohydrodynamic Simulations of Jets from Black Hole Accretions Disks: Two-Component Jets Driven by Nonsteady Accretion of Magnetized Disks*, The Astrophysical Journal, Volume 495, Issue 1, pp. L63-L66, 1998.

[85] Koide S. et al., in *Proceedings of the 19th Texas Symposium on Relativistic Astrophysics*, E. Aubourg, T. Montmerle, J. Paul, Eds. (World Scientic, Paris, 1999), 01/15, pp. 1-10.

[86] Komossa S. et al., *Radio-loud Narrow-Line Type 1 Quasars*, The Astronomical Journal, Volume 132, Number 2, 2006.

[87] Kraemer S.B., Schmitt H.R., Crenshaw D.M. et al., *Multi-wavelength probes of obscuration toward the narrow-line regionin Seyfert galaxies*, Astrophys. J., 727, 130, doi:10.1088/0004-637X/727/2/130, 2011.

[88] Kukula M.J., Dunlop J.S., Hughes D.H., and Rawlings S., *The radio properties of radio-quiet quasars*, Mon. Not. R. Astron. Soc., 297, 366382, doi:10.1046/j.1365-8711.1998.01481.x, 1998.

[89] Laing R. A., Jenkins C. R., Wall J. V., Unger S. W., *The First Stromlo Symposium: The Physics of Active Galaxies*, ASP Conference Series, 54, 201, 1994.

[90] Laor A., *On black hole masses and radio loudness in active galactic nuclei*, Astrophys. J. Lett., 543, L111L114, doi:10.1086/317280, 2000.

[91] Landt H. et al., *A near-infrared relationship for estimating black hole masses in active galactic nuclei*, arXiv:1303.1923v1 [astro-ph.CO] 8 Mar 2013.

[92] Lawrence A., *The UV peak in active galactic nuclei: a false continuum from blurred reflection?*, Mon. Not. R. Astron. Soc., in press, arXiv:1110.0854, 2012.

[93] LedlowM. J., Owen F. N., *20 CMVLA Survey of Abell Clusters of Galaxies. VI. Radio/Optical Luminosity Functions*, Astronom J. 112: 9-22. doi:10.1086/117985 , 1996.

[94] Li Y. et al., *Spitzer 70μm emissiion as a star formation rate indicator for sub-galactic regions*, The Astrophysical Journal, Volume 725, Number 1, 2010.

[95] Liang E.P.T. and Price R.H., *Accretion disk coronae and CygnusX-1*, Astrophys. J., 218, 247252, doi:10.1086/155677 , 1977.

[96] Lin D.B. et al., *Correlations of Disk and Jet Emission Deviating from the Fundamental Plane*, arXiv:1505.03674 [astro-ph.HE], 2015.

[97] Livio M., Ogilvie G.I., Pringle J.E., *Extracting Energy from Black Holes: The Relative Importance of the Blandford-Znajek Mechanism*, The Astrophysical Journal, Volume 512, Number 1, 1999.

[98] Lu Y. and Yu Q., *Two Different Accretion Classes in Seyfert 1 Galaxies and QSOs*, Astrophys J. 526(1):L5-L8, 1999.

[99] Lupton R., Gunn J. E., Ivezic Z. et al., in *Astronomical Data Analysis Software and Systems X*, eds. F. R. Harnden Jr., F. A. Primini, e H. E. Payne, ASP Conf. Ser., 238, 269, 2001.

[100] Malizia A., Molina M., Bassani L., Stephen J. B., Bazzano A., Ubertini P., Bird A. J., *The INTEGRAL High-energy Cut-off Distribution of Type 1 Active Galactic Nuclei*, Astrophys J Lett 782: L25.doi:10.1088/2041-8205/782/2/L25, 2014.

[101] Malkan M.A. and Sargent W.L.W., *The ultraviolet excess of Seyfert 1 galaxies and quasars*, Astrophys. J., 254, 2237, doi:10.1086/159701, 1982.

[102] J. Magorrian et al., *The Demography of Massive Dark Objects in Galaxy Centers*, The Astronomical Journal, Volume 115, Issue 6, pp. 2285-2305, 1998.

[103] Mannheim K., *The proton blazar*, Astron Astrophys 269: 67, 1993.

[104] Maraschi L., Ghisellini G., and Celotti A., *A jet model for the gamma-ray emitting blazar 3C 279*, Astrophys. J. Lett., 397, L5L9, doi:10.1086/186531, 1992.

[105] Marziani P., Sulentic J. W., Dultzin-Hacyan D., Calvani M. and Moles M. , *Comparative Analysis of the High- and Low-Ionization Lines in the Broad-Line Region of Active Galactic Nuclei*, ApJS 104, 37+. doi:10.1086/192291, 1996.

[106] Marziani, P.; Sulentic, J. W.; Stirpe, G. M.; Zamfir, S.; Calvani, M., *VLT/ISAAC spectra of the H region in intermediate-redshift quasars. III. H broad-line profile analysis and inferences about BLR structure*, Astronomy and Astrophysics, Volume 495, Issue 1, pp.83-112, 2009.

[107] Marziani, P.; Sulentic, J. W.; Negrete, C. A.; Dultzin, D.; Zamfir, S.; Bachev, R., *Broad-line region physical conditions along the quasar eigenvector 1 sequence*, Monthly Notices of the Royal Astronomical Society, Volume 409, Issue 3, pp. 1033-1048, 2010.

[108] Marziani, P.; Sulentic, J. W.; Plauchu-Frayn, I.; del Olmo, A., *Is MgIIλ2800 a reliable virial broadening estimator for quasars?*, Astronomy & Astrophysics, Volume 555, id.A89, 16 pp., 2013.

[109] Marziani P. and Sulentic J. W., *Highly accreting quasars: sample definition and possible cosmological implications*, Mon. Not. R. Astron. Soc. 442, 12111229. doi:10.1093/mnras/stu951, 2014.

[110] P. Marziani, D. Dultzin, J. W. Sulentic, A. Del Olmo, C. A. Negrete, M. L. Martnez-Aldama, M. DOnofrio, E. Bon, N. Bon, G. M. Stirpe, *A main sequence for quasars*, arXiv:1802.05575v1 [astro-ph.GA], 2018.

[111] Mateos S. et al., *Revisiting the relationship between 6 μm and 210 keV continuum luminosities of AGN*, Mon. Not. R. Astron. Soc., Volume 449, Issue 2, 2015.

[112] Mathur S., *Narrow-line Seyfert 1 galaxies and the evolution of galaxies and active galaxies*, Mon. Not. R. Astron. Soc., Volume 314, Issue 4, 2000.

[113] McKinney J.C., Tchekhovskoy A., Sadowski A., Narayan R., *Three-dimensional general relativistic radiation magnetohydrodynamical simulation of super-Eddington accretion, using a new code HARMRAD with M1 closure*, Mon. Not. R. Astron. Soc., 441, 31773208 , 2014.

[114] Meier L., Koide S., Uchida Y., *Magnetohydrodynamic Production of Relativistic Jets*, Science, Volume 291, Issue 5501, pp. 84-92, 2001.

[115] Menou, Kristen, *Black Hole Accretion Disks on the Edge*, The Astrophysical Journal, Volume 596, Issue 1, pp. 414-420, 2003.

[116] Merloni A., Heinz S., Di Matteo T., *A Fundamental Plane of black hole activity*, Mon. Not. R. Astron. Soc., Volume 345, Issue 4, pp. 1057, 2003.

[117] Merloni A., *The anti-hierarchical growth of supermassive black holes*, arXiv:astro-ph/0402495, 2004.

[118] David Merritt1, R. D. Ekers, *Tracing Black Hole Mergers Through Radio Lobe Morphology*, Science 23 Aug 2002: Vol. 297, Issue 5585, pp. 1310-1313 DOI: 10.1126/science.1074688.

[119] David Merritt1 and M. Milosavljevic, *Massive Black Hole Binary Evolution*, arXiv:astro-ph/0410364v2 12 Sep 2005.

[120] Miller P., Rawlings S., Saunders R., *The Radio and Optical Properties of the $Z < 0.5$ BQS Quasars*, Monthly Notices of the Royal Astronomical Society, Vol. 263, NO.2, pp. 425, 1993.

[121] Mineshige S. and Watarai K., *Galactic black hole candidates shining at the Eddington luminosity*, PASJ, 52, 133-141, 2000.

[122] Mirabel I. F., Rodriguez L. F., *Sources of Relativistic Jets in the Galaxy*, Annu. Rev. Astron. Astrophys., 37, 409, 1999.

[123] Murgia, M.; Fanti, C.; Fanti, R.; Gregorini, L.; Klein, U.; Mack, K.-H.; Vigotti, M., *Synchrotron spectra and ages of compact steep spectrum radio sources*, Astronomy and Astrophysics, v.345, p.769-777, 1999.

[124] Narayan R., Yi I., *Advection-dominated accretion: A self-similar solution*, The Astrophysical Journal, vol. 428, no. 1, pt. 1, p. L13-L16, 1994.

[125] Narayan R., Igumenshchev I. V., Abramowicz M. A., *Magnetically Arrested Disk: an Energetically Efficient Accretion Flow*, Publications of the Astronomical Society of Japan, Vol.55, No.6, pp. L69-L72, 2003.

[126] C. Alenka Negrete1, Deborah Dultzin, Paola Marziani, and Jack W. Sulentic, *Reverberation and photoionization estimates of the broad-line region radius in low-z quasars*, The Astrophysical Journal, Volume 771, Number 1, 2013.

[127] Nelson C.H., *Black hole mass, velocity dispersion, and the radio source in active galactic nuclei*, Astrophys. J. Lett., 544, L91 L94, doi:10.1086/317314, 2000.

[128] Netzer H., Lutz D., Schweitzer M. et al., *Spitzer quasar and ULIRG evolution study (QUEST). II. The spectral energy distributions of PalomarGreen quasars*, Astrophys. J., 666, 806816, doi:10.1086/520716, 2007.

[129] Netzer H., *Revisiting the Unified Model of Active Galactic Nuclei*, arXiv:1505.00811 [astro-ph.GA], 2015.

[130] Oke J.B. and Sargent W.L.W, *The nucleus of the Seyfert galaxy NGC 4151*, Astrophys. J., 151, 807, doi:10.1086/149486, 1968.

[131] Ohsuga K., Mineshige S., *Global structure of three distinct accretion flows and outflows around black holes from two-dimensional radiation-magnetohydrodynamic simulations*, Astrophys. J., 736, 1, 2005.

[132] Padovani P. et al., *The very large array survey of the Chandra deep filed South. IV. Source population.*, The Astrophysical Journal, Volume 694, Number 1, 2009.

[133] Padovani P., *The microjansky and nanojansky radio sky: source population and multiwave-length properties*, MNRAS 411:15471561, DOI 10.1111/j.1365-2966.2010.17789.x, 2011.

[134] Padovani P., *The faint radio sky: radio astronomy becomes mainstream*, arXiv:1609.00499v1 [astro-ph.GA], 2016.

[135] Padovani P. et al., *Active Galactic Nuclei: whats in a name?*, arXiv:1707.07134v1 [astro-ph.GA], 2017.

[136] Panessa F. et al., *Narrow-line Seyfert 1 galaxies at hard X-rays*, Mon. Not. R. Astron. Soc. 417, 24262439, 2011.

[137] Penna R.F., Sadowski A., Kulkarni A.K., Naraya R., *The Shakura-Sunyaev viscosity prescription with variable* $\alpha(r)$, MNRAS, Volume 428, Issue 3, p.2255-2274, 2013.

[138] Penrose R., *Gravitational Collapse: The Role of General Relativity*, Rev. Nuovo Cimento 1, Special No. 252, 1969.

[139] Pier J. R., Munn J. A., Hindsley R. B. et al., *Astrometric Calibration of the Sloan Digital Sky Survey*, Astrophys. J., 125, 1559, 2003.

[140] Gabriele Ponti, Mark R. Morris, Regis Terrier and Andrea Goldwurm, *Traces of past activity in the Galactic Centre*, arXiv:1210.3034v1 [astro-ph.GA] 10 Oct 2012.

[141] Richstone D.O. and Schmidt M., *The spectral properties of a large sample of quasars*, Astrophys. J., 235, 361376, doi:10.1086/157640, 1980.

[142] Sandage A., *The Existence of a Major New Constituent of the Universe: the Quasistellar Galaxies*, Astrophys. J., 141:1560, DOI 10.1086/148245, 1965.

[143] Sanders D. B., Phinney E. S., Neugebauer G., Soifer B. T., Matthews K., *Continuum energy distribution of quasars - Shapes and origins*, Astrophys. J., Part 1 (ISSN 0004-637X), vol. 347, p. 29-51, 1989.

[144] Sani E. et al., *Enhanced star formation in narrow-line Seyfert 1 active galactic nuclei revealed by Spitzer*, Mon. Not. R. Astron. Soc. 403, 12461260, 2010.

[145] Sani E. et al., *Physical properties of dense molecular gas in centres of Seyfert galaxies*, Mon. Not. R. Astron. Soc., vol. 424, pp. 19631976, 2012.

[146] Schlafly Edward F., Finkbeiner Douglas P., *Measuring Reddening with Sloan Digital Sky Survey Stellar Spectra and Recalibrating SFD*, The Astrophys. J., Volume 737, Issue 2, article id. 103, 13 pp., 2011.

[147] Schlegel D. J., Finkbeiner D. P. and Davis M., *Maps of Dust Infrared Emission for Use in Estimation of Reddening and Cosmic Microwave Background Radiation Foregrounds*, The Astrophys. J., vol. 500, Issue 2, p. 525-553, 1998.

[148] Scott J.E., Kriss G.A., Brotherton M. et al., *A composite extreme-ultraviolet QSO spectrum from FUSE*, Astrophys. J., 615, 135149, doi:10.1086/422336, 2004.

[149] Shakura N.I. and Sunyaev R.A., *Black holes in binary systems. Observational appearance*, Astron. Astrophys., 24, 337355, 1973.

[150] Shang Z., Brotherton M.S., Green R.F. et al., *Quasars and the big blue bump*, Astrophys. J., 619, 4159, doi:10.1086/426134, 2005.

[151] Yue Shen and Luis C. Ho, *The diversity of quasars unified by accretion and orientation*, Astrophys. J., arXiv:1409.2887v1 [astro-ph.GA], 2014.

[152] Shields G.A., *Thermal continuumfrom acretion disks in quasars*, Nature, 272, 706 708, doi:10.1038/272706a0, 1978.

[153] Sikora M., Stawarz L. and Lasota J.P., *Radio loudness of active galactic nuclei: Observational facts and theoretical implications*, The Astrophys. J., 658, 815828, doi:10.1086/511972, 2007.

[154] Sikora M., Begelman M.C., *Magnetic flux paradigm for radio loudness of active galatic nuclei*, The Astrophys. J., 764, L24, 2013.

[155] Smee S. A., Gunn J. E., Uomoto A. et al., *The Multi-object, Fiber-fed Spectrographs for the Sloan Digital Sky Survey and the Baryon Oscillation Spectroscopic Survey*, The Astrophys. J., 146:32 (40pp), 2013.

[156] Smith J. A., Tucker D. L., Kent S. et al., *The u'g'r'i'z' Standard-Star System*, The Astrophys. J., 123, 2121, 2002.

[157] Sobolewska M. A., Siemiginowska A., Zycki P. T., *High- Redshift Radio-quiet Quasars: Exploring the Parameter Space of Accretion Models. II. Patchy Corona Model*, Astrophys J 617: 102- 112. doi:10.1086/425262, 2004.

[158] Soldi S., Trler M., Paltani S. et al., *The multiwavelength variability of 3C 273*, Astron. Astrophys., 486, 411425, doi:10.1051/0004-6361:200809947, 2008.

[159] Sopp H. M., Alexander P., *A composite plot of far-infrared versus radio luminosity, and the origin of far-infrared luminosity in quasars*, Monthly Notices of the Royal Astronomical Society (ISSN 0035-8711), vol. 251, p. 14P-16P, 1991.

[160] Sulentic J. W., Zwitter T., Marziani P. and Dultzin-Hacyan, D., *Eigenvector 1: an optimal correlation space for active galactic nuclei*, Astrophys. J. 536, L5-L9 , 2000.

[161] Sulentic J. W., Marziani P. and Dultzin-Hacyan D., *Phenomenology of Broad Emission Lines in ARA& A 38*, 521571. doi:10.1146/annurev.astro.38.1.521 , 2000.

[162] Sulentic J. W., Calvani M., and Marziani P., *Eigenvector 1: an H-R diagram for AGN?*, The Messenger 104, 2528 , 2001.

[163] Sulentic J. W., Marziani P., Zamanov R., Bachev R., Calvani M. and Dultzin-Hacyan D., *Average Quasar Spectra in the Context of Eigenvector 1*, ApJL 566, L71L75. doi:10.1086/339594, 2002.

[164] Sulentic J. W., Bachev R., Marziani P., Negrete C. A. and Dultzin D., *C IV λ1549 as an Eigenvector 1 Parameter for Active Galactic Nuclei*, ApJ 666, 757777. doi:10.10n-86n-/n-51n-99n-16, 2007.

[165] Takahashi H.R., Ohsuga K., *Radiation drag effects in black hole outflows from supercritical accretion disks via special relativistic radiation magnetohydrodynamics simulations*, Publications of the Astronomical Society of Japan, Volume 67, Issue 4, 2015.

[166] Yoshiaki Taniguchi and Wada, Keiichi, *The Nuclear Starburst Driven by a Supermassive Black Hole Binary*, APJ, NED, 1996.

[167] Kip S. Thorne, *Disk-accretion onto a black hole. II. Evolution of the hole*, The Astrophysical Journal, 191:507-519, 1974.

[168] Thorne, K. S.; Braginskii, V. B., *Gravitational-wave bursts from the nuclei of distant galaxies and quasars - Proposal for detection using Doppler tracking of interplanetary spacecraft*, Astrophysical Journal, vol. 204, Feb. 15, 1976, pt. 2, p. L1-L6.

[169] Trump J.R., Impey C.D., Kelly B.C. et al., *Accretion rate and the physical nature of unobscured active galaxies*, Astrophys. J., 733, 60, doi:10.1088/0004-637X/733/1/60, 2011.

[170] Trumpler R. J., *Absorption of Light in the Galactic System*, PASP, Vol. 42, No. 248, p.214, 1930.

[171] Turner T. J., George I. M., Nandra K., and Turcan D., *On X-Ray Variability in Seyfert Galaxies*, ApJ 524, 667673. doi:10.1086/307834, 1999.

[172] Ulvestad J. S., *An investigation of the star-burst model for radio emission from Seyfert galaxies*, Astrophysical Journal, Part 1, vol. 259, p. 96-102, 1982.

[173] Urry C.M. and Padovani P., *Unified schemes for radio-loud active galactic nuclei*, Publ. Astron. Soc. Pac., 107, 803, doi:10.1086/133630, 1995.

[174] Wang T., Brinkmann W. and Bergeron J., *X-ray properties of active galactic nuclei with optical FeII emission*, Astron. Astrophys. 309, 81-96, 1996.

[175] Wills B. J. and Browne I. W. A., *Relativistic beaming and quasar emission*, Astrophys. J. 302, 56-63, 1986.

[176] Wilson A. S., Colbert E. J. M., *The difference between radio-loud and radio-quiet active galaxies*, The Astrophys. J., 438, 62, 1995.

[177] Wright E. L. et al., *The Wide-field Infrared Survey Explorer (WISE): Mission Description and Initial On-orbit Performance*, The Astrophys. J., 140, 1868, 2010.

[178] Wu Q., *The black hole mass, Eddington ratio, and $M_{BH} - \sigma_{[OIII]}$ relation in young radio galaxies*, arXiv:0905.3663 [astro-ph.GA], 2009.

[179] Yuan F., Gan Z., Narayan R. et al., *Numerical simulation of hot accretion flows. III. Revisiting wind properties using the trajectory approach*, The Astrophys. J., 804, 101, 2015.

[180] Zamanov, R. et al., *Kinematic Linkage between the Broad- and Narrow-Line-emitting Gas in Active Galactic Nuclei*, MNRAS 387, 856870. ApJL 576, L9L13, 2002.

[181] Zamfir S., Sulentic J. W. and Marziani P., *New insights on the QSO radio-loud/radio-quiet dichotomy: SDSS spectra in the context of the 4D eigenvector1 parameter space*, MNRAS 387, 856870. doi:10.1111/j.1365-2966.2008.13290.x, 2008.

[182] Zirbel Esther L., Baum Stefi A., *On the FR I/FR II Dichotomy in Powerful Radio Sources: Analysis of Their Emission-Line and Radio Luminosities*, Astrophysical Journal v.448, p.521, 1995.